

Chemodynamical Adaptive Mesh Refinement Simulations of Galaxies

C. Gareth Few

A THESIS SUBMITTED IN PARTIAL FULFILMENT
OF THE REQUIREMENTS FOR THE DEGREE OF
DOCTOR OF PHILOSOPHY

Jeremiah Horrocks Institute for Astrophysics and Supercomputing
University of Central Lancashire

28 September 2012

Declaration

The work presented in this thesis was carried out at the Jeremiah Horrocks Institute for Astrophysics and Supercomputing, University of Central Lancashire.

I declare that while registered as a candidate for the research degree, I have not been a registered candidate or enrolled student for another award of the University or other academic or professional institution.

I declare that no material contained in the thesis has been used in any other submission for an academic award. Data and models used in this thesis that are not my own are clearly cited in the text.

Abstract

In this thesis I bring together three projects that comprise my postgraduate studies; using numerical simulations of galaxy formation in a cosmological context. The first of these projects involves the simulation of a suite of galaxies in loose group and field environments. This suite of galaxies is used to compare properties such as the metallicity gradients and morphology to determine if systematic differences are apparent as a function of subtle environmental differences. Almost no distinction is seen between galaxies in the field and the loose group environments: individual assembly histories of the galaxies dominate over ambient environmental effects with the exception of the vertical velocity dispersion of the stellar disc where loose group galaxies tend to exhibit a greater number of instances of impulsive heating of the disc.

In the second project I present further analysis of this suite of galaxies and a comparison with other galaxies simulated using contrasting methodologies, in addition to several semi-numerical galaxy formation models. The focus of this work is the evolution of metallicity gradients and star formation profiles, finding that galaxies form in an inside-out fashion. This leads to steeper metallicity gradients in young stellar populations at high redshift compared with the present day. By considering present day stellar populations with different ages in these galaxies the converse is found, older populations have flatter gradients. This suggests that while the metallicity gradient starts out steep, it flattens over time due to stellar migration/mixing. This flattening due to stellar migration happens at a faster rate than

the flattening of the gas phase metallicity gradient.

Finally, I present an update to the N-body and adaptive mesh refinement hydrodynamical code RAMSES that introduces a more sophisticated feedback treatment, this code is dubbed RAMSES-CH. Under the new scheme, energetic and elemental feedback is contributed by stars throughout their lifetime rather than (as previously) in a single burst. This relaxation of the ‘instantaneous feedback approximation’ in RAMSES-CH opens up the opportunity for studying chemical evolution using adaptive mesh refinement hydrodynamics where previous studies were limited to smoothed particle hydrodynamical codes or semi-numerical models. The new code is applied to the simulation of a typical disc galaxy using different stellar initial mass functions and supernovae type-Ia progenitor models. The influence of these model inputs on the ratio of elemental abundances and supernovae rates in the simulated galaxies are compared as a means of constraining chemical evolution models. The conclusions drawn from this work are discussed in the broader context of galaxy formation simulations.

Contents

Declaration	ii
Abstract	iii
Acknowledgements	xii
1 INTRODUCTION	1
1.1 Background	1
1.2 Numerical Simulation	8
1.3 Chemical Evolution Models	12
1.3.1 Initial Mass Function	17
1.3.2 Stellar Lifetimes	18
1.3.3 Nucleosynthesis	19
1.4 Thesis Outline	21
2 RAMSES DISC ENVIRONMENT STUDY	23
2.1 Introduction	25
2.2 Simulations	28
2.2.1 Gravitational Dynamics	29
2.2.2 Grid Refinement	31
2.2.3 Hydrodynamics	33
2.2.4 Polytropic Equation of State	37

2.2.5	Star Formation	39
2.3	Galaxy Samples	41
2.3.1	Environment	41
2.3.2	Merger History	47
2.3.3	Disc Decomposition	50
2.3.4	Star Formation History	53
2.3.5	Mock Observations	53
2.4	Individual Galaxy Properties	56
2.5	Results	58
2.5.1	Disc Fraction	58
2.5.2	Metallicity Gradients	64
2.5.3	Colour-Magnitude Diagram	69
2.5.4	Age-Velocity Dispersion Relation	71
2.6	Conclusions	76
3	ABUNDANCE GRADIENT EVOLUTION	79
3.1	Introduction	81
3.2	Simulations	85
3.2.1	RaDES	85
3.2.2	MUGS	86
3.2.3	Gal1	92
3.2.4	KN11	93
3.2.5	Chemical Evolution Models	94
3.2.6	Comparing Galaxies from Different Codes	96
3.3	Present-Day Gradients	100
3.3.1	Radial Gradients	100
3.3.2	Vertical Gradients	108
3.4	Evolution of the Radial Gradients	112

3.5	Summary	119
4	RAMSES-CH: A NEW CHEMODYNAMICS CODE	123
4.1	Introduction	124
4.2	Chemical Evolution Models	126
4.2.1	Initial Mass Function	126
4.2.2	Stellar Lifetimes	133
4.2.3	Nucleosynthesis	134
4.2.4	Solar Abundance Determination	137
4.3	Technical Implementation	139
4.3.1	Chemical Evolution Model	139
4.3.2	RAMSES-CH	145
4.4	Chemodynamics of an L_* Galaxy	148
4.4.1	Model Parameters	148
4.4.2	Results	151
4.5	Model Comparison	155
4.5.1	Supernovae Rates	157
4.5.2	Abundance Ratios	162
4.6	Conclusions	168
5	CONCLUSIONS AND FUTURE WORK	172
5.1	The Milky Way Environment	172
5.2	Inside-out Formation	176
5.3	A New Chemical Evolution Code	179
5.4	Future Work	182

List of Tables

2.1	Resolution and mass of different phases in the RAMSES disc environment study galaxies	45
2.2	Simulated galaxy scale length, gradients, metallicities and magnitudes	62
2.3	Test parameters searching for velocity dispersion steps as a function of stellar age	75
3.1	Mass of different phases, disc scale lengths and various metallicity gradients of simulated galaxies from MUGS, RaDES, Rahimi et al. (2011) and Kobayashi & Nakasato (2011)	88
4.1	Chemical evolution models tested in RAMSES-CH	157

List of Figures

1.1	Large-scale structure of a simulated Λ CDM cosmology	3
1.2	Abundance ratios, age-metallicity relation, metallicity distribution and vertical stellar velocity versus metallicity	6
2.1	Adaptive mesh refinement grid in a cosmological simulation	32
2.2	Cooling functions used in RAMSES	36
2.3	$\Delta x/\lambda_J$ versus gas density for grid cells composing the galaxy	38
2.4	The Schmidt-Kennicutt relation for a simulated galaxy	40
2.5	Examples of environments considered in Chapter 2	44
2.6	Major merger time versus merger severity for loose group and field galaxies.	48
2.7	Angular momentum distributions of the simulated galaxies	50
2.8	Simulated galaxy rotation curves	52
2.9	Simulated star formation histories	54
2.10	Mock images of simulated galaxies	55
2.11	Disc mass versus spheroid mass for simulated galaxies	60
2.12	$M_{*,\text{spheroid}}/M_{*,\text{disc}}$ cumulative distribution functions	61
2.13	Young metallicity gradients of the RAMSES disc environment study galaxies	66
2.14	Young stellar metallicity gradients of the RAMSES disc environment study galaxies	67

2.15	Simulated galaxy colour-magnitude diagram	70
2.16	Present day stellar velocity dispersions with age derivatives	74
3.1	Dark-to-stellar mass ratio as a function of stellar mass	97
3.2	Comparison of star formation histories of simulated galaxies	99
3.3	Radial metallicity gradients, for young, intermediate and old stars . .	102
3.4	Distribution of simulated galaxy radial metallicity gradients	105
3.5	Star formation profiles as a function of time for numerically simulated galaxies and semi-numerical models	107
3.6	Vertical metallicity gradients of simulated galaxies	109
3.7	Distribution of simulated galaxy vertical metallicity gradients	110
3.8	Radial metallicity profiles of simulated galaxies at different times . . .	114
3.9	Temporal evolution of simulated and semi-numerical metallicity gra- dients	115
4.1	Commonly used initial mass functions from chemical evolution models	127
4.2	Comparison of solar abundance determinations	138
4.3	Ejection rate of dominant elemental isotopes from a simple stellar population	142
4.4	Mass of elements ejected by stars as a function of their mass. SNIa yield is also shown	144
4.5	Gas distribution of 109-CH	149
4.6	Star formation and supernova rates for a galaxy simulated with RAMSES- CH	152
4.7	Abundance ratios of stars for a fiducial disc galaxy simulated with RAMSES-CH	154
4.8	Abundance ‘strata’ and ‘streams’ for a simulated galaxy	156
4.9	Cumulative supernovae rates for a stellar particle comparing different chemical evolution models	158

4.10 Star formation and supernovae rates for different chemical evolution models	161
4.11 Rotation curves for different realisations of 109-CH	163
4.12 Abundance ratios for different chemical evolution models.	164
4.13 Stellar oxygen abundance (normalised to solar) versus stellar age . . .	166
4.14 Stellar iron abundance (normalised to solar) versus stellar age	167

Acknowledgements

I am indebted to my supervisor, Brad Gibson for all his patient encouragement to go beyond myself and for *asking* rather than *telling*. I warmly thank Stéphanie Courty for her advice (academic and personal) and for hosting me at Observatoire de Lyon, her frank wisdom has been extremely helpful. Many thanks go out to Chris Brook, Greg Stinson, Leo Michel-Dansac, Francesco Calura, Daisuke Kawata, Romain Teyssier, Kate Pilkington and Awat Rahimi for taking the time to help me out. I also thank Rob Thacker for allowing me to visit St. Mary's University, Halifax and to the gang there who provided the warmest of welcomes. I must also mention several individuals who have been responsible for guiding me on the path to my present studies, Mr. Murphy, Alfonso Aragon-Salamanca and Frazer Pearce from whom I drew much inspiration.

None of the work presented herein would have been possible without funding and technical support, the STFC has funded most of my work but I owe no small debt to the COSMOS consortium and UCLan's own HPCF support staff. I must also voice my appreciation for the flexibility and support of the JHI director, Gordon Bromage and research degrees tutor, Tim Cawthorne.

I must also thank my friends, Mike Maxwell for introducing me to the jolliest of green giants, Nicky Agius who (in a couple of her more humane moments) was kind enough to trim my flowing locks and Caroline Alexander, for providing some

(mostly) healthy competition (and occasionally letting me copy her homework). Special thanks go to Lewis Niven for his enduring faith in me and for being there when it really mattered and to Caroline Thomas for being a friend in a strange city.

I cannot express in words the gratitude that I feel towards my mother and father whose unwavering pride has been a real comfort. I am constantly aware that in spite of my contrary nature I am every bit a product of my upbringing, I am perpetually grateful that they made me who I am.

This thesis is dedicated to Jennifer, I would be lost without her kindness and devotion. She has tolerated my absence and presence with equal grace and for that I am eternally grateful.

Chapter 1

INTRODUCTION

For, usually and fitly, the presence of an introduction is held to imply that there is something of consequence and importance to be introduced.

Arthur Machen

1.1 Background

It is widely believed that the early Universe lacked elements other than hydrogen and helium) that compose both our surroundings and ourselves. This makes the search for an understanding of chemical evolution almost a quest for our own origins. The interplay between the evolution of elemental composition and the dynamical processes that have shaped objects of outstanding beauty in the Universe is rich in detail and deeply fascinating. In this thesis we examine the currently accepted paradigms of galaxy formation and chemical evolution, applying them to numerical simulations of galaxy formation to develop a self consistent model of chemodynamics. In the preparation of this thesis we started by testing the effect of environment on

simulated disc galaxies in terms of morphology, kinematics and metallicity gradients. The comparison is conducted between galaxies in isolated field environments and those that inhabit an environment somewhat more similar to that of the Local Group. Following on from this we studied how the star formation distribution affects metallicity gradients and disc scale lengths comparing the previous results with those of other simulations. The final part of this thesis is a description of how the simulation code was developed into a more sophisticated version with the inclusion of more detailed aspects of stellar physics and chemical evolution.

In 1774 Messier published his catalogue of astronomical objects which were widely assumed to exist within the bounds of the Milky Way. It was not until 1924 when Hubble measured the distance to some of these nebulae using Cepheid variables that it was realised that they are extragalactic objects. Hubble later went on to determine that the redshift of galaxies correlates with the distance to them. This led to the concept of a universally expanding Universe that persists until today.

Another piece of the puzzle originates in a discovery by Zwicky in 1933 that there is an inconsistency between the magnitude of the velocities of galaxies in the Coma cluster and the mass inferred from their luminosity. The most widely accepted explanation for this is that there is a non-luminous mass phase (in fact the dominant mass phase) termed ‘dark matter’. Further evidence for the existence of dark matter is to be found in the rotation curves of galaxies (Rubin & Ford 1970), the stability of numerical models of galaxy discs (Ostriker & Peebles 1973), excess X-ray gas emission from ellipticals (Mathews 1978), globular cluster dynamics (Huchra & Brodie 1987), gravitational lensing (Tyson et al. 1990) and the Bullet cluster (Clowe et al. 2004). Most of this evidence also suggests that dark matter is not only non-luminous and transparent to light, but also has a low interaction cross-section with all phases of matter.

Early work intended to constrain the distribution of dark matter quickly ruled

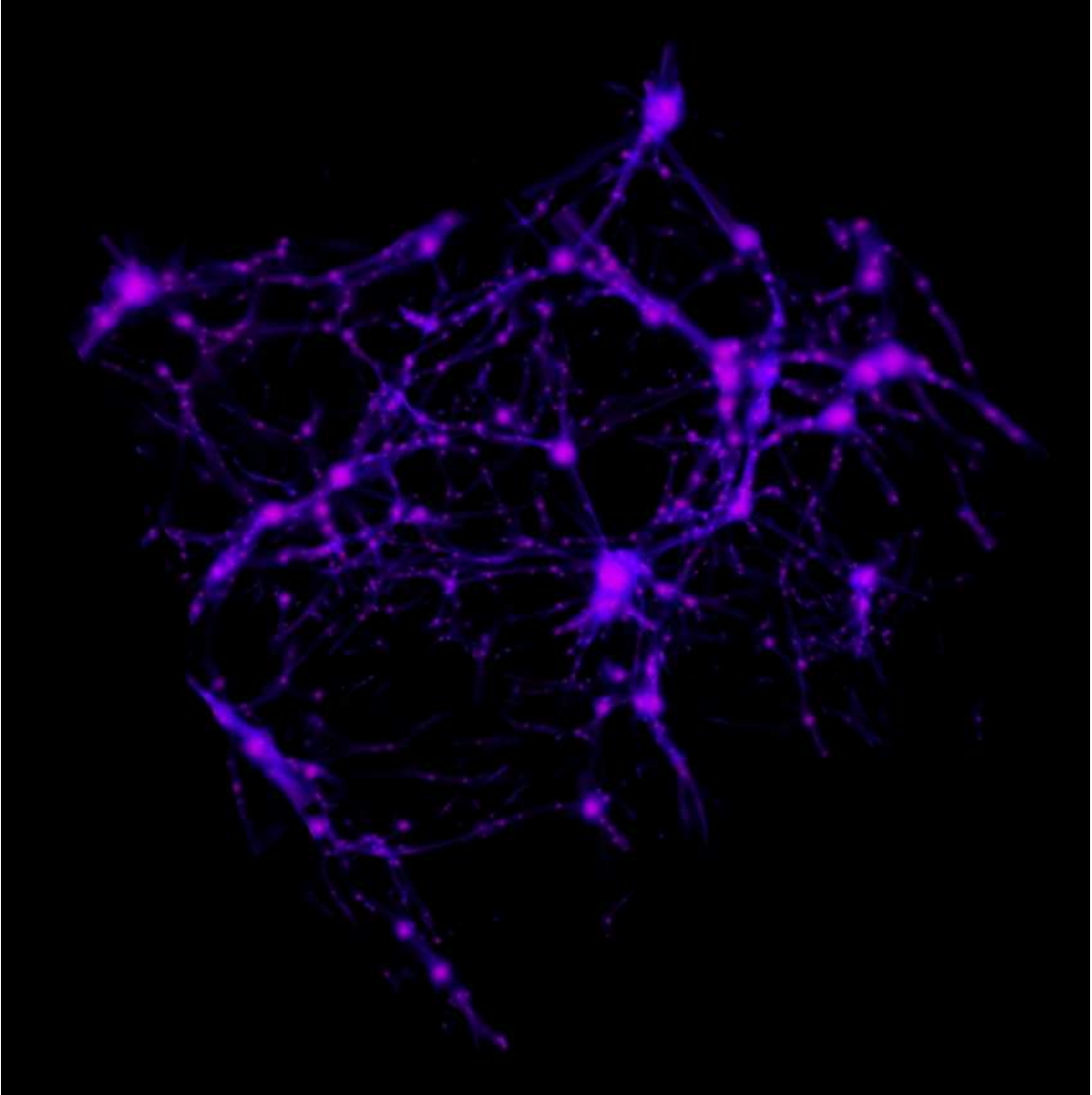


Figure 1.1: Large-scale structure in the Universe is illustrated here by the dark matter distribution in a $20 h^{-1}$ Mpc periodic box with a Λ CDM cosmology. Dark matter haloes are shown connected by a web of filaments, the largest haloes contain entire galaxy clusters while others are found in the voids with a single galaxy at the centre.

out hot (relativistic) dark matter. A Universe filled with hot dark matter would have a smoother distribution but models of hot dark matter are unable to explain the observed clustering of baryons (regular matter). Lower momentum, ‘cold dark

matter’ (Blumenthal et al. 1984) is currently supported by the scientific community. Cold dark matter collapses over time into large-scale filaments with dark matter ‘haloes’ forming at the nodes of the filament network.

The power spectrum of the Universe, a measure of the scale of density perturbations, is now well constrained by observations of the cosmic microwave background and galaxy distributions (Tegmark 1996; Tegmark & Zaldarriaga 2002; Larson et al. 2011). The dark matter distribution of an expanding cold dark matter (Λ CDM) cosmology is shown in Figure 1.1, a network of dark matter haloes can be seen joined by thin filaments occasionally giving a ‘beads on a string’ effect where haloes are aligned on a filament. Two issues remain with the Λ CDM cosmology, though it is not clear how insurmountable they are. The first is the universal presence of steep density cores called ‘dark matter cusps’ that are found in models but are not observed (Flores & Primack 1994; de Blok 2010), this is called the ‘cuspy halo problem’. Recent work suggests however that time variant gravitational potentials caused by baryon outflows may flatten these cusps into cores (Macciò et al. 2012; Pontzen & Governato 2012). The second inconsistency with Λ CDM is the ‘missing satellite problem’; numerical simulations predict the existence of many more dwarf galaxies than are observed (Moore et al. 1999; Klypin et al. 1999) though it is possible these structures are simply inefficient at producing stars and are thus simply unobserved (Simon & Geha 2007).

In tandem with the changing view of cosmology, so too has the understanding of galaxy formation evolved. The diversity of galaxy morphology was first formalised as the Hubble sequence (which despite the common misunderstanding never implied an evolutionary track). The sequence begins with spherical ‘early type’ galaxies moving through ellipticals with increasing ellipticity to the intermediate class of ‘lenticulars’ that exhibit hybrid properties of galaxies on either side of the sequence. The sequence divides here with one class exhibiting bar structure in the central

regions and one that does not. Both barred and un-barred classes are referred to as ‘late types’ or disc galaxies and have a weak spheroidal component and a disc structure that has spiral arms that become less tightly wound further along the sequence. A fourth class of galaxies are called ‘irregulars’ which are transient stages resulting from galaxy mergers, intense star formation or destructive outflows that result in unusual morphologies. Further examination of galaxies revealed that even within each galaxy class there is variation in mass and internal structure. Recognition of separate stellar populations first came with the work of Baade (1944) who identified two populations of stars, with early type galaxies made up of only population II stars but with both population I and II being present in late type galaxies. Population II stars are more metal poor than population I and represent an earlier phase in star formation; they are characteristic of globular clusters and the bulge and halo components of disc galaxies. The distribution of stellar populations with different ages and abundance ratios are now much studied and will be the subject of this thesis.

The origin of angular momentum in galaxies is a result of gravitationally induced tidal torque from large-scale structure (Peebles 1969) which drives the formation of disc structures during the collapse of a primordial gas cloud. The prevailing opinion on mass assembly has moved away from the ‘monolithic’ (smooth collapse of matter on to a single site) of Eggen et al. (1962) towards a more hierarchical scenario (Searle & Zinn 1978; White & Rees 1978) where small fragments gather together gradually through a series of discrete merger events (Fall & Efstathiou 1980). In very simple terms, early mass assembly creates the bulge and halo of disc galaxies, with later gas accretion leading to a lower star formation rate during which time the rotating disc forms. Elliptical galaxies are the remnants of the catastrophic mergers between galaxies that erase the previous structure leaving an elliptical body behind. A new stellar component, the ‘thick disc’ was discovered in the Milky Way by Gilmore &

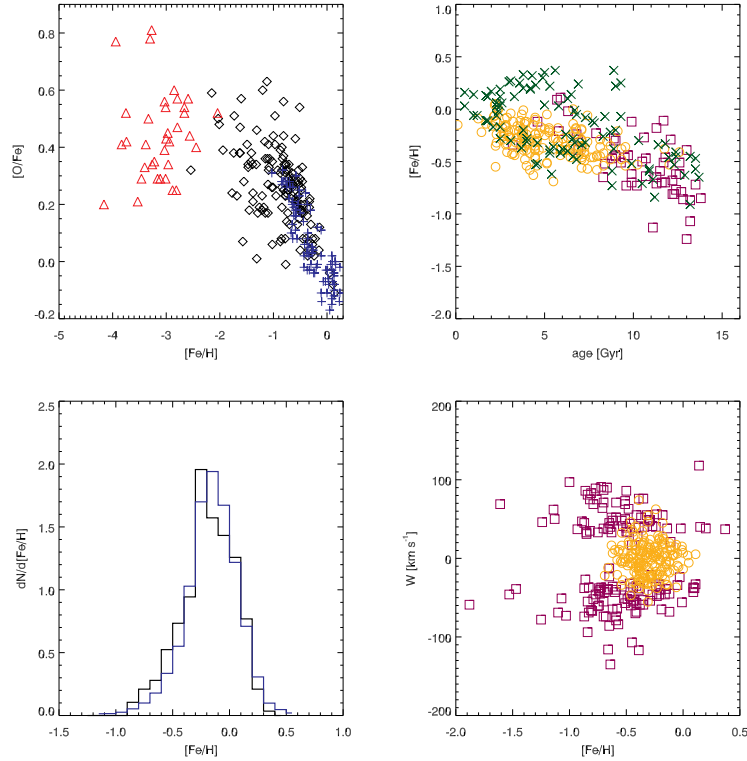


Figure 1.2: Top left: Abundance ratio plot, $[O/Fe]$ versus $[Fe/H]$. Disc dwarf stars from Edvardsson et al. (1993) are plotted as blue crosses, thick-disc and halo stars from Gratton et al. (2003) are black diamonds and very metal-poor stars from Cayrel et al. (2004) are red triangles. Top right: Age-metallicity relation for thin- and thick-disc F and G dwarf stars from Bensby et al. (2005), Reddy et al. (2003) and Reddy et al. (2006) plotted as green crosses, orange circles and magenta squares respectively. Bottom left: Metallicity distribution of the solar neighbourhood from Wyse & Gilmore 1995 (black) and Nordström et al. 2004 (blue). Bottom right: Velocity perpendicular to the disc plane versus metallicity. Orange circles are thin-disc stars from Reddy et al. (2003), purple squares are thick-disc stars from Reddy et al. (2006). Thick-disc stars have a greater vertical velocity dispersion and a much greater range in metallicity.

Reid (1983). The thick disc has a greater scale height than the traditional thin disc. The thick disc has properties that are intermediate between the thin disc and the halo in both kinematics and chemical abundances: see Figure 1.2. The formation process of the thick disc is still debated and it is not clear whether it represents dynamical heating of older disc stars, accretion of satellites or in-situ star formation from high velocity dispersion molecular clouds (Gilmore et al. 1989, and references therein). In Dalcanton & Bernstein (2002) thick disc structures were found to exist in late-type galaxies over a range of masses and although a definitive explanation of the origin of the thick disc has not yet been presented, it is clear that it represents an important feature of galaxy formation, indeed to what extent the thick disc should be considered a discrete feature at all is also thought provoking (Bovy et al. 2012; Brook et al. 2012).

Once the influence of mergers and the complications of star formation are considered, galaxy formation is by its very nature quite non-linear. This makes analytical descriptions of these processes inherently weak and numerical methods prove to be invaluable tools in testing models of galaxy formation and evolution. One of the first great insights to come from numerical simulation of galaxy formation was the confirmation of the so-called ‘angular momentum catastrophe’ (often referred to as ‘over-cooling’, e.g. Navarro et al. 1995) that refers to the excessively efficient collapse of baryons into dark matter potential wells. Historically the angular momentum catastrophe is a numerical effect driven by two-body interactions that leads to an artificial loss of angular momentum. In addition to this there is a ‘cooling catastrophe’ whereby the gaseous phase cools too efficiently, collapsing into the centre of the halo and forming too many star particles, contributing to the loss of angular momentum. The requirement for some kind of energetic feedback from stars to counteract this collapse had been predicted analytically by White & Rees (1978) and Cole (1991) but an accurate study of the feedback mechanisms

was not possible without numerical simulations. These mechanisms tend to restrain star formation, despite star formation itself being responsible for creating feedback sources. The non-linear interaction of star formation and supernovae (SNe) feedback is an intricate mechanism that has attracted much interest in the astrophysical community.

1.2 Numerical Simulation

Many cosmological simulations combine the techniques of N-body dynamics and hydrodynamics to study the behaviour of large scale structure formation. The combination of phenomena that influence vastly different length scales make these simulations useful for connecting star formation and feedback processes with the larger scales of galaxy mergers and cosmological expansion. All the approaches described below must simulate dark matter, stars and baryonic gas. Dark matter and stars are represented by collisionless particles whose dynamics are modelled using N-body methods. The treatment of gas is more complex and different techniques are employed by different groups. Some form of feedback is now a ubiquitous feature of galaxy formation simulations, either in the form of a photoionising UV background (Navarro & Steinmetz 1997), SN feedback (Katz 1992; Metzler & Evrard 1994; Kay et al. 2002) or AGN feedback (Teyssier et al. 2011). The common finding in the majority of the literature concerning this kind of simulation is that the coupling between feedback and the interstellar medium (ISM) must be very efficient (Katz 1992) if galaxies are to avoid the over-cooling that leads to excessive bulge fractions and discs that are too concentrated. Numerical simulations are now at the forefront of theoretical studies of structure formation and provide genuine insight into the various modes and internal processes of galaxy formation and evolution. This thesis is concerned with simulations of cosmological volumes and spatial resolutions

of the order of several hundred parsecs. These simulations are unable to numerically account for physics on smaller scales such as ISM turbulence and molecular cloud formation which are parametrised if necessary. In this section we describe the technical methods used in these complex models.

The majority of simulation codes use Lagrangian, Smoothed Particle Hydrodynamical (SPH) schemes (e.g. Gingold & Monaghan 1977; Lucy 1977; Monaghan 1992; Katz et al. 1996; Springel 2010b) which represent fluid flow with particles. The virtues of using SPH methods lie in the way that the resolution elements move with the flow of the fluid that is represented. This means that the fluid field is more densely sampled in physically dense regions and sparsely sampled where there is little of interest. It also makes tracing the trajectory of all phases of matter through time possible. SPH schemes do however tend to suffer from the inability to accurately resolve instabilities and shocks (O’Shea et al. 2005; Agertz et al. 2007). Gas particles do not naturally experience viscosity which must be accounted for with artificial viscosity terms (Price 2012, and references therein). This artificial viscosity prevents the penetration of a region of low velocity gas by high velocity particles, a situation which should instead lead to the formation of a shock front. Artificial viscosity terms allow the conversion of a gas particles velocity into pressure and hence temperature such that high velocity gas may shock cold gas into a hot dense interface rather than passing straight through.

A different approach uses a spatially fixed grid to calculate the fluid field properties for different regions as a function of time and is known as Eulerian (or ‘grid’) hydrodynamics. Traditionally a uniform cartesian grid delineates cells that each possess a set of attributes that fully describe the fluid state and as gas flows it is transferred across the interfaces of these cells (e.g. Cen & Ostriker 1992; Ryu et al. 1993). To attain sufficient resolution for an accurate description of the gas flow with a uniform grid is costly, which limits the dynamic range of the simulations. This

drawback is circumvented by using a grid that has smaller cells in regions of interest (such as around galaxies) and is known as Adaptive Mesh Refinement (AMR) (Berger & Oliger 1984; Berger & Collela 1989). Early versions of the AMR method used ‘patch-based’ refinements to overlay high resolution regions where required (a scheme that is still employed to good effect in Quilis 2004), while the more sophisticated ‘tree-based’ AMR provides a way of adapting more easily to the gas properties (Khokhlov 1998; Teyssier 2002). The interaction of kinetic with thermal energy in grid codes must be handled differently from SPH codes as the cells are stationary with the gas flowing across the boundary of the cells. The interface between cells represents a discontinuity which, together with the conservation laws that the gas must satisfy, represents a Riemann problem. The use of a Riemann solver allows the hydrodynamical scheme to convert kinetic to thermal energy (and vice versa) so that shocks and free expansion may be achieved.

AMR codes are subject to some flaws, one of which is that they are not Galilean invariant. Gas mixing is a result of numerical advection and thus is more efficient when the gas has a larger velocity relative to the grid (Wadsley et al. 2008); though the authors state that in a test with physically motivated velocities the numerical diffusion is “*probably of the right order to mimic the expected turbulent diffusion*”. A further drawback is the need to initialise the grid which adds an overhead in computational cost to the run-time and potentially makes AMR codes slower. Nevertheless AMR codes offer conservative Euler equation solutions while naturally accounting for gas mixing, viscosity and allow stricter controls to be placed upon the resolution by the user.

There is also a third method for tracing hydrodynamics using a ‘moving mesh’, it is in some sense Lagrangian as the mesh moves with the fluid flow (Gnedin 1995; Pen 1995) to refine overdensities: in principle this makes them Galilean invariant. Difficulties in controlling the mesh during gravitational collapse (Gnedin & Bertschinger

1996) left this method in obscurity until the recent creation of the AREPO code Springel (2010a). This uses a Voronoi grid rather than a regular cartesian grid for fluid elements as a compromise between the virtues of SPH and AMR techniques.

Comparisons of AMR and SPH are performed for various codes in O’Shea et al. (2005), Agertz et al. (2007), Tasker et al. (2008), House et al. (2011), Pilkington et al. (2012a), and Scannapieco et al. (2012). O’Shea et al. (2005) perform tests that compare adiabatic cosmological simulations and find that the SPH code GADGET (Springel et al. 2001) is more efficient than AMR code ENZO (Bryan & Norman 1997, of which two versions are tested) but there is generally a similarity in the results with the only major distinction being the larger fraction of baryons within the virial radius (a difference of 10%, ENZO having the most efficient collapse). It is not clear from the discussion why the collapse is more efficient given that the simulations are adiabatic. In Agertz et al. (2007) a direct comparison of a number of codes through their ability to resolve dynamical instabilities is shown with AMR methods coming away as clear favourites for resolving Kelvin-Helmholtz and Rayleigh-Taylor instabilities. The codes ENZO (both varieties) and GADGET2 (Springel 2005) are again compared in addition to FLASH (Fryxell et al. 2000, , AMR) and HYDRA (Couchman et al. 1995, , SPH) in Tasker et al. (2008). All codes ‘passed’ the standard shock tube and blast wave tests (though several concerning issues are raised for ENZO and GADGET2). The most interesting finding is that the SPH codes are weaker at resolving shocks (and in void regions) while AMR codes are weaker in the centre of collapsed objects. Most recently (and the only comparison involving the code used in this thesis, RAMSES) is Scannapieco et al. (2012) where the complete simulation of a galaxy is performed and compared between codes, showing vastly different galaxies arising from the same assembly history. It would be unfair to attribute these differences entirely to the hydrodynamical scheme as there is a great diversity in the feedback prescriptions. The significant conclusion from Scannapieco

et al. (2012) is that, due to these differences even state-of-the-art simulations are a poor way of making predictions concerning galaxy formation and are better suited to studying the role and relative significance of different processes. A strength of AMR codes that seems to have gone largely unsaid is of particular interest in the context of chemical evolution models. The mixing that is absent in SPH codes (without special consideration) and present in AMR schemes is extremely important when elements are distributed in gas because the diffusion of metals may have a strong impact on both cooling and the global chemical evolution. A final point to note on the comparison of the two methods is that as the sophistication of these codes grows, new versions overcome old short-comings and the issues described above are only general points on the codes. Given the subtle diversity of codes it is wise to consider different implementations of the same methods individually.

The majority of simulations presented in this thesis are performed using RAMSES which is a three-dimensional Eulerian hydrodynamical code. RAMSES also includes an N-body particle-mesh scheme that computes self gravity. The code includes temperature, density and metallicity dependent plasma cooling rates (Kay et al. 2000) and an ultra-violet radiation background (Haardt & Madau 1996). Dense gas forms stars according to a Schmidt-Kennicutt rate and Type-II supernova (SNII) feedback injects energy, momentum and mass back into the ISM. The code is described in more detail in Teyssier (2002), Dubois & Teyssier (2008) and Chapter 2.

1.3 Chemical Evolution Models

While a great deal may be inferred about structure formation from dynamics alone, the element abundances of stars and gas also present valuable and trustworthy contributions to our understanding of galaxy formation. Elements are often referred to as ‘ α -process elements’ if the common isotope of that element is formed through successively adding helium nuclei in nuclear reactions; such elements are C, N, O, Ne,

Mg, Si, S, Ar, Ca and Ti. The other commonly used term for classifying elements that is relevant to chemical evolution is ‘iron-peak elements’, these are elements such as V, Cr, Mn, Fe, Co and Ni and are among the heaviest stable elements produced in stars. Observations reveal that α -process elements are produced in the galaxy on shorter timescales than iron-peak elements (Tomkin et al. 1985; Carbon et al. 1987; Edvardsson et al. 1993; Reddy et al. 2006; Ramírez et al. 2007). This is thought to be a consequence of varying nucleosynthetic processes in stars of different masses and different initial element abundances. Nucleosynthesis also depends upon some of the extreme conditions that arise during the final stages of a star’s life when it may erupt as a SN. The two main types of SN observed are SNII which have broad hydrogen lines in their spectra and SNIa which lack hydrogen and have a strong ionised silicon (Si II) line. SNII are widely thought to represent the end-stage of a massive star’s life and therefore have shorter lifespans than SNIa which are thought either to originate in binary systems where a white dwarf accretes matter from its companion or two white dwarfs merging after emission of gravitational energy (both scenarios take much more time than the lifespan of a massive star). The broad picture emerges of long-lived metal sources (low mass stars or SNeIa) producing predominantly iron-peak elements with the shorter-lived SNeII and other massive stars producing larger quantities of α -elements, this trend is shown in Figure 1.2 (top left panel) that shows the evolution of α -process element oxygen relative to iron, $[O/Fe]$, versus the iron abundance, $[Fe/H]$.¹ Further details to this model come from the unique element abundance ratios that are seen in galactic substructures, allowing the chemical properties of stars to be used as a way of linking populations of stars together even if they are uncorrelated spatially or kinematically.

A successful chemical evolution model (CEM) should be able to recover the

¹The square bracket notation used for stating element abundance ratios is defined as, $[a/b] \equiv \log_{10}(N_a/N_b) - \log_{10}(N_{a,\odot}/N_{b,\odot})$, where N is the number of atoms of a particular element. N may be substituted by mass to attain the same value of $[a/b]$

observed metallicity growth rate and dispersion (Twarog 1980; Meusinger et al. 1991; Edvardsson et al. 1993; Bensby et al. 2005; Ramírez et al. 2007). It is however an unfortunate reality that large uncertainties are associated with the derivation of stellar ages which makes the age-metallicity diagram (top right panel of Figure 1.2) a less reliable constraint than the α -iron diagram (top left panel of Figure 1.2). The dispersion of the iron abundance (Wyse & Gilmore 1995; Nordström et al. 2004) is an observation that may be used to understand the dispersion in metallicity, this is shown in the lower left panel of Figure 1.2.

The relatively modern term of ‘galactic archaeology’ refers to the study of chemical composition of different stellar populations in concert with their kinematics, ages and distribution from which a unified picture of galaxy formation might be established. It is from galactic archaeology that the concept of *inside-out formation* (White & Rees 1978; Fall & Efstathiou 1980) arises in which stars form in the central regions first and later accretions of gas collapse to form stars at the edge of the existing disc. This creates an age gradient and stars in the inner disc and bulge continue to form from the gas enriched by the stars that preceded them and metallicity gradients are born. The evolution of stellar gradients are complicated by the inevitable flattening that comes from secular radial mixing and from mergers. Oxygen gradients are typically measured to be $-0.04 \text{ dex kpc}^{-1}$ for local disc galaxies (Zaritsky et al. 1994; Kaufer et al. 1994; van Zee et al. 1998; Andrievsky et al. 2002, 2004; Dors & Copetti 2005; Bensby et al. 2005; Reddy et al. 2006; Lemasle et al. 2007). It is important to consider that galaxies have been found to have metallicity gradients that correlate somewhat with the scale length of the galaxy (Garnett et al. 1997; van Zee et al. 1998; Prantzos & Boissier 2000) when making comparisons between simulated galaxies that are not precisely Milky Way clones, and note that local spiral galaxies have gradients as steep as $-0.231 \text{ dex kpc}^{-1}$ and as shallow as $0.021 \text{ dex kpc}^{-1}$. Another key constraint on CEMs is the Fe distribution of G and K

dwarf stars (Pagel & Patchett 1975; Wyse & Gilmore 1995; Rocha-Pinto & Maciel 1996) which is perhaps the most effective way of tracing the chemical history of the solar neighbourhood. Inherent in measuring this distribution is defining the solar neighbourhood for a model that is not necessarily identical to the Milky Way: the galactocentric radius and extent of a model ‘solar neighbourhood’ affect the peak and width of the metallicity distribution.

A traditional issue in simple closed-box CEMs is that the models predict a larger number of long-lived metal-poor stars than observations suggest (van den Bergh 1962; Pagel 1997), this is known as the G dwarf problem. The G dwarf problem may arise from poor selection of stars (Bazan & Mathews 1990), though this explanation likely does not provide enough of a correction to observations to fully explain the problem. Another explanation is that the mass function of stars forming in low metallicity gas is skewed away from the low mass end to diminish the number of G dwarfs that might be observed today (Schmidt 1963; Larson 1998). The most successful solution to the G dwarf problem tackles short-comings in the model itself with the addition of a gradual infall rate that allows some early enrichment without excessive star formation (Larson 1972), this kind of infall is included quite naturally in the hydrodynamical simulations described here.

The earliest CEMs were semi-numerical, assuming an initial mass function (IMF) and star formation history (SFH) to calculate the metal content of a region as the result of stellar nucleosynthesis, examples of which may be found in Talbot & Arnett (1971), Pagel & Patchett (1975), Tinsley (1980), Matteucci & Francois (1989), Carigi (1994), Giovagnoli & Tosi (1995), Prantzos & Aubert (1995), Pagel (1997), Chiappini et al. (1997), and Ramírez et al. (2007). These models are extremely useful tools as they allow numerous realisations to be examined, but at the expense of a self-consistent dynamical component. To alleviate this drawback the technique has been applied to merger trees simulated with N-body codes to create *semi-analytical*

simulations (Lacey & Silk 1991; Devriendt & Guiderdoni 2000; Hatton et al. 2003; Pipino et al. 2009) that include analytical descriptions of the effect of mergers to capture some of the dynamical behaviour while keeping simulation run-time short enough to allow for comprehensive parameter studies to be conducted.

The formalism of these models may also be applied to sub-grid chemical evolution treatments in fully hydrodynamical simulations. CEMs have been incorporated into cosmological hydrodynamical codes (all of them SPH codes) to various extents (Lia et al. 2002; Valdarnini 2003; Kawata & Gibson 2003; Kobayashi 2004; Tornatore et al. 2004; Romeo et al. 2005; Scannapieco et al. 2005; Martínez-Serrano et al. 2008b; Oppenheimer & Davé 2008; Wiersma et al. 2009; Stinson et al. 2010; Rahimi et al. 2010; Shen et al. 2010). The results of these models indicate that the cosmological nature of galaxy formation has an impact on the global metallicity and the distribution of metals in the gas and stellar populations. The lower right panel of Figure 1.2 plots the velocity of stars in the direction vertical to the disc plane against $[\text{Fe}/\text{H}]$. Thin disc stars from Reddy et al. (2003) are plotted as orange circles and thick-disc stars Reddy et al. (2006) are plotted as purple squares. The thick disc population is notable for greater velocities and a large dispersion in metallicity when compared with the thin disc. Mergers have a particularly strong impact on chemical evolution, disturbing the distribution of metals and flattening existing gradients (Perez et al. 2011). Gas from the merging body may be funnelled to the central regions (Barnes & Hernquist 1996) and ignite a new burst of star formation in a previously quiescent galaxy. The merger brings not only unenriched gas from the outer regions of the merging body but also pre-enriched stars and gas to add to the newly merged system. Subsequent star formation takes place as more gas is accreted to form a new younger disc structure in place of the disturbed older disc. Secular dynamical processes are also important because bar and spiral structures inspire radial migration to flatten metallicity gradients.

The metallicity of gas is of further interest as it not only acts a historical tracer of galaxy formation but is a significant feature of it. Chemical evolution can have marked effect on the galaxy formation via the metallicity dependence of radiative cooling rates of plasma. Scannapieco et al. (2005) show that the cooling rates of the gas phase results in differing internal stellar dynamics depending on the efficiency with which metals are diffused in the galaxy. This presents a painful quandary as studies show that SPH schemes do not represent turbulent behaviour as accurately as AMR schemes do (O’Shea et al. 2005; Agertz et al. 2007; Tasker et al. 2008) and yet these codes represent the vast majority of cosmological CEMs. Traditional implementations of these codes do not include any treatment of interparticle mixing which further hinders their ability to correctly trace the evolution of metal diffusion (Pilkington et al. 2012b). Mixing is particularly relevant to recovering the metallicity distribution of the solar neighbourhood, plotted in the lower left panel of Figure 1.2. Without sufficient mixing in simulations the metallicity distribution will have excessive number of stars in the extremely metal-poor tail of this distribution (Pilkington et al. 2012b). The introduction of artificial mixing in SPH codes goes some way to improving this drawback (Shen et al. 2010) however the magnitude of this mixing remains a free parameter.

1.3.1 Initial Mass Function

The nucleosynthetic processes and lifetimes of stars are dependent upon their mass and therefore one of the premier ingredients in a chemical evolution model is the IMF. The IMF $\varphi(m)$ defines the total mass of stars, M of that are born with mass m in a given interval dm ,

$$\varphi(m) \propto \frac{dM}{dm}. \quad (1.1)$$

While a qualitative understanding of the form of the IMF was achieved in 1955

in the seminal work of Salpeter (1955), the degree of uncertainty in the actual slope of the IMF is still large enough to result in significant variations in model galactic abundance patterns, e.g. $[\text{O}/\text{Fe}]$ can vary by as much as 0.3 dex depending on the slope of the IMF: see Chapter 4 for details.

The earliest IMF was that proposed by Salpeter (1955) in which the luminosity function of stars is used to determine the mass function of stars at the time they formed. This function fitted as a simple power law with a slope -1.35 over the mass range $0.4 < M/M_{\odot} < 10$. Work on determining the IMF continued with more complex IMFs being proposed to capture the behaviour of the substellar regime. These are multislope IMFs, which are piecewise functions (Tinsley 1980; Scalo 1986; Kroupa et al. 1993; Scalo 1998; Kroupa 2001; Chabrier 2003) and predict a luminosity function that is much closer to the observed value. These IMFs are described in detail and a comparison of the chemical evolution resulting from several choices of IMF is presented in Chapter 4.

1.3.2 Stellar Lifetimes

The stellar lifetimes define the time at which stars move off the main sequence and return nucleosynthesised gas to the ISM. The lifetime is a function of stellar mass and has a lesser dependence on metallicity. For stars that make an energetic contribution to the ISM, the timing of this contribution is also controlled by theoretical stellar lifetimes. In concert with the IMF the lifetimes allow the number and mass of stars evolving from the main sequence to be calculated as a function of the time since the formation of the simple stellar population. After this time stars exist purely as remnants with no further mass or energy output to the ISM.

Different groups have proposed different analytical forms for the lifetimes of stars as a function of mass (Tinsley 1980; Tosi 1982; Maeder & Meynet 1989) and differ significantly only in the substellar regime. In Romano et al. (2005) they find that

stellar lifetimes are generally in better agreement with observations if the substellar lifetimes are longer (Padovani & Matteucci 1993; Kodama 1997) and that deficiencies exist in the [O/Fe] ratio of the model when the massive stars have shorter lifetimes (e.g. Tinsley 1980). Despite the differences in the substellar regimes, the order of the effect that lifetimes have upon chemical evolution is small compared with the IMF and with the uncertain nucleosynthetic yields that are discussed in the next subsection.

1.3.3 Nucleosynthesis

In combination with the IMF and stellar lifetime together with some assumed star formation rate, the final component of a chemical evolution model is the nucleosynthesis model, this describes the build up of more massive elements via nuclear fusion. The nucleosynthetic processes that occur throughout the lifetime of a star and during the explosive processes that cause mass to eject into the ISM are extremely complex. The complexity of these nuclear reactions means that detailed study of these alone is an entire subject of its own, however grids of elemental yields for stars of different masses and metallicities have been published. Note that for the purposes of galactic chemical evolution it is not simply the mass of elements produced throughout the star that concerns us. Elements produced in the core of the star can be transported to the surface and the abundance of various elements are not homogeneously spread throughout the star. This means that some thought must also be given to the mechanism by which elements are ejected as it is the abundance of elements in the material that is ejected and recycled into the ISM that is important.

Yields for low- and intermediate-mass stars are presented in a number of publications including Iben & Truran (1978), van den Hoek & Groenewegen (1997), Marigo (2001), Izzard et al. (2004), Karakas & Lattanzio (2007), Karakas (2010),

and Doherty et al. (2010) and for massive stars in Arnett (1978), Chiosi & Caimmi (1979), Maeder (1992), Woosley & Weaver (1995), Limongi & Chieffi (2003), Chieffi & Limongi (2004), and Kobayashi et al. (2006). The diversity of the physics that is important in stars of different mass regimes and with different evolutionary mechanisms means that nucleosynthetic models do not self consistently cover the mass range from AGB stars to SNeII. To study galactic chemical evolution however it is necessary to consider the full mass range and the yields from different sources in literature are often combined into a single model.

Massive stars, such as would result in SNeII tend to produce predominantly α -process elements and also have short lifetimes which results in an initial phase of chemical enrichment producing an α -enhanced plateau (see the top left panel of Figure 1.2). As time passes, stars with lower masses begin to eject their elements into the ISM as the outer layers of the star are thrown off during the AGB phase, the time at which this occurs depends upon the star's mass. Still later the most long-lived sources of metals in the Universe (SNeIa) begin to eject mass. The contribution of SNeIa to galactic CEM is distinct from the other sources as the elemental yield is quite well constrained (Nomoto et al. 1984; Iwamoto et al. 1999). The greatest uncertainty is the lack of knowledge of precisely what a SNIa progenitor is. Two models are popular, the first imagines a single degenerate C/O white dwarf (WD) with an orbiting companion (Iben & Tutukov 1984; Whelan & Iben 1973). The secondary star acts as an accretion source for the WD during thermal pulsation to allow the WD to surpass the Chandrasekhar mass (the theoretical limit for hydrostatic support of degenerate matter) and hence a thermonuclear runaway occurs. A similar mechanism of a WD surpassing the Chandrasekhar mass is also envisioned for the second mechanism but in this case the mass source is a second WD where collision occurs following an extremely long period of radiation of gravitational energy (Iben & Tutukov 1984; Webbink 1984). Both these processes take a long time

and the elements produced by SNeIa are mainly iron-peak elements, this manifests in Figure 1.2 as a down-turn in $[\text{O}/\text{Fe}]$ at around $[\text{Fe}/\text{H}] = -1$.

1.4 Thesis Outline

In this thesis we use numerical adaptive mesh refinement simulations to consider a number of issues. The main objectives are to study the effect of galaxy environment, gain insight into galaxy evolution and apply that understanding in enhancing the simulation technique. Up to this point we have described the broad background of the subject of galaxy formation in a cosmological context and the chemical evolution of galaxies. In Chapter 2 we describe a suite of 19 simulated galaxies taken from loose group and field environments; loose groups are environments similar to the Local Group while the field galaxies are entirely isolated. These galaxies are used to test the assumption that simulated field galaxies are comparable with the Milky Way which inhabits a sparse group environment. In this initial run of simulations we search for systematic differences in the metallicity gradients, kinematics and morphology of galaxies inhabiting different environments. The main motivation here is to ascertain whether galaxies that are isolated from the influence of other galaxies (as are commonly simulated) are apt for comparison with the Milky Way (which inhabits the Local Group environment). Chapter 3 describes some work done in comparing the galaxy suite from Chapter 2 with galaxies produced using other codes and semi-numerical models. This comparison work considers how star formation profiles evolve in simulated galaxies naturally leading to “inside-out” formation of the galaxy disc. The evolution of metallicity gradients is considered finding that young stellar gradients are steeper at high redshift than today but conversely (and in contradiction to observation) older stellar populations have flatter gradients than younger ones at the present day. Chapter 4 describes the new cosmological chemodynamical simulation code RAMSES-CH that builds on the feedback scheme used

in RAMSES(v3.07) to include SNIa feedback and detailed chemical evolution. The validity of the approach taken is first demonstrated with a test run before different chemical evolution models are applied that show how different IMFs and SNIa progenitor models affect the chemical properties of galaxies. The conclusions drawn throughout this thesis are stated in Chapter 5 and there is a discussion of potential future work using the advancements presented here.

Chapter 2

RAMSES DISC ENVIRONMENT STUDY

In science one tries to tell people, in such a way as to be understood by everyone, something that no one ever knew before. But in poetry, it's the exact opposite.

Paul Dirac

Abstract

Cluster and group environments are known to influence the properties of the galaxies they harbour. It is however common for theoreticians to simulate galaxies in cosmological field environments or even in complete isolation and compare the results with observations of the Milky Way which inhabits a small group. We test the validity of comparing simulated field disc galaxies with the empirical properties of systems situated within an environment more comparable to the Local Group. This is achieved through the simulation of a suite of cosmological disc

galaxies in field and in environments with properties similar to the Local Group. Apart from environmental differences in the galaxies, the samples are kept as homogeneous as possible with equivalent ranges in the last major merger time, halo mass and halo spin parameter. Comparison of these two samples allows systematic differences to be identified.

A kinematic decomposition is employed to objectively quantify the spheroid-to-disc ratio and to isolate the stellar disc population. Metallicity gradients, disc scale lengths and age-velocity dispersion relations are studied for each galaxy in the suite and the strength of the link between these and the environment of the galaxy is examined.

We note an increased likelihood for loose group galaxies to have a more step-like form to their age-velocity dispersion relations suggesting that impulsive heating is more prevalent in the denser environment of the loose group than in the field. Other properties exhibit no difference as a function of environment where the assembly history and secular evolution of each galaxy dominates the morphology distribution and metallicity gradients. Metallicity gradients are found to be consistent with observations of HII regions in spiral galaxies and correlate with total galaxy mass, also in agreement with observations. The galaxy morphologies are for the most part disc dominated with only the least massive galaxies possessing dominant spheroids. We conclude that at the resolution employed here (~ 400 pc) disc galaxy simulations may safely compare properties against observations of galaxies in the Local Group provided care is taken in matching the assembly history.

2.1 Introduction

It is well established that galaxy interactions and mergers result in significant changes in a system's star formation rate (Barton et al. 2000; Lambas et al. 2003; Nikolic et al. 2004; Ellison et al. 2008) and its chemical properties (Donzelli & Pastoriza 2000; Márquez et al. 2002; Fabbiano et al. 2004; Kewley et al. 2006a; Michel-Dansac et al. 2008; Rupke et al. 2008; Kewley et al. 2010b; Sol Alonso et al. 2010). Studies have shown that in denser large-scale environments the star formation rate of galaxies tends to be lower (Gómez et al. 2003). It is often suggested that galaxies in clusters are older and have therefore consumed the limited gas available for star formation (Lilly et al. 1996), or that proximity to other galaxies means that the reservoir of infalling gas must be shared (Lewis et al. 2002). It is also thought that the star formation rate may be reduced in dense environments via the ram pressure stripping that removes the gas envelope from field galaxies as they are accreted to groups and clusters (Balogh et al. 2004b).

Proximity to a cluster centre is also known to impact the morphology of galaxies, and clusters have a greater fraction of early type galaxies; i.e. the so-called morphology-density relation (Dressler et al. 1997). While the accretion of field galaxies into denser environments may strip gas from the galaxy and leave a slowly reddening S0 galaxy, it will do little else to alter the morphology. Morphological transformations are therefore attributed to gravitational interactions with other group members (Moore et al. 1996; Weinmann et al. 2006). There is also a link between the likelihood of galaxy mergers and the density of the environment although this depends on the redshift considered as established clusters at low redshift can have a lower merger rate than smaller galaxy groups (Gottlöber et al. 2001) due to the hotter dynamics in cluster environments. Gottlöber et al. (2001) does show that isolated environments have lower merger rates than groups at almost all redshifts even if the merger rate in galaxy clusters is significantly less than both of the more

sparse environments after $z \sim 2$. The environmental dependence on merger rates is supported by the findings of McGee et al. (2008) where an enhancement in the number of asymmetric discs is found in group environments (these groups typically have velocity dispersions less than 700 km s^{-1} , smaller than the larger clusters considered in many other works). The authors also put forward the intriguing conclusion that while the groups exhibit a larger fraction of galaxies that are bulge dominated, *no evidence is found that the group environment has any effect on the bulk properties of the disc galaxy population.*

Mergers have a direct impact on both the star formation history of the galaxies and the metal distribution. Hydrodynamical simulations by Hernquist & Katz (1989) and Barnes & Hernquist (1996) show that mergers funnel gas into the central regions of galaxies. This would tend to dilute the gas phase metallicity at small radii and trigger centrally concentrated star formation (Rupke et al. 2010a; Montuori et al. 2010; Perez et al. 2011). This trend is consistent with observations of flattened metallicity gradients in luminous and ultraluminous infrared galaxies that are identified as merged systems (Rupke et al. 2008) and in interacting galaxy pairs (Ellison et al. 2008; Michel-Dansac et al. 2008; Kewley et al. 2010b) where the influence on star formation rates extends to projected separations of up to $40 \text{ h}^{-1} \text{ kpc}$ (Ellison et al. 2008).

Interactions are far more common in denser environments and one would expect to see the effect of these interactions imprinted on the metallicity of cluster and group galaxies when compared with those in the field. Cooper et al. (2008) observe that not only do members of clusters have greater metallicities but also that on average galaxies that are closer to other cluster members have greater oxygen abundances (an effect of order 0.05 dex). The conclusion of the work is that metallicity effects are not driven by the cluster as a whole but only by the specific proximity of each galaxy to others; consistent with past findings (Balogh et al. 2004a; Martínez et al. 2008).

The independence of metallicity on large-scale environment is perhaps refuted by the findings of Ellison et al. (2009) where a residual metallicity-environment effect is found observationally even after the dependence on luminosity and colour have been accounted for, these two results are however not entirely irreconcilable. Martínez-Vaquero et al. (2009) select simulated dark matter systems based on the mass and circular velocity of haloes, the mutual proximity of the haloes and the distance to a halo with the same mass as the Virgo cluster. These simulations explore the properties of the haloes while relaxing these criteria and find that the nearness of massive external haloes is the most significant factor determining the dispersion of Local Group systems: the coldness of the Local Group can be attributed mostly to its isolation from clusters.

Recent simulations have employed higher resolution and more advanced SN feedback prescriptions which ameliorate the traditional failings of galaxy simulations (Robertson et al. 2004; Governato et al. 2007; Scannapieco et al. 2009; Sánchez-Blázquez et al. 2009; Stinson et al. 2010; Rahimi et al. 2010; Brooks et al. 2011). It is now possible (and prudent) to examine the more subtle factors that influence galaxy properties. Given the demonstrable difference between galaxies in different (albeit extremely so) environments it is reasonable to expect that galaxies in loose groups such as our own Local Group may differ from those in the field.

At present the majority of literature on this topic focuses on constrained simulations based upon cosmological initial conditions that will purposefully give rise to systems with the properties of the Local Group (Gottlöber et al. 2010; Peirani 2010; Libeskind et al. 2011; Peirani et al. 2012) or the use of extremely large simulation volumes to search for analogous systems (Springel et al. 2005; Snaith et al. 2011, and references therein). Here we provide a complementary approach by identifying Local Group analogs in a suite of hydrodynamical simulations. In what follows, we will explore the hypothesis that simulated field galaxies can be considered suitable

proxies for Local Group analogs.

The purpose of this work is not to reproduce artificial clones of the Local Group but rather to gauge the systematic offset in properties between field galaxies and those with a similar degree of interaction with neighbours such as is encountered between the Milky Way and Andromeda. These groups are henceforth termed as ‘loose groups’ to be clear that the systems in the loose group sample are not Local Group clones from initial conditions designed to reproduce the exact layout of the local Universe but are chosen from cosmological simulations based on certain similarities to the Local Group. In doing so a sample of galaxies is created, the RAMSES disc Environment Study (RaDES) sample, with a range of merger histories that nonetheless produce disc galaxies. It is hoped that the discrepancy between the properties of these two samples will place constraints on future simulations and present insight into the failings of field galaxy simulations when attempting to recover the properties of Local Group galaxies. A description of the RAMSES code is given in §2.2, the method employed in producing the samples and reducing the data are described in §2.3; a description of the global properties of the galaxies is also given here. In §2.5 we present an analysis of the galaxy disc fractions, metallicity gradients and velocity dispersions and discuss the meaning of these results in §2.6.

2.2 Simulations

The galaxies presented here were simulated using the AMR code RAMSES (v3.01) (Teyssier 2002). RAMSES is a three-dimensional Eulerian hydrodynamical code with an N-body particle-mesh scheme to compute self-gravity. The mesh automatically refines according to the local particle density in addition to a static refinement of nested regions that reduces the run-time while maintaining high resolution around the galaxy of interest. Details of the refinement scheme are described by Teyssier

(2002). RAMSES includes temperature, density and metallicity dependent radiative cooling rates, assuming ionisation equilibrium with an ultra-violet radiative background (Haardt & Madau 1996). We now describe some of the details in the implementation of the main technical components of RAMSES.

2.2.1 Gravitational Dynamics

Gravitational dynamics are eminently important on cosmological scales, dominating over all other forces. In N-body simulations the mass distribution of the Universe is modelled through the gravitational attraction of an ensemble of collisionless point masses. Both dark matter and stars may be modelled in this way (gas dynamics requiring a more complicated scheme) and differ only in that star particles have additional properties such as elemental abundances and ages. The motion of collisionless particles in a gravitational potential can be described using the following equations:

$$\frac{d\mathbf{r}_i}{dt} = \mathbf{v}_i, \quad (2.1)$$

$$\frac{d\mathbf{v}_i}{dt} = -\nabla\Phi, \quad (2.2)$$

$$\nabla^2\Phi = 4\pi G\rho, \quad (2.3)$$

where \mathbf{r}_i and \mathbf{v}_i are the position and velocity vectors of particle i , Φ is the scalar gravitational potential and ρ is the density field. Equation 2.3 is Poisson's equation and relates the density distribution to the gravitational potential. The simulations discussed in this work are cosmological in nature and these equations may be recast in comoving coordinates $\mathbf{x} = \mathbf{r}/a(t)$ and conformal time $d\tau = dt/a(t)$ where $a(t)$ is the cosmological expansion factor (Peebles 1980; Bertschinger 1998):

$$\frac{d\mathbf{x}_i}{d\tau} = \mathbf{v}_i, \quad (2.4)$$

$$\frac{d^2\mathbf{x}_i}{d\tau^2} + \frac{\dot{a}}{a} \frac{d\mathbf{x}_i}{d\tau} = -\nabla\Phi' \quad (2.5)$$

$$\nabla^2\Phi' = 4\pi Ga^2(\rho(\mathbf{x}, \tau) - \bar{\rho}(\tau)), \quad (2.6)$$

where ∇ has been redefined as $\nabla = \partial/\partial\mathbf{x}$ in place of $\partial/\partial\mathbf{r}$ that is used in equations 2.2 and 2.3. Note also that the $\rho(\mathbf{x}, \tau)$ is the mass density while $\bar{\rho}(\tau)$ is the spatial mean density.

Integrating these equations is far from trivial because it is important to conserve energy and reduce errors while at the same time minimising integration time. Integrators now exist that can handle particle numbers greater than 10^9 with a great deal of reliability. It is beyond the scope of this thesis to discuss N-body methods in detail and instead we refer the reader to Dehnen & Read (2011) for a critical review of N-body techniques.

The N-body solver used in the RAMSES simulations is similar (though not identical) to that of ART (Kravtsov et al. 1997) and uses the AMR technique of Berger & Olinger (1984) to dynamically evolve a three dimensional grid such that overdense regions are covered by a finer grid. This grid defines the local resolution and so allows overdensities to be better resolved. The grid refinement scheme is described in §2.2.2. Once the grid is established the discretised mass distribution is calculated using a cloud-in-cell interpolation (Hockney & Eastwood 1981). From the mass distribution Equation 2.3 may be used to calculate the gravitational potential field using the one-way interface scheme (Jessop et al. 1994; Kravtsov et al. 1997). For the coarse grid, which is unrefined and thus uniform, a fast Fourier transform is used to quickly solve Poisson's equation (Hockney & Eastwood 1981). On finer levels of the grid, the algorithms described in Kravtsov et al. (1997); Teyssier (2002) are used to

interpolate the potential to finer levels. A second order midpoint scheme is used to advance the particle positions and velocities for which the Courant-Friedrich-Levy condition must be satisfied. This is assisted by allowing variable time steps, i.e. the time resolution follows the local grid resolution for a given particle. To preserve synchronisation between the time steps of different levels the time step at a level l is half the timestep at level $l - 1$. The variation in time step introduces a source of error if a particle crosses from a grid cell to a new grid cell on a different level as it experiences a factor of two difference in the time step. This effect is fortunately very small and does not have a significant impact on a simulated system (Kravtsov & Klypin 1999; Yahagi & Yoshii 2001).

2.2.2 Grid Refinement

The grid refinement scheme is central to the success of AMR, the fineness of the grid should reflect the underlying mass distribution or gradients in physical quantities (in this way shock fronts may be resolved) to enhance resolution in regions of interest. The basic element of the grid structure is an “oct”, that is 2^{dim} cells with a common vertex, where dim is the number of dimensions. Each oct is described by its level, l and by links to its parent at level $l - 1$, the $2 \times dim$ octs that neighbour its parent, the 2^{dim} children octs on level $l + 1$ and to the octs that are before and after it in the linked list of level l .

The refinements must be smooth to avoid large steps in refinement between neighbouring cells (even diagonally) which may cause spurious numerical effects at the boundary of the two regimes. The highest level cells are refined first and then each subsequent coarser level is considered in turn, marking cells for refinement if they fulfil a certain criterion. If a cell contains a newly refined child then it and the surrounding $3^{dim} - 1$ cells are marked for refinement. A further two passes through each level divides marked cells into 2^{dim} children and destroys the children

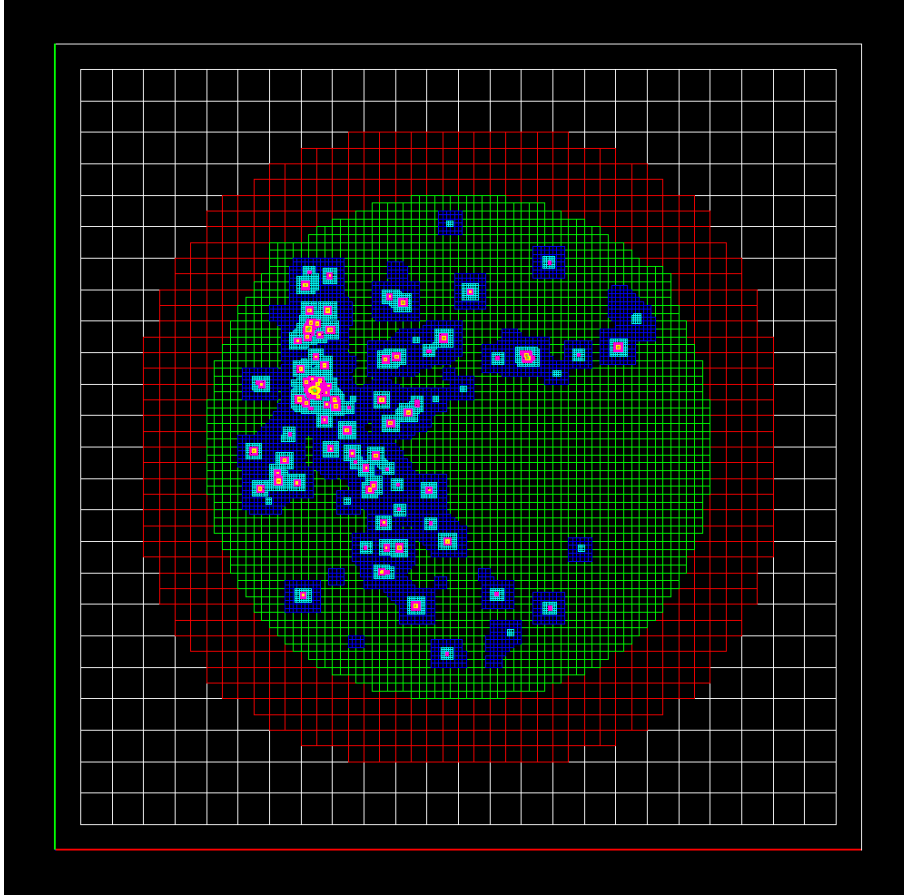


Figure 2.1: Adaptive mesh refinement grid for a cosmological simulation, the volume depicted is a $20 h^{-1}$ Mpc cube. Adaptive refinement is only allowed in the central region with static refinements closer to the center.

of unmarked cells. While time consuming, *adjusting* the grid in this way is far more efficient than building the grid from scratch at every time step and is afforded this by virtue of the low number of cells that are eligible for refinement at every time step and the elegance of the double linked list described above.

The refinement criterion is adjustable to suit the needs of a given simulation, for example, pure gas runs benefit from refining the grid based upon the first or second derivative of flow variables to accurately trace shocks. For cosmological scale simulations the grid is important for gravitational interactions and is refined according to the mass that a cell contains, this is termed ‘quasi-Lagrangian’ as the

grid is finer in regions of high particle density (as with SPH codes) which avoids Poisson noise and two-body relaxation effects. Two-body relaxation occurs as a particle is disturbed from the path it would follow in a smoothly distributed medium by the coarseness of the actual medium that surrounds it, this coarseness is due to the representation of many stars (or dark matter particles) as the ensemble particles used in simulations. The quasi-Lagrangian scheme is achieved in practice by marking cells for refinement if they contain more total mass than a given threshold. All simulations run with RAMSES in this thesis use a threshold that is eight times greater than the initial mass content of a grid cell. Although using this factor for all simulations leads to a reduction in the ease of refinement for dark matter-only simulations the recommended threshold for this type of simulation is much higher (Teyssier 2002) so no numerical issues arise from lack of refinement.

In addition to the adaptive refinements allowed by the scheme described so far RAMSES also allows static refinements. The adaptive refinement may only be permitted in a central ellipsoid which also may be surrounded by other concentric ellipsoids with decreasing resolution at larger radii. This allows the grid to be much coarser at large distances from the region of interest to reduce computation time while retaining high resolution where it matters (Bryan & Norman 1997; Abel et al. 2000). An example of a typical refinement geometry is demonstrated in Figure 2.1, but please note that the refinement geometry may be set up in almost any way.

2.2.3 Hydrodynamics

The most complicated component of cosmological simulations is the treatment of baryonic gas. A complete description of this component cannot be described analytically except in the most simple of cases. Numerical integration of several equations does however provide a means of studying the flow of gas in simulations. Here we describe the essentials of hydrodynamics and several of the methods used to simulate

astrophysical fluid flow.

The equations governing fluid flow are derived from conservation laws, the first being conservation of mass. This is valid in the absence of sources or sinks of mass and while this condition is not strictly enforced, as star formation and stellar feedback act as mass sources and sinks respectively, we separate these processes in the algorithm to avoid the conflict. From the assumption of mass conservation we may derive the continuity equation,

$$\frac{\partial \rho_g}{\partial t} + \nabla \cdot (\rho_g \mathbf{u}) = 0, \quad (2.7)$$

where ρ_g is the gas density and \mathbf{u} is the flow velocity.

The second conservation law is for momentum, an expression of Newton's second law. It is used for calculating the change in the momentum of a fixed volume due to pressure (p) and gravitational forces as well as momentum flux through the volume surface,

$$\rho_g \frac{\partial \mathbf{u}}{\partial t} + \rho_g \mathbf{u} \cdot \nabla \mathbf{u} = -\nabla p - \rho_g \nabla \Phi. \quad (2.8)$$

The two equations stated thus far are incomplete and while Φ may be expressed in terms of the known total mass distribution ρ using Equation 2.3 there is no way of determining p without further constraint. From the first law of thermodynamics and adding a term to account for energy transport we can derive the *energy equation*,

$$\frac{\partial \epsilon}{\partial t} + \mathbf{u} \cdot \nabla \epsilon + \frac{p}{\rho} \nabla \cdot \mathbf{u} = \frac{\Gamma - \Lambda}{\rho}, \quad (2.9)$$

where ϵ is the specific internal energy of the gas. The energy equation introduces ϵ , which together with ρ_g , p , Φ and the three components of \mathbf{u} is seven dependent variables and yet only six equations have been stated; equations 2.3, 2.7, 2.9 and three components of Equation 2.8. A seventh equation is required and for this the equation of state is used, which for an ideal gas may be phrased,

$$p = \rho\epsilon(\gamma - 1) \quad (2.10)$$

but which may take other forms under certain assumptions (see §2.2.4 where a polytropic equation of state is described). The last term in Equation 2.9 is the energy transport term where Γ is the heating rate and Λ is the cooling rate. In practice the only source of cooling and heating that need be considered is radiative. On the scale of hundreds of parsecs, convection and conduction are less relevant and need not be treated on a cell-by-cell case. Energy may be lost or gained by the gas via radiation and this is one of the most important considerations in cosmological models that include baryon physics. The cooling and heating of gas as a function of density, temperature and metallicity is considered in the simulations presented in this thesis. The cooling (and heating) rates are computed assuming ionisation equilibrium with a uniform UV background. Cooling curves are shown in Figure 2.2 in the absence of UV heating (which is nevertheless included in the simulations as a heating source with a dependence on redshift; the model of Haardt & Madau (1996) is used) as a function of temperature for different metallicities and densities. The contribution from metals at temperatures above 10^4 K is accounted for through a fit of the difference between the cooling rates at solar metallicity and those at zero metallicity using photoionisation code CLOUDY (Ferland et al. 1998), again assuming ionisation equilibrium. For gas cooler than 10^4 K, metal fine-structure cooling rates are taken from Rosen & Bregman (1995) however the polytropic equation of state (see §2.2.4) that is used in these simulations prevents the overwhelming majority of the gas from falling into this temperatures regime. The net energy change ($\Gamma - \Lambda$) for each grid cell is calculated at each timestep and used in solving Equation 2.9.

In RAMSES the hydrodynamical equations are solved in their conservative form using a second-order Godunov method (Toro 1997) and is based on Collela (1990) and Saltzman (1994) and is described as ‘almost exact’ by Teyssier (2002). Provided

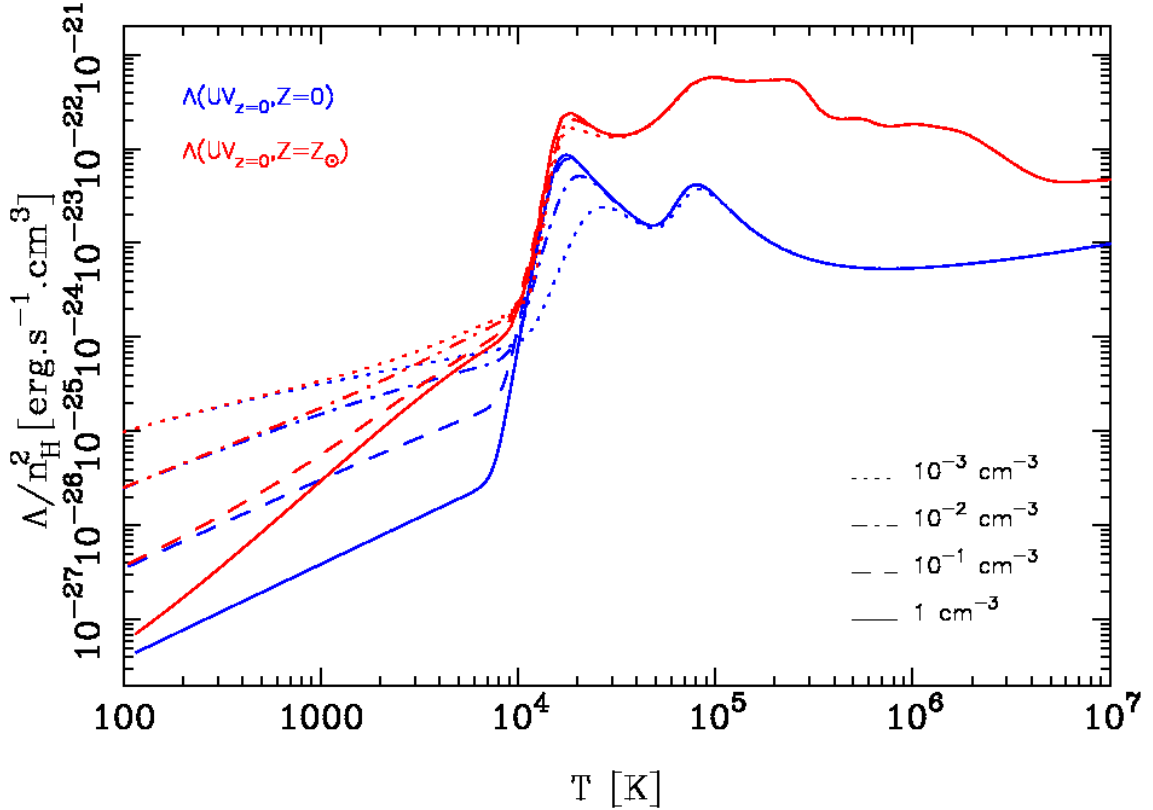


Figure 2.2: Cooling functions used in RAMSES at different densities and metallicities. The UV background “heating” is not included in this figure but is used in determining the photoionisation state of the gas for which the UV strength at redshift $z=0$ is used. Densities of 10 cm^{-3} (solid line), 1 cm^{-3} (dashed line), 10^{-2} cm^{-3} (dot-dashed line), and 10^{-4} cm^{-3} (dotted line) with colour indicating zero (blue) or solar metallicity (red).

that gravity terms are ignored the solutions to the above equations using this method are exact: energy conservation is not guaranteed when gravity is included. Energy variations of order 1% are found at the times when the grid is being restructured the most (at redshift 2–3 in cosmological runs). Extensive testing of the N-body and hydrodynamical components of RAMSES is presented in Teyssier (2002) and we have confirmed the accuracy of the results ourselves. Test methods include tracing

the acceleration of particles in response to point masses, Sod’s shock tube test, Sedov blast waves (Sedov 1993) in 1, 2 and 3 dimensions and the response of a shock moving from a coarse to a fine grid region (Khokhlov 1998). The results are generally positive with only small departures from the analytical solution seen for the 3D blast wave test and for shocks moving from a coarse to a fine grid regime, though Teyssier (2002) points out that this is a rare occurrence in cosmological contexts.

2.2.4 Polytropic Equation of State

Hydrodynamical simulations may suffer from artificial fragmentation of gas if it is poorly resolved in comparison to the scale of perturbations. This is caused by numerical perturbations growing under what are real physical instabilities and is an undesirable consequence of the current inability to easily resolve the Jeans’ length (Jeans 1902) in high density regions. If increasing resolution is impossible from technical constraints then a different approach is called for and the introduction of a polytropic equation of state allows this fragmentation to be prevented by altering the gas temperature as a function of density to enforce a floor in the Jeans’ length. The equation of state may be expressed as

$$P \propto \rho_g^\gamma. \quad (2.11)$$

This equation is used for gas that is cooler than $T_{\text{poly,th}}$ and denser than $\rho_{\text{poly,th}}$. A suitable value of γ prevents the unphysical fragmentation of gas and subsequent (unphysical) formation of stars. The value of γ , $T_{\text{poly,th}}$ and $\rho_{\text{poly,th}}$ are chosen such that the Jeans’ length remains resolved by the simulation grid. The specific choice of γ , $T_{\text{poly,th}}$ and $\rho_{\text{poly,th}}$ depend upon the simulation resolution and one another. Choosing $\gamma = 2$ allows resolution of the Jean’s length at all densities and (for the

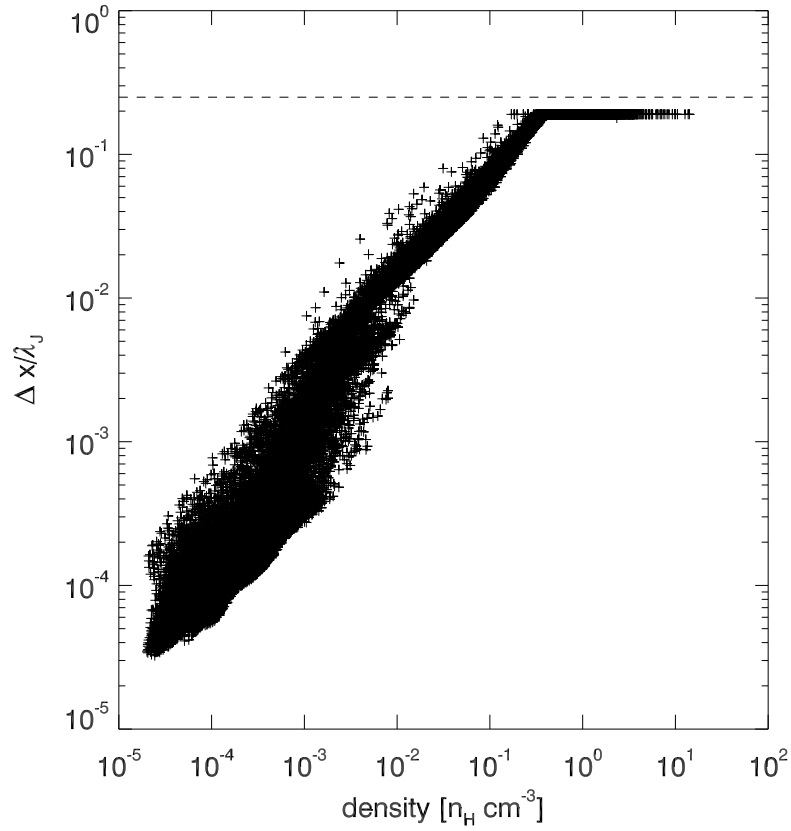


Figure 2.3: $\Delta x/\lambda_J$ versus gas density for grid cells composing the galaxy. The effect of introducing a polytrope (in this case with $\gamma = 2$) is clearly seen as the Jeans' length remains resolved by more than 4 grid cells (denoted with a dashed line) even at high densities.

right choice of $T_{\text{poly,th}}$ and $\rho_{\text{poly,th}}$ depending on the specific resolution of the simulation) independent of resolution. Figure 2.3 shows the ratio of the grid resolution Δx to the Jeans' length, λ_J versus density for grid cells, the resolution is $\Delta x = 436$ pc and $\gamma = 2$. A dashed line denotes the maximum $\Delta x/\lambda_J$ at which the Jeans' length is resolved according to Truelove et al. (1997).

2.2.5 Star Formation

In the densest regions of the galaxy star formation converts gas into collisionless star particles and in the process returns some gas to the ISM with more energy and momentum. This instantaneous return of matter emulates the feedback from SNeII. Gas cells with a number density n_g exceeding a star formation threshold of $n_0 = 0.1 \text{ cm}^{-3}$ form stars at a rate of $\dot{\rho}_s = \rho_g/t_*$. The star formation timescale t_* is itself a function of the density and the free-fall time through the free parameter, t_0 , as follows: $t_* = t_0(\rho_g/\rho_0)^{-1/2}$ (Dubois & Teyssier 2008). We use $t_0 = 8 \text{ Gyr}$, corresponding to a 2% star formation efficiency for $n_0 = 0.1 \text{ cm}^{-3}$. This star formation scheme reproduces the Schmidt-Kennicutt relation (Schmidt 1959; Kennicutt 1998) shown in Figure 2.4 with the equivalent star formation and gas surface densities of gas cells for one of the RaDES galaxies.

The kinetic feedback mode of RAMSES is used, aiming to reproduce the energetic and chemical enrichment of SNeII explosions: after 10^7 years, star particles release some mass, momentum and energy into a 2-cell radius feedback-sphere centred on the star particle. The distribution of ejected properties in this sphere is done according to a Sedov blast wave formalism, i.e. the velocity of ejected matter increases linearly with radius. A Salpeter (1955) IMF with SNeII progenitors ranging from 8–40 M_\odot is characterised with the parameter $\eta_{\text{SN}} = 10\%$ and the mass loading factor $\epsilon_{\text{sw}} = 0$ (the fraction of the stellar mass formed that is swept up in the SNeII wind). The energy injected into the gas phase is in the form of kinetic energy with 100% efficiency (i.e. $10^{51} \text{ erg SN}^{-1}$). Under this feedback scheme the typical velocity that is imparted to the gas is $\sim 3000 \text{ km s}^{-1}$, however this only takes into account the mass ejected from the stars and ignores the extra mass of the gas that is influenced by feedback which will slow the shock front considerably. Chemical enrichment of the gas is followed through the global metallicity Z using a yield of 10%, Calculations described in Chapter 4 demonstrate that this is the effective yield produced by a

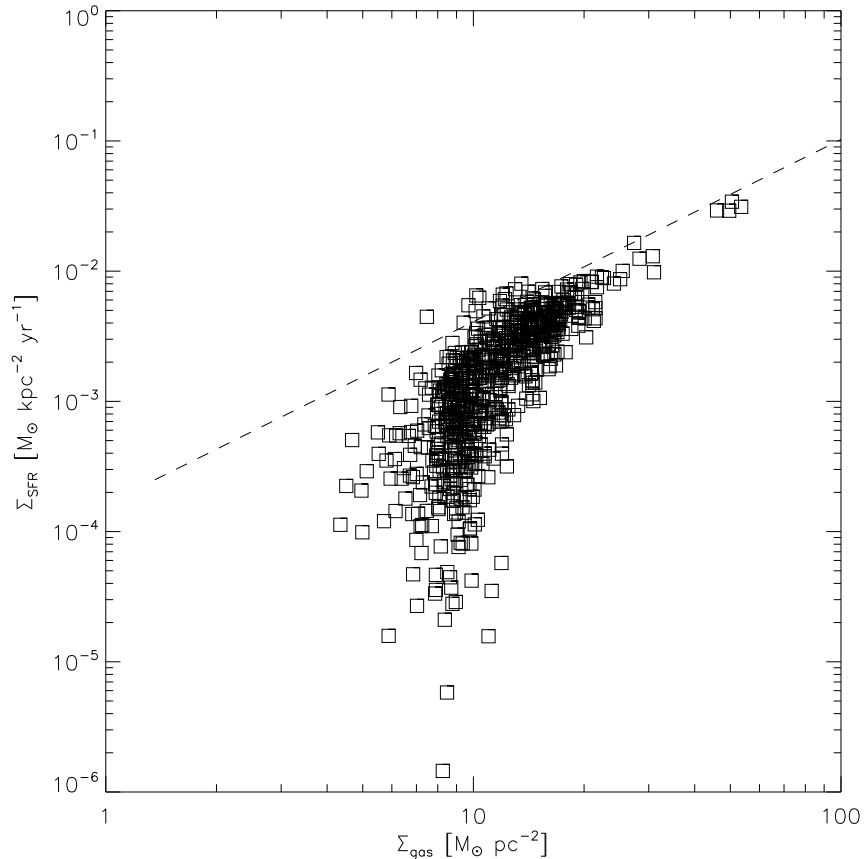


Figure 2.4: The star formation and gas surface densities of gas cells for a simulated galaxy using the star formation scheme described in the main text. The empirical (Kennicutt 1998) relation is shown for comparison. The downturn in the simulated relation at $\Sigma_{\text{g}} \sim 10 \text{ M}_{\odot} \text{pc}^{-2}$ is also well established in observations (e.g Bigiel et al. 2008) and is due to variations in local (three dimensional) density that reduce the star formation rate (as some of the gas is below the star formation threshold) while leaving the gas surface density relatively constant.

stellar population with a Salpeter (1955) IMF and $\eta_{\text{SN}} = 10\%$. RAMSES includes a polytropic equation of state with an index of 5/3 to prevent non-physical gas fragmentation in all gas cells with a hydrogen density larger than the star formation density threshold. The understanding that $\gamma = 2$ guarantees resolution of the Jeans'

length came only after these simulations were complete: while $\gamma = 5/3$ used here ameliorates the fragmentation problem somewhat it is still *possible* that this kind of fragmentation exists in these runs for the very high density gas. The temperature threshold is $T_{\text{th}} = 10^4$ K and in the analysis and Table 2.2 in particular, we set the temperature of the high-density gas cells to 10^4 K to account for unresolved cold gas. A detailed description of the star formation and feedback treatments may be found in Dubois & Teyssier (2008). The v3.01 RAMSES has a different technical implementation of the kinetic feedback but they are effectively the same.

2.3 Galaxy Samples

2.3.1 Environment

A rich literature exists comparing simulated field disc galaxies with observations of the Milky Way (e.g. Brook et al. 2004; Scannapieco et al. 2005; Sánchez-Blázquez et al. 2009; Kobayashi & Nakasato 2011; House et al. 2011; Guedes et al. 2011). The purpose of our work here is to determine whether or not environments comparable to those of the Local Group, the true environment of the Milky Way, result in any measurable characteristics which would call into question this fundamental tenet of simulation versus observation comparison.

Candidate haloes for this work were identified from dark matter simulations and then resimulated with baryonic physics and a more refined grid around regions of interest, using the same technique as in Sánchez-Blázquez et al. (2009). The simulations are conducted in a cosmological framework with $H_0 = 70 \text{ km s}^{-1} \text{ Mpc}^{-1}$, $\Omega_{\text{m}} = 0.28$, $\Omega_{\Lambda} = 0.72$, $\Omega_{\text{b}} = 0.045$, and $\sigma_8 = 0.8$. H_0 is the Hubble constant, Ω_{m} , Ω_{Λ} and Ω_{b} are the fraction of the critical density comprising mass (dark matter and baryons), dark energy and baryons respectively, σ_8 is the linear power spectrum amplitude at a scale of $8 h^{-1} \text{ Mpc}$. Two volumes are used with a size of $20 h^{-1} \text{ Mpc}$

and $24 h^{-1}$ Mpc and the maximum refinement achieved (16 levels) corresponds to 436 pc and 523 pc respectively. The dark matter particles masses are $5.5 \times 10^6 M_{\odot}$ and $9.5 \times 10^6 M_{\odot}$ respectively. We now describe the selection of our candidate haloes.

The virial mass (M_{vir}) is calculated for each dark matter structure, this being the mass contained within an ellipsoid that satisfies the virial condition, i.e. that the ensemble of matter is gravitationally bound. Dark matter haloes with virial mass in the range $5 \times 10^{11} - 1 \times 10^{12} M_{\odot}$ are considered as candidate haloes. Further selection criteria for the loose group sample are such that large groups are excluded; each halo must have a companion with a comparable virial mass (less than a factor of 10 difference) at a distance of 500–700 kpc but have no haloes more massive than $5 \times 10^{12} M_{\odot}$ within 5 Mpc. Please note that the loose groups are not specifically constrained to be pairs, rather they may include up to four haloes each with $M_{\text{vir}} > 1 \times 10^{11} M_{\odot}$.

The field sample consists of galaxies that have no other dark matter haloes of mass $M_{\text{vir}} > 3 \times 10^{11} M_{\odot}$ within a 3 Mpc radius. These field environment galaxies are far more common than the loose groups and those presented here were chosen based upon properties such as mass, spin parameter and number of mergers such that a similar range in each of these can be found in both the loose group and field samples. The spin parameter (λ) is,

$$\lambda = \frac{J|E_{\text{total}}|^{1/2}}{GM^{5/2}}, \quad (2.12)$$

where J is the angular momentum, E_{total} is the total energy ($E_{\text{gravitational}} + E_{\text{potential}}$) and M is the total mass of each dark matter halo. The spin parameters of the dark matter haloes chosen in this study range from 0.007 to 0.08, this range encompasses the majority of dark matter halos and is simply used to exclude outliers. The merger trees of the galaxies are used to select loose group and isolated haloes to avoid galaxies that have any mergers after $z=1$, where the merging halo's

mass exceeds $1/3$ of the host halo’s mass. This is done to ensure that disc galaxies are formed and also prevents the increased likelihood of mergers in denser environments from dominating the systematic differences. The full sample of galaxies covers a range in virial mass from $1 \times 10^{11} - 1 \times 10^{12} M_{\odot}$ and includes the field galaxies and all the group galaxies in this mass range, i.e. massive satellites in addition to the dominant group members.

There are ten loose group galaxies (taken from three groups) and nine field galaxies. The dark matter distributions of a field galaxy and a loose group are shown in Figure 2.5. Each sample is roughly divided into two different resolutions corresponding to the different cosmological volumes. None of the galaxies have passed pericentre with one another as of $z=0$ and so one should not expect dramatic tidal or merger effects. Two of the galaxies do have recent mergers, but for the analysis presented here are studied at an earlier timestep (that is unaffected by the $z=0$ merger, as described later). The details of each galaxy can be found in Table 2.1. A preliminary study of the metallicity gradients in these galaxies has been conducted in comparison with metallicity gradients found in other simulated galaxies and in semi-numerical models in Pilkington et al. (2012a); that work demonstrated that when compared with other models the RaDES galaxies tend to possess shallower metallicity gradients and have a more subtle evolution as a function of time, something the authors attribute to the more uniform star formation profile. This issue is discussed further in §2.5.2.

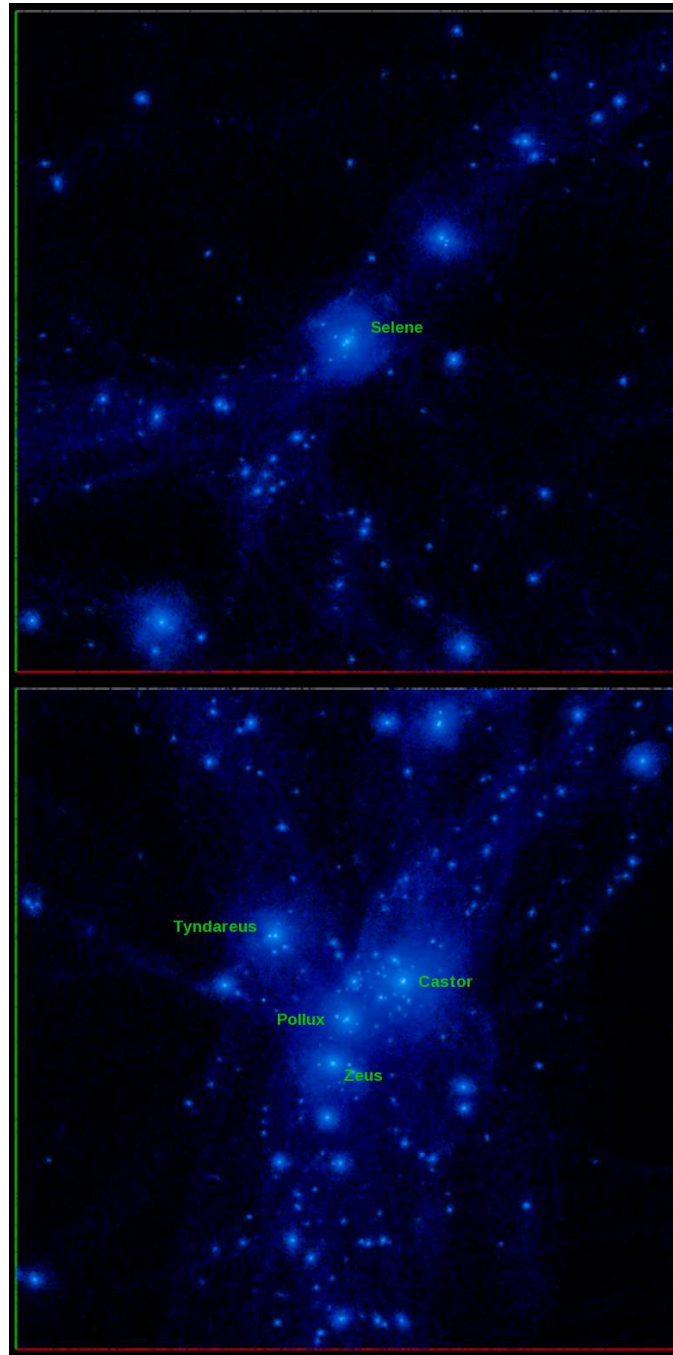


Figure 2.5: Examples of the different environments considered in this work. The dark matter haloes of the field galaxy *Selene* (top) and the loose group galaxies *Castor*, *Pollux*, *Tyndareus* and *Zeus* (bottom) are shown as blue particles (lighter colours correspond to denser regions). Images are $4 \times 4 \text{ Mpc}^2$ in size and have a depth of 4 Mpc.

Table 2.1: List of the disc galaxies simulated for this work, with their total, dark matter, baryonic, stellar and gaseous masses: all properties are measured at $z=0$ and include all matter within the virial radius (R_{vir}). The spatial resolution of the simulation they originate from and their host environment is also quoted.

Name	Environment	Resolution (pc)	M_{tot} (M_{\odot})	M_{DM} (M_{\odot})	M_{baryon} (M_{\odot})	M_{stellar} (M_{\odot})	M_{gas} (M_{\odot})
Castor	loose group	436.	1.05×10^{12}	8.70×10^{11}	1.77×10^{11}	1.10×10^{11}	6.76×10^{10}
Pollux	loose group	436.	4.23×10^{11}	3.48×10^{11}	7.54×10^{10}	4.99×10^{10}	2.55×10^{10}
Zeus	loose group	436.	2.33×10^{11}	1.97×10^{11}	3.60×10^{10}	2.57×10^{10}	1.03×10^{10}
Tyndareus	loose group	436.	3.30×10^{11}	2.82×10^{11}	4.82×10^{10}	3.24×10^{10}	1.59×10^{10}
Apollo	loose group	523.	8.94×10^{11}	7.39×10^{11}	1.55×10^{11}	1.06×10^{11}	4.89×10^{10}
Artemis	loose group	523.	7.45×10^{11}	6.46×10^{11}	9.84×10^{10}	5.61×10^{10}	4.23×10^{10}
Daphne	loose group	523.	3.09×10^{11}	2.58×10^{11}	5.14×10^{10}	2.90×10^{10}	2.24×10^{10}
Leto	loose group	523.	2.49×10^{11}	2.05×10^{11}	4.38×10^{10}	2.92×10^{10}	1.46×10^{10}
Luke	loose group	523.	1.13×10^{12}	9.40×10^{11}	1.88×10^{11}	1.07×10^{11}	8.13×10^{10}
Leia	loose group	523.	3.93×10^{11}	3.25×10^{11}	6.76×10^{10}	4.75×10^{10}	2.01×10^{10}
Ben	field	523.	7.74×10^{11}	6.42×10^{11}	1.32×10^{11}	8.16×10^{10}	5.08×10^{10}
Tethys	field	523.	7.21×10^{11}	5.94×10^{11}	1.27×10^{11}	8.21×10^{10}	4.51×10^{10}
Krios	field	523.	5.68×10^{11}	4.78×10^{11}	8.98×10^{10}	6.15×10^{10}	2.84×10^{10}
Atlas	field	523.	6.48×10^{11}	5.55×10^{11}	9.35×10^{10}	6.15×10^{10}	3.20×10^{10}
Hyperion	field	523.	1.03×10^{12}	8.58×10^{11}	1.72×10^{11}	1.13×10^{11}	5.92×10^{10}
Eos	field	436.	4.64×10^{11}	3.92×10^{11}	7.19×10^{10}	4.68×10^{10}	2.52×10^{10}

Table 2.1 – continued

Name	Environment	Resolution (pc)	M_{tot} (M_{\odot})	M_{DM} (M_{\odot})	M_{baryon} (M_{\odot})	M_{stellar} (M_{\odot})	M_{gas} (M_{\odot})
Helios	field	436.	1.05×10^{12}	8.91×10^{11}	1.62×10^{11}	1.23×10^{11}	3.93×10^{10}
Selene	field	436.	6.07×10^{11}	5.09×10^{11}	9.87×10^{10}	6.71×10^{10}	3.16×10^{10}
Oceanus	field	436.	1.12×10^{12}	9.19×10^{11}	1.97×10^{11}	1.41×10^{11}	5.59×10^{10}

2.3.2 Merger History

The predominant strength of using cosmological simulations to develop this suite of galaxies is that a self-consistent merger tree provides the basis of the evolution for each galaxy. This ensures the conditions in the environments selected here are consistent with the current understanding of cosmology and not biased by artificial initial conditions that may affect the results. We begin by demonstrating that there is at least a superficial similarity between the merger histories of the two samples in spite of the environmental differences.

At each timestep a catalogue of haloes and subhaloes is created using the *Adaptahop* algorithm (Aubert et al. 2004). The halo catalogues are then linked into merger trees for the selected haloes using the “most massive substructure method” detailed in Tweed et al. (2009). Under this formalism, at any given branch in the tree the most massive progenitor is considered the parent halo.

It is not however a trivial exercise to define mergers in this context, and the following definition of a merger is adopted: a merger occurs when an object is identified as a subhalo in a given output but not in the previous output. In practice, the subhalo continues to exist as an identifiable structure orbiting the host halo for several Gyr. Due to dynamical friction, the subhalo gradually sinks into the potential well of the host halo and is slowly stripped of mass before dissolving completely, at which point all particles are attributed to the host halo. With the merger time definition above there is a delay of up to 4 Gyr between the merger time and any real interaction with the disc, i.e. there is a delay time between the dark matter merger and the galaxy disc merger. The definition above is used because the amount of mass loss before the subhalo dissolves is unpredictable and the mass ratio of subhalo to host is a more useful quantity for the purpose of evaluating the magnitude of the merger. The magnitude and timing of mergers for each galaxy are shown in Figure 2.6. This figure shows that most mergers a galaxy experiences

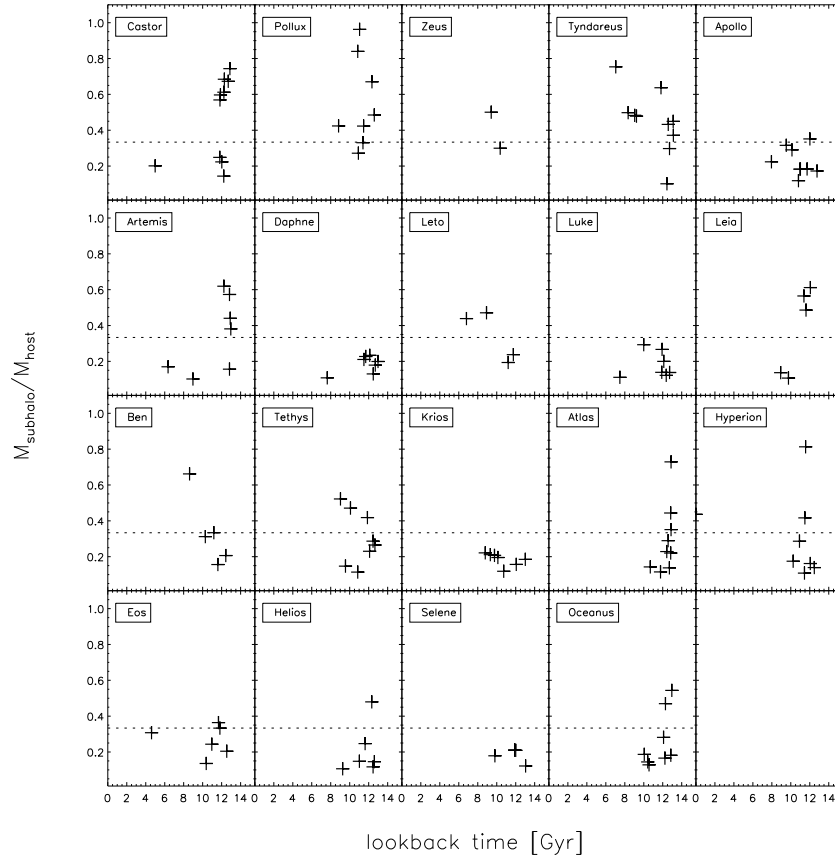


Figure 2.6: Major mergers distributions, the top two rows are loose group galaxies and the bottom two rows are field galaxies, a convention that is followed throughout this work. The magnitude of the merger is represented by the virial mass of the host halo divided by the virial mass of the merging body. As stated in the text, mass ratios are calculated at the time the haloes first come into contact as the mass associated with merging structures is often greatly diminished by the time the disc is disrupted. The majority of mergers take place at early times when the galaxy halo still has a low mass and assembly is mostly hierarchical. Only mergers shown above to occur further back than 4 Gyr are found to have any significant influence on the disc structure since subhaloes can take several Gyr to descend far enough into the halo to disrupt the disc. A dashed line shows the lower bound of the commonly used definition of major mergers.

occur at early times and that these early mergers tend to have mass ratios closer to unity. This is partly due to universal expansion reducing the merger likelihood and partly to the limited size of haloes at early times limiting the mass range and making equal mass mergers more likely.

The traditional definition of a major-merger, $M_{\text{host}}/M_{\text{sub}} \leq 3$, has been made significantly more generous ($M_{\text{host}}/M_{\text{sub}} \leq 10$) in this work due to the low number of 3:1 mergers in the sample. The low number of such mergers is due to selection effects, these galaxies are chosen from dark matter haloes based partly on the merger trees and haloes with many mergers were discounted as unsuitable for hosting disc galaxies. A commonly used metric of the merger history is the time at which the last major-merger took place. At this point we note that two of the galaxies (identified by the names, *Castor* and *Eos*) show obvious signs of disturbance at $z=0$ due to an ongoing merger that makes the disc of the galaxy difficult to identify. The presence of mergers may at first be considered counter to the previously mentioned constraint that the galaxies have no recent major mergers, in both cases the merger did not appear in the dark matter-only simulation and only became apparent following the inclusion of baryons. This is remedied in both cases by analysing the galaxy disc at a snapshot immediately preceding the disturbance. While these galaxies appear in the analysis as a low redshift ($z \approx 0.03$) late-type objects, they may also be considered as more local irregular galaxies if the $z=0$ output is analysed. With the exception we have just mentioned, all analysis is conducted at $z=0$. We conclude this section by stressing that the objective here is not to quantify the effect of mergers on disc galaxies but to examine what effect the environment might have (i.e. via ambient effects) when the increased instance of mergers is discounted. We point to Figure 2.6 as evidence that the loose group galaxies have the same diversity of merger history as do the field galaxies.

2.3.3 Disc Decomposition

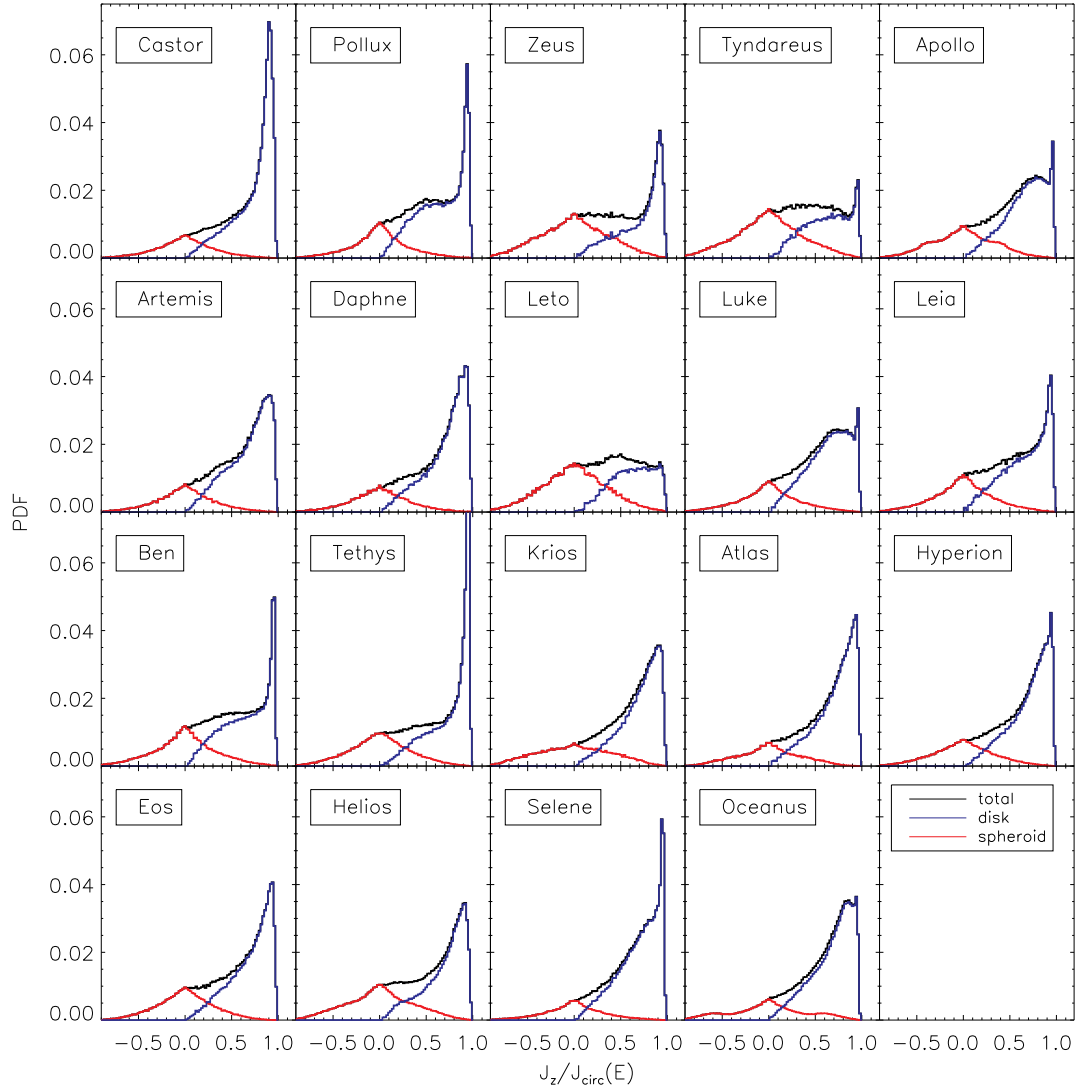


Figure 2.7: J_z/J_{circ} distribution of stars within the virial radius (black). Blue and red lines shows the distribution of the disc and spheroid components respectively. Note the existence of a third intermediate component included in the distribution that is associated with the disc in some of the galaxies.

We now separate the stellar particles into spheroidal and disc populations using

a kinematic decomposition similar to that of Abadi et al. (2003).¹ Stars are assumed to belong to either a spheroidal or a rotating disc component through analysis of the orbital circularity, i.e. the ratio of their angular momentum, J_z to the circular orbit angular momentum J_{circ} for a given particle energy. The distribution of this ratio is shown in Figure 2.7. The peak at $J_z/J_{\text{circ}} = 0$ is considered to be the spheroidal component and the distribution of the negative side is used to dictate what the distribution of the positive side will be, i.e. we assume that when decomposed the spheroidal component (shown in Figure 2.7 as the red curve) should have a symmetrical distribution. In the intermediate region, particles are stochastically attributed to each component so that the spheroidal distribution is symmetrical and all remaining stars are tagged as disc stars. Thus it is not necessarily true that stars identified as belonging to the spheroid did not form as disc stars. The spheroidal component will therefore contain disturbed disc stars (which is arguably appropriate) and more critically, circularly rotating bulge stars will be attributed to the inner regions of the decomposed disc. This does not skew the spheroid-to-disc mass ratio as the vast majority of star particles have equal mass, furthermore the order of this effect should be small as shown in Figure 2.9 which plots the star formation history for the entire galaxy (solid line) and the disc (dashed line) and demonstrates that the selected disc stars well represent the stars formed at late times.

In the analysis that follows we define a disc annulus to exclude contamination by bulge stars and avoid halo stars at the disc edge. Figure 2.8 shows the rotation curves for the galaxies (and circular velocities for each phase of matter) and choice of disc annulus (indicated by diamond symbols at an arbitrary vertical position). The outer extent of the stellar disc region is first constrained by examination of the rotation curve of the young stars (less than 100 Myr old), the departure of the

¹Leo Michel-Dansac performed the decomposition.

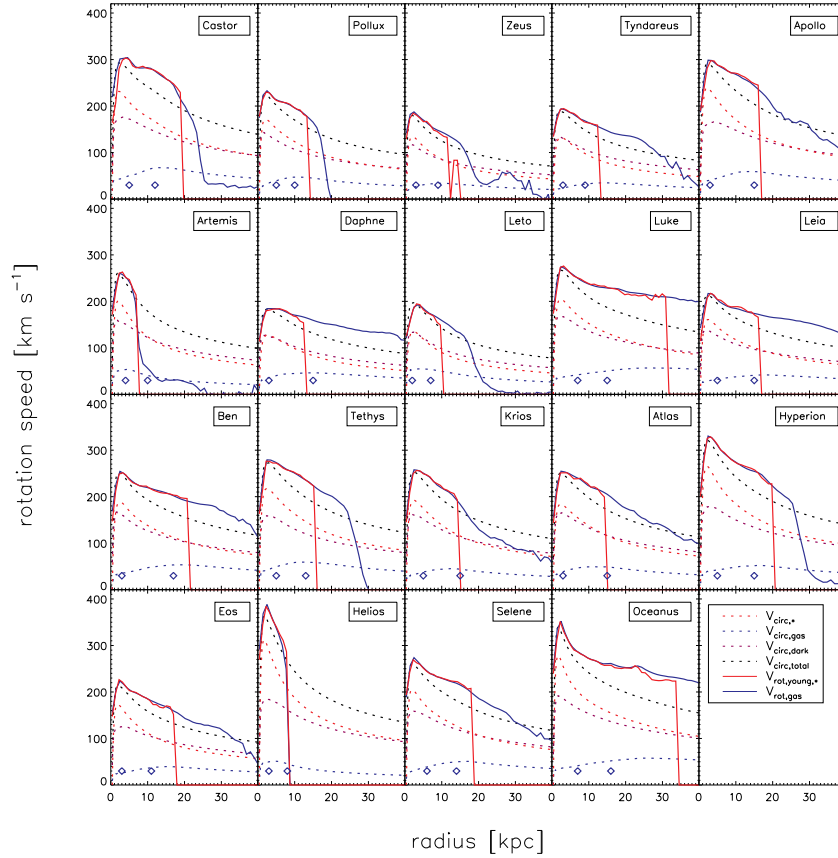


Figure 2.8: Rotation curves showing the circular velocity for stars (red), gas (blue), dark matter (purple) and the total (black) as dashed lines and rotation velocities (solid lines) of young stars (age<100 Myr) and gas as a function of radius. Two blue diamonds denote the inner and outer ‘disc radii’ at an arbitrary vertical position. These values are chosen from inspection of the rotation curve of the gas, surface density maps, stellar surface density profiles and metallicity profiles. The most conservative choice is made to avoid spurious fits but to maintain consistency throughout the analysis.

young stars rotation curve (solid red line) from the gaseous rotation curve (solid blue line) is a useful indicator of the stellar disc edge. Consideration is also given to the stellar density profiles and metallicity gradients of each galaxy, in several

cases the density profile or metallicity gradient extends beyond or falls short of the young disc edge. The final disc annulus is conservative to allow for gradients to be measured for each property over a consistent region while avoiding bias from unusual features. Despite this there are cases where the region over which gradients and scale length are determined has been changed to reflect the characteristics of the galaxy in question. A summary of the galaxy properties can be found in Table 2.2.

2.3.4 Star Formation History

One of the key ways of understanding the formation of galaxies is by examining the star formation history of the different components. The distribution of star formation in time tells us a great deal about how the different components of a galaxy form. In the course of this work the signature of mergers were found to be identifiable in the bursts of star formation seen in Figure 2.9. These bursts can in some cases be associated with steps in the velocity dispersion described in §2.5.4, however we find that the magnitude of the star formation bursts is a poor indicator of the strength of the kinematic disturbance induced by the merger from which they both originate. The dichotomy of the star formation burst magnitude and the kinematic effects of mergers is evidence that the signature of a merger depends on the gas fraction or phase space configuration of the merging bodies. Note the restrained recent star formation of the disrupted galaxy *Artemis* compared with the more disc dominated *Apollo* or *Oceanus*.

2.3.5 Mock Observations

The galaxy’s stellar and gaseous distributions, ages and metallicities have been used by the ray tracing program SUNRISE (Jonsson 2006) to produce mock images. The *Starburst99* stellar population models (Leitherer et al. 1999) define the colour and magnitude of stellar particles. Scattering and extinction are determined by assuming

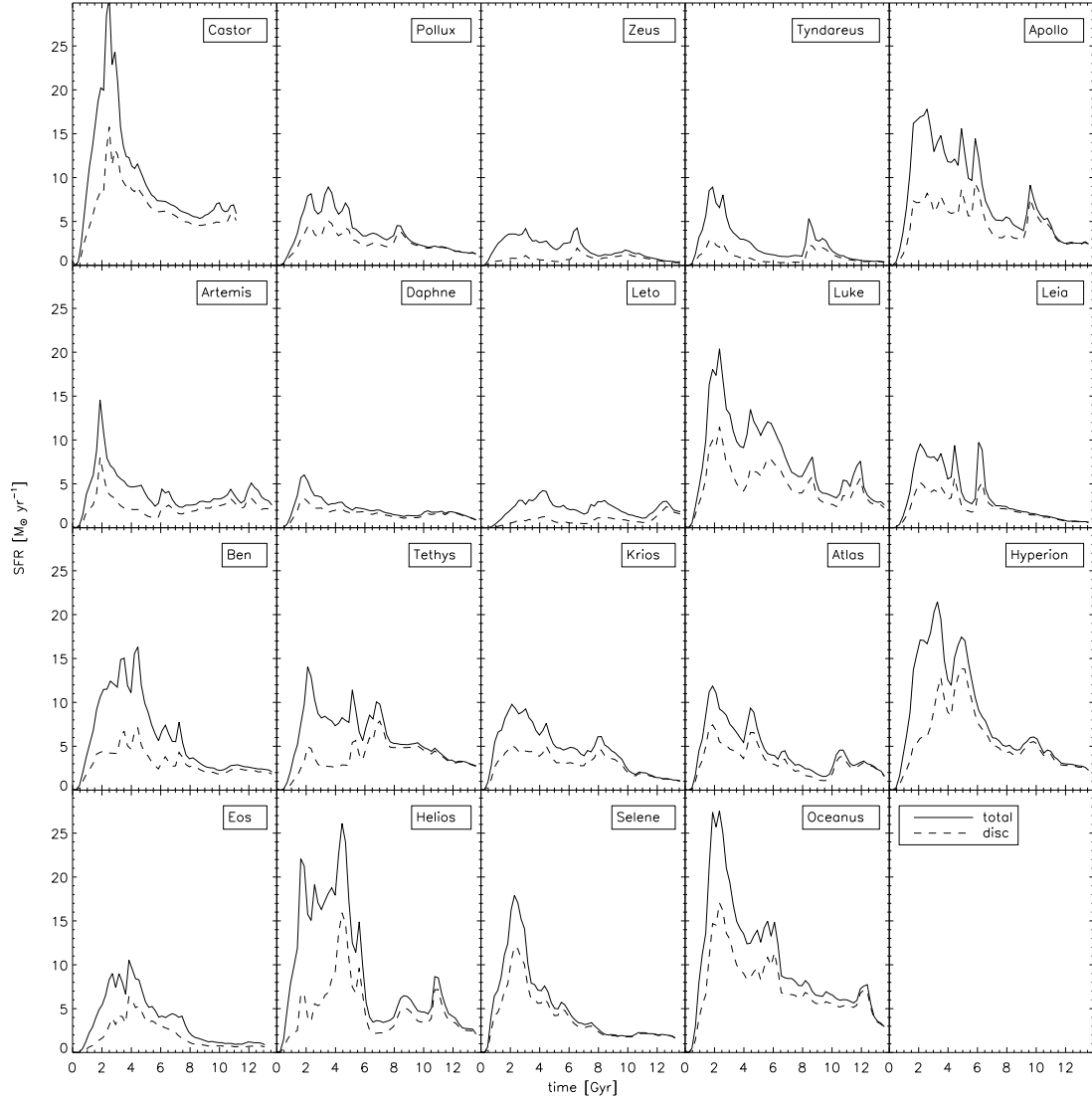


Figure 2.9: Star formation histories of the sample galaxies. The star formation rate of all stars within the virial radius at $z=0$ are shown by the solid line, the dashed line is all stars tagged as disc stars at $z=0$.

that dust follows the gas phase metallicity distribution. Mock images of the galaxies may be found in Figure 2.10, each image being $50 \times 50 \text{ kpc}^2$ in size and produced using SDSS g , r and i filters. We draw the reader's attention to the asymmetry of the more extended discs of *Luke* and *Oceanus*, the warped discs of *Castor*, *Tyndareus*, *Krios* and *Hyperion* and to the red, spheroid-dominated *Helios*.

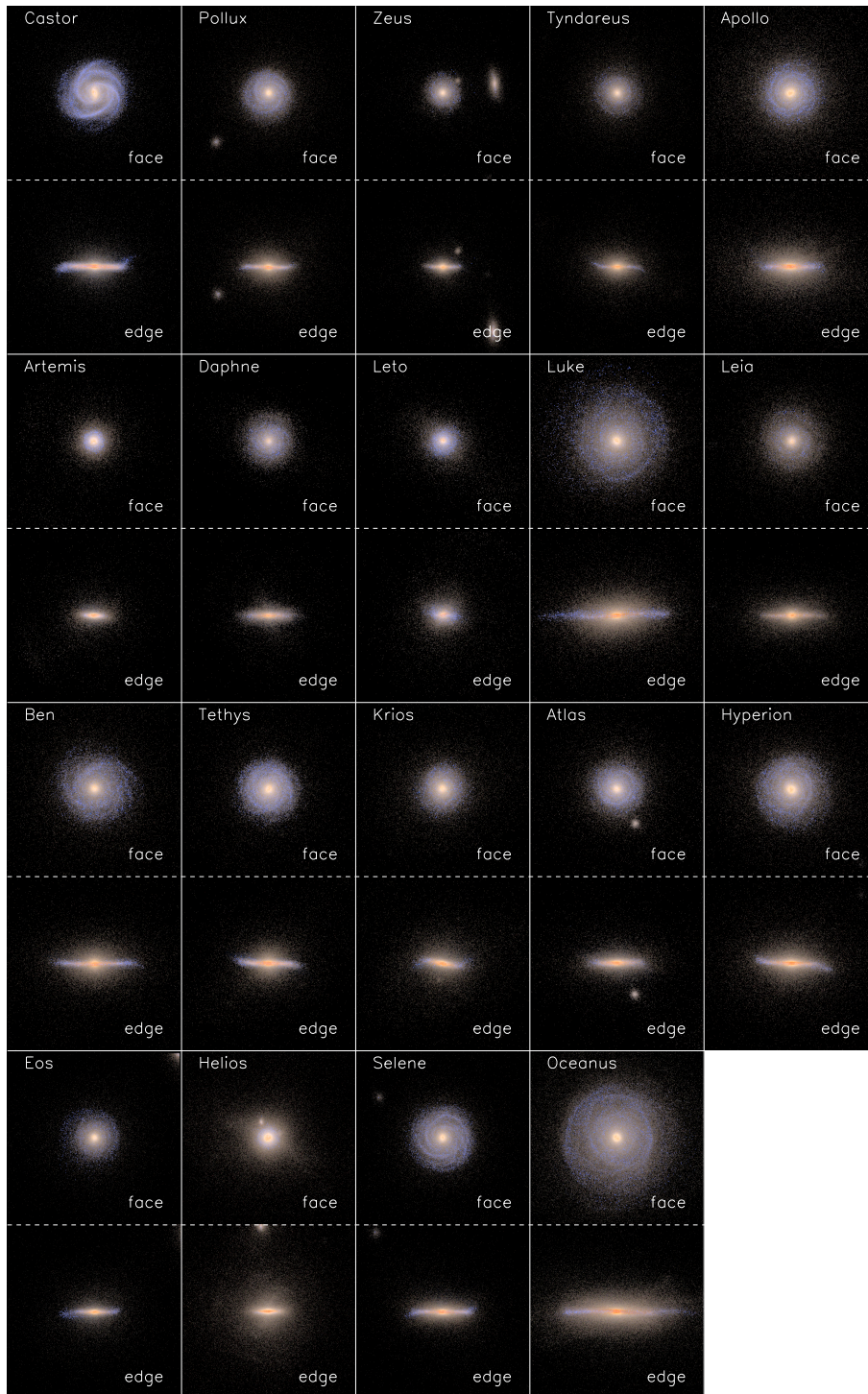


Figure 2.10: Mock images of the galaxies. Face- and edge-on views are separated by dashed lines, images are created by combining SDSS g, r and i filters and are each $50 \times 50 \text{ kpc}^2$ in size.

2.4 Individual Galaxy Properties

Here we describe some of the individual characteristics of each galaxy that may be important, for example we mention any outlier properties that come from the particular merger history or environmental conditions of the galaxies. These properties have been considered in the analytical method as sometimes the determination of some property depends upon the morphology and peculiarities can skew the results if care is not taken.

- *Castor* is the only galaxy in the sample to exhibit a bar, perhaps reflecting the greater resolution or the more isotropic nature of its group (compared with, for example, the filamentary structure of the *Apollo* group). It also presents the clearest example of spiral structure of the entire sample. The spiral structure presents challenges when quantifying the stellar scale length as the arms appear as a bump in the density profile. The young stars present in the arms mean that this is even more pronounced when measuring the brightness profile. *Castor* also has the most pronounced (and abrupt) disc warp, initially this was believed to be evidence of poor resolution at the disc edge but investigation has revealed no particularly favoured alignment of the disc warps in this sample. Analysis of *Castor* has been conducted on a snapshot slightly before $z=0$ due to the irregular shape induced by a late merger in this snapshot.
- *Artemis* is unusual in that it has a reasonably low spheroid-to-disc fraction (0.32), relatively massive dark matter halo ($7.45 \times 10^{11} M_{\odot}$), and flat metallicity profile ($-0.0068 \text{ dex kpc}^{-1}$), yet its disc scale length is only 1.87 kpc and is truncated at a radius of 7 kpc. It also possesses a gaseous polar disc (though it is not dense enough to form stars) and yet the vertical velocity dispersion changes very little as a function of age. This suggests that the last major merger experienced by *Artemis* left star-forming gas with a similar velocity

dispersion to the older stars, an effect not seen in the other galaxies.

- *Leto* is the least massive galaxy within the *Apollo* group and the most spheroid dominated of the galaxies. This spheroid is not composed of older stars as in the other galaxies, there is a significant fraction of the spheroid stars that are young. This is the result of a low star formation rate at early times compounded by a recent, disruptive event that is evident in the velocity dispersion-age relation.
- *Eos* undergoes a merger at late times that leaves it with an extremely irregular morphology at the last time step, analysis of this galaxy is performed on a snapshot prior to this event.
- *Helios* is the most early type galaxy in the entire sample. Despite its great mass it is the reddest galaxy and has young stars with around twice the vertical velocity dispersion of much of the rest of the sample. It also exhibits a prolonged early star formation episode, this contrasts with the lack of an identifiable late merger to result in such a morphology.
- *Selene* has few mergers in its history and is one of the most quiescent galaxies, forming the largest disc fraction of all the galaxies and having definite spiral structure.
- *Oceanus* has the greatest stellar mass in the sample (though others have comparable halo masses) and has a rotating gaseous disc that extends as far as 40 kpc from the centre. This disc is dense enough to form stars and hence this galaxy has an extremely long scale length (6.63 kpc) and one of the flattest metallicity gradients.

2.5 Results

2.5.1 Disc Fraction

One of the potential differences that may be seen between the galaxies in different environments is the bulge-to-disc ratio. There is a body of evidence suggesting that a morphology-density relation exists (Dressler 1980; Giuricin et al. 1995; Bamford et al. 2009) due to harassment by neighbours and the increased likelihood of mergers. The stellar spheroid and disc masses of galaxies in the sample are shown in Figure 2.11 and it is immediately apparent that the majority are disc dominated ($M_{*,\text{spheroid}}/M_{*,\text{disc}} < 1$) in spite of the spheroid containing the net mass of the stellar halo in addition to the bulge. Only the smallest group members are spheroid dominated (*Leto*, *Tyndareus* and *Zeus*) with many of the larger galaxies having disc masses exceeding spheroid masses by a factor of 2–4. There is no noticeable tendency for the galaxies with more disturbed discs and smaller galaxies to be spheroid dominated; *Artemis* has a disturbed disc and yet still exhibits a spheroid-to-disc ratio of 0.326, likewise the low mass galaxies *Daphne*, *Pollux* and *Eos* have quite strong disc components in contrast with the similarly less massive ($< 4 \times 10^{11} M_{\odot}$) galaxies *Zeus*, *Tyndareus* and *Leto*.

The cumulative distribution functions of $M_{*,\text{spheroid}}/M_{*,\text{disc}}$ for each sample are shown in Figure 2.12. While it is clear that the two samples are very similar at low spheroid fractions there is a small deviation as the loose group galaxy sample has several galaxies with large $M_{*,\text{spheroid}}/M_{*,\text{disc}}$ values. This deviation is not significant however as a Kolmogorov-Smirnov test of the two distributions finds that there is a 0.925 probability that the samples are drawn from the same distribution and given the sample size it is unwise to draw conclusions about the environmental effect on morphology from this metric. The lack of a clear separation in the loose group and field populations with regard to the spheroid-to-disc ratio may point to the fact that

the environments here are not sufficiently different to allow the galaxies to manifest different disc properties and that galaxies differ significantly only if they inhabit more extreme overdensities. It also reflects the dynamics of these groups. None of the galaxies have undergone much interaction with any other massive group member, having not passed pericenter with one another at $z=0$. This removes harassment by massive galaxies as a possible source of disruption and leaves only the possibility of complete mergers with smaller satellite galaxies than those shown in Figure 2.6 as a possible explanation.

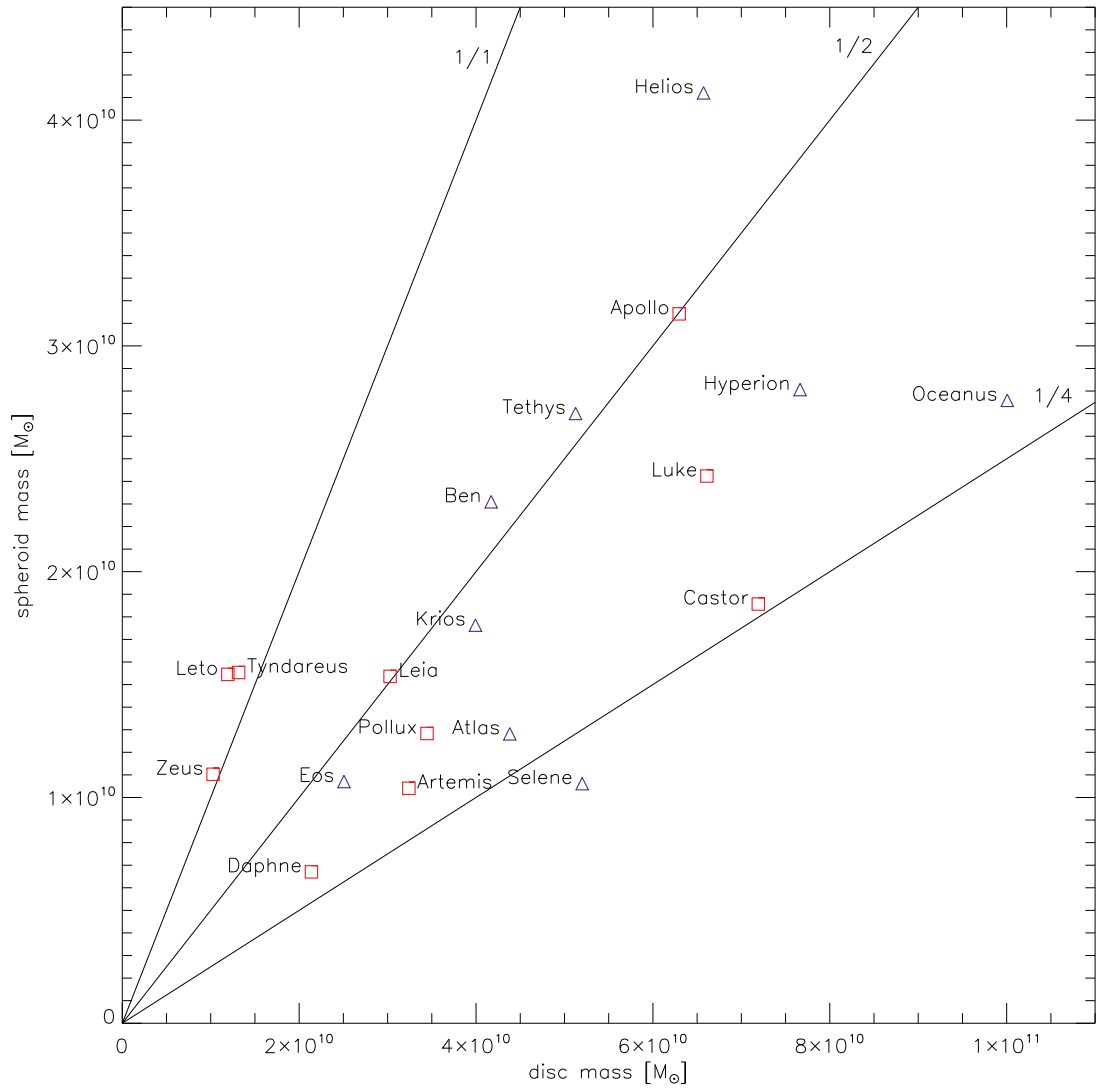


Figure 2.11: Spheroid and disc masses as determined by kinematic decomposition of the stellar phase. Squares and triangles indicate the loose group and field populations respectively, this convention is continued throughout this chapter. Radial lines have constant spheroid-disc ratios.

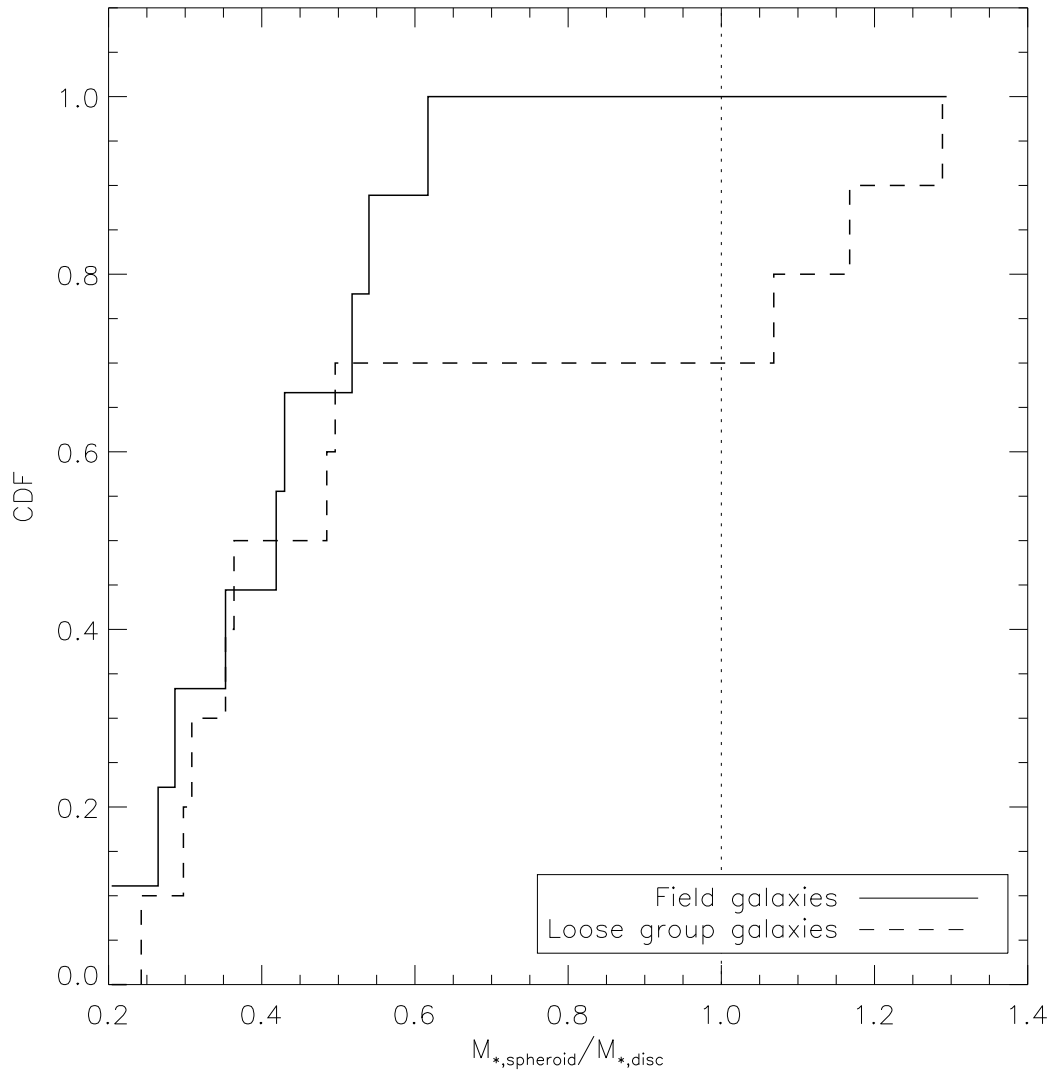


Figure 2.12: Cumulative distributions of $M_{*,\text{spheroid}}/M_{*,\text{disc}}$ for the loose group and field galaxy samples. The loose group distribution is plotted with a dashed line and the field sample distribution with a solid line. The dotted line indicates equal spheroid and disc mass. While a small deviation is seen between the two samples (with the loose group sample having several galaxies with high spheroid-disc fractions) a Kolmogorov-Smirnov test finds that the two samples are drawn from the same distribution with a probability of 0.925.

Table 2.2: Galaxy properties of the simulated discs: scale length and young stellar metallicity gradient (age less than 100 Myr) calculated over the region shown by blue diamonds in Figure 2.8, cold gas mass-weighted metallicity average ($T < 1.5 \times 10^4$ K), stellar mass (kinematically defined bulge and disc stars), cold gas mass (within r_{vir}), and magnitudes (b and r SDSS filters). Note that for the gas mass and metallicity determinations, spatial cuts are used to exclude satellites.

Name	Environment	scale length (kpc)	d[Z]/dR (dex kpc ⁻¹)	mean [Z]	stellar bulge mass (M _⊙)	stellar disc mass (M _⊙)	gas disc mass (M _⊙)	M _b	M _r
Castor	loose group	3.88	-0.034	-0.194	1.86×10^{10}	7.19×10^{10}	3.32×10^{10}	-21.67	-22.30
Pollux	loose group	3.07	-0.052	-0.139	1.28×10^{10}	3.45×10^{10}	7.64×10^9	-20.58	-21.33
Zeus	loose group	1.76	-0.044	-0.159	1.10×10^{10}	1.03×10^{10}	6.25×10^9	-19.70	-20.52
Tyndareus	loose group	2.27	-0.048	-0.086	1.55×10^{10}	1.32×10^{10}	8.38×10^9	-19.77	-20.61
Apollo	loose group	2.86	-0.057	-0.269	3.14×10^{10}	6.30×10^{10}	2.25×10^{10}	-21.22	-22.00
Artemis	loose group	1.75	-0.047	-0.239	1.04×10^{10}	3.24×10^{10}	1.06×10^{10}	-20.52	-21.30
Daphne	loose group	2.64	-0.060	-0.139	6.70×10^9	2.14×10^{10}	1.40×10^{10}	-20.20	-20.92
Leto	loose group	1.56	-0.057	-0.207	1.55×10^{10}	1.19×10^{10}	7.51×10^9	-20.32	-21.01
Luke	loose group	5.19	-0.035	-0.164	2.42×10^{10}	6.61×10^{10}	4.58×10^{10}	-21.30	-22.05
Leia	loose group	3.94	-0.019	-0.130	1.54×10^{10}	3.03×10^{10}	1.22×10^{10}	-20.22	-21.06
Ben	field	3.85	-0.033	-0.272	2.31×10^{10}	4.17×10^{10}	2.70×10^{10}	-20.96	-21.67
Tethys	field	2.77	-0.050	-0.231	2.70×10^{10}	5.12×10^{10}	1.52×10^{10}	-21.24	-21.97
Krios	field	2.50	-0.051	-0.204	1.76×10^{10}	3.99×10^{10}	1.19×10^{10}	-20.61	-21.43
Atlas	field	2.71	-0.042	-0.170	1.28×10^{10}	4.38×10^{10}	1.22×10^{10}	-20.88	-21.61
Hyperion	field	3.59	-0.040	-0.199	2.81×10^{10}	7.66×10^{10}	1.46×10^{10}	-21.24	-22.05

Table 2.2 – continued

Name	Environment	scale length (kpc)	d[Z]/dR (dex kpc ⁻¹)	mean [Z]	stellar bulge mass (M _⊙)	stellar disc mass (M _⊙)	gas disc mass (M _⊙)	M _b	M _r
Eos	field	1.96	-0.069	-0.279	1.07×10 ¹⁰	2.51×10 ¹⁰	1.14×10 ¹⁰	-20.07	-20.87
Helios	field	1.56	-0.037	-0.069	4.12×10 ¹⁰	6.57×10 ¹⁰	5.26×10 ⁹	-21.01	-21.93
Selene	field	3.54	-0.061	-0.244	1.06×10 ¹⁰	5.20×10 ¹⁰	1.66×10 ¹⁰	-20.83	-21.56
Oceanus	field	6.45	-0.029	-0.103	2.76×10 ¹⁰	1.00×10 ¹¹	2.99×10 ¹⁰	-21.61	-22.39

2.5.2 Metallicity Gradients

We now examine the metallicity gradients of the galaxies for evidence of environmental influences. Metallicity gradients of interacting and merged galaxies are known to be flatter (Ellison et al. 2008; Rupke et al. 2008; Kewley et al. 2010b; Perez et al. 2011) and as such, abundance gradients provide a probe of the dynamical mixing. To make comparisons with observed HII gradients we select stars that are younger than 100 Myr and calculate the mass-weighted average metallicity of annuli at different radii. The global metallicity is used and the range over which the gradient is calculated is a conservative cut from the edge of the bulge to the edge of the young stellar disc (see §2.3.3 for how the rotation curves are used to determine this), but further cuts are made to avoid particular features that affect either the metallicity gradients or the scale length (R_d) on an ad-hoc basis, e.g. in *Castor* the spiral arms are almost rings which misleads the scale length if the outer radius of the disc is taken at the radius of these arms. The radial extent of the disc used for these calculations is shown as blue diamonds in Figure 2.8, bear in mind that the kinematic decomposition has also been applied. Young stellar metallicity gradients are shown in Figure 2.13 as a function of total galaxy mass.

The gradients exhibited by the RaDES galaxies range from -0.07 to -0.02 dex kpc^{-1} , consistent with observations by Zaritsky et al. (1994) of spiral galaxies in the field (-0.231 to 0.021 dex kpc^{-1}). Gradients are also calculated for spiral galaxies in van Zee et al. (1998) spanning -0.07 to -0.04 dex kpc^{-1} and Garnett et al. (1997) with a range of -0.083 to -0.020 dex kpc^{-1} , the RaDES galaxies are remarkably close to these values. The metallicity gradient of the Milky Way is found to be in the range -0.06 to -0.04 dex kpc^{-1} for HII regions (Deharveng et al. 2000; Esteban et al. 2005; Rudolph et al. 2006) and with the shallower value of -0.016 dex kpc^{-1} (Yong et al. 2006) for Cepheids. A gradient of -0.06 has been calculated from HII regions in M31 by Galarza et al. (1999) however a much shallower value of -0.006 dex kpc^{-1} is

found using B-type supergiants as tracers by Trundle et al. (2002) and the gradient in M33 is found to be $-0.038 \text{ dex kpc}^{-1}$ by Magrini et al. (2007) again using HII regions. The RaDES simulations seem to be in agreement with the gradients found using HII regions in these three Local Group galaxies yet the gradients that are found using young stellar tracers are much shallower.

Metallicity gradients are thought to be flatter for galaxies in denser environments and has been demonstrated to be true for close interacting binaries by Kewley et al. (2010b) where HII region metallicity gradients are found between -0.040 to $-0.007 \text{ dex kpc}^{-1}$. While there is no obvious distinction between the two samples presented here it is worth bearing in mind that the RaDES loose group galaxies are an order of magnitude more distant from each other than the galaxy pairs in Kewley et al. (2010b). Furthermore the simulated gradients are not dramatically inconsistent with those measured for interacting binaries. We note that the simulated loose group galaxies do not have appreciably flatter young stellar gradients (with the exception of *Leia*), however they likewise do not have steeper gradients, which leaves the possibility that the statistical sizes of the samples here may be too small to probe such a slight effect.

Another feature of Figure 2.13 is the trend for less massive galaxies to have steeper gradients. *Leia* is a notable outlier from this trend, having a particularly flat metallicity distribution, however when the gradient is calculated on stars of all ages the trend remains and *Leia* does not appear to be peculiar. This is counter to what might be expected since these galaxies have less massive dark matter haloes and therefore may be more easily perturbed and have flattened metallicity gradients. The Spearman's rank correlation coefficient (r_s) for the data shown in Figure 2.13 is $r_s=0.492$ with a significance of 0.032 and with the exclusion of *Leia* the coefficient becomes $r_s=0.657$ with a significance of 0.003. In Prantzos & Boissier (2000), cosmologically motivated scaling relations are used to demonstrate that the metallicity

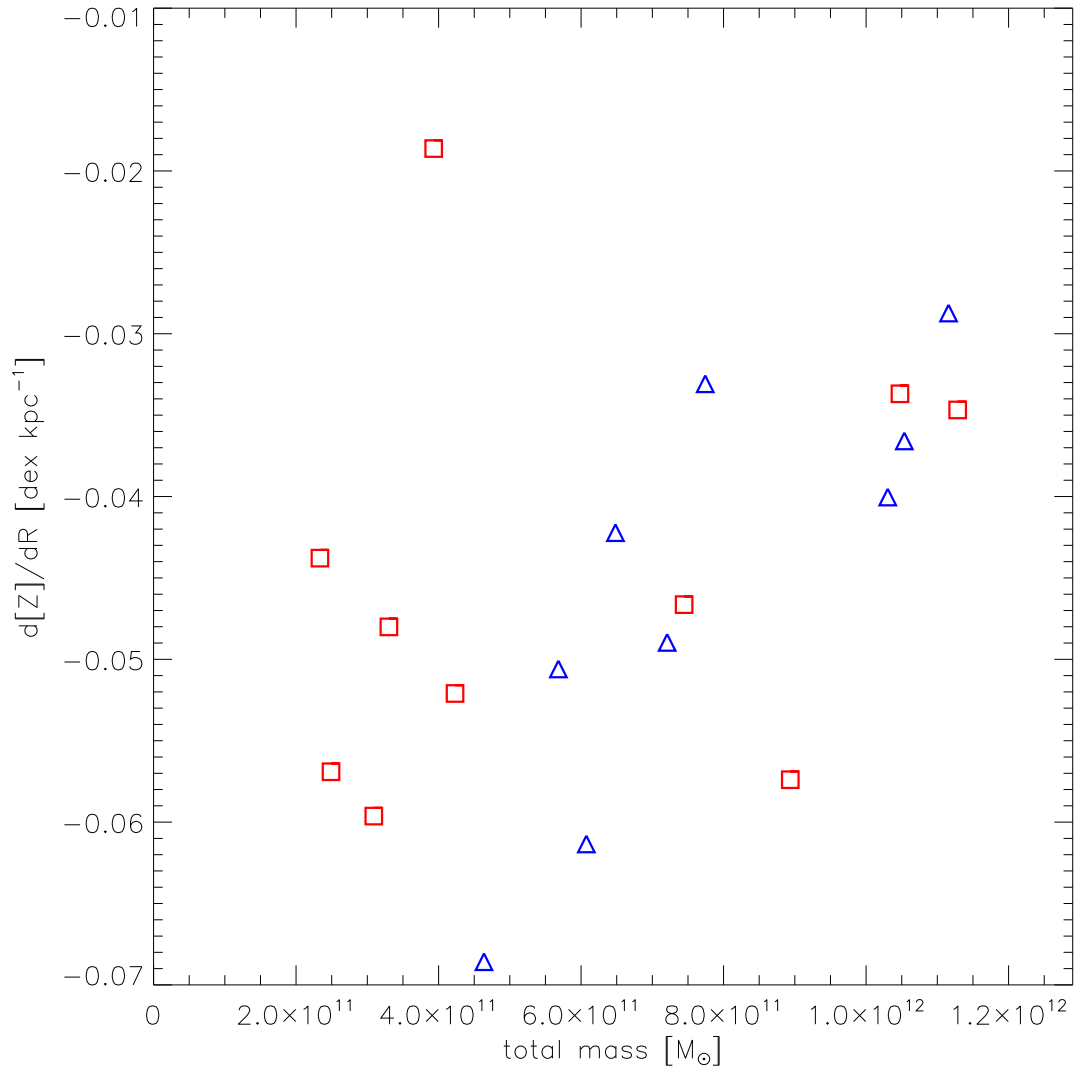


Figure 2.13: Young metallicity gradients of the disc stars plotted against the total mass of the galaxy halo, blue triangles represent field galaxies, red squares are loose group galaxies. A trend toward shallower gradients with increasing mass is evident for both environment samples with a slight offset to flatter gradients for the loose group galaxies.

gradients of spiral galaxies are steeper in less massive galaxies when expressed in dex kpc^{-1} but not so when expressed in $\text{dex } R_d^{-1}$ where R_d is the disc scale length. This is a consequence of the shorter scale length of the less massive discs arising from

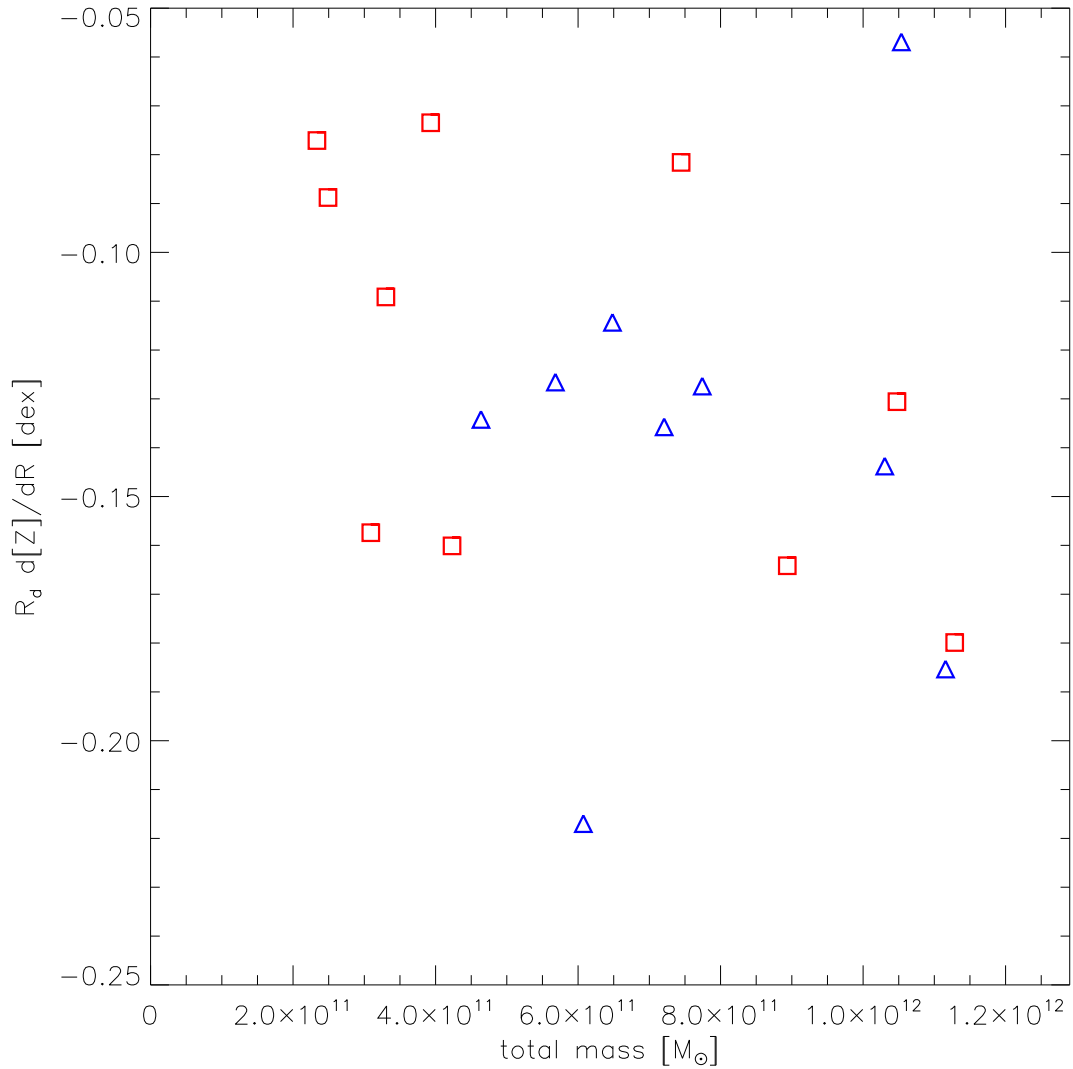


Figure 2.14: Young stellar metallicity gradients normalised by stellar scale length plotted against the total galaxy mass, symbols are as in Figure 2.13.

a steeper star formation rate profile which results in a greater metal production rate in the inner disc compared with the disc periphery. This behaviour is supported by observations (Garnett et al. 1997; van Zee et al. 1998) where it is shown that less luminous spiral galaxies have steeper gradients than brighter galaxies when the absolute gradient is measured. When observed gradients are normalised to the disc scale length however no significant variation with luminosity is apparent. Another finding

of Garnett et al. (1997) is that the dispersion of absolute gradients is larger for less luminous galaxies but when normalised the dispersion is consistent with brighter galaxies pointing to the existence of some degree of co-evolution of metallicity and density profiles. The scale length normalised metallicity gradients of young stars are shown in Figure 2.14 where $r_s=0.353$ with a significance of 0.139 which is a considerably weaker relation than is seen when not normalised to the scale length, confirming that metallicity gradients likely have a common origin with the stellar density profile. This is explored in more depth in Chapter 3 where clear links are made between the star formation profile and metallicity gradients.

The absolute metallicity gradients of the RaDES galaxies are consistent with values found in literature (Garnett et al. 1997) however the normalised gradients are around an order of magnitude flatter suggesting that the measured density profiles are too steep, a feature that is consistent with the known issue of excess star formation at early times and highly peaked rotation curves in simulations (Navarro & Benz 1991; Governato et al. 2004; Guo et al. 2010; Sawala et al. 2011). A result that is relevant to this work is that of Dutil & Roy (1999). Here the authors find that HII metallicity gradients are flatter for earlier morphological types, but critically, that the trend is weaker when the gradients are normalised to some isophotal or effective radius. While no correlation between gradient and morphology is shown (indeed no attempt is made to identify the classical morphology of these galaxies) it is clear that the metallicity gradient has some degree of co-evolution with the scale length.

It is known that the stellar mass fraction of simulated galaxies is too high, particularly for older stellar populations. This is true of the RaDES galaxies (stellar masses are stated in Table 2.1) with the stellar:total mass fraction is a factor of 2–3 times too high when counting all mass in the virial radius (Mandelbaum et al. 2006; Moster et al. 2010; Leauthaud et al. 2012). We do not however believe it has

a drastic impact on this analysis. Firstly, the issue affects galaxies independent of environment, so comparisons of the loose group and field samples are not systematically offset by this effect. Secondly, the early formation of stars would lead to an overly concentrated disc or large spheroid. Figure 2.11 shows that the spheroid mass is *not* extreme although as we have said in the previous paragraph the disc stars are too concentrated, i.e. disc scale lengths are too short. We leave a fuller discussion of the metallicity gradients in these galaxies to Chapter 3.

2.5.3 Colour-Magnitude Diagram

We use SUNRISE to produce seven different projections ranging from face-on to edge-on and display the values in a colour-magnitude diagram (Figure 2.15) that overplots the observed (uncorrected) colour-magnitude diagram from SDSS data (Bailin & Harris 2008). We represent the change in magnitude and colour as a function of projection angle for each galaxy in Figure 2.15 with an arc that starts with a symbol denoting the face-on projection (blue triangles are fields galaxies and red squares are loose group galaxies), the end of the arc denotes an edge on projection. Face-on magnitudes for each galaxy are given in Table 2.2. Almost all the galaxies populate the blue cloud with only *Helios* appearing within the red sequence. Much as expected, as the galaxies becomes more inclined they appear to dim and redden; many of the galaxies therefore have edge-on projections that stray into the dimmest end of the red sequence. There is a selection effect at work here as the galaxies are *a priori* chosen to be disc galaxies with ongoing star formation: that only *Helios* is particularly red is reassuring. We ask the reader to bear in mind that the over production of stars at early times will artificially lead to redder colours and (particularly as we are using M_r to plot the magnitude) brighter galaxies.

There is no apparent separation of the two samples once the obvious outlier of *Helios* has been discounted. There is some observational evidence that the colour

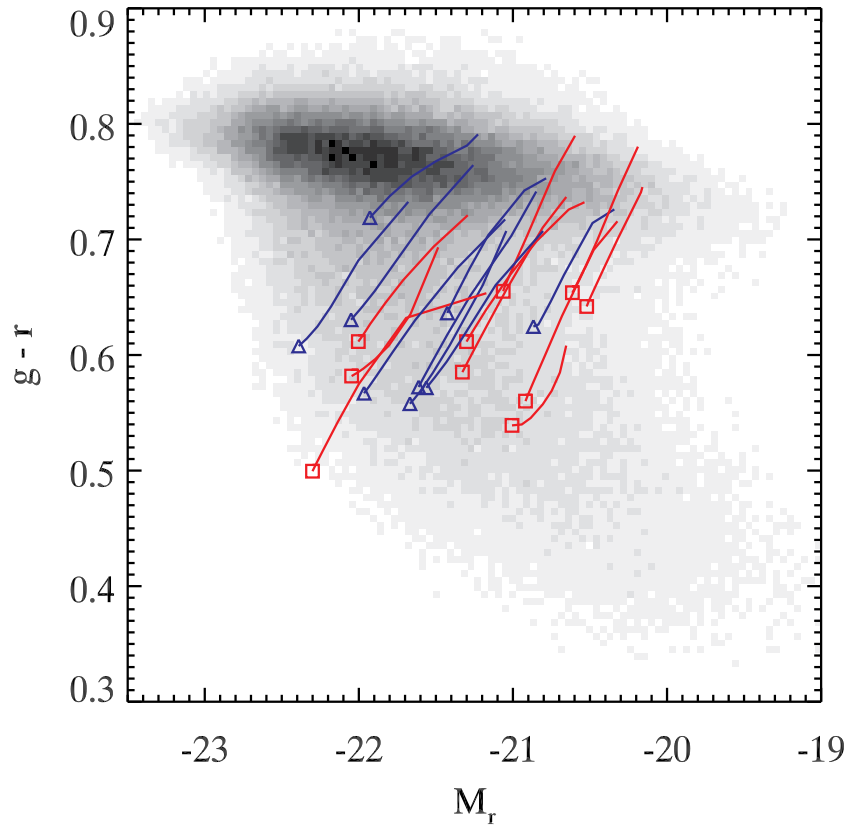


Figure 2.15: Colour-magnitude diagram. The background data are SDSS galaxies with no inclination correction. Field and loose group galaxies are represented by blue triangles and red squares respectively, the symbol denotes the face-on colour and magnitude. The tails traces the change in orientation from face- to edge-on.

distribution of late-type galaxies is only weakly dependent on environment and that it is more strongly influenced by the luminosity or mass through intrinsic evolution (Balogh et al. 2004b). The distribution in r-band magnitude is consistent with the mass of each galaxy and the colour of galaxies can be considered a probe of their star formation history (Figure 2.9). Taking *Helios* as an example, an initially prolonged star formation phase is seen in comparison with other galaxies that have

star formation rates that are less disparate throughout time. We discuss evidence for impulsive interactions of the disc with respect to kinematics in the next subsection.

2.5.4 Age-Velocity Dispersion Relation

We now move away from morphology and chemistry to examine kinematics and use the temporal behaviour of the stellar velocity dispersion for this purpose. The velocity dispersion of a region analogous to the ‘solar neighbourhood’ is used to quantify the influence that external interactions have on the kinematics of the disc. To remove the bias that arises from the velocity dispersion gradient as a function of disc radius we select stars from an annulus of width 2 kpc, centred on $2 \times R_d$ and a height of less than 3 kpc above and below the equatorial plane. Figure 2.16 shows the velocity dispersion of stars orthogonal to the disc plane (σ_z), as a function of their age (τ_*) at $z=0$. While many of the RaDES galaxies attain the observed velocity dispersion of the Milky Way (10–20 km s⁻¹ found by Soubiran & Girard 2005; Holmberg et al. 2007; Soubiran et al. 2008) when the youngest stars are considered, the older populations have far greater dispersions than observed. The Age-Velocity Dispersion Relations (AVRs) shown in Figure 2.16 exhibit a greater increase in σ_z as a function of τ_* and the appearance of more discrete steps than are apparent in observations. Greater velocity dispersions are to be expected in simulations as less than ten resolution elements are found in the would-be thin disc (if such a structure were resolvable). The high early velocity dispersions found even in field galaxies with the fewest mergers (e.g. *Krios* or *Selene*) may indicate that these galaxies experience excess kinematic heating from mergers. Another possibility is that very early in the galaxy’s formation cold flows (rather than discrete mergers) are responsible for forming the majority of stars. As it is well known that cosmologically simulated galaxies form too many stars at early times (see Table 2.1 for the stellar mass fractions) it is possible that the high velocity dispersion of old stars is simply

reflecting this shortcoming. We note however that maps of the gas distribution at high redshift clearly show discrete gaseous objects merging and no evidence is found for cold gas streams after $z=2$.

The AVRs do not at first display any obvious distinction between field and loose group environments, so a more rigorous analysis is called for. We have attempted to quantify the difference between a “stepped” and a smooth AVR by looking for spikes in the age-derivative of $\sigma_z(\tau_*)$. If the age-derivative of $\sigma_z(\tau_*)$ exhibits spikes above some significance level (the step-threshold) it will betray the existence of steps in the velocity dispersion. Galaxies that have steps with magnitude exceeding a threshold (the step-threshold) that is a factor of β greater than the average of the age-derivative of σ are defined as having a “stepped profile”. For the annulus displayed in Figure 2.16 and $\beta = 5$, seven out of ten loose group galaxies have stepped profiles while only three of the nine field galaxies do. The radius, thickness and height of this annulus was varied to avoid bias that may arise from sampling a spiral arm. The results of these different experiments are shown in Table 2.3. The radius of the annulus is varied between 2 and 3 times the disc scale length, the thickness between 2 and 6 kpc and a height limits of ± 1 kpc and ± 3 kpc are tested. The value of β is varied from 5 to 6, if a value much lower than this is used the criterion classifies noise as a “step”, much higher and no steps are found whatsoever. Typically the number of stars in each age bin (and in every case where a step is found) is large enough to keep the Poisson error less than $\sim 10\%$, this is not high enough to add enough detected steps to change the interpretation nor to cast doubt on steps that *are* detected. Table 2.3 shows the fraction of galaxies in each sample with “steps” for a number of different annuli, height cuts and β : in each case the loose group galaxy sample has a higher fraction of “stepped” profiles. We do note that the low number of galaxies in each sample makes the significance of this results quite weak and repetition of this method with a larger number of simulated galaxies

is prudent before accepting the findings. For now we assume the findings are reliable and offer an interpretation.

The physical mechanism shaping the AVR can be simply thought of as stars being heated to greater dispersion by all mergers subsequent to their formation and to an extent that depends on the severity of the merger (Villalobos & Helmi 2008; Di Matteo et al. 2011). A series of gentle mergers therefore results in a smoother decline in dispersion towards younger stars (Kazantzidis et al. 2008) while a large and disruptive merger excites all stars formed previously to a plateau that gives a more step-like appearance to the AVR (Brook et al. 2004). This contrasts with the conclusions of House et al. (2011) where stars are found to form with a velocity dispersion and retain it as a signature of the gas state at that time, however in either scenario the analysis performed in this work is a valid measure of the effect of disc disruption on stellar kinematics. The results shown in this work would seem to suggest that, in spite of a superficially similar major-merger history, there are in fact some differences in the mergers experienced by the galaxy disc and the interaction histories. Firstly galaxy disc major mergers could impact the galaxies differentially depending on the gas fraction (Cox et al. 2006; Hopkins et al. 2009; Lotz et al. 2010), the orbital configuration (Barnes 2002; Robertson et al. 2006) and the large-scale tidal field (Martig & Bournaud 2008). Secondly, the number of minor mergers or interactions with orbiting satellites could have an impact in shaping the AVR (Quinn et al. 1993; Abadi et al. 2003; Bournaud et al. 2005). Third, the interaction of the galaxy with the intragroup medium may have an impact as found by Bekki & Couch (2011) wherein the authors find that repetitive harassment in groups can lead to star formation bursts and disc heating.

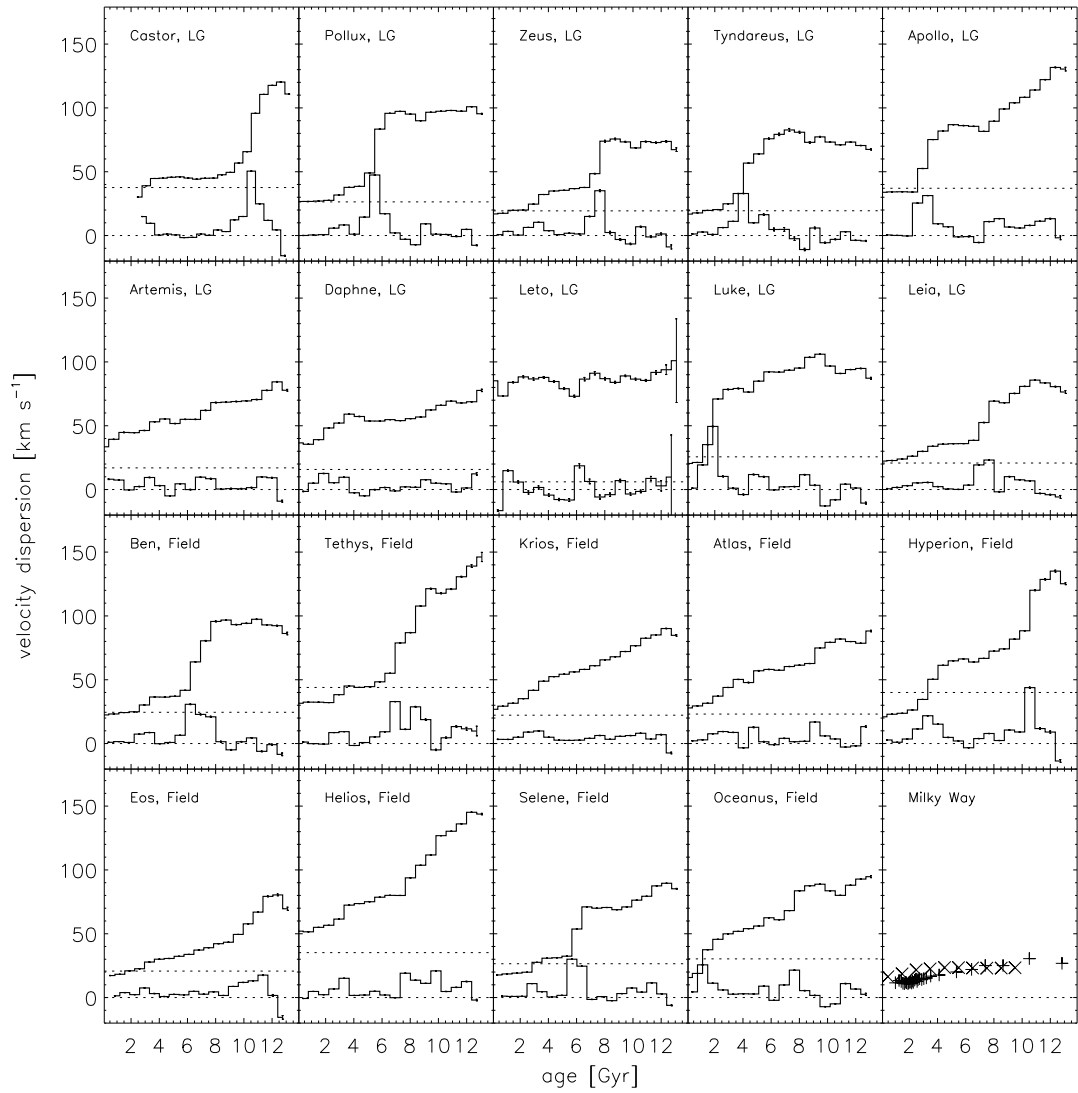


Figure 2.16: Present day stellar vertical velocity dispersion as a function of τ_* for an annulus of thickness 6 kpc centred on $2 \times R_d$ and a height of 3 kpc above and below the equatorial plane. The lower line is the age-derivative of this function, $d\sigma_z/d\tau_*$, error bars denote 2 standard deviations. Horizontal dotted lines define the zero point and a step-threshold that is $5 \times \langle d\sigma_z/d\tau_* \rangle$. The bottom-right tile shows observations of Milky Way stars, plus symbols are the 4065 F and G dwarfs with age errors less than 25% from the solar neighbourhood (Holmberg et al. 2007). Thin-disc clump giant stars from Soubiran et al. (2008) are plotted as crosses.

Table 2.3: Different choices of disc annulus, height cut-off and β are made, the final two columns state the fractions of galaxies in each sample that exhibit steps based on these criteria.

Radius of annulus	Annulus width	Height	β (threshold factor)	Loose Group	Field
R_d	(kpc)	(kpc)			
2	± 1	± 1	5	9/10	6/9
2	± 1	± 3	5	8/10	5/9
2	± 3	± 3	5	7/10	3/9
3	± 1	± 1	5	9/10	6/9
3	± 1	± 3	5	9/10	4/9
3	± 3	± 3	5	9/10	2/9
2	± 1	± 1	6	9/10	3/9
2	± 1	± 3	6	7/10	2/9
2	± 3	± 3	6	7/10	3/9
3	± 1	± 1	6	9/10	3/9
3	± 1	± 3	6	8/10	2/9
3	± 3	± 3	6	9/10	2/9

2.6 Conclusions

We have presented a suite of cosmological simulations with the intention of comparing field galaxies with galaxies in Local Group environments. The galaxies are taken from cosmological simulations where a zoom method is used to allow sub-kpc resolution while simultaneously accounting for large-scale structure formation. A kinematic decomposition has been performed to separate disc stars from spheroid stars and we have analysed the morphology of the galaxies. We have also examined the metallicity gradients finding trends with total mass (within R_{vir}) but a very weak or non-existent correlation with environment. Finally the stellar velocity dispersion is studied and tentative evidence of a dependence on environment is found in the signature of impulsive heating in group galaxies. The results of this work are pertinent to the comparison of simulated field galaxies with observations of the Milky Way. The conclusions of this work are summarised here:

1. No distinction between loose group and field galaxies is seen when considering the spheroid-to-disc ratio although examination of galaxies with greater spheroidal components shows that they all have interactions that disturb their disc rather than forming from kinematically hotter gas. This is however far from conclusive as there are only four galaxies with significantly higher spheroidal components of the total 19.
2. Metallicity gradients of loose group galaxies are very similar to those of field galaxies with the same total mass, a result that is still consistent with observations of strongly interacting galaxies (Kewley et al. 2010b) though no conclusive evidence is seen that loose group galaxies should have significantly flatter gradients compared with their counterparts in the field. The absolute gradients are consistent with observations (Zaritsky et al. 1994; Garnett et al. 1997; van Zee et al. 1998) yet when normalised by disc scale length gradients

are an order of magnitude flatter than observed suggesting that density profiles are too concentrated. Observations also show that more massive spiral galaxies have flatter gradients, this has previously been matched by semi-analytical models (Prantzos & Boissier 2000) using scaling relations but the trend has now also been shown to exist for our numerically simulated galaxies. We also find a link between metallicity gradients and stellar density gradients that suggests that galaxies in the mass range studied here have similar metallicity gradients when expressed in dex/R_d . Variance in this value is perhaps attributable to radial migration or disruptive mergers.

3. Examination of the age-velocity dispersion relation reveals that, as expected, the velocity dispersion of old stars in the simulated galaxies ($\sim 75\text{--}160 \text{ km s}^{-1}$) is greater than observed for the Milky Way disc ($\sim 20\text{--}30 \text{ km s}^{-1}$). Loose group galaxies exhibit more *stepped* relations that suggest mergers/harassment do have a greater impact on the loose group galaxies than field galaxies. This is at odds with the apparent similarities in the major merger frequency of the two samples and suggests that the major merger history of dark matter haloes may not be an accurate probe of the galaxy disc merger history. Care should be taken with this result as it is not entirely consistent with the other findings in this chapter here and as a test of environmental effects is less reliable than the other properties.

The main conclusion to come from this work is that in such sparse environments where the galaxies are not directly interacting galaxies exhibit different properties depending on individual merger histories and infall rates but that loose groups environments are only very weakly different to the field. It has been suggested for cluster galaxies that it is likely that galaxies are shaped more by direct mergers and their own secular behaviour rather than the large-scale environment that impacts the aforementioned only indirectly (McGee et al. 2008). Structures further than

~ 1 Mpc distant have little influence for galaxies with masses presented here.

The method used to define mergers in this work may be insufficient to link mergers to the signatures of the impact they have on the disc properties and a future study to follow this should develop a larger suite using only dark matter simulations to quantify the satellite distribution and minor merger rates with a greater statistical significance. Simulations at higher resolution should also be employed to determine conclusively if any systematic difference in metallicity gradients exists. We finish by stating that at the resolutions considered here simulated galaxies may be safely compared with Milky Way properties whether they inhabit loose group or field environments, however attention must be given to the aggregated merger properties, mass and internal structure for such comparisons to be meaningful.

Chapter 3

ABUNDANCE GRADIENT EVOLUTION

All we ever see of stars are their
old photographs.

Dr. Manhattan

Abstract

In this chapter we examine radial and vertical metallicity gradients using a suite of disc galaxy hydrodynamical simulations, supplemented with two classic chemical evolution approaches. We determine the rate of change of gradient slope and reconcile the differences existing between extant models and observations within the canonical ‘inside-out’ disc growth paradigm.

A suite of 25 cosmological discs is used to examine the evolution of metallicity gradients; this consists of the 19 galaxies in the RaDES (RAMSES Disc Environment Study) sample (Chapter 2), realised with the AMR code RAMSES, including nine drawn from the ‘field’ and ten from ‘loose group’ environments. Four discs are selected from the MUGS

(McMaster Unbiased Galaxy Simulations) sample (Stinson et al. 2010), generated with the smoothed particle hydrodynamics (SPH) code GASOLINE, alongside discs from Rahimi et al. (2011: GCD+) and Kobayashi & Nakasato (2011: GRAPE-SPH). Two chemical evolution models (CEMs) of inside-out disc growth (Chiappini et al. 2001; Mollá & Díaz 2005) were employed to contrast the temporal evolution of their radial gradients with those of the simulations.

We first show that generically flatter gradients are observed at redshift zero when comparing older stars with those forming today, consistent with expectations of kinematically hot simulations, but counter to that observed in the Milky Way. The vertical abundance gradients at $\sim 1\text{--}3$ disc scalelengths are comparable to those observed in the thick disc of the Milky Way, but significantly shallower than those seen in the thin disc. Most importantly, we found that systematic differences exist between the predicted evolution of radial abundance gradients in the RaDES and CEMs, compared with the MUGS sample; specifically, the MUGS simulations are systematically steeper at high redshift, and present much more rapid evolution in their gradients.

We show that the majority of the models predict radial gradients today which are consistent with those observed in late-type discs, but they evolve to this self-similarity in different fashions, despite each adhering to classical ‘inside-out’ growth. We find that radial dependence of the efficiency with which stars form as a function of time drives the differences seen in the gradients; systematic differences in the sub-grid physics between the various codes are responsible for setting these gradients. Recent, albeit limited, data at redshift $z \sim 1.5$ are consistent with

the steeper gradients seen in our SPH sample, suggesting a modest revision of the classical chemical evolution models may be required. This work has been published as Pilkington et al. (2012a) and credit is owed to the co-authors for the contribution of data, analytical methods and useful discussions.

3.1 Introduction

The recognition that metals are not distributed homogeneously throughout the disc of the Milky Way (Shaver et al. 1983) has proven to be fundamental in our efforts to understand the role of interactions, mergers, accretion, migration, and gas flows, in shaping the formation and evolution of galaxies. A rich literature now exists which confirms these radial abundance trends in both spirals (e.g. Simpson et al. 1995; Afflerbach et al. 1997; Mollá et al. 1999; Carrera et al. 2008; Kewley et al. 2010a; Sánchez-Blázquez et al. 2011) and ellipticals (e.g. Kormendy & Djorgovski 1989; Franx & Illingworth 1990; Peletier et al. 1990). Vertical trends have been studied somewhat less frequently (e.g. Marsakov & Borkova 2005, 2006; Soubiran et al. 2008; Navarro et al. 2011), but provide unique insights into the discrete nature (or lack thereof) of the thin disc – thick disc interface (and associated kinematical heating processes).

Observations of nearby spiral galaxies show that the inner discs have higher metallicities than their associated outer disc regions; at the present day, typical gradients of ~ -0.05 dex kpc^{-1} are encountered. These somewhat shallow gradients have provided *critical* constraints on models of galaxy formation and evolution, and are fundamental to the predictions of the classical ‘inside-out’ paradigm for disc growth. Predictions have been made of the time evolution of metallicity gradients in CEMs (e.g. Mollá et al. 1997; Fu et al. 2009) and observationally from planetary nebulae (e.g. Maciel et al. 2003), although until recently, we have had essentially

no *direct* observational constraints on what the magnitude of the time evolution of the gradients should be. This has changed with the work of Cresci et al. (2010), Jones et al. (2010), Queyrel et al. (2012), and Yuan et al. (2011), who have, for the first time, extended radial abundance gradient work to high redshifts. Yuan et al. (2011) show that for at least one ‘grand design’ disc at redshift $z\sim 1.5$, the gas phase metallicity gradient is significantly steeper (-0.16 dex kpc^{-1}) than the typical gradient encountered today. At even higher redshifts ($z\sim 3.3$), Cresci et al. (2010) and Troncoso et al. (2012, in prep), as part of the AMAZE/LSD surveys, suggest that *both* inverted gradients (higher abundances in the outskirts, relative to the inner disc) *and* standard declining gradients are seen. From the latter surveys, inverted gradients (ranging from $+0.0$ to $+0.1$ dex kpc^{-1}) appear associated with very massive stellar discs at these high-redshifts ($M_* > 3 \times 10^9 M_\odot$), while declining gradients (ranging from -0.0 to -0.2 dex kpc^{-1}) appear associated with lower mass stellar discs ($M_* < 3 \times 10^9 M_\odot$). Cresci et al. (2010) speculate that the inverted gradients may be due to recent infall of pristine material into the inner disc. These observations use emission lines (e.g. $[\text{OIII}]/\text{H}\beta$) that may be affected by the presence of shocks or AGN (the Cresci et al. 2010 galaxies are checked to ensure no AGN are present) and thus there are some doubts that the interpretation of the results as metallicity gradient is correct (Jones et al. 2012). These Lyman Break Galaxies, with their ~ 1 – 2 orders of magnitude greater star formation rates (relative to the typical Milky Way progenitor at that redshift), are more likely associated with massive spheroids in clusters/groups today (e.g. Nagamine 2002), as opposed to the Milky Way, and so are not directly comparable with the simulations described here. Constraining the metallicity gradients of galaxies beyond the local Universe remains a challenge for the future.

Using SPH simulations of disc galaxy mergers, Rupke et al. (2010a) show strong correlations of metallicity with environment and merger history, focussing on the

effects of gas inflows and star formation rate. Observations by Cooper et al. (2008) show that higher metallicity galaxies are more abundant in group environments and Kewley et al. (2006b) showed that interacting pairs of galaxies have systematically lower metallicities (~ 0.2 dex lower) than field galaxies or more loosely associated pairs. Radial gradients have been shown to flatten for galaxies that have experienced recent mergers (Kewley et al. 2010a); these also result in higher velocity dispersions and redistribution of the cold gas. In agreement with this, Michel-Dansac et al. (2008) studied the mass-metallicity relation for merging galaxies and concluded that the infall of metal poor gas during merger events lowers the gas phase metallicity. However, the timescale over which redistributed gas develops into a gradient like those we see in spiral galaxies today is unknown.

There have been several studies of chemistry within cosmological hydrodynamical simulations (e.g. Raiteri et al. 1996; Kawata & Gibson 2003; Okamoto et al. 2008; Scannapieco et al. 2008; Zolotov et al. 2010; Rahimi et al. 2010; Wiersma et al. 2011; Kobayashi & Nakasato 2011), each modelling certain observational properties with varying degrees of success. Some studies have examined the radial and/or vertical gradients using hydrodynamical codes (e.g. Rupke et al. 2010a; Rahimi et al. 2011), but the numerical study of radial gradients has predominantly been in the context of classical galactic chemical evolution codes (e.g. Prantzos & Boissier 2000; Chiappini et al. 2001; Mollá & Díaz 2005). Here we use 25 simulations realised with four different cosmological hydrodynamical codes: GASOLINE (Wadsley et al. 2004), GCD+ (Kawata & Gibson 2003), and GRAPE-SPH (Kobayashi & Nakasato 2011) all gravitational N-Body + SPH (Monaghan 1992) codes, and RAMSES (Teyssier 2002), an AMR code. Alongside these, we use the results from the CEMs of Chiappini et al. (2001) and Mollá & Díaz (2005).

This work aims to fill an important gap in the field, by complementing orbital parameter studies (e.g. Rupke et al. 2010a; Perez et al. 2011), systematic sub-grid

physics parameter studies (e.g. Wiersma et al. 2011), and detailed dissections of individual systems (e.g. Rahimi et al. 2011; Zolotov et al. 2010; Kobayashi & Nakasato 2011), with a statistical sample of Milky Way analogs. The approach taken here is different, but complementary, to the careful and compelling parameter study of Wiersma et al. (2011); there, the goal was to vary the input physics and examine the outcome, regardless of whether or not the simulated end-products might be classified still as Milky Way-like. Instead, we sampled a range of codes, sub-grid physics, and initial conditions, each of which has been ‘calibrated’, in some sense, by their respective authors, to resemble a classical Milky Way-like system. With that calibrated sample, our unique contribution is to examine the ‘path’ by which the gradients evolve, search for both random and systematic trends/differences between the samples, and compare with new empirical data at high-redshift. In spirit, this is exactly the approach taken in the seminal galactic chemical evolution comparison project (Tosi 1996), which examined the time evolution of classic chemical evolution models calibrated to the solar neighbourhood, in order to see where they differed ‘away’ from this calibrated boundary condition. This is the first time such a comparison of the temporal evolution of metallicity gradients has been undertaken with a statistical sample of simulated disc galaxies.

The outline of this chapter is as follows. The main differences between the codes are described in §3.2, where we describe the relevant mechanisms associated with the treatment of star formation and feedback (both energetic and chemical). The metallicity gradients inferred today for stellar populations of different ages are presented in §3.3. This is expanded upon in §3.4 where the radial metallicity gradients of the young stellar population as a function of redshift are considered. Finally, we summarise our findings in §3.5.

3.2 Simulations

The simulations used in this paper are fully described in Stinson et al. (2010: MUGS), Rahimi et al. (2011: *Gal1*), Kobayashi & Nakasato (2011: *KN11*) and Few et al. (2012: RaDES, see Chapter 2); the main characteristics of the simulations and their parent codes are described here and itemised in Table 3.1. The CEMs are fully described in Chiappini et al. (2001) and Mollá & Díaz (2005), but again we describe the main aspects in the following section.

3.2.1 RaDES

RaDES (RAMSES disc Environment Study), was simulated using the AMR code RAMSES (v3.01 Teyssier 2002). The motivation behind these simulations was to determine the systematic differences between simulated galaxies with neighbouring dark matter haloes similar to the Local Group and those in the field. The RAMSES simulations include gravity, radiative cooling, and heating from a uniform ionising UV background radiation (Haardt & Madau 1996). Hydrodynamic behaviour of the gas phase and gravitational potential is calculated on a spatially adaptive grid. A full description of the star formation model used in RAMSES is given Dubois & Teyssier (2008); refer to chapter 2 for details of the code. Here we simply state the input parameters for comparison with the other codes described.

Gas cells with density greater than a given threshold allow stars to form at a rate proportional to the density, $\dot{\rho}_s = \rho_g/t_*$, where t_* is the star formation timescale, which itself is proportional to the dynamical time ($t_0(\rho_g/\rho_0)^{-1/2}$), as first described by Rasera & Teyssier (2006). After Dubois & Teyssier (2008), we use a threshold of $n_0=0.1 \text{ cm}^{-3}$ and $t_0=8 \text{ Gyr}$. In combination, these choices correspond to an adopted star formation efficiency of 2%. Feedback from SNeII occurs instantaneously and the mass carried away is parametrised as $(\eta_{\text{SN}} + \eta_w)$, where η_{SN} is the fraction of a stellar particle’s mass that is ejected by SNeII and η_w is the fraction that is swept

up in the SNII wind.¹ In the RaDES simulations, $\eta_{\text{SN}}=0.1$ and $\eta_{\text{w}}=0$, which for these runs, led to less strongly peaked rotation curves. The metallicity of SN ejecta is determined by converting a fixed fraction, f_{Z} , of the non-metal content of new stars into metals; all galaxies in the RaDES sample used $f_{\text{Z}}=0.1$.

The cosmology of the RaDES simulation boxes is $H_0=70 \text{ km s}^{-1}\text{Mpc}^{-1}$, $\Omega_{\Lambda}=0.72$, $\Omega_{\text{m}}=0.28$, $\Omega_{\text{b}}=0.045$, and $\sigma_8=0.8$. The sample consists of nine isolated (field) galaxies and ten situated within loose groups.

3.2.2 MUGS

The MUGS galaxies were run using the gravitational N-body + SPH code GASOLINE which was introduced and described in Wadsley et al. (2004). Below, we emphasise the main points concerning the star formation and feedback sub-grid physics used to generate this suite of simulations, but first remind the reader of the background framework in which they were evolved and their basic characteristics.

The MUGS sample (Stinson et al. 2010) consists of 16 galaxies randomly drawn from a cosmological volume $50 h^{-1} \text{ Mpc}$ on a side, evolved in a Wilkinson Microwave Anisotropy Probe Three (WMAP3) Λ CDM cosmology with $H_0=73 \text{ km s}^{-1} \text{ Mpc}^{-1}$, $\Omega_{\text{m}}=0.24$, $\Omega_{\Lambda}=0.76$, $\Omega_{\text{b}}=0.04$, and $\sigma_8=0.76$. Each galaxy is resimulated at high resolution by using the volume renormalisation technique (Klypin et al. 2001), with a gravitational softening length of 310 pc. In the central regions of the simulation there is an effective resolution 2048^3 particles in total and within each the confines of each galaxy approximately 45% of these are gas particles and the rest are dark matter with additional star particles being created. The galaxies range in mass from 5×10^{11} to $2 \times 10^{12} M_{\odot}$. The four galaxies with the most prominent discs were

¹SNIIa are not accounted for in RaDES, see Chapter 4 for details of the chemodynamical upgrade to RAMSES which parallels that implemented within GCD+ (§3.2.3).

selected: $g422$,² $g1536$, $g24334$, and $g15784$, the latter of which is the closest to a Milky Way analog in the sample. Here ‘prominent’ means the inclusion of those for which there was unequivocal identification of the disc (from angular momentum arguments constructed from the gas and young star distributions, as discussed in §3.3.1). In a secondary sense, this eliminated extreme values of bulge-to-total, but formally, we only included those discs for which alignment based upon the gas/young stars was obvious.

² $g422$ was not described in the original MUGS paper (Stinson et al. 2010) but was produced identically to the rest of the MUGS suite.

Table 3.1: Basic present-day ($z=0$) characteristics of the 25 simulated discs. Column (1): simulation suite to which the code used to simulate the galaxy, Column (2), belongs; Column (3): total mass of baryons and dark matter within the virial radius; Column (4): mass of the stellar disc, after application of the kinematic and spatial cuts described in §3.3; Column (5): exponential scalelength of the stellar disc; Column (6): local environment of the galaxy, field or local group (LG); Column (7): mass-weighted vertical stellar abundance gradient, averaged over the radial range $2.5R_d \pm 2$ kpc; Column (8): mass-weighted radial *young* (stars born within the past 100 Myr) stellar abundance gradient, after application of the kinematic and spatial cuts described in §3.3.1.

Suite	Galaxy	M_{tot} ($10^{11} M_{\odot}$)	$M_{*,\text{disc}}$ ($10^{10} M_{\odot}$)	R_d (kpc)	Environment	$d[Z_{*,\text{all}}]/dh$ (dex kpc $^{-1}$)	$d[Z_{*,\text{young}}]/dR$ (dex kpc $^{-1}$)
MUGS	g15784	14.0	5.9	3.2	Field	−0.06	−0.04
	g422	9.1	2.0	2.8	Field	−0.06	−0.08
	g1536	7.0	3.3	2.5	Field	−0.07	−0.05
	g24334	7.7	2.7	1.0	Field	−0.03	−0.19
GCD+	Gal1	8.8	4.1	2.7	Field	−0.04	−0.01
Grape-SPH	KN11	11.0	2.0	4.7	Field	−0.03	−0.04
RaDES	Castor	10.5	7.2	4.0	LG	−0.17	−0.03
	Pollux	4.2	3.4	3.0	LG	−0.06	−0.05
	Tyndareus	3.3	1.3	1.3	LG	−0.02	−0.05
	Zeus	2.3	1.0	1.7	LG	−0.07	−0.04
	Apollo	8.9	6.3	3.0	LG	−0.04	−0.06

Table 3.1 – continued

Suite	Galaxy	M_{tot} ($10^{11} M_{\odot}$)	$M_{*,\text{disc}}$ ($10^{10} M_{\odot}$)	R_d (kpc)	Environment	$d[Z_{*,\text{all}}]/dh$ (dex kpc $^{-1}$)	$d[Z_{*,\text{young}}]/dR$ (dex kpc $^{-1}$)
	Artemis	7.5	3.2	1.9	LG	-0.08	-0.05
	Daphne	3.1	2.1	2.7	LG	-0.03	-0.06
	Leto	2.5	1.2	1.8	LG	-0.04	-0.05
	Luke	11.3	6.6	5.4	LG	-0.01	-0.03
	Leia	3.9	3.0	4.1	LG	-0.05	-0.02
	Tethys	7.2	5.1	2.8	Field	-0.08	-0.05
	Krios	5.7	4.0	2.5	Field	-0.10	-0.05
	Atlas	6.5	4.4	2.8	Field	-0.06	-0.04
	Hyperion	10.0	7.7	3.6	Field	-0.07	-0.04
	Eos	4.6	2.5	2.0	Field	-0.19	-0.07
	Helios	10.5	6.6	1.6	Field	-0.11	-0.04
	Selene	6.1	5.2	3.5	Field	-0.05	-0.06
	Oceanus	11.0	10.0	6.6	Field	-0.03	-0.03
	Ben	7.7	4.2	3.9	Field	-0.04	-0.03

Star formation and supernovae feedback uses the blast wave model (Stinson et al. 2006) whereby gas particles can form stars when they are sufficiently dense ($>1 \text{ cm}^{-3}$) and cool ($<15000 \text{ K}$).³ Gas particles which satisfy these criteria can form stars according to,

$$\frac{dM_s}{dt} = \epsilon_* \frac{M_g}{t_{\text{dyn}}}, \quad (3.1)$$

where ϵ_* is the star formation efficiency and is fixed to be 0.017. M_g is the mass of the gas particle forming the star particle of mass M_s and t_{dyn} is the dynamical time of the gas which depends on the local gas density;

$$t_{\text{dyn}} = \sqrt{\frac{1}{4\pi G \rho_g}}. \quad (3.2)$$

Heating from a uniform ultraviolet ionising background radiation field (Haardt & Madau 1996) is employed, and cooling is derived from the contributions of both primordial gas and metals; the metal cooling grid is derived using CLOUDY (v.07.02: Ferland et al. 1998), under the assumption of ionisation equilibrium, as detailed by Shen et al. (2010).

The CEM used in GASOLINE is fully described in Raiteri et al. (1996); here, we only discuss the main points. All stars with masses above $8 M_\odot$ explode as SNeII. An efficiency factor couples 40% of a given supernova’s energy ($E_{\text{SN}}=10^{51} \text{ erg}$) to the surrounding interstellar medium (ISM). Energy and metals from SNII originating in star particle j are distributed by volume weighting over the SPH kernel W_{ij} : affected gas particles mass m_i receive a fraction of the ejected energy and metals proportional to $m_i W_{ji}$. After Stinson et al. (2006) SNII feedback also triggers a cooling delay in the gas for particles found in a ‘blast wave’ of radius

³A typo in Stinson et al. (2006) incorrectly states the density threshold of star formation as 0.1 cm^{-3} .

$$R_{\text{bw}} = 10^{9.74} E_{51}^{0.32} n_{\text{amb}}^{-0.16} k_{\text{B}}^{0.2} P_{\text{amb}}^{-0.2} \text{ pc}, \quad (3.3)$$

for a duration of,

$$t_{\text{bw}} = 10^{9.65} E_{51}^{0.32} n_{\text{amb}}^{0.34} k_{\text{B}}^{0.7} P_{\text{amb}}^{-0.7} \text{ yr}, \quad (3.4)$$

where $E_{51} = E_{\text{SN}}/(10^{51}\text{erg})$, n_{amb} and P_{amb} are the ambient hydrogen density and ambient pressure calculated over the SPH kernel and k_{B} is the Boltzmann constant.

SNIa feedback is deposited only in the nearest gas particle. The SNeIa eject iron and oxygen; for every SNIa, $0.76 M_{\odot}$ of ‘metals’ is ejected, divided between iron ($0.63 M_{\odot}$) and oxygen ($0.13 M_{\odot}$). The binary model for SNeIa is based upon the single-degenerate progenitor formalism of Greggio & Renzini (1983), with secondaries spanning in mass from 1.5 to $8.0 M_{\odot}$. We have excluded secondaries in the 0.8 – $1.5 M_{\odot}$ range; doing so, regardless of IMF, only impacts on the SNIa rate at the $\sim 20\%$ level. Enrichment from SNeII is based upon power law fits in stellar mass to the nucleosynthesis yield tables of Woosley & Weaver (1995), convolved with a Kroupa (Kroupa et al. 1993) IMF, in order to determine the mass fraction of metals ejected. The total metallicity in this version of the code is tracked by assuming $Z \equiv \text{O} + \text{Fe}$.⁴ For these runs, only the $Z = Z_{\odot}$ yields were used, and long-lived SNeIa progenitors (those with secondaries with mass $m < 1.5 M_{\odot}$) were neglected. The metals that are tracked in this version of GASOLINE (O and Fe) all come from supernovae and are allowed to diffuse between neighbouring SPH particles, after Shen et al. (2010). The diffusion of metals is controlled using the trace-free shear tensor that increases diffusion when the velocity shear is high, i.e. compressive flows

⁴By assuming $Z = \text{O} + \text{Fe}$, we admittedly underestimate the global metal production rate by nearly a factor of two; the next generation runs with GASOLINE employ a more detailed CEM, incorporating the nucleosynthetic by-products of asymptotic giant branch evolution and thereby ameliorating this effect.

where there is no shear velocity will not diffuse gas properties while a collimated outflow will diffuse properties at the edges of the flow.

3.2.3 Gal1

Gal1 is a higher-resolution re-simulation of galaxy D1 (originally using a gravitational softening of 2.15 kpc for dark matter, *Gal1* uses 1.1 kpc) from Kawata et al. (2004) using the SPH code GCD+ (Kawata & Gibson 2003); while its characteristics have been discussed previously by Bailin et al. (2005), Rahimi et al. (2010), and Rahimi et al. (2011), an overview is provided here for completeness. Employing a comparable volume renormalisation, ‘zoom-style’ technique to that described in §3.2.2 (with a gravitational softening of 570 pc in the highest resolution region), *Gal1* was realised within a Λ CDM cosmological framework with $H_0=70$ km s⁻¹ Mpc⁻¹, $\Omega_m=0.3$, $\Omega_\Lambda=0.7$, $\Omega_b=0.04$, and $\sigma_8=0.9$, resulting in a Milky Way analog of virial mass $8.8\times 10^{11} M_\odot$. The effect of the ultraviolet background radiation field was neglected, while metal-dependent radiative cooling (adopted from MAPPINGS-III Sutherland & Dopita 1993) was included.

The star formation prescription employed requires (i) the hydrogen number density to be above a threshold of 0.1 cm^{-3} , (ii) a convergent gas flow to exist, and (iii) the gas to be locally Jeans unstable, i.e. $h/c_s > t_{\text{dyn}}$ where h is the smoothing length of gas and c_s is the local sound speed. Equation 3.1 is used to calculate the local star formation rate as in GASOLINE but in GCD+, $\epsilon_* = 0.5$ after Kawata (2001) and t_{dyn} is instead

$$t_{\text{dyn}} = \sqrt{\frac{3\pi}{16G\rho_g}}. \quad (3.5)$$

A standard Salpeter (1955) IMF was assumed, along with pure thermal feedback from both SNeII and SNeIa being coupled to the surrounding SPH particles. Feedback is distributed over the smoothing kernel as described for GASOLINE with

$E_{\text{SN}}=10^{51}$ erg of which 10% is divided between (99.8%) thermal and (0.2%) kinetic feedback. The mass that is ejected by SN is calculated according to the chemical evolution models employed for calculating the mass of each element produced by a star particle as a function of time.

The chemical evolution implementation within GCD+ takes into account the metal-dependent nucleosynthetic by-products of SNeII (Woosley & Weaver 1995), SNeIa (Iwamoto et al. 1999), and low- and intermediate-mass AGB stars (van den Hoek & Groenewegen 1997). Relaxing the instantaneous recycling approximation, GCD+ tracks the temporal evolution of the nine dominant isotopes of H, He, C, N, O, Ne, Mg, Si, and Fe. The SNeIa progenitor formalism of Kobayashi et al. (2000) is adopted.

3.2.4 KN11

KN11 corresponds to the so-called ‘Wider Region’ model described by Kobayashi & Nakasato (2011), realised used a hybrid GRAPE-SPH code. This model was drawn from the 5 Milky Way-analogs which eventuated from a larger suite of 150 semi-cosmological simulations. The term ‘semi-cosmological’ denotes that the simulated field was not large enough to sample the longest perturbations and as such, underestimates the degree of gravitational tidal torque which would otherwise be present in a fully cosmological framework. To compensate for this the initial system is provided with an initial angular momentum via the application of rigid rotation with a constant spin parameter $\lambda=1$. The cosmological parameters employed match those of §3.2.3, and led to a Milky Way analog of mass $1.1 \times 10^{12} M_{\odot}$. The effect of the ultraviolet background radiation field was included, as was metal-dependent radiative cooling from MAPPINGS-III (Sutherland & Dopita 1993).

The star formation prescription employed requires (i) the gas must be cooling, (ii) a convergent gas flow to exist, and (iii) the gas to be locally Jeans unstable.

The star formation rate is calculated using Equation 3.1 with Equation 3.2 as the dynamical timescale, the star formation efficiency is chosen to be $c=0.1$. A Salpeter (1955) IMF was assumed (with lower and upper mass limits of 0.07 and $120 M_{\odot}$, respectively), along with pure thermal feedback from both SNeII (50% of the massive stars are assumed to end their lives as SNeII, while the remaining 50% are assumed to end their lives as $10\times$ more energetic hypernovae) and SNeIa ($\sim 10^{51}$ erg SN^{-1}) being distributed to the surrounding SPH particles within 1 kpc (weighted by the SPH kernel).

The chemical evolution implementation within GRAPE-SPH takes into account the metal-dependent nucleosynthetic by-products of SNeII (Kobayashi et al. 2006), SNeIa (Nomoto et al. 1997), and low- and intermediate-mass AGB stars (Karakas 2010).

3.2.5 Chemical Evolution Models

In this work, we compare our results from the hydrodynamical simulations described in §3.2.2–3.2.1 to two CEMs both designed to reproduce the main features of our Galaxy. The models are described by Chiappini et al. (2001) and Mollá & Díaz (2005), and we refer the reader to these papers for full details.

In the model by Chiappini et al. (2001), the Milky Way forms by means of two main infall episodes, both represented by exponential infall rates. The first infall episode, characterised by the rate $\dot{\sigma}_{\text{H}} \propto A e^{-t/\tau_{\text{inf,H}}}$, is associated with the formation of the halo and thick disc, with an e -folding timescale ($\tau_{\text{inf,H}}$) of ~ 1 Gyr. The constant A is determined by requiring that the present-day mass surface density of the halo is reproduced.

The second infall phase is represented as $\dot{\sigma}_{\text{D}} \propto B(R) e^{-t/\tau_{\text{inf,D}}}$, and is associated with the formation of the thin disc. The thin disc is represented by independent annuli, each 2 kpc wide, with no exchange of matter between them, i.e. no radial gas

flows. The e -folding timescale ($\tau_{\text{inf,D}}$) of the second infall is assumed to be a linear function with increasing galactocentric radius (i.e. $\tau_{\text{inf,D}}(R) \propto R$) enforcing the so-called ‘inside-out’ paradigm for disc growth, with the gas accumulating faster in the inner regions of the disc, relative to the outer disc. The timescales here vary from ~ 2 Gyr in the inner disc, to ~ 7 Gyr in the solar neighbourhood, and up to ~ 20 Gyr in the outermost parts of the disc. The constant $B(R)$ is fixed in order to reproduce the present-day total surface mass density (stars + gas) in the solar neighbourhood. The star formation rate $\dot{\sigma}_*$ is expressed by the common Schmidt-Kennicutt law, $\dot{\sigma}_* \propto \nu \sigma_g^k(R, t)$, where $\sigma_g(R, t)$ represents the gas density at the radius R and at the time t , and $k = 1.5$. The star formation efficiency ν is set to 1 Gyr^{-1} , and becomes zero when the gas surface density drops below a certain critical threshold, adopted here to be $\sigma_{\text{th}} = 7 M_\odot \text{ pc}^{-2}$. The nucleosynthesis prescriptions for AGB stars, SNeIa and SNeII are drawn from the same sources listed in §3.2.3.

The CEM of Mollá & Díaz (2005) differs from that of Chiappini et al. (2001) in several aspects, in that it is multiphase, treating the ISM as a mixture of hot diffuse gas and cold molecular clouds. Each galaxy is assumed to be a two-zone system, comprised by a halo formed in an early gas-rich phase and a disc. The gas of the disc is acquired from the halo through an imposed infall prescription characterised by the inverse of the collapse time, which itself depends upon the total mass of the galaxy. The mass profile is imposed to adhere to the Persic et al. (1996) universal rotation curve. Similar to Chiappini et al. (2001), each galaxy is divided into concentric cylindrical zones 1 kpc wide. The collapse timescale depends on radius via an exponential function $\tau_{\text{inf}}(R) \propto e^R$, rather than the linear dependence upon R employed by Chiappini et al. (2001). Another important difference concerns the treatment of star formation: in the Mollá & Díaz (2005) model, stars form in two stages: first, molecular clouds condense with some efficiency out of the diffuse gas reservoir, and second, stars form with a second efficiency factor based upon

cloud-cloud collision timescales. In spirit, this mimics the effect of the threshold effect in the Chiappini et al. (2001) model: specifically, stars may form only in dense regions. The relation between the star formation rate and the gas density can be approximated by a power law with $n > 1$, again, in qualitative agreement with the law employed by Chiappini et al. (2001). In the halo, star formation follows a Schmidt-Kennicutt law with exponent $n = 1.5$. Extensive testing and tuning of the main parameters resulted in a grid of 440 models spanning 44 different masses (from dwarfs to giants, with 10 different star formation efficiencies per mass model). The chemical prescriptions for SNeIa and SNeII are again similar to those listed in §3.2.3.

3.2.6 Comparing Galaxies from Different Codes

When comparing the properties of galaxies evolved under different numerical schemes that start from different initial conditions we must take great care in our interpretation. Here we describe the general properties of the simulated galaxies in comparison with each other.

It is well known that simulated galaxies have excessive stellar mass fractions compared with their halo mass. This is shown in Figure 3.1 where the simulated values are compared with empirical virial-to-stellar ratios as a function of stellar mass. The majority of the galaxies have stellar masses around the minimum in the observed relation however it must be remembered that as they almost universally have virial-to-stellar ratios that are an order of magnitude too low, they should in fact (given the halo mass of each one as a constant) fall upon the low mass end of the relation. Comparing the simulations with each other reveals that the MUGS galaxies have slightly greater virial-to-stellar mass ratios than the RaDES galaxies with *Gal1* having a lower value than both (though again this is not dramatically different) while *KN11* has a significantly greater stellar mass. The star formation

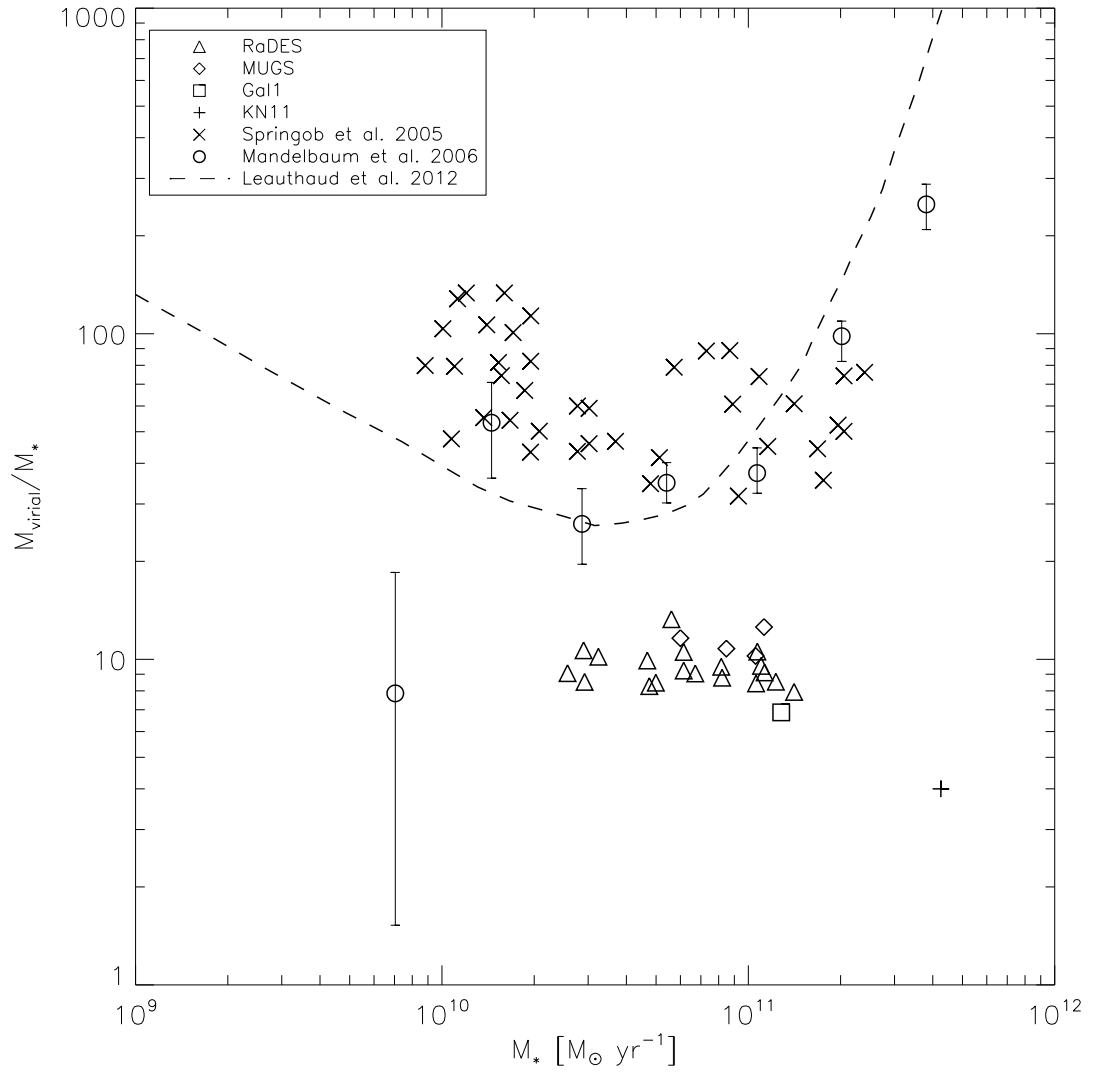


Figure 3.1: Dark-to-stellar mass ratio as a function of stellar mass. Observations are shown from Springob et al. (2005) taking the Tully Fisher relation (Tully & Fisher 1977) as a probe of the stellar mass as a function of the dark halo mass, from Mandelbaum et al. (2006) and Leauthaud et al. (2012) where weak lensing is used to determine the dark halo mass. Simulation data are also shown as having stellar masses around the minimum in the empirical relation and having dark-to-stellar mass ratios that are too low by an order of magnitude.

efficiency of each simulation may be expressed in the form,

$$\frac{d\rho_s}{dt} = \frac{\epsilon_{*,\text{eff}}\rho_g^{3/2}}{10^{11}\text{g}^{-1/2}\text{cm}^{3/2}\text{Gyr}^{-1}}, \quad (3.6)$$

where $\epsilon_{*,\text{eff}}$ is the dimensionless star formation efficiency, which is for each of the simulations presented here; 3.058 (RaDES), 5.202 (MUGS), 53.096 (*Gal1*) and 28.892 (*KN11*). While $\epsilon_{*,\text{eff}}$ is a useful number for comparing the star formation efficiencies of different simulations, you may note from Figure 3.1 that it by no means correlates monotonically with the galaxy formation efficiency, i.e. the stellar mass formed as a fraction of the virial mass of the dark matter halo it resides within. This is because SN (and other) feedback processes with different efficiencies and the precise implementation of star formation and feedback can strongly influence the properties of the resultant galaxy.

Figure 3.2 shows the star formation histories of the galaxies (however only two RaDES galaxies have been included for clarity, the star formation histories of all RaDES galaxies may be seen in Figure 2.9) including all stars within the virial radius. The data required to plot the star formation history of *KN11* is no longer available but it has a peak at 1 Gyr of $\sim 190 M_\odot \text{ yr}^{-1}$ declining to a present day value of $\sim 9 M_\odot \text{ yr}^{-1}$ (which as seen in Figure 3.1 makes it the galaxy with the greatest stellar mass) but has no significant bursts of star formation after the initial 5 Gyr. Apart from the slightly earlier onset of star formation in *Gal1* and *KN11* the star formation histories are superficially similar with an initial peak declining to a present day magnitude of $\sim 2 M_\odot \text{ yr}^{-1}$. The main difference between the galaxies is the time at which bursts in star formation occur.

The scale lengths of the galaxy discs may be found in Table 3.1, the RaDES galaxies have scale lengths ranging from 1.3–5.4 kpc (although there is an outlier with 6.6 kpc) and while the MUGS scale lengths tend to be in the lower end of this distribution (1.0–3.2) the two samples are consistent with one another, as are *Gal1*

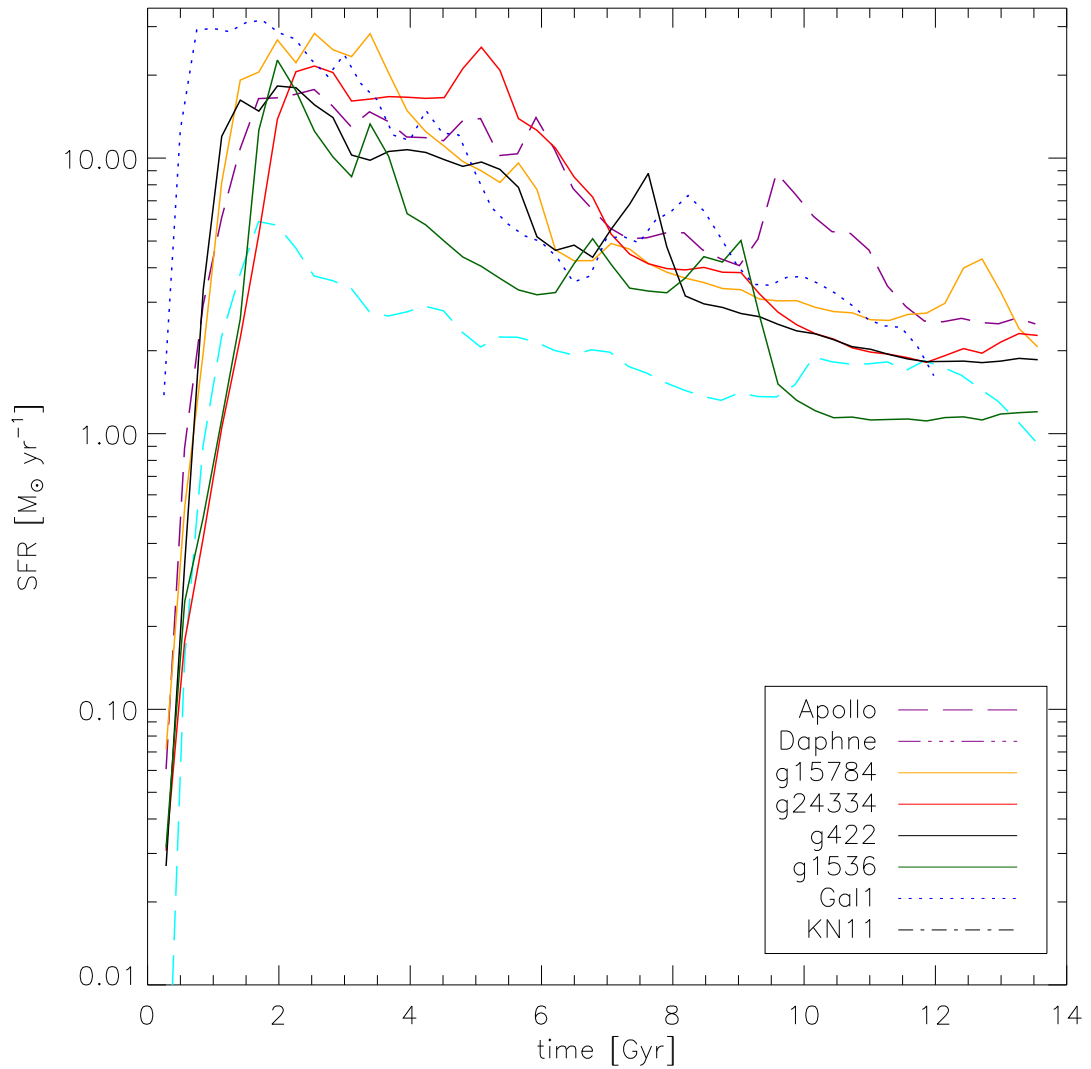


Figure 3.2: Star formation histories for the simulated galaxies presented in this chapter, stars within the virial radius are included. To avoid confusing the plot excessively, two representative RaDES galaxies have been chosen (*Apollo* and *Daphne*). Note that the main difference between the galaxies is in the placement of the star formation bursts, they all follow the same early peak followed by a decline with occasional further bursts. It may be significant that *Gal1* has its initial peak approximately 1 Gyr earlier than the other models.

(2.7 kpc) and *KN11* (4.7 kpc). The bulge/total mass ratio (B/T) of the MUGS galaxies are 0.652 (*g422*), 0.348 (*g15784*), 0.433 (*g1536*) and 0.584 (*g24334*). Both *KN11* and *Gal1* are bulge dominated with B/T values of 0.66 and 0.60 respectively which are approximate matches to the two bulge dominated MUGS galaxies. The RaDES galaxies tend to be disc dominated with fairly low B/T values ranging from 0.17 to 0.56 (see Figure 2.11). It is clear that all the galaxies studied here have large bulges but they are not critically dissimilar given that much of the difference stems from the feedback scheme employed in each case. We believe that the galaxies presented here are sufficiently similar in terms of the innate assembly to allow comparison, the differences between the methodology of each code are certainly of interest while the difference between galaxies that form differently is made in Chapter 2.

3.3 Present-Day Gradients

3.3.1 Radial Gradients

In this section, the present-day radial abundance gradients of the MUGS and RaDES simulations are presented. We focus here on one MUGS (*g15784*) and one RaDES galaxy (*Apollo*), which have been chosen as fiducial representatives of these two suites of simulations. Observational constraints on the abundance gradient of $z=0$ late-type galaxies may be found in, for example, Zaritsky et al. (1994) who measured a mean gradient of $-0.058 \text{ dex kpc}^{-1}$ for local spiral galaxies and van Zee et al. (1998) who found a comparable mean gradient from their sample ($-0.053 \text{ dex kpc}^{-1}$). In Kewley et al. (2010a) close galaxy pairs were found to have systematically shallower gradients (typically, $-0.021 \text{ dex kpc}^{-1}$). In each of these cases, the gradients are inferred from gas-phase nebular emission, which provides a ‘snapshot’ of the present-day gradient, similar to that inferred from, for example, B-stars, i.e. stars with ages $<100 \text{ Myr}$. Loose group galaxies in the RaDES suite exhibit no qualitative flattening

of metallicity gradients when compared with their ‘field’ equivalents. The dispersion in the RaDES metallicity gradients is smaller (~ 0.06 dex kpc^{-1}) than the systematic differences found between the RaDES and MUGS galaxies (~ 0.05 – 0.2 dex kpc^{-1}). A comprehensive analysis of the (subtle) systematic differences between the field and loose group galaxies within RaDES has been discussed in Chapter 2 but note the effect is minor in this context.

We employed a strict kinematic decomposition of spheroid and disc stars for each of the 25 simulations following the Abadi et al. (2003) formalism. The kinematic decomposition employed for the MUGS galaxies differs from that used in the original Stinson et al. (2010) analysis, in that J_z/J_{circ} for each star was derived self-consistently taking into account the shape of the potential, rather than assuming spherical symmetry and using the enclosed mass at a given star particle’s position. As in Chapter 2 the kinematic decompositions were performed by Leo Michel-Dansac (private correspondence). Additional (conservative) spatial cuts were employed to eliminate any satellite interlopers that might pass the initial kinematic decomposition. We define three age bins: young (stars born in the last 100 Myrs, to correspond roughly with B-stars), intermediate (stars formed 6–7 Gyr ago), and old (stars older than 10 Gyr).

Observational studies of radial gradients typically show higher metallicities in the inner disc relative to the outer disc (e.g. Rupke et al. 2010b). As noted above, observations of external systems typically make use of gas-phase oxygen abundances, as measured from HII regions, but consistency exists between that tracer and others known to provide a ‘snapshot’ of the gradient, e.g. short-lived main sequence B-stars. Our gas-phase and young (B-star) gradients are identical in amplitude and gradient, and hence in what follows, we employ ‘young stars’ (those formed in the previous 100 Myr period) to determine the abundance gradients.

The RaDES sample only tracks global metallicity Z , but as oxygen consistently

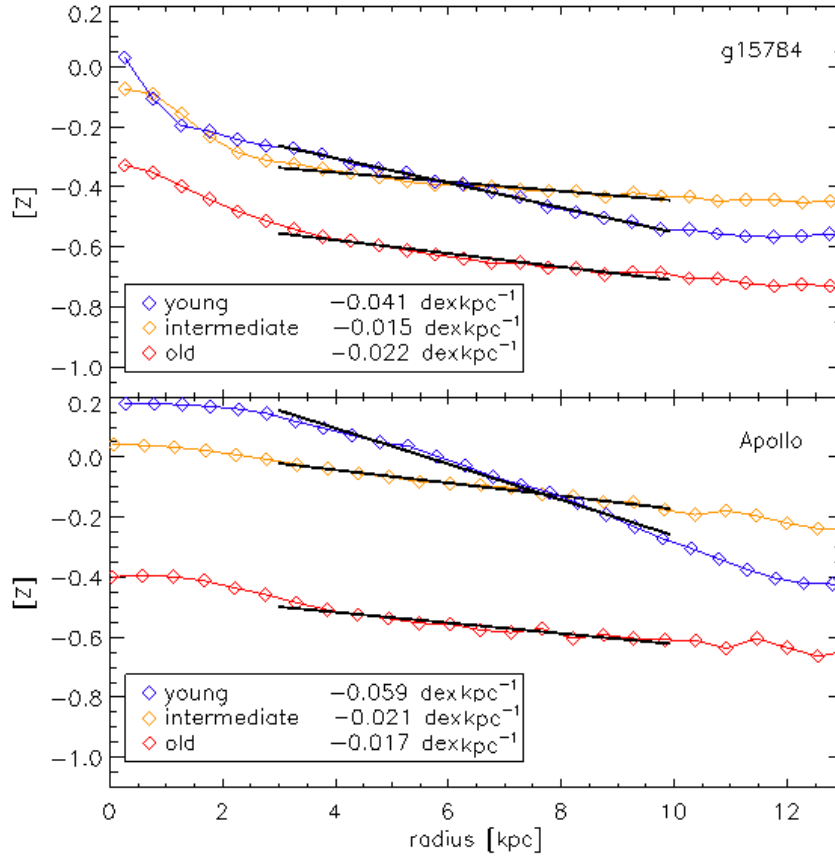


Figure 3.3: Stellar radial $[Z]$ profiles, for disc stars in three different stellar populations: young (blue) is defined as stars formed in the last 100 Myrs, intermediate (yellow) is defined as stars formed 6 to 7 Gyr ago, and old (red) is defined as stars older than 10 Gyr. Fits to the disc are overdrawn in black; the length of the black line corresponds to the region of the disc used in the fitting (see text for details). For clarity, only two galaxies are shown, one from MUGS (*g15784*, upper panel) and one from RaDES (*Apollo*, lower panel).

accounts for $\sim 50\%$ of Z , we use Z as a first-order proxy for oxygen, when making comparisons with observations. The version of GASOLINE employed for these MUGS runs track both O and Fe (from SNeII and SNeIa), and assume $Z \equiv O + Fe$; as noted earlier, this latter assumption leads to an ~ 0.2 dex underestimate of the global metallicity in the MUGS sample. This does not impact upon our gradient analysis, but does serve to explain why the RaDES and MUGS galaxies are offset by ~ 0.2 dex from one another in $[Z]$ in the figures presented here.

Figure 3.3 shows the mass-weighted radial gradients at $z=0$ in $[Z]$ for one MUGS galaxy (*g15784*, top panel) and one RaDES galaxy (*Apollo*, lower panel). The radial gradients are calculated using linear fits over the noted disc regions (overdrawn in black). These are chosen to exclude the central region, avoiding any residual co-rotating bulge stars that escaped the kinematic decomposition. The outer edge of the disc is taken as the point at which the surface brightness profile of the young stars (effectively, the cold gas) deviates from an exponential. To ensure that an appropriate region is considered here, we have been conservative in choosing the ‘disc region’. The gradient is robust to the choice of outer radius; reducing the choice of inner radius from 5 to 2 kpc has only a ± 0.007 dex kpc^{-1} impact on the inferred formal gradient, i.e. the differences in gradients between young, intermediate, and old populations are not significantly affected. Throughout this chapter we use the Asplund et al. (2009) values for the solar metallicity.

As one considers progressively older stellar populations (at the present-day), Figure 3.3 shows that the measured radial metallicity gradient becomes progressively flatter. Such behaviour is not unexpected in cosmological simulations which include gas infall, radial flows, high velocity dispersion gas, kinematically hot discs, and dynamical mixing/radial migration which is more pronounced for older stars (e.g. Sánchez-Blázquez et al. 2009; Rahimi et al. 2011). The timescale of the mixing that flattens the gradients in the MUGS and RaDES simulations is shorter than

the difference between intermediate and old populations of stars, as evidenced by radial gradients for the two populations, regardless of simulation suite, being quite similar. The degree of flattening of the *stellar* abundance gradients is such that by the present day, *within the simulations*, the older stellar tracers show a flatter abundance gradient than the younger tracers (recall Figure 3.3, reiterating results shown by Sánchez-Blázquez et al. (2009) and Rahimi et al. 2011). This is counter to what is observed in the Milky Way when inferring gradients using younger planetary nebulae versus older planetary nebulae (e.g. Maciel et al. 2003), but again, this is fully expected given the degree of kinematic (stellar) heating within these cosmological simulations, and does *not* impact on the use of gas-phase and young-star probes of the gradients (both possess the expected steeper abundance gradients at early-times). Future work in this area can, and should, make use of this powerful constraint on migration/heating; specifically the fact that (empirically) older stellar probes today have a steeper abundance gradients than younger stellar probes, while extant kinematically hot simulations show the opposite trend.

For completeness, in Table 3.1 we list the present-day mass-weighted young stellar radial metallicity gradients ($d[Z_{*,\text{young}}]/dR$, in units of dex kpc^{-1}) for each of the 25 simulations employed here (column 8) and plot the distribution in Figure 3.4. The similarity of the gradients is readily apparent, save for the MUGS galaxy *g24334*, which was included in the sample despite its stellar fraction being dominated by accreted stars, rather than *in situ* star formation (discussed further in §3.4). Its relatively small disc scalelength (1.0 kpc) also made fitting its gradient more challenging than the other MUGS discs.

Following Sánchez-Blázquez et al. (2011), we examined the effect of applying a different weighting scheme in determining the mean metallicities. When examining just the young stars or the gas, the weighting employed has no effect upon the inferred gradient. However, when deriving a composite gradient making use of

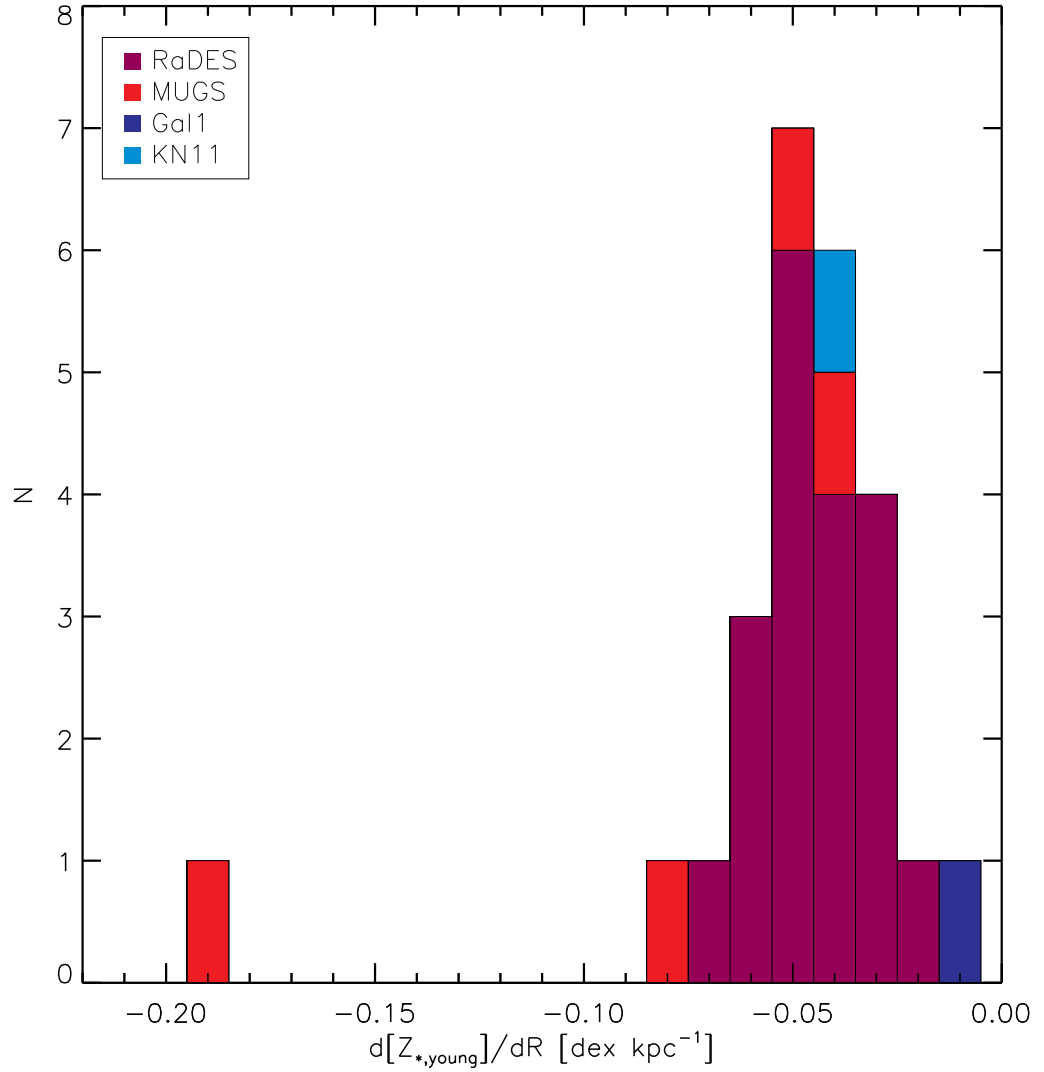


Figure 3.4: The distribution of young stellar radial metallicity gradients. The RaDES galaxies are shown in magenta, the MUGS galaxies in red, *Gal1* is dark blue and *KN11* is light blue. The steepest gradient is seen in *g24334* at -0.19 dex kpc^{-1} .

all stars in the disc, the weighting can become important, as Sánchez-Blázquez et al. (2011) suggested. We explored the impact of using, for example, luminosity-weighting (and log-weighting), by deriving the absolute magnitude of each simulated star particle, making use of its age, metallicity, and IMF, alongside the Marigo et al. (2008) isochrones.⁵ As expected from the Sánchez-Blázquez et al. (2011) analysis, the mean abundance shifted by ~ 0.1 dex depending upon the weighting employed, but the inferred gradient was not affected.

The abundance gradient of young stars (or equivalently, the ISM) is shaped by the time evolution of the radial star formation rate. To illustrate this we show the normalised star formation rate per unit surface area as a function of galactocentric radius in Figure 3.5. To match the CEMs of Chiappini et al. (2001) for the Milky Way (with the understanding that our simulations are not constructed *a priori* to be perfect replicas of the Milky Way), we normalise the star formation rate to have a value of $1 \text{ M}_{\odot} \text{ Gyr}^{-1} \text{ pc}^{-2}$ at a galactocentric radius of 8 kpc. The ‘normalised’ and ‘pre-normalised’ star formation rate surface densities (at 8 kpc), for each of the simulations, are not dissimilar; the latter lie in the range $\sim 1\text{--}2 \text{ M}_{\odot} \text{ Gyr}^{-1} \text{ pc}^{-2}$, save for the (known) discrepant MUGS galaxy *g24334* (which, pre-normalised, lies at $\sim 0.2 \text{ M}_{\odot} \text{ Gyr}^{-1} \text{ pc}^{-2}$, reflective of the fact that its stellar content is more dominated by its accreted component, rather than in situ star formation).

Each of the star formation rate profiles behave qualitatively like the classic inside-out CEMs of Chiappini et al. (2001) and Mollá & Díaz (2005): over time the star formation moves outwards from the inner to the outer disc. An important systematic difference between these representative simulations is apparent though, at least at higher redshifts ($1 < z < 2$). Specifically, the gradient in the star formation rate per unit area is steeper at higher redshifts for the MUGS galaxies; it is not clear if this is symptomatic of a single difference between the MUGS and RaDES galaxies,

⁵http://stev.oapd.inaf.it/cgi-bin/cmd_2.1

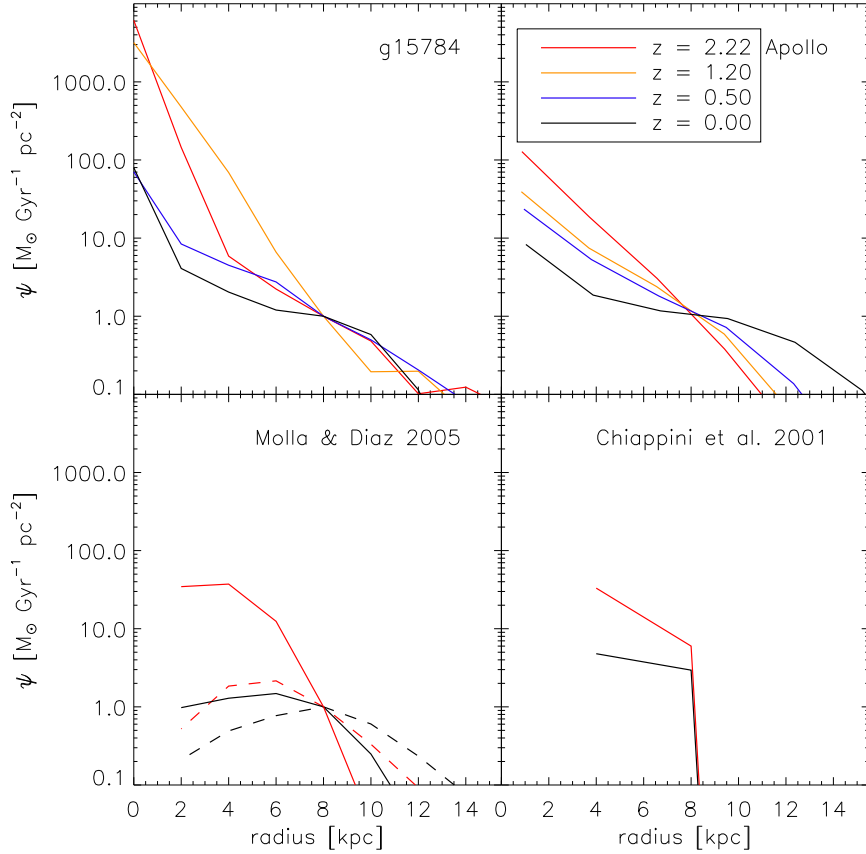


Figure 3.5: Star formation rate per unit surface area as a function of radius for the MUGS galaxy *g15784* (upper-left panel) and the RaDES galaxy *Apollo* (upper-right panel). The simulations are shown at four different redshifts: $z=0.0$, 0.5 , 1.2 , and 2.2 , as noted in the inset to the upper-right panel. 1 kpc annuli are used along with a height cut of ± 5 kpc above and below the disc. The mass of stars formed in the last 100 Myrs is calculated for each annulus out to a radius of 15 kpc. The curves have been normalised to $1 \text{ M}_{\odot} \text{ Gyr}^{-1} \text{ pc}^{-2}$ at galactocentric radius 8 kpc. The bottom panels show the corresponding predicted behaviour of the Chiappini et al. 2001 (right) and Mollá & Díaz 2005 (left) models. Only redshifts 0.0 and 2.2 are shown, other redshifts are excluded as these models evolve smoothly from $z=2.2$ to $z=0.0$. Two of the Mollá & Díaz (2005) models are shown, one with high star formation efficiency (dashed lines) and one with low star formation efficiency (solid lines).

or (more likely) a combination of factors including the star formation threshold, star formation efficiency, feedback schemes, and resolution of the respective simulations. Regardless, it is clear that *star formation is more centrally-concentrated in the MUGS sample at early stages in the formation of the disc which unsurprisingly leads to steeper abundance gradients in the early disc* (a point to which we return shortly).

3.3.2 Vertical Gradients

The mass-weighted vertical stellar abundance gradients in the simulations (*g15784* and *Apollo*) are presented in Figure 3.6. A ‘solar neighbourhood’ is defined for each simulation as being a 2 kpc annulus situated at a galactocentric radius of 2.5 disc scalelengths (column 5 of Table 3.1). These radial scalelengths were derived from exponential fits to the stellar surface density profiles.

Classic work from, for example, Marsakov & Borkova (2005, 2006) and Soubiran et al. (2008), and soon-to-be-released work using SDSS-SEGUE and RAVE datasets, show that vertical metallicity profiles can provide extremely effective tools for separating the thin disc from the thick disc. With $\sim 300\text{--}500$ pc softening/grid cells, we do not resolve the thin-thick disc transition. Figure 3.6, shows the vertical gradient for the MUGS galaxy *g15784* (orange) and the RaDES galaxy *Apollo* (purple), along with observational data for the Milky Way from Marsakov & Borkova (2005) and Marsakov & Borkova (2006). The two vertical lines show the respective resolutions of the MUGS and RaDES simulations.

The vertical metallicity gradients (in their respective ‘solar neighbourhoods’) for the 25 simulations analysed here are listed in column (7) of Table 3.1, the distribution is shown in Figure 3.7. We find little variation between the simulations in question, with the typical vertical gradient lying in the -0.05 ± 0.03 dex kpc^{-1} range. Only *Eos*, *Castor*, *Helios* and *Krios* lie outside this range, possessing somewhat steeper

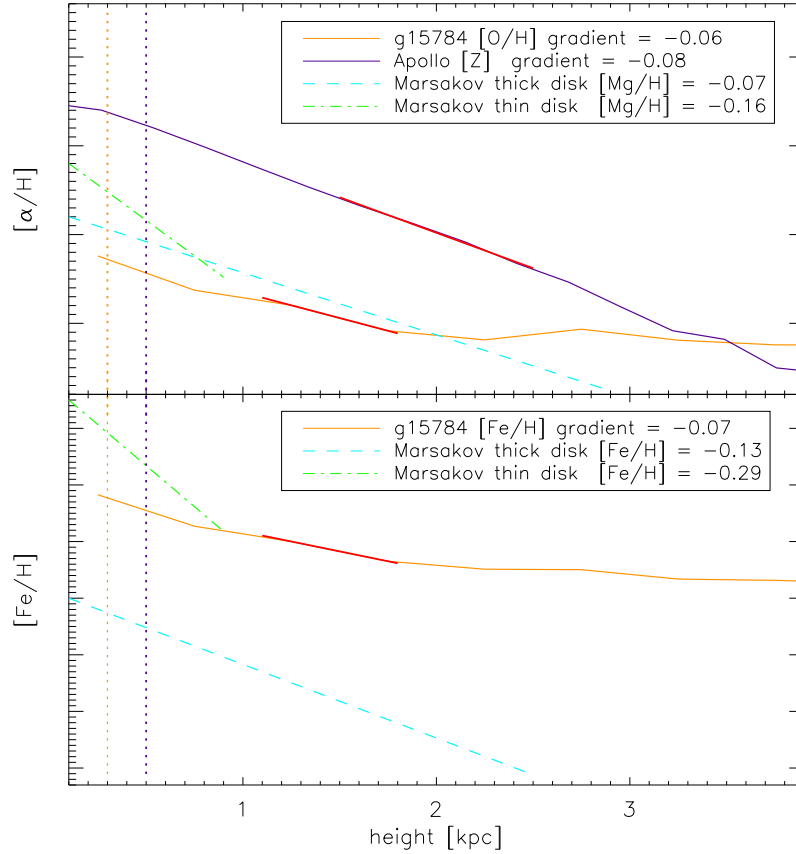


Figure 3.6: The vertical gradients of disc stars in the simulations. The top panel shows the [Z] vertical gradient of *Apollo* (purple, grad = -0.08) with the [O/H] gradient of *g15784* (orange, grad = -0.06) and observational data from Marsakov & Borkova (2005, 2006) of [Mg/H] gradients in the thin (blue, grad = -0.16) and thick (green, grad = -0.07) disc of the Milky Way. The lower panel shows the [Fe/H] gradients of the Marsakov & Borkova (2005, 2006) thin (grad = -0.29) and thick (grad = -0.13) disc data along with the *g15784* (grad = -0.07) [Fe/H] gradient. Overplotted vertically are the softening length of the MUGS (orange) and the minimum grid size of the RaDES (purple) simulations. The bold red lines show the region used to calculate the gradient.

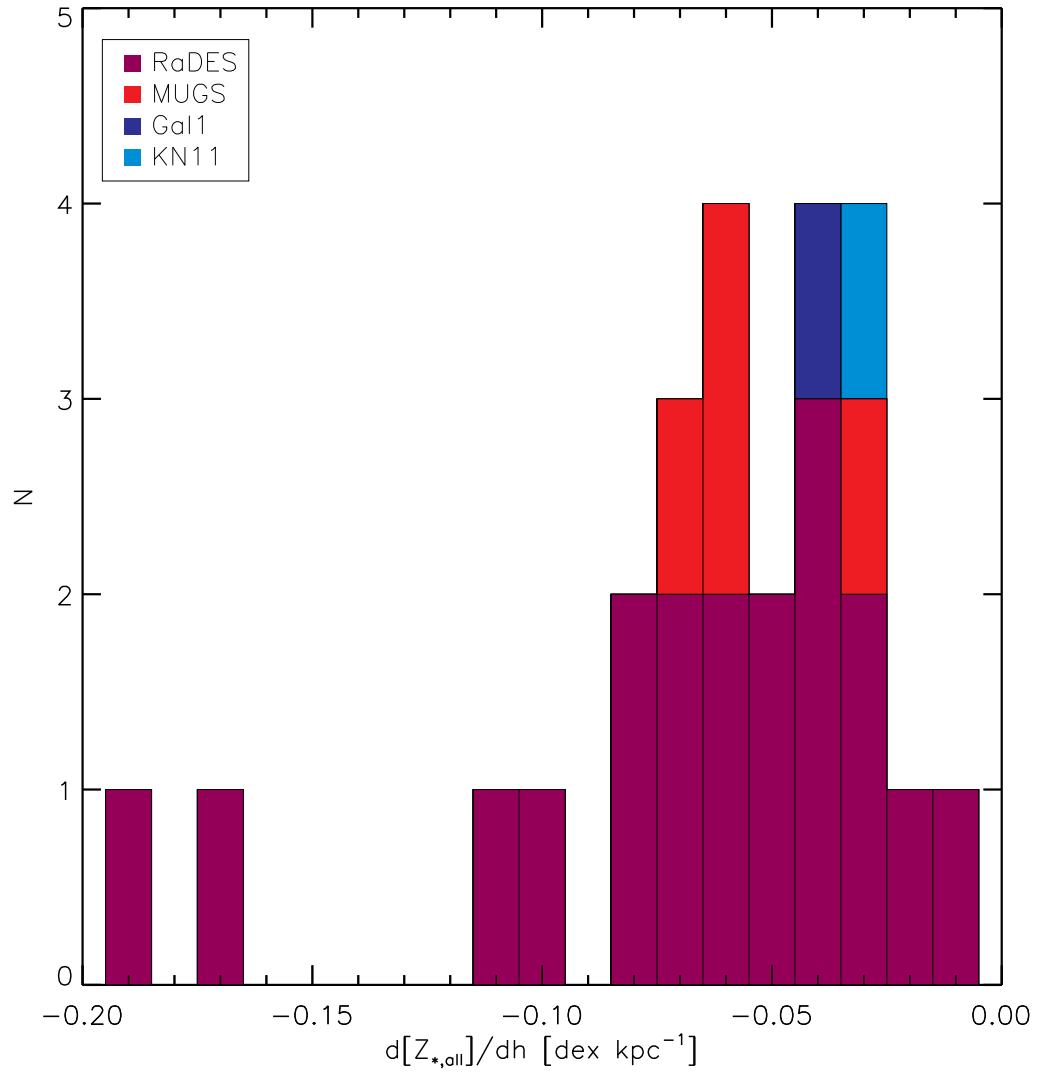


Figure 3.7: The distribution of vertical stellar metallicity gradients. The RaDES galaxies are shown in magenta, the MUGS galaxies in red, *Gal1* is dark blue and *KN11* is light blue. The two steepest gradients vertically belong to the two galaxies (*Castor* and *Eos*) about to undergo a merger that will disrupt the disc.

vertical abundance gradients. These three undergo the most extended late-time period of ‘quiescent’ evolution, as commented upon in Chapter 2.

At face value, the vertical gradients in $[\alpha/\text{H}]^6$ and $[\text{Fe}/\text{H}]$ inferred from the simulations are consistent with the observed values seen in the thick disc of the Milky Way (~ -0.05 to ~ -0.08 dex kpc^{-1}). The vertical gradients in the Milky Way’s thin disc, though, are consistently much steeper (where many authors find the thin disc gradient to be between ~ -0.25 to ~ -0.35 dex kpc^{-1} (e.g. Soubiran et al. 2008; Marsakov & Borkova 2006; Bartašiūtė et al. 2003; Chen et al. 2003) than the results we obtain from our simulations. Our spatial ‘resolutions’ range from ~ 300 – 500 pc, and the results appear compromised on vertical scales up to ~ 2 – 3 resolution ‘elements’, i.e. any putative ‘thin’ disc would be (not surprisingly) unresolved. In a chemical sense, these discs are too ‘hot’, in much the same way that their ISM and stellar populations are also kinematically hot (e.g. House et al. 2011).

On this issue of ‘resolution’, the global star formation rates reported are comparatively well converged as a function of resolution (Stinson et al. 2006, §5.2.4) The most notable change with increasing resolution is the addition of higher redshift populations, containing comparatively little mass, as earlier generations of halos are resolved. This is at least partially a result of star formation models largely being constrained to reproduce observed star formation rates.

The dependence of gradients on resolution though is far less predictable. At our current resolution we resolve sufficient substructure and disc dynamics to capture the salient physical mechanisms involved in migration, however while we do see net migration within in the stellar disc it should also be noted that there is a large non-physical heating effect in the simulations which make real and numerical effects impossible to disentangle at this resolution. Increasing resolution does resolve the physics behind migration processes better but it also makes the diffusion model in

⁶Total metallicity is again used as a proxy for α in the RaDES suite, while oxygen is used for the MUGS and GCD+ suites; magnesium is used in the observational datasets described by Marsakov & Borkova (2005, 2006).

GASOLINE more localised. Equally importantly, it is not clear to what extent the numerous processes involved in migration will interact with one another as resolution is increased. Taking the alternative approach of lowering resolution makes processes less likely to be captured (particularly substructure-induced migration), so it is not clear that convergence happens in a simple fashion. Ultimately, a definitive answer on the impact of resolution on migration requires far higher resolution than we are currently able to achieve and future work is required to address this issue.

3.4 Evolution of the Radial Gradients

While there exist a handful of studies of radial abundance gradients at high redshift (Jones et al. 2010; Cresci et al. 2010; Yuan et al. 2011), the difficulties in obtaining high resolution data for likely Milky Way-like progenitors has meant that theoreticians have had very few constraints on their models; as noted earlier, inside-out galactic CEMs can be constructed which recover the present-day gradients seen in the Milky Way, but they can take very different paths to get there. Some such models predict a steepening with time starting from initially inverted or flat gradients (e.g. Chiappini et al. 2001), while others predict an initially negative gradient that flattens (e.g. Mollá & Díaz 2005).

To make progress in this area, we now analyse the time evolution of the gradients within our 25 simulations, supplemented with two classical CEMs, making fits radially at each timestep for which a clear disc could be identified. As the disc is continually growing and evolving, we examined each timestep visually, identifying the outer ‘edge’ using the cold gas and young stars as a demarcation point. It should be noted here that the kinematic decomposition used to identify ‘disc stars’ in §3.3.1 and §3.3.2 was not used for this component of our analysis. By working only with very young stars at 2–3 disc scalelengths, when fitting gradients at each timestep, kinematic decomposition of disc vs spheroid stars becomes unnecessary.

Radial gradients were then derived by fitting typically from the outer edge of the disc to the inner part of the disc, where the inner point corresponds to the point at which the surface density profile deviates from an exponential. Again, as we are only using the stars formed in the previous 100 Myrs (B-stars) at a given timestep, the relevant disc (rather than star-forming bulge) regime is not difficult to identify.

In Figure 3.8, we show the time evolution of the radial gradient for our two ‘fiducial’ simulations: MUGS (*g15784*, right panel) and RaDES (*Apollo*, left panel). The gradients measured at each timestep are noted in the inset to each panel. Much steeper abundance gradients at high-redshift ($z > 1$) are seen within the MUGS galaxy. Further, the offset in mean metallicity between the two, as already alluded to, can be traced to the manner in which chemistry was included in the version of GASOLINE employed (i.e. the assumption that $Z \equiv O + Fe$, which affects the mean metallicity, but not the gradient).

In Figure 3.9, we show the time evolution of the $[Z]$ gradients for the 4 MUGS galaxies, the GCD+ galaxy (*Gal1*), the GRAPE-SPH galaxy (*KN11*), and the 19 RaDES galaxies. Importantly, we have also shown the time evolution of the predicted gradients for the CEMs of Chiappini et al. (2001) and two of the Milky Way-like models of Mollá & Díaz (2005);⁷ with the Mollá & Díaz (2005) data, the fits to determine the gradient at each timestep evolved as they did in the hydrodynamical simulations. As the disc grew, the fits were made at larger radii, to exclude the central region. From the earliest timestep to the latest the fitted region shifts ~ 3 kpc in radius (reflecting the growth of the disc over the timescales under consideration). The Chiappini et al. (2001) data were fit over the radial range 4 to 8 kpc at each timestep, reflecting the fewer relevant annuli available over which to make the fit. Chiappini et al. (2001) fit their gradients to the same chemical evolution models over a broader radial range (4–14 kpc), but our interests here are restricted

⁷Models kindly provided by Cristina Chiappini (private correspondence) and Mercedes Mollá via <http://adsabs.harvard.edu/abs/2005yCat...73580521M>

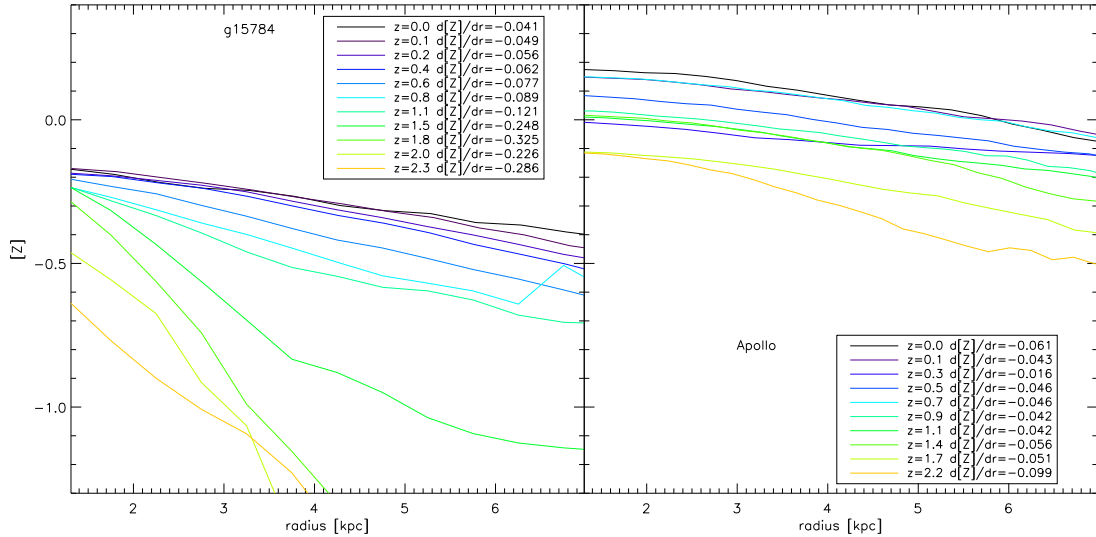


Figure 3.8: The radial $[Z]$ profiles of young stars in *g15784* (left panel) and *Apollo* (right panel). The different colours correspond to different redshifts running from $z=0$ (black) to $z=2.2$ (yellow), illustrating the time evolution of the abundance gradients in both simulations. Note the more dramatic flattening of the MUGS (*g15784*) relative to that of RaDES (*Apollo*). The fitted gradients were not done in an ‘automated’ fashion; we examined each timestep’s surface density, kinematic, and abundance profiles, to take into account the growth of the disc and identify the ‘cleanest’ disc region within which to determine the gradient.

to the inner discs of these models, where the star formation density threshold is less important in shaping the metallicity gradient.

For the Mollá & Díaz (2005) models, we show a low-efficiency (28,8) and high-efficiency (28,2) example, (where model 28 corresponds to a circular velocity of $\sim 200 \text{ km s}^{-1}$ and the efficiency factors correspond to the combined efficiency of molecular cloud formation and cloud-cloud collisions). The Chiappini et al. (2001) and, to a lesser extent, the high efficiency Mollá & Díaz (2005) models (at least since $z \sim 1$) steepen with time. The Chiappini et al. (2001) models have gradients which are mildly inverted at high-redshift ($\sim +0.02 \text{ dex kpc}^{-1}$ at redshift $z \sim 2$);

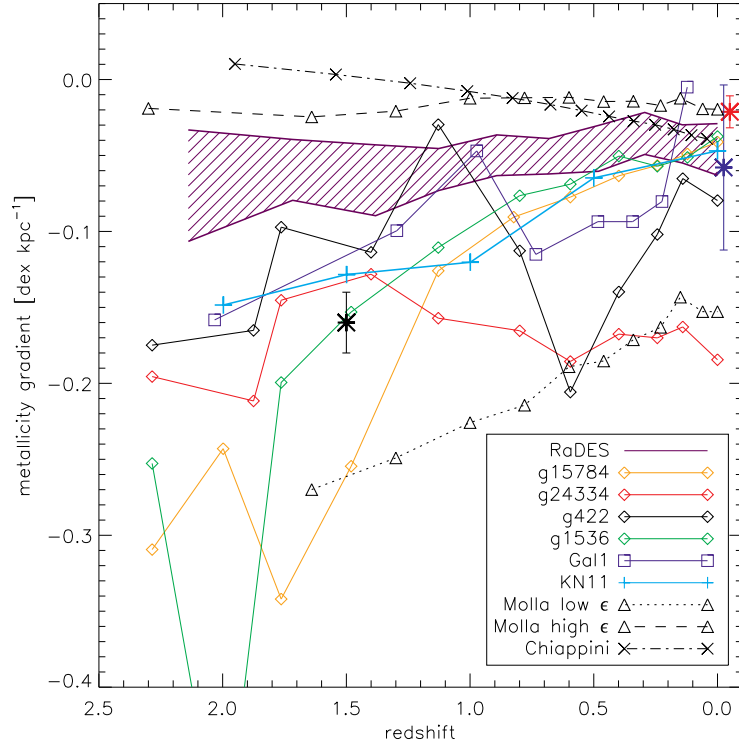


Figure 3.9: Radial $[Z]$ gradients of young stars plotted as a function of redshift. The discs are examined at each redshift to determine the appropriate galactocentric radius over which to measure the gradients. Four MUGS galaxies; $g15784$ (orange diamonds), $g24334$ (red diamonds), $g422$ (black diamonds) and $g1536$ (green diamonds) are shown, with *Gal1* (blue squares), *KN11* (cyan plus symbols), and the 19 RaDES galaxies (the purple hatched area shows the region encapsulating 1σ of the gradients measured at a given redshift). The two CEMs are also shown: Chiappini (black dot dashed crosses), and Mollá high efficiency (black dashed triangles) and low efficiency (black dotted triangles). The black asterisk corresponds to the lensed grand design spiral at $z \sim 1.5$ (Yuan et al. 2011), the blue asterisk to the typical gradient inferred in nearby spirals (Zaritsky et al. 1994), and the the red asterisk to the typical gradient seen in interacting discs (Kewley et al. 2010a); these latter local points are offset slightly at $z=0$, for clarity.

this works in the same direction as the inverted gradients observed by Cresci et al. (2010) at $z \sim 3$, albeit the gradients claimed by the latter are significantly more inverted (i.e. $\sim +0.1 \text{ dex kpc}^{-1}$) than encountered in any of the simulations or CEMs. It is important to remember though that the AMAZE/LSD samples at $z \sim 3.3$ are (a) primarily Lyman-Break Galaxies with star formation rates ($\sim 100\text{--}300 M_{\odot} \text{ yr}^{-1}$) well in excess of that expected for Milky Way-like progenitors, and are not likely ideal progenitors against which to compare these simulations or CEMs, and (b) in none of the current simulations are we able to unequivocally identify stable rotationally-supported discs, like those compiled by AMAZE/LSD. We require targeted simulations with much higher resolution at high-redshift than we have access to here, and tuned to be more representative of high-redshift Lyman-break galaxies, before commenting further on this potentially interesting constraint.

Conversely to the RaDES sample (represented by the purple hatched region, which encompasses 1σ of the gradient values at a given redshift) shows a mild flattening with time, more in keeping with full time evolution of the high efficiency Mollá & Díaz (2005) model. The MUGS sample shows not only steeper gradients as a whole at $z > 1$ (except for *g24334*, to which we return below), but also three of the four show the more significant degree of flattening alluded to in relation to Figure 3.8; this degree of flattening is more dramatic than that seen in any of the RaDES galaxies or the CEMs (except for the low efficiency models of Mollá & Díaz 2005). It is worth noting that no obvious trend is seen when comparing the field and group galaxies in the RaDES sample. This is perhaps attributable to our selection criteria; by removing strongly interacting galaxies (at or near a pericentre passage), the sort of systematic differences seen in the work of Rupke et al. (2010a,b); Perez et al. (2011), for example, would not be encountered here.

Shown also in Figure 3.9 are the typical gradients encountered in nearby isolated (Zaritsky et al. 1994, blue asterisk) and interacting (Kewley et al. 2010a, red asterisk)

disc galaxies (offset at $z=0$, for clarity, in Figure 3.9). The black asterisk at redshift $z\sim 1.5$ corresponds to the recent determination of a steep metallicity gradient in a high-redshift grand design spiral by Yuan et al. (2011). While intriguing, it is important to bear in mind that one should not necessarily make a causal link between these disparate data points; until a statistical sample of high-redshift gradients has been constructed, linking the Yuan et al. (2011) point with those at low-redshift should be done with caution.

For this latter reason, we have also included one MUGS galaxy (*g24334*) in our analysis (red curve: Figure 3.9) that does not have a present-day gradient consistent with the typical late-type spiral. This is done in order for the reader to see one example of a disc which possesses a steep gas-phase abundance gradient at high-redshift, comparable in slope to the Yuan et al. (2011) observation, but one which does not evolve in time to resemble the shallower slopes seen in nature today. *g24334* differs from the other MUGS galaxies, in the sense that the fraction of its stellar population born ‘in situ’, as opposed to ‘accreted’, is significantly lower. Further, its disc is less extended than the other Milky Way-analogs and its abundance gradient was derived at $\sim 0.5\times$ disc scalelengths, where the gradient is more robust to interaction-induced flattening (e.g. Perez et al. 2011).

These differences are ultimately traced to the underlying treatment of star formation and feedback within the simulations; for example, the MUGS galaxies have a higher star formation threshold than the RaDES suite (1 cm^{-3} vs 0.1 cm^{-3}). As such, both the MUGS sample and the low efficiency models of Mollá & Díaz (2005) preferentially form stars in the inner disc where the densities are higher; the RaDES galaxies and the remaining CEMs, with the lower threshold, have star formation occurring more uniformly throughout the early disc. Further, both MUGS and RaDES employ a standard blast-wave formalism for energy deposition into the ISM (Stinson et al. 2006), but the latter imposes a minimum blast wave radius of 2

grid cells, which means that ejecta is in some sense more ‘localised’ in the MUGS simulations (for the same SN energy, the RaDES blast waves are $\sim 2\text{--}3\times$ larger); distributing energy (and metals) on larger radial scales can result in a more uniform (i.e. flattened) metallicity distribution. The trend of *Gal1* lies somewhat between the extremes of MUGS and RaDES, which can be traced to the fact that *Gal1* uses a lower star formation threshold density (0.1 cm^{-3}), and almost negligible feedback, resulting in more localised metal enrichment. *KN11* also lies very close to the MUGS fiducial (*g15784*) in terms of the temporal evolution of its abundance gradient; both employ high SNe feedback efficiencies, albeit on different spatial scales (a density-dependent blast wave radius in the case of *g15784* and a fixed 1 kpc radius in the case of *KN11*) and with different star formation prescriptions (a 1 cm^{-3} star formation density threshold in the case of *g15784* and an absence of a threshold for *KN11*). Note that although these hydrodynamical simulations experience different merger histories, the metallicity gradients are more affected by the recipe of sub-grid physics. This is highlighted by our large samples of simulations generated with different codes.

As detailed in §3.2.5, Chiappini et al. (2001) use a two infall model; at early times the infall of primordial gas is rapid and independent of galactocentric radius, while at later times, gas is assumed to fall preferentially on the outer regions of the disc, causing a steepening of the gradient with time. The radial dependence of this disc infall timescale is fairly gentle (linear with increasing radius); on the other hand, Mollá & Díaz (2005) calculate the overall infall rate as a function of the mass distribution and rotation of the galaxy, and assume a much stronger radial dependence for the infall timescale. Specifically, the inner disc’s infall timescale is much more rapid than that of Chiappini et al. (2001), while the outer disc’s infall timescale is much longer. In combination, the gradient tends to flatten with time (particularly for their low efficiency models).

We find clear evidence of inside-out formation in the star formation profiles at different redshifts. Starting from an initially concentrated distribution, this flattens with time to the present-day, where star formation is more extended (and close to constant) over a large fraction of the disc (Figure 3.5). The radial dependence of star formation rate to infall rate sets the magnitude of the abundance gradient (Chiappini et al. 2001); a stronger radial dependence resulting in a steeper gradient. Such a configuration appears to come about naturally in the MUGS simulations, due in part to their higher star formation rate density threshold and perhaps the higher star formation efficiency and more localised chemical/energetic feedback. This contributes to the steeper gradients seen at early times in these simulations, relative to the other models. The RaDES galaxies behave more like the high efficiency model of Mollá & Díaz (2005). It should be noted however that despite the significant differences seen in the early stages of these galaxies’ evolution, the star formation distribution in the majority of these simulations is very similar at the present day.

3.5 Summary

This work provides evidence in support of the *imposed* inside-out disc growth paradigm adopted within CEMs; this growth is a natural outcome of both Eulerian and Lagrangian hydrodynamical simulations of disc galaxy formation within a cosmological context. We have examined how this inside-out growth impacts on the magnitude and evolution of abundance gradients in these galaxies, using a suite of simulations and models which were calibrated to recover the present-day shallow gradients observed in late-type spirals. This is not meant to be a comprehensive, systematic, examination of sub-grid physics, in the vein of Wiersma et al. (2011), for example; instead, we have shown (in some sense) the ‘best’ Milky Way-like simulations from several groups, using different codes, different initial conditions, and different assembly histories, and conducted a ‘blind’ experiment on the outputs, to quantify *how*

the gradients evolved to the imposed boundary condition of a shallow present-day gradient. Our findings include the following:

1. All galaxy models and simulations described here exhibit inside-out formation of the disc with varying degrees of centrally-concentrated star formation at early times (Figure 3.5). The evolving radial star formation rate dependence directly influences the resulting metallicity gradient; put another way, the signature of the star formation profile is embedded within the gradient of the young stars at each timestep. This signature though is diluted on the timescale of a few Gyrs. This is reflected in the differing gradients at the present-day between old and young stars (Figure 3.3); young stars at high-redshift within the MUGS sample (and observationally, it would appear, tentatively) form with a steep metallicity gradient, while those same stars today (now, old) have a fairly flat metallicity gradient (see Pilkington & Gibson 2012).
2. Within the suite of 25 cosmological hydrodynamical simulations the derived vertical abundance gradients are comparable to those observed locally in the Milky Way's thick disc. The resolution is, however, not sufficient to discriminate between thin and thick discs.
3. The evolution of simulated metallicity gradients depends strongly on the choice of sub-grid physics employed and as such the magnitude and direction of its evolution depends critically upon the specific details of the recipes implemented. While it is difficult to disentangle the behaviour of the star formation profile *a priori*, it is clear that simulated galaxies with more centrally-concentrated star formation have initially steeper abundance gradients. These are more consistent with the (albeit limited) observation of high redshift normal grand design spiral galaxies (Yuan et al. 2011).

4. All the models and simulations tend to similar present-day abundance gradients, despite the diversity at earlier times, save for *g24334* (which was chosen specifically in violation of the imposed shallow present-day gradient boundary condition, for illustrative purposes). In almost every case this requires the gradient to flatten with time, the exception being the CEM of Chiappini et al. (2001). This model starts with an initially positive gradient that is independent of its halo phase. The gradient then inverts to become negative, with a gradient similar to other chemical evolution models.
5. The diversity of the evolution of metallicity gradients is for the first time highlighted by our large sample of both hydrodynamical simulations and CEMs. Our results indicate that observations of the metallicity gradient for disc galaxies at different redshifts and that for the different age populations in the Galaxy are key to reveal the formation processes of disc galaxies and better constrain the sub-grid physics implemented with all the codes sampled.

Future work in this area will see us employ a finer temporal cadence, in order to better track the precise influence of merger events on the abundance gradients (both the magnitude of the effect and the timescale for re-establishing a stable abundance gradient). This study will also yield a deeper understanding of how the non-linear processes of star formation and feedback influence systematic differences between the various simulations presented here. The major upgrade to RAMSES (detailed in Chapter 4) will allow resimulation of the RaDES suite with a broad spectrum of chemical elements, including those from SNeII, SNeIa, and AGB stars. With ongoing and future large scale spectroscopic surveys and missions such as RAVE, APOGEE, SEGUE, HERMES, LAMOST, and Gaia, providing detailed information on the phase and chemical space signatures of the Milky Way and beyond, such a chemodynamical exploration will be both timely and critical for understanding the origin and evolution of abundances in galaxies, and their link to the underlying

CHAPTER 3

physics of galaxy formation.

Chapter 4

RAMSES-CH: A NEW CHEMODYNAMICS CODE

Every act of creation is first an act
of destruction.

Pablo Picasso

Abstract

In this chapter we present a new chemodynamical code, RAMSES-CH, for simulating the self-consistent evolution of chemical and hydrodynamical properties of galaxies within a fully cosmological framework. Building upon the adaptive mesh refinement code RAMSES, which includes a treatment of self-gravity, hydrodynamics, star formation, radiative cooling, and supernovae feedback. The new code traces the dominant isotopes of C, N, O, Ne, Mg, Si, and Fe. RAMSES uses the instantaneous recycling approximation meaning that metals are returned to the ISM immediately following star formation and in a single burst. RAMSES-CH relaxes the instantaneous recycling approximation, accounting for the contribution of Type Ia and II supernovae in addition to low- and intermediate-mass

asymptotic giant branch stars. The new chemical evolution modules are highly flexible and portable, lending themselves to ready exploration of variations in the underpinning stellar and nuclear physics. The new code is applied to cosmological simulations of a typical L_* galaxy to demonstrate that it can successfully recover basic empirical constraints regarding $[\alpha/\text{Fe}]$ – $[\text{Fe}/\text{H}]$ and Type Ia/II SN rates. A comparison of the various chemical evolution models tested is also discussed.

4.1 Introduction

The determination of elemental abundance patterns is one of the primary diagnostics of galaxy formation, with numerous spatial and temporal trends between age, kinematics, and chemistry guiding our insights into the underpinning physical processes. A great deal is known about the abundance of different elemental species of each part of the galaxy and the forthcoming Gaia mission will provide massive amount of dynamical information for the Milky Way that will be accompanied by the Gaia Chemodynamical Survey to further our understanding of the coupling between dynamics and chemistry. Observations of abundance ratios corroborate our understanding of the nuclear physics governing α -element production, in that they are produced on shorter timescales than iron-peak elements (e.g. Carbon et al. 1987; Edvardsson et al. 1993; Reddy et al. 2006; Ramírez et al. 2007) as a consequence of the mass-dependent nuclear burning processes acting within the relevant progenitor stars. Galactic chemical evolution (CE) models are predicated upon a coupling of these elemental production sites/timescales with phenomenological (yet, empirically constrained) parametrisation of star formation and gas inflows/outflows. The resulting predicted abundance patterns can be compared directly with observations in order to shed light on the formation and evolution of the system under study.

The formalism associated with the semi-numerical approach to galactic CE (e.g.

Talbot & Arnett 1971; Pagel & Patchett 1975; Tinsley 1980; Matteucci & Francois 1989; Carigi 1994; Gibson 1997; Chiappini et al. 1997; Ramírez et al. 2007) is a powerful tool when applied to sub-grid chemical evolution treatments within fully hydrodynamical simulations. The inclusion of CE schemes has been achieved in a number of cosmological hydrodynamical codes (e.g. Lia et al. 2002; Valdarnini 2003; Kawata & Gibson 2003; Kobayashi 2004; Tornatore et al. 2004; Romeo et al. 2005; Martínez-Serrano et al. 2008a; Oppenheimer & Davé 2008; Wiersma et al. 2009; Shen et al. 2010), each of which is based upon smoothed particle hydrodynamics (SPH). Key lessons can be learned from an examination of the role that chemical evolution plays in the physics of the interstellar medium. This is manifest in the metallicity-dependent radiative cooling rates of plasmas and their impact on the efficiency of metal transport throughout the disc and its consequent impact on stellar chemodynamics (Scannapieco et al. 2005). This impact upon turbulence-driven metal transport can be problematic, in light of known issues concerning the ability of conventional treatments of SPH to resolve the associated instabilities in certain regimes; such problems are ameliorated (though not entirely) by Eulerian approaches to fluid dynamics, including adaptive mesh refinement schemes (e.g. O’Shea et al. 2005; Agertz et al. 2007; Tasker et al. 2008).

In its simplest form, interparticle ‘mixing’ of SPH particles does not occur, i.e. metal-rich and metal-poor gas particles may co-exist near each other without sharing/mixing of their associated metals. The impact of this lack of mixing is readily apparent in a galaxy simulation’s metallicity distribution function and age-metallicity relation, as well as the abundance ratio plane (e.g. Pilkington et al. 2012b). The inclusion of turbulent mixing models within SPH remedies this lack of implicit diffusion (Shen et al. 2010), even if the associated diffusion coefficient is a necessary additional free parameter (albeit, informed by turbulence theory).

With the intention of providing a complementary (AMR) approach to extant

(SPH) chemodynamical and semi-numerical CEMs, we present what is, to our knowledge, the first cosmological AMR code which implements a temporally-resolved SN feedback and chemical evolution prescription. Written as a patch to the gravitational cosmological N-body and hydrodynamical code RAMSES, we now include the effects of SNeII, SNeIa, and low- to intermediate-mass asymptotic giant branch (AGB) stars, both from an energetic and chemical perspective. Nucleosynthetic processes are accounted for as a function of progenitor mass and metallicity.

The details of CEMs are described in §4.2 following which we explain the technical implementation of RAMSES-CH both in terms of the chemical evolution model and the way it is employed within the code itself in §4.3. The new code is applied to a fiducial model that broadly fits physical constraints, this is presented with the SN rates and abundance ratios of the resulting galaxy in §4.4. Different CEMs are used in resimulations in §4.5 where the influence of the IMF and SNIa progenitors is considered. The conclusions drawn and lessons learned from this work are discussed in §4.6.

4.2 Chemical Evolution Models

4.2.1 Initial Mass Function

The initial mass function is at the same time simple in principle and powerful in its effect on galactic chemical evolution. The extent of this influence is the subject of the latter parts of this chapter where the slope is shown to have a strong influence on abundance ratios. A qualitative description of the IMF was first formalised by Salpeter (1955) as a description of the “original mass function” but numerous multi-slope IMFs have now been proposed. These IMFs are shown in Figure 4.1. Multislope IMFs (Tinsley 1980; Scalo 1986; Kroupa et al. 1993; Scalo 1998; Kroupa 2001; Chabrier 2003) present a predicted luminosity function that is much closer

to observations. A comparison of the impact of the choice of IMF is conducted in Romano et al. (2005), the main conclusions are that Scalo (1986), Kroupa et al. (1993) and Chabrier (2003) give good fits to observations of the solar neighbourhood metallicity function. Salpeter (1955) and Scalo (1998) are the weakest, but the authors note that the uncertainties in the observations mean that the conclusions drawn by models using these IMFs are not invalid.

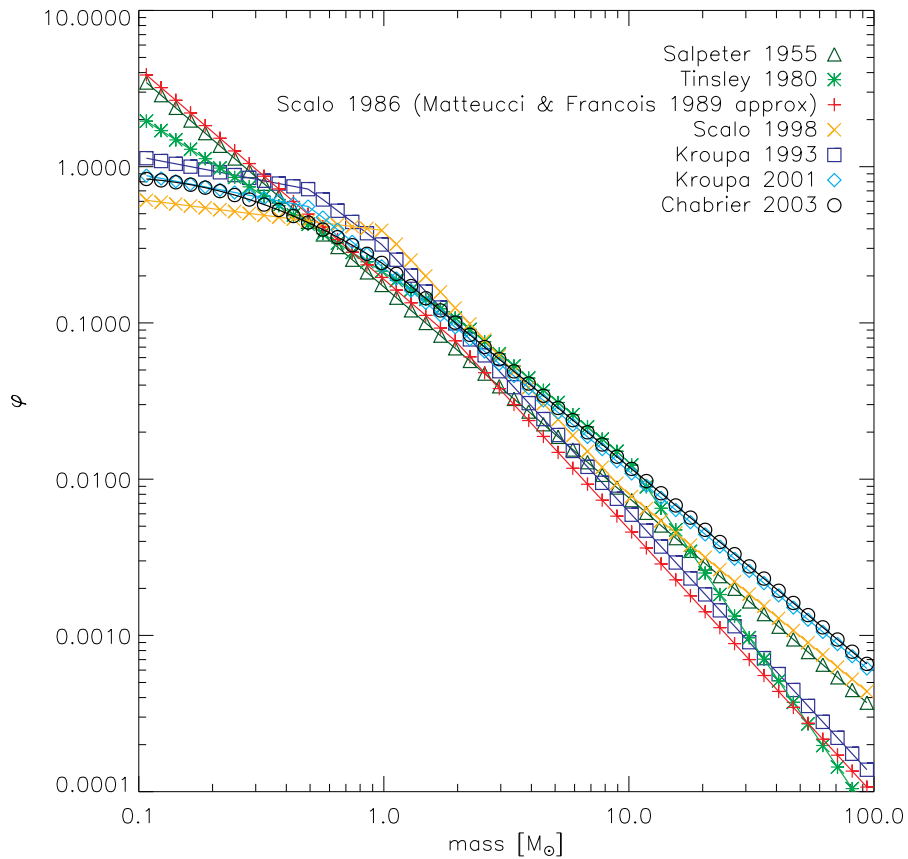


Figure 4.1: Initial mass functions that are commonly used in chemical evolution models (Salpeter 1955; Tinsley 1980; Scalo 1986, 1998; Kroupa et al. 1993; Kroupa 2001; Chabrier 2003).

The IMFs commonly used in CEMs (Salpeter 1955; Tinsley 1980; Scalo 1986, 1998; Kroupa et al. 1993; Kroupa 2001; Chabrier 2003) are given here for completion

and because there is often confusion between the IMF by mass (where the slope in log-space is conventionally labelled x) and the IMF by number (where the slope is conventionally termed $\alpha = x + 1$). Unless stated otherwise, the term IMF refers to an IMF ‘by mass’, i.e. a function that when integrated is dimensionless. The normalisation constants for each IMF are such that,

$$\int_{m_{\text{low}}}^{m_{\text{up}}} \varphi(m) dm = 1, \quad (4.1)$$

where φ is the IMF and m_{low} and m_{up} are the lower and upper mass boundaries of objects that are considered stars.¹ While the range of mass over which each IMF is valid varies, it is common (but not universal) practice to perform the normalisation over the range 0.1–100 M_{\odot} and the normalisation constants quoted below are calculated under this assumption. The IMFs are stated here (and shown in Figure 4.1) for comparison:

$$\varphi_{\text{Salpeter}}(m) = \mathcal{A}_{\text{Salpeter}} m^{-1.35} \quad (4.2)$$

$$\mathcal{A}_{\text{Salpeter}} \approx 0.17;$$

$$\varphi_{\text{Tinsley}}(m) = \begin{cases} \mathcal{A}_{\text{Tinsley}} m^{-1.0} & \text{if } m < 2 M_{\odot} \\ \mathcal{B}_{\text{Tinsley}} m^{-1.3} & \text{if } 2 < m/M_{\odot} < 10 \\ \mathcal{C}_{\text{Tinsley}} m^{-2.3} & \text{if } m > 10 M_{\odot}, \end{cases} \quad (4.3)$$

$$\mathcal{A}_{\text{Tinsley}} \approx 0.21, \mathcal{B}_{\text{Tinsley}} \approx 0.26, \mathcal{C}_{\text{Tinsley}} \approx 2.6;$$

$$\varphi_{\text{Scalo 86}}(m) = \begin{cases} \mathcal{A}_{\text{Scalo 86}} m^{-1.35} & \text{if } m < 2 M_{\odot} \\ \mathcal{B}_{\text{Scalo 86}} m^{-1.70} & \text{if } m > 2 M_{\odot}, \end{cases} \quad (4.4)$$

¹The mass range considered should more correctly be the full mass range of objects that form as a result of interstellar gas collapse to the degree that it no longer constitutes part of the galactic gas phase.

$$\mathcal{A}_{\text{Scalo 86}} \approx 0.19, \mathcal{B}_{\text{Scalo 86}} \approx 0.24,$$

(note that this is a simplified two-slope approximation after Matteucci & Francois (1989) and Romano et al. 2005);

$$\varphi_{\text{Kroupa 93}}(m) = \begin{cases} \mathcal{A}_{\text{Kroupa 93}} m^{-0.3} & \text{if } m < 0.5 M_{\odot} \\ \mathcal{B}_{\text{Kroupa 93}} m^{-1.2} & \text{if } 0.5 < m/M_{\odot} < 1 \\ \mathcal{C}_{\text{Kroupa 93}} m^{-1.7} & \text{if } m > 1 M_{\odot}, \end{cases} \quad (4.5)$$

$$\mathcal{A}_{\text{Kroupa 93}} \approx 0.58, \mathcal{B}_{\text{Kroupa 93}} = \mathcal{C}_{\text{Kroupa 93}} \approx 0.31;$$

$$\varphi_{\text{Scalo 98}}(m) = \begin{cases} \mathcal{A}_{\text{Scalo 98}} m^{-0.2} & \text{if } m < 1 M_{\odot} \\ \mathcal{B}_{\text{Scalo 98}} m^{-1.7} & \text{if } 1 < m/M_{\odot} < 10 \\ \mathcal{C}_{\text{Scalo 98}} m^{-1.3} & \text{if } m > 10 M_{\odot}, \end{cases} \quad (4.6)$$

$$\mathcal{A}_{\text{Scalo 98}} = \mathcal{B}_{\text{Scalo 98}} \approx 0.39, \mathcal{C}_{\text{Scalo 98}} \approx 0.16;$$

$$\varphi_{\text{Kroupa 01}}(m) = \begin{cases} \mathcal{A}_{\text{Kroupa 01}} m^{0.7} & \text{if } m < 0.08 M_{\odot} \\ \mathcal{B}_{\text{Kroupa 01}} m^{-0.3} & \text{if } 0.08 < m/M_{\odot} < 0.5 \\ \mathcal{C}_{\text{Kroupa 01}} m^{-1.3} & \text{if } m > 0.5 M_{\odot}, \end{cases} \quad (4.7)$$

$$\mathcal{A}_{\text{Kroupa 01}} \text{ is undefined, } \mathcal{B}_{\text{Kroupa 01}} \approx 0.45, \mathcal{C}_{\text{Kroupa 01}} \approx 0.22.$$

This IMF is that from (Kroupa 2001, p. 234) and not the revised version given later in the paper. The last IMF that is occasionally used in numerical models is,

$$\varphi_{\text{Chabrier}}(m) = \begin{cases} \mathcal{A}_{\text{Chabrier}} e^{-(\log m - \log m_c)^2 / 2\sigma^2} & \text{if } m \leq 1 M_{\odot} \\ \mathcal{B}_{\text{Chabrier}} m^{-x} & \text{if } m > 1 M_{\odot}. \end{cases} \quad (4.8)$$

The normalisation of the latter IMF is a little more complicated as Chabrier (2003) suggests that the IMF has some dependence on environment and the value of m_c and x reflect this. The Milky Way disc has an IMF that is well fitted with $m_c = 0.079 M_\odot$, $\sigma = 0.69$ and $x = 1.3$, in which case,

$$\mathcal{A}_{\text{Chabrier}} \approx 0.85, \mathcal{B}_{\text{Chabrier}} \approx 0.24.$$

The concept of the IMF carries the implicit assumption that there exists a single function that universally describes the stellar mass distribution of star forming regions under any conditions (e.g. local density, metallicity or turbulence). That so many forms exist may be taken as evidence that the concept of IMF universality is false but, this is hardly compelling and given the difficulty in quantifying the IMF, is more likely to point to variations in the method of detection. The shape of the IMF warrants some discussion as it has a strong impact upon the galactic chemical evolution.

The most often discussed potential dependence of the IMF is on metallicity. The overabundance of α -process elements relative to iron-peak elements in metal-poor stars suggests efficient pre-enrichment from massive stars which has led to the concept of a population-III that has a top-heavy IMF. Furthermore the apparent lack of metal-poor stars in the solar neighbourhood (the so called G dwarf problem) could result from a top-heavy IMF in population-III stars that reduces the mean life span of the population (Martinelli & Matteucci 2000). This effect is not simple to reproduce theoretically, for example, Myers et al. (2011) find analytically that the IMF varies very little even if the metallicity varies by a factor of 100. Considering smaller scales Goodwin & Kouwenhoven (2009) and Bate (2009) find that the same IMF may be reproduced by very different star formation scenarios, such degeneracy makes it difficult to draw conclusions about the specifics of star formation even from observation of an invariant IMF.

The theoretical work of Wyse & Gilmore (1992) places a maximum steepness of

~ 0.3 relative to the present-day IMF for a primordial IMF, well within observation error for the IMF slope determination. Earlier work by Hartwick (1976) and Searle & Zinn (1978) suggests that gas should be expelled during early star formation which allows an invariant IMF to reproduce abundance ratio observations in models. More direct methods of measuring the IMF as a function of metallicity are inherently troublesome because the luminosity function has its own dependence on metallicity: determining the stellar mass from observables is a non-trivial exercise (Castellani et al. 2001). It may be possible to detect the signature of a primordial IMF through the number of WDs relative to low mass unevolved stars in the halo. A number of these WDs have been found (Ibata et al. 1999; Méndez & Minniti 2000) suggesting that the IMF at early times was more peaked in the range $1\text{--}8 M_{\odot}$. It is also stated in Kroupa (2001) that if the IMF is in some way dependent on metallicity then it is likely that the effect is greatest in the sub-solar regime where turbulent fragmentation from metal cooling dominates. This is supported by Padoan et al. (1997) and also by Larson (1998) who makes a convincing case for the *possibility* of a top-heavy IMF at early times in a galaxy's formation due to the hydrodynamical state of gas (higher temperatures in molecular clouds) that manifests as moderate reductions in the slope exclusively at the low mass end. This neatly explains the lack of metal-free stars in the present-day and the α -enhancement in metal-poor stars while remaining consistent with directly measured IMFs. Another justification for a variable IMF of this kind is stated well in Larson (1998); the energy imparted to hot gas by SNe at early times will be higher. In David et al. (1996), calculations show that more SNe are required to produce the level of thermal energy per unit mass in hot gas than are predicted by a standard IMF. This is a particularly intriguing result in light of the excessive bulge fractions often found in simulated galaxies, a variable IMF that has a greater feedback efficiency at early times may help to resolve this issue.

It would also be reasonable to expect a different form of the IMF in regions with high star formation rates. To some extent this is probed in Feltzing et al. (1999) where the luminosity functions of a dwarf spheroidal galaxy and a globular cluster (with similar age and metallicity) are compared. There is a striking lack of any distinction between these two systems in the mass range $0.45\text{--}1 M_{\odot}$ despite the very different star formation rates of these objects. Observations by Jeffries et al. (2004) again show consistency of the IMF between different environments but puts forward tentative evidence of differences below the hydrogen burning limit; however due to incompleteness in the sample, a variable brown dwarf mass function is merely *consistent with* the observations rather than conclusive evidence for it. An extreme star formation rate is found in the nuclei of starburst galaxy M82 and in this case an IMF that is biased against stars with mass $<3 M_{\odot}$ is found by Rieke et al. (1980). The effect is also seen in fainter galaxies where evidence for an IMF truncated at the high mass end may be found (e.g. Pflamm-Altenburg & Kroupa 2008; Hoversten & Glazebrook 2008; Tsujimoto & Bekki 2011) and for top-heavy IMFs in massive systems (e.g. Nagashima et al. 2005; Loewenstein 2006; van Dokkum 2008). This facet of star formation is also considered in Baldry et al. (2008) where the cosmic star formation rate is combined with stellar population synthesis models and compared with the observed luminosity density by assuming a universal IMF. In that work an invariant IMF with an upper mass slope close to that of Salpeter (1955) provides an acceptable fit, while reasonably showing that a Scalo (1986) IMF is unlikely to fulfil this role.

A compilation of the different IMF slopes found in literature is well illustrated throughout Kroupa (2001) where a particular feature of the IMF is noted; the slope of the IMF in different mass regimes (i.e. above and below $1 M_{\odot}$) is sometimes determined through observations of different regions and the consistency of the slope in these cases should not be assumed. It seems to be the case that the conjunction

of observational uncertainties coupled with the low number of stars that share a common environment and the inherent difficulties in measuring the luminosity function consistently in regions near and far makes it impossible to detect systematic variations in the IMF. Any variation that does exist is smaller than the variations caused by these factors and for this reason there is presently no conclusive evidence for systematic variations in the IMF.

4.2.2 Stellar Lifetimes

Stars are assumed to eject mass into the ISM when they move off the main sequence and either create a stellar wind during the AGB phase or become SNI. In the case of SNeIa with a single degenerate star the lifetime of the system is the time taken for the less massive secondary star to overflow its Roche lobe and this is again approximately the time spent on the main sequence. The main sequence lifetime of a star is a function of its metallicity and mass. Stellar lifetimes are therefore an extremely important component of CEMs, controlling the time at which mass and energy are expelled by a stellar population. Though in reality individual stars produce a stellar wind of some kind over their lifetimes, the model approximates this as a single outburst as the star passes the main sequence turnoff, following this outburst any remnant mass remains exclusively as a mass sink.

The analytical form of the stellar lifetime as a function of mass, and in some cases metallicity, only vary significantly in the subsolar regime with the more recent models favouring longer lifetimes for stars less massive than the Sun (Tinsley 1980; Tosi 1982; Maeder & Meynet 1989; Padovani & Matteucci 1993; Kodama 1997). A critical analysis of these lifetime models was conducted by Romano et al. (2005) where model abundance ratios fit observed values better when the longer subsolar lifetimes of Padovani & Matteucci (1993) or Kodama (1997) are used (in this work we have used the Kodama (1997) lifetimes). One of the weaker models is that of

Tinsley (1980) that has shorter lifetimes for massive stars than other models do. Despite these differences, the size of the variations between the models are not large enough to result in changes to the abundance ratios on the same order as sensible changes in the IMF does.

4.2.3 Nucleosynthesis

Nucleosynthesis is the process through which gas that is capable of nuclear fusion (in stars or the early Universe) changes the abundance of elements, tending to create more massive elements. The abundance pattern resulting from nucleosynthetic processes in stars is characteristic of the conditions that give rise to it. The sheer complexity of this subject hinders understanding as nucleosynthesis models are highly non-linear and depend a great deal on the mass and initial abundance patterns in stars. It is further complicated by the distribution of elements within stars and the explosion mechanisms that eject them.

Calculation of the nucleosynthetic yield of stars was first presented for low- and intermediate-mass stars in Iben & Truran (1978) and for massive stars in Arnett (1978), Chiosi & Caimmi (1979) and Maeder (1992). For a model of galactic chemical evolution, the yields of stars of all masses, metallicities and progenitor types must be considered. The dominant sources of metals are massive stars that die as SNeII, SNeIa and lower mass stars as they enter the AGB, three processes with very different internal physics. For this reason the yields of different sources in literature are often combined into a single model despite inconsistencies between them rather than using a single consistent model. Since its publication the model of Woosley & Weaver (1995) has been a common choice for the yields of massive stars in chemical evolution models though more recent works exist (Limongi & Chieffi 2003; Chieffi & Limongi 2004; Kobayashi et al. 2006; Portinari et al. 1998). Massive stars have a distinctive high abundance of α -process elements and short lifetimes that manifests

in galactic abundances as old, low metallicity stars that are α -enhanced (see the top left panel of Figure 1.2 and in Figure 4.7).

While massive stars dominate the energy produced by a stellar population via SN explosion, it is the stars under $\sim 8 M_{\odot}$ that compose most of the mass in any population of stars. The mass range covered by these stars is large and the yields vary a great deal. Nucleosynthetic models for these low- and intermediate-mass stars may be found in Iben & Truran (1978), van den Hoek & Groenewegen (1997), Marigo (2001), Izzard et al. (2004), Karakas & Lattanzio (2007), Karakas (2010), and Doherty et al. (2010).

The contribution of SNeIa is unique in that the main uncertainty is in the lifetime rather than the relatively well constrained yield (Nomoto et al. 1984; Iwamoto et al. 1999). The progenitor model of SNeIa is not well understood, but SNIa rates suggest a binary system is likely with a carbon-oxygen white dwarf orbiting either another white dwarf or a main sequence star. Knowledge of how the system comes to exist is not essential for galactic chemical evolution except to predict the lifetime. The abundance ratios of SNeIa are quite uniform and well constrained. The SN rate gives a good handle for understanding the relative number of these systems compared with SNeII.

A comparison of the numerous combinations of these different methods would be extensive and remains a topic for future study using the methods developed in this thesis but is unfortunately not afforded consideration due to time constraints. For a comparison of the different nucleosynthesis models the reader is directed to François et al. (2004) and Romano et al. (2010). In François et al. (2004) a semi-numerical model is used to apply the yields of different groups (Woosley & Weaver 1995; Nomoto et al. 1997; Limongi & Chieffi 2003) to a model of the Milky Way. The model with the best fits to observations is that of Woosley & Weaver (1995) with no correction required to fit Ca, Fe, Zn, Ni and O, however Mg, Si, Ti, K, Sc, Co, Cr and

Mn yields would require corrections to fit the data. The O yield of Limongi & Chieffi (2003) compared favourably to observations but other elements from this model and that of the Nomoto et al. (1997) model are less impressive. Small modifications to SNeIa yields by Iwamoto et al. 1999 (which are the yields used in this work) are also noted as requiring some adjustment, specifically Mg, Ti, Sc, Zn and Co yields should be increased while K and Ni are decreased. This may seem like a critical point of failure in the models but the reader should note that only O and Fe abundances are considered here as other elements are, to varying degrees, less trustworthy. In Romano et al. (2010) a great diversity in the chemical evolution of the model galaxy exists depending upon the chosen yields. The common choices for stellar yields are the van den Hoek & Groenewegen (1997) and Woosley & Weaver (1995) models, Romano et al. (2010) finds that this combination tends to agree reasonably well with the ‘best’ combination of Karakas (2010) and Kobayashi et al. (2006) for the evolution of $[O/Fe]$ and $[C/Fe]$ but differs significantly for many other elements (Na and Sc are particularly notable) that are key observables. Romano et al. (2010) also finds that not one of the models considered is capable of explaining the trend of $[N/Fe]$ versus $[Fe/H]$, the evolution of nitrogen being particularly troublesome to model.

In this thesis a CEM is coupled with cosmological hydrodynamic simulations; it is then applied to tests of the IMF and SNIa models. It is however not the best tool for studying the different nucleosynthetic models which is more appropriately conducted using semi-numerical methods (as in François et al. 2004 and Romano et al. 2010). The subtle nuances of nucleosynthesis models may be tested in this way but fully numerical simulations add little of value at the cost of much computational time.

4.2.4 Solar Abundance Determination

Stellar abundances are often quoted in the form $[A/B]$, normalised to the solar abundance of elements A and B. Over time the fashionable abundance values for the solar photosphere have changed (by as much as 0.2 dex in some cases) and consequently it is difficult to make comparisons between abundance measurements quoted in literature. Provided that a given set of observations are using a consistent solar abundance pattern the issue is somewhat irrelevant, however note that important differences exist in the way that stellar abundances are calculated which should also be considered. Another method by which the solar composition may be deduced is analysis of meteoric abundances. Discrepancies exist between the two methods and while meteoric abundances may be misleading with respect to certain elements, the solar iron abundance may be reliably deduced in this way (Holweger et al. 1991; Biemont et al. 1991).

Two widely used solar abundance model are Anders & Grevesse (1989) and Grevesse & Sauval (1998) which make various assumptions concerning turbulence and convection in the Sun that systematically offset the results if relaxed. These models were in agreement with helioseismic observations (Delahaye et al. (2010) and references therein). More recent models use 3D numerical simulations of convection (Asplund et al. 2000, and others in the series) and find a different abundance pattern. These models also include Non-Local-Thermodynamic-Equilibrium (NLTE) effects and have a greater influence on some abundances than others with light elements being most strongly affected, i.e. C, N and O (Asplund et al. 2009). While these more sophisticated methods account for more physics, they come into conflict with those same helioseismic observations (e.g. Guzik et al. 2005) that 1D LTE models found consistency with and are therefore still controversial in the scientific community.

Unless one is particularly interested with the abundance of elements in the Sun

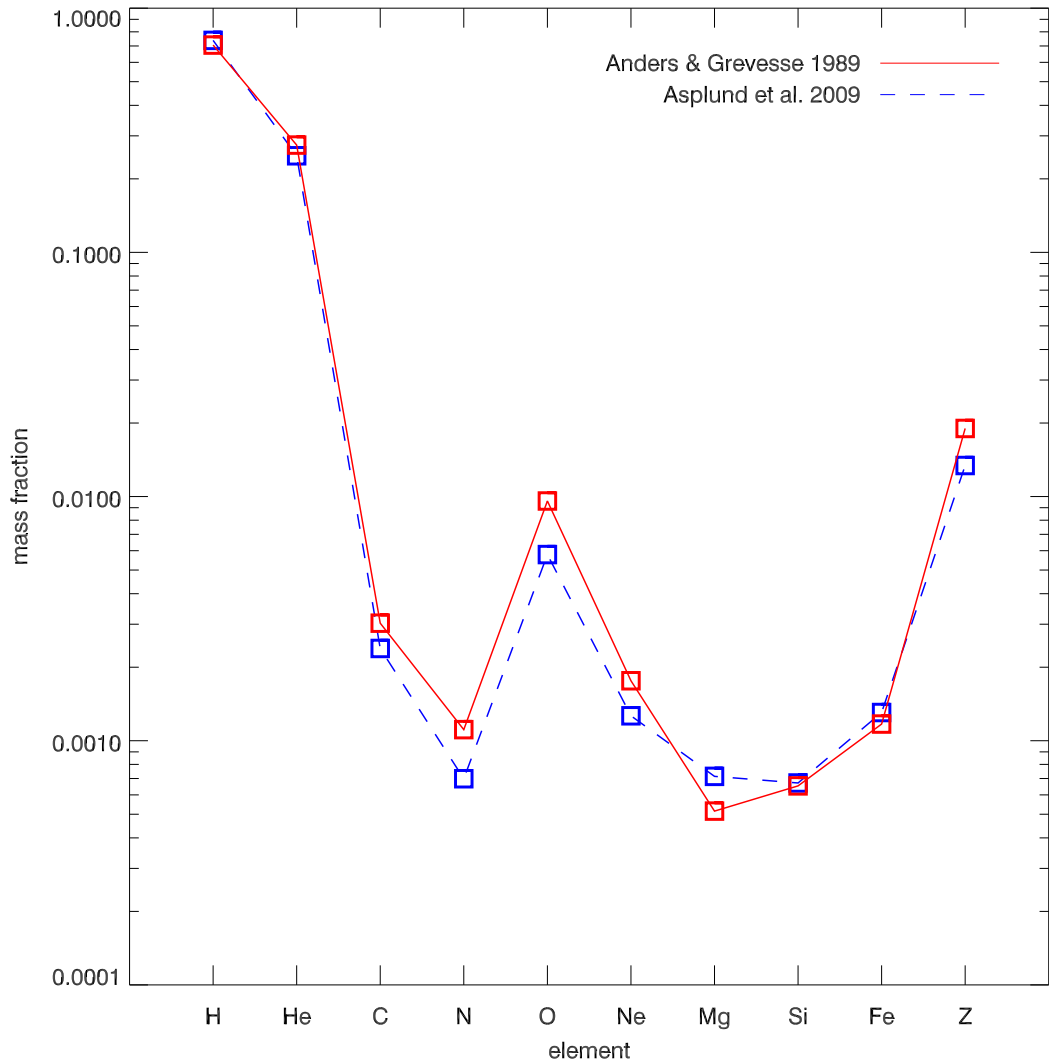


Figure 4.2: Solar abundance determinations from Anders & Grevesse 1989 (red solid line) and Asplund et al. 2009 (blue dashed line) demonstrating the scale of the discrepancy of ~ 0.2 dex for some of the lighter metals.

itself, the particular choice of the model described above is rather arbitrary. A more detailed analysis of the differences in these models can be found in Delahaye & Pinsonneault (2006) and Pinsonneault & Delahaye (2009) in which a value that is intermediate between the older and the more recent abundances is recommended.

Two of the commonly used solar abundance models (Anders & Grevesse 1989; Asplund et al. 2009) are compared in figure 4.2, which shows for example that the difference in the oxygen abundance is $[O_{\text{asplund2009}}/O_{\text{anders1989}}] = 0.219$, whereas for iron it is only $[Fe_{\text{asplund2009}}/Fe_{\text{anders1989}}] = -0.062$. This means an offset of -0.27 in $[O/Fe]$ from Anders & Grevesse (1989) to Asplund et al. (2009). For this thesis the photospheric abundances of Anders & Grevesse (1989) have been chosen as a zero-point for all abundance values. Observational values have been renormalised to ensure a consistent zero-point.

4.3 Technical Implementation

4.3.1 Chemical Evolution Model

The underlying CEM used to determine the relative rates of SNeII:SNeIa:AGB, and the associated chemical enrichment, for a stellar population governed by a given IMF, is generated prior to the simulation being run. It is a complex matter to calculate the mass of elements ejected during a time interval as a function of the stellar populations age and metallicity. For this reason the CEM is approximated before run-time to avoid expensive and redundant calculations during run-time. The resulting ‘look-up tables’ (henceforth referred to as ‘feedback tables’) provide the SNeII, SNeIa, and isotopic return rates as a function of time for a range of Simple Stellar Population (SSP) metallicities. It is particularly important here to note the distinction between ‘stars’ which are not resolved by the code and ‘stellar particles’ which represent SSPs and are the real fundamental stellar object in the simulations. The code (provided as part of the RAMSES-CH patch) is flexible, allowing the user to readily modify relevant stellar physics, via the importation of different SNe and AGB yields, stellar lifetimes, IMFs and SNeIa Delayed Time Distributions (DTDs).

We now describe the generation of a feedback table. The table is initialised for

a number of metallicities which range from primordial to well above solar to ensure that when a star particle is formed in the simulation its metallicity is included in the table: in practice the metallicity of star particles is rarely more than 0.5 dex above solar. The table also covers a range of ages from zero to beyond the Hubble time, again, it must be impossible for a star to have an age exceeding the range of the table. Then stepping through each metallicity entry in the table and for each age, the stellar lifetime models are consulted to determine the main sequence turn-off mass, $m_{\text{to}}(\tau_*, Z_{\text{sp},0})$, associated with a stellar population of the current age (τ_*) and metallicity ($Z_{\text{sp},0}$). A convolution of the IMF and the nucleosynthetic yields as a function of mass is then integrated over using a trapezium method with the integration limits from the upper mass limit of SNII to the current turn-off mass. The IMF by number is integrated over the same range (for as long as the turn-off mass exceeds the lowest mass of a SNII progenitor) to calculate the total *number* of SNeII (N_{SN}) that have exploded in a star particle with formation mass $M_{\text{sp},0}$, throughout that particles current lifetime,

$$N_{\text{SN}}(\tau_*, Z_{\text{sp},0}) = M_{\text{sp},0} \int_{m_{\text{to}}(\tau_*, Z_{\text{sp},0})}^{m_{\text{up},\text{SNII}}} \frac{\varphi(m)}{m} dm, \quad (4.9)$$

where $m_{\text{up},\text{SNII}}$ is the upper mass limit of SNII progenitors. The number of SNII per unit stellar mass is parametrised in the standard implementation of RAMSES with η_{SN} . For a Salpeter (1955) IMF with SNII mass limits of 8–40 M_{\odot} the equivalent $\eta_{\text{SN}}=0.1$, for a Kroupa et al. (1993) IMF with SNII mass limits of 8–40 M_{\odot} , $\eta_{\text{SN}}=0.07$. For a Kroupa (2001) IMF with the same mass limits the parametrisation would be $\eta_{\text{SN}}=0.15$ and with mass limits 8–100 M_{\odot} it would be $\eta_{\text{SN}}=0.2$. A similar exercise is conducted to calculate the number of SNeIa: following Kobayashi et al. (2000) and Kawata & Gibson (2003) a single degenerate SNIa model is considered and a

double integral is used.² SNeIa are assumed to have uniform yield regardless of the mass of the stars in the binary system and thus only the number of progenitors is required to calculate the mass of elements ejected by SNeIa. The double integral is similar to that of Kobayashi et al. (2000) and Kawata & Gibson (2003) with the simplification that the IMF slope for both the primaries and secondaries was taken to be identical.

The method described above is used to compile a feedback table with each entry containing the total mass for each element that has been ejected by a $1 M_{\odot}$ stellar particle from its birth to that particular entry's age, i.e. the table is cumulative in age. This is illustrated in Figure 4.3 which shows the isotopic ejection rate (per unit mass) from an SSP. A cumulative table is used to avoid expensive summation over age during simulation run-time, instead each star particle need only record the time since its last feedback episode and subtract the cumulative feedback of that time from that which corresponds to the present time step. This is essential because the time steps of the feedback table cannot be matched to the simulation time steps as they are variable.

This method provides a great deal of flexibility that would be impossible if the CEM were to be coded directly into the simulation. It makes it possible to easily generate feedback tables for any combination of published nucleosynthesis yields, stellar lifetimes, IMF and SNIa progenitor model with the mass ranges of different stellar feedback phenomena easily altered between runs. Due to time constraints a comprehensive study of the available options has not been possible and all simulations presented in this chapter use a common set of nucleosynthetic yields with only variations in the IMF and the SNeIa DTD. The yields for AGB stars (van den Hoek & Groenewegen 1997), SNeII (Woosley & Weaver 1995) and SNeIa (Iwamoto

²An alternative method is used based upon empirically measured SNIa rates and are parametrised with a DTD and a scaling factor that is fit to local measurements of SNIa rates in the present day.

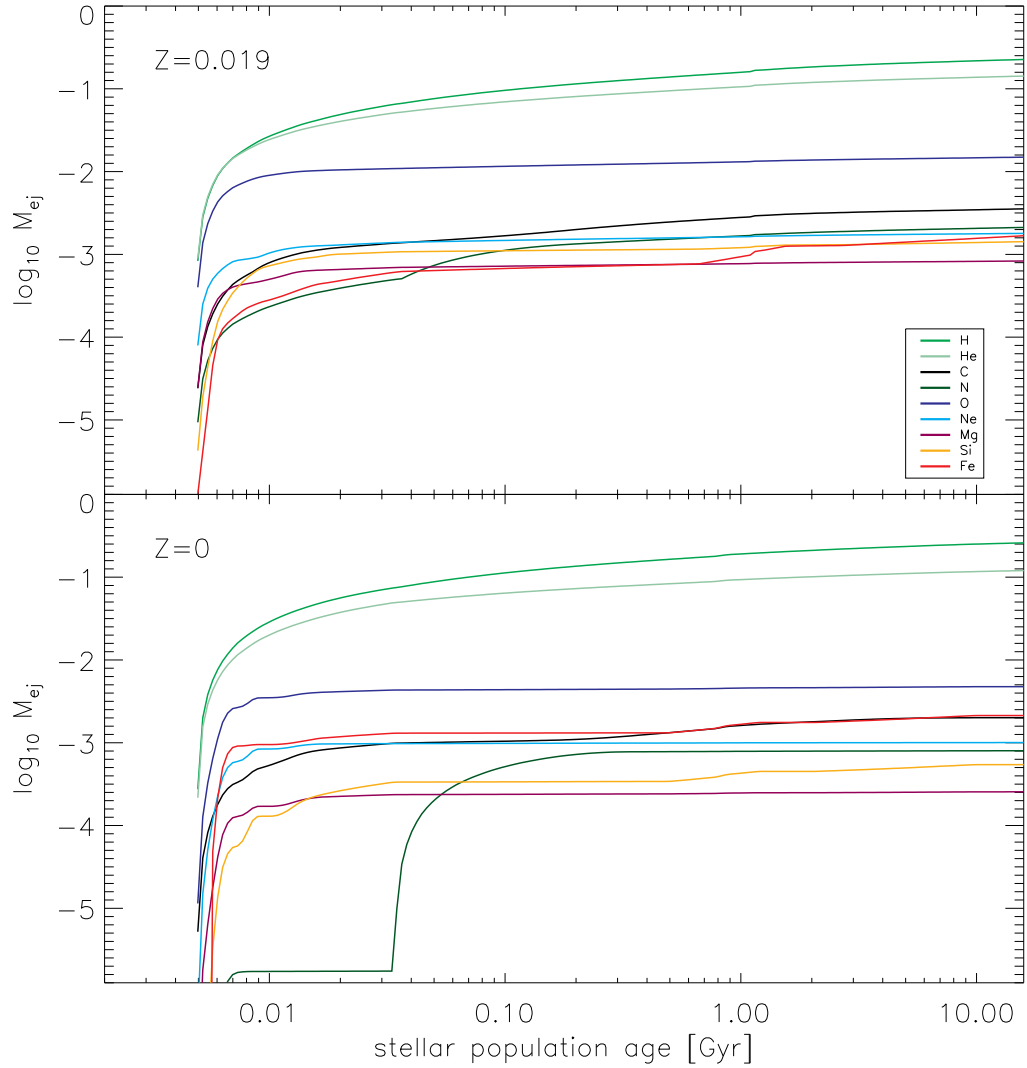


Figure 4.3: Ejection rate of dominant elemental isotopes, per unit stellar mass, as a function of age for a Kroupa (2001) IMF. The upper and lower panels correspond to solar and Population III metallicity simple stellar populations respectively.

et al. 1999) are illustrated in Figure 4.4. Squares denote the values that are used in the production of the feedback table, those adjoined by solid lines are the values given in the respective literature sources. The SNeIa yields are plotted as horizontal arrows at an arbitrary position on the abscissa.

Figure 4.4 highlights an important issue in the creation of the feedback table. Different sources are used for the yields of AGB stars and SNeII because no single model exists that covers AGB stellar winds, SNeII and SNeIa. The models published in the literature do not cover the entire mass range of stars that need to be considered in galactic chemical evolution. Which values should be adopted for stars between the upper mass of the AGB yields and the lowest mass of the SNeII yields? What value is appropriate for stars below the the lowest mass AGB yields, or above the highest mass SNeII? In these regimes an appropriate extrapolation is required, and the scaling that has been used for this work is shown in the form of dot-dashed lines. In this work the lower mass bound of SNeII (and upper mass bound for AGB stars) is assumed to be $8 M_{\odot}$, and the lowest mass stars formed are assumed to be $0.1 M_{\odot}$. Extrapolation based upon the gradient of the lines in Figure 4.4 is undesirable as it leads to extreme changes in the abundance ratios with little physical motivation. For this reason the relative fraction of each element is retained from the nearest relevant progenitor model and is simply scaled with the mass of the star. The upper mass limit of star formation is taken as $100 M_{\odot}$ for integration of the IMF, however for the fiducial model described later the highest mass star that may contribute SNII feedback is $40 M_{\odot}$ (to coincide with the upper mass of the Woosley & Weaver (1995) yields) with higher masses assumed to result in the formation of a black hole that contributes no energy or mass to the ISM. In the models where the SNII upper mass is higher than $40 M_{\odot}$ the extrapolation is again simply scaled by mass. Increasing the upper mass limit of SNII causes a larger number of SNII per unit stellar mass to be produced and a greater fraction of the mass to be returned to the ISM via

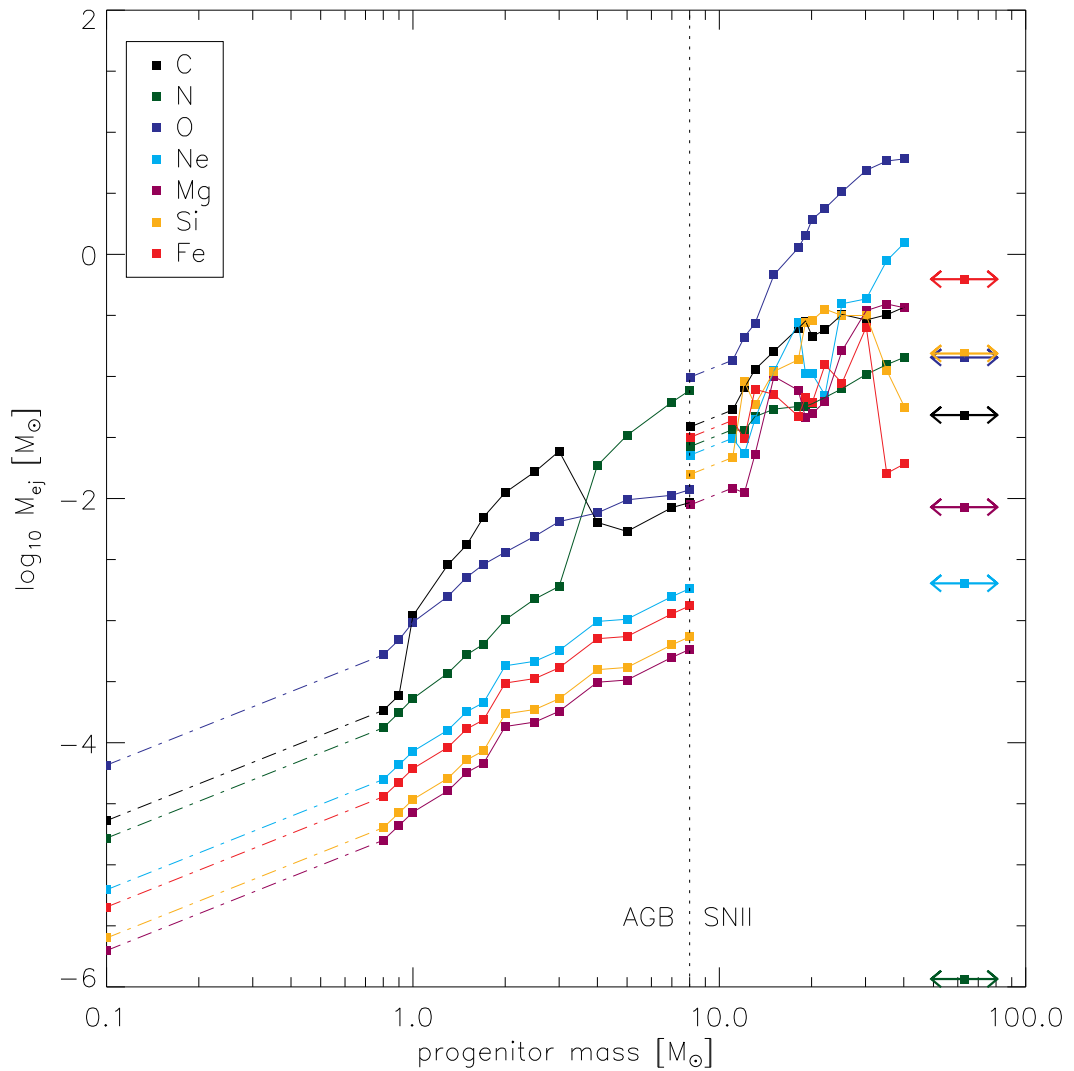


Figure 4.4: Mass of elements ejected by stars as a function of initial mass. Also shown are the abundances for a single SNIa (horizontal arrows) for comparison (the position along the abscissa is arbitrary, chosen to avoid conflict with other data). The mass above which stars are considered to be SNeII progenitors is indicated at $8 M_{\odot}$. Data for AGB stars are taken from van den Hoek & Groenewegen (1997), SNeII from Woosley & Weaver (1995), and SNIa from Iwamoto et al. (1999). Points connected by solid lines denote the original data, those connected by dot-dash lines show adopted extrapolations to lower masses. Extrapolations are linear and scaled to the mass of the progenitor star.

the SNII wind. As SNII primarily create α -process elements, any increase in the upper mass limit for SNII progenitors results in a greater fraction of these elements relative to those from other sources, i.e. iron-peak elements.

4.3.2 RAMSES-CH

The second component of RAMSES-CH is the patch to the RAMSES code (Teyssier 2002) itself, details of the hydrodynamical and N-body schemes of which can be found in Chapter 1. The patch is applied to RAMSES v3.07 which has minor differences with RAMSES v3.01 which is used for the simulations in chapters 2 and 3. In RAMSES the evolution of the total gas metallicity, Z is traced under the assumption of the instantaneous recycling approximation and Z is treated as a passive scalar quantity that is advected by the hydrodynamical flow. Our new chemodynamical version also employs passive scalars in the tracking of the dominant isotopes of H, C, N, O, Mg, Ne, Si, and Fe, and the chemical composition of the gas from which the stellar particles form is ‘tagged’ onto the new particles.

As described by Dubois & Teyssier (2008), star particles are created in high-density gas ($\rho_g > \rho_0$) and are spawned by a random Poisson process at a rate given by $\dot{\rho}_s = \epsilon_* \rho_g / t_{\text{ff}}$, where t_{ff} is the local free-fall time of the gas, $(3\pi/32G\rho_g)^{1/2}$, and ϵ_* is the star formation efficiency. ϵ_* is a free parameter but may be constrained by matching the Schmidt-Kennicutt relation just as t_0 is constrained for the standard version of RAMSES (see Figure 2.4). Stellar particles enrich the ISM according to their chemical history defined by its initial metallicity (examples show in Figure 4.3). At each time step and for each star particle the code consults the feedback table, interpolating in metallicity and stellar age to determine the mass of each element (and also the number of SNeIa and II) that has been ejected over its entire lifetime. The respective quantities calculated during the previous feedback episode of the star is subtracted from this to give the mass of elements ejected and amount of

SN energy (via the number of SNe) for the current timestep. Chemical elements and energy are then simultaneously injected into the ISM. In this first incarnation of the RAMSES-CH patch, the feedback is treated slightly differently depending on whether it comes from SNeII or AGB/SNeIa. During the SNII phase, early in the population's lifetime, a kinetic feedback mode is used. As the population ages and AGB/SNIa feedback takes over, energy is thermally injected into the local gas cell. Adding further sophistication in separating AGB and SNIa feedback modes is left for future updates to the scheme. Kinetic feedback is employed for SNII feedback as it is more efficient at resisting the collapse of gas in the galaxy and reducing star formation than thermal feedback is. As SNII occur early in the galaxy's evolution and in sites of star formation it is important for this feedback to efficiently blow away gas that might go on to form more stars. For each instance of kinetic feedback, mass, momentum, energy and metals are deposited in all gas cells within a feedback-sphere of user specified radius centered upon the star particle. The sphere should be as close as possible to the size of a SNe super-bubble but should remain resolved by the gas resolution and its radius is thus chosen throughout to be twice the maximum resolution. Variations in the super-bubble radius from 1-3 grid cells does not have a serious impact on the final structure of the galaxy but a larger bubble can lead to very efficiently mixed metals, i.e. homogeneous abundance ratios.³ The number of SNeII (N_{SNII}) is given by the feedback table and is used to calculate the kinetic energy of the ejected gas,

$$E_{\text{g,K}} = \epsilon_{\text{SN}} N_{\text{SNII}} E_{\text{SN}}, \quad (4.10)$$

where $E_{\text{SN}} = 10^{51}$ erg is the energy per SN and ϵ_{SN} is the efficiency with which the energy couples to the ISM. The velocity of the gas in the SNe super-bubble is linearly interpolated with the bubble radius and depends upon the mass of gas

³Oscar Agertz, private correspondence.

swept up in the blast wave in addition to the mass ejected by the star particle itself. The swept up gas mass is parametrised as f_w times the mass of gas ejected. We again stress here that this scheme is not applied for SNIa or AGB feedback because there are a great deal fewer SNeIa compared with SNeII and AGB feedback is not energetic. Despite this, the same ϵ_{SN} is used for the ISM coupling efficiency of the SNeIa and the energy and mass ejected by SNeIa and AGB stars is injected to the local gas cell, this is termed ‘thermal feedback’.

The gas is cooled and heated the same as the simulations in Chapter 2 (see Figure 2.2) using the global metallicity to scale between the metal-free and solar metallicity cases assuming photoionisation equilibrium. The only change to the cooling rates from the standard runs is that the metallicity distribution may change as it is now ejected into the gas on different time scales, however the typical metallicity of the gas does not change dramatically and so the difference should be minimal. It is more likely that changes to the density and temperature distribution of the gas will give rise to changes in the cooling rates but this is far from predictable and is less a function of the improved feedback scheme and more of the parameters employed in each run. The mass-weighted average temperature of gas in the regions where feedback is most prevalent (essentially the disc region) is 1.0×10^4 K and with a typical density of 0.21 nH cm^{-3} , approximately half of the gas is thus above the critical 1.0×10^4 K where gas cooling is efficient (see Figure 2.2) and the rest is below it. The majority of the hottest gas is found at small galactocentric radii. It is in principle possible to use the new traced elemental abundances to inform a detailed cooling calculation for the simulations but this will add much computational time and remains as a potential future development.

4.4 Chemodynamics of an L_* Galaxy

4.4.1 Model Parameters

We now present a fiducial realisation of a late-type disc galaxy to illustrate the strengths and weakness of the chemodynamics scheme. This galaxy is chosen for its broad success at meeting observational constraints but should not be taken as representing either an optimal parameter set, nor as a unique result. The galaxy presented here is from a cosmological simulation with a box size of $L=20 h^{-1}$ Mpc and dark matter particle masses of $6 \times 10^6 M_\odot$ in the central region. The spatial resolution is $L/2^{l_{\max}}=436$ pc at $z=0$, with a maximum refinement level of $l_{\max}=16$. A map of the gas distribution is shown in Figure 4.5 to illustrate the morphology and resolution scale, the image is 40 kpc in scale. The initial conditions are the same as those used for the galaxy presented in (Sánchez-Blázquez et al. 2009) with $H_0=70 \text{ km s}^{-1} \text{ Mpc}^{-1}$, $\Omega_m=0.3$, $\Omega_\Lambda=0.7$, $\Omega_b=0.042$, and $\sigma_8=0.92$.⁴ This galaxy is henceforth identified as 109-CH and has a virial mass of $\sim 7 \times 10^{11} M_\odot$.

This realisation uses a star formation threshold n_0 of 0.3 cm^{-3} with a star formation efficiency of $\epsilon_* = 1\%$ (equivalent to $t_0 = 9.4$ Gyr in a standard RAMSES run) and $\epsilon_{\text{SN}}=1$. The feedback mass loading is set at $f_w=10$ corresponding to a mass loading factor of $\eta_w=1$ for a standard RAMSES run with a massive star fraction of 10%. A polytropic equation of state, $T = T_{\text{th}}(\rho_g/\rho_{\text{th}})^{\gamma-1}$, is used in high-density ($n_g > n_{\text{th}}$, where $n_{\text{th}}=n_0$) and cool gas ($T_{\text{th}}=2900$ K); see §2.2.4 for a discussion of the polytrope. At the resolution employed here an index $\gamma=2$ allows the Jeans' length to be resolved by more than 4 cells at all times given the density and temperature regime in which it is applied.

A direct comparison of galaxies run with the standard RAMSES and the new

⁴The cosmological parameters stated in Sánchez-Blázquez et al. (2009) are misquoted, the parameters above are the correct ones for the simulations in this chapter and in Sánchez-Blázquez et al. (2009).

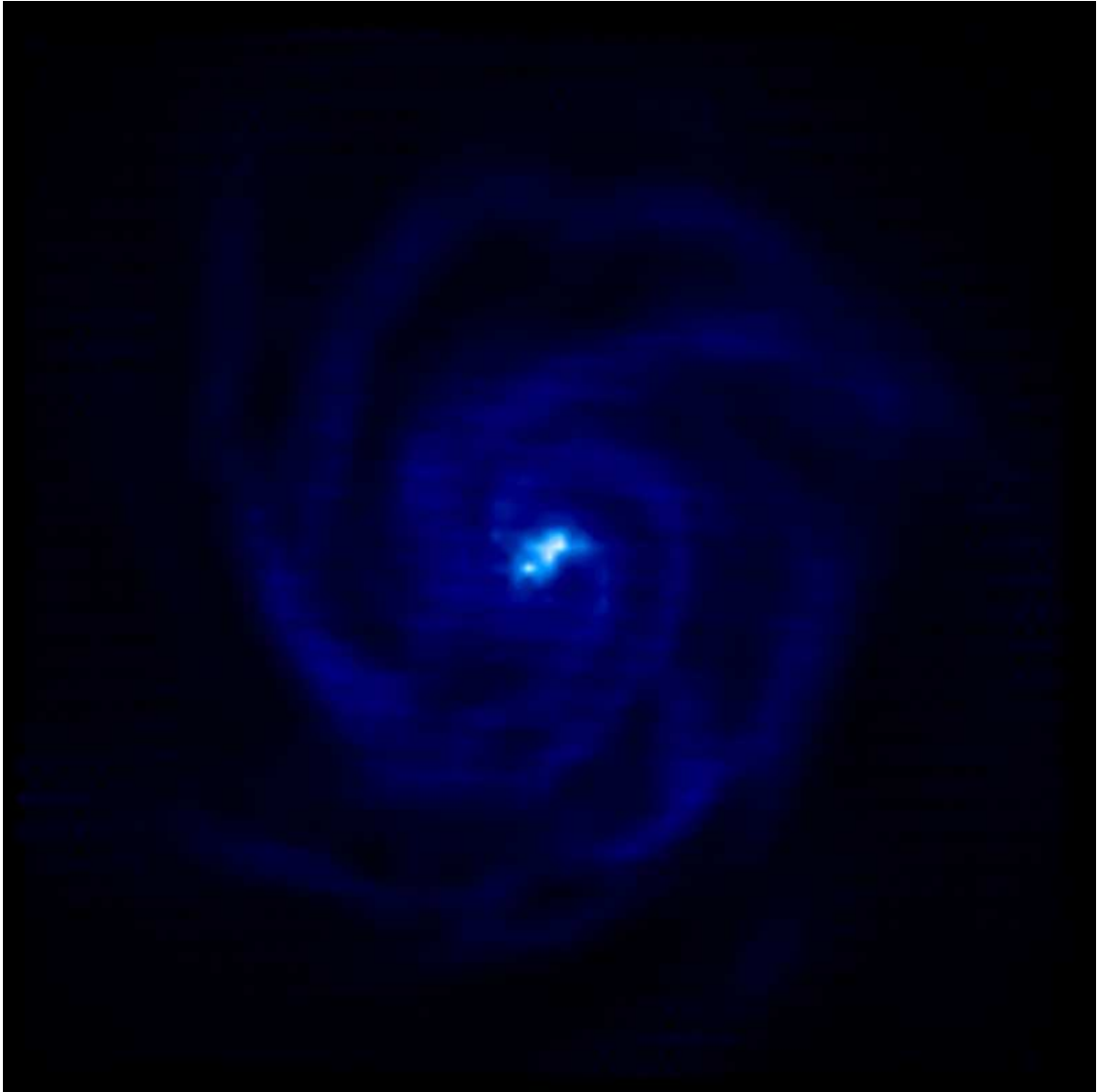


Figure 4.5: Gas density map of 109-CH. Dark lines in the image are artifacts from aligning the volume to the disk plane, blocky artifacts at the edge of the image are caused by lower resolution in low density regions. The image is of a 40 kpc box.

chemodynamical RAMSES-CH is not strictly possible as the parameters take on slightly different meanings and the feedback is now distributed over time rather than released in a single outburst. We have however considered the differences for certain cases. Comparing a standard and a chemodynamical run with the same f_w reveals that the two methods create entirely different galaxies. The chemodynamical run creates a galaxy with a baryon and stellar mass fraction that is higher than the standard version. This is a warning that the parameters applied to the standard version runs are not necessarily informative regarding the parameters in the chemodynamical version. Although it is not presented here, a RAMSES-CH run with $f_w=1$ presents a larger gas disc, a lower star formation rate, a slightly more enriched halo and a lower stellar mass fraction: parameter studies are ongoing and will be discussed in a forthcoming paper, in this thesis only the influence of the CEM is considered.

For this initial work, we adopted a fairly standard CEM, using a Kroupa (2001) IMF with mass limits of 0.1–100 M_\odot . Stellar lifetimes are taken from Kodama & Arimoto (1997) and depend on both mass and initial metallicity. Nucleosynthetic yields for SNeII are taken from Woosley & Weaver (1995) and for $m > 30 M_\odot$ we adopt the yields associated with the Model B explosion energies, after Timmes et al. (1995) and Kawata & Gibson (2003). As suggested by Timmes et al. (1995) we halve the Woosley & Weaver (1995) iron yield. Stars in the mass range 8–40 M_\odot are assumed to explode as SNeII, with all stars below 8 M_\odot contributing AGB yields from van den Hoek & Groenewegen (1997).

As noted earlier, yields for SNeIa were taken from Iwamoto et al. (1999) with the progenitor masses following constraints set out by Hachisu et al. (1999), Kobayashi et al. (2000) and Kawata & Gibson (2003). A double integral is used to find the number of binary systems with primaries in the mass range 3–8 M_\odot that have secondaries that are red giants (0.9–1.5 M_\odot) or main sequence stars (1.8–2.6 M_\odot).

In Kawata & Gibson (2003) the IMF of the secondaries is shallower than that of the primaries, we have chosen to use the same IMF for primaries and secondaries but admit that this is for simplicity. Hachisu et al. (1999) also suggest the use of a metallicity floor to suppress SNeIa at low metallicities. This limit supposedly represents the inability of low metallicity gas to support stable accretion of matter from the secondary to the WD primary star: preventing the system from reaching the Chandrasekhar mass. In light of the ongoing controversy regarding this metallicity floor, we have ignored this constraint and allowed SNeIa events at all metallicities. The nucleosynthetic yields described here are used in all realisations of 109-CH presented in this thesis. This realisation of 109-CH is identified with the name *K01-uM40-IaH*.

4.4.2 Results

The instantaneous recycling approximating has been relaxed and the new model incorporates SNeIa where the standard RAMSES does not. The first metric considered here is the predicted supernovae rates for comparison with empirical constraints. The time evolution of the supernovae rates is shown together with the star formation rate in Figure 4.6. The fiducial 109-CH has a present-day SNIa rate of 0.131 SNUM (SNe per century per $10^{10} M_{\odot}$ stellar mass) and a SNII rate of 0.959 SNUM. These values are consistent with the SN rates found by Mannucci et al. (2008) for field Sbc/d galaxies: $0.140_{-0.035}^{+0.045}$ SNUM for SNeIa and $0.652_{-0.134}^{+0.164}$ SNUM for SNeII. The relative rate of SNeII to SNeIa is approximately correct when compared with these observations (SNeII/SNeIa ≈ 7).

Moving beyond the SN rates, the abundance ratios of readily observed elements are regularly employed to constrain the timescales of star formation, and therefore both feedback modes and fundamental nucleosynthesis. The recovery of empirical trends found locally in the solar neighbourhood is a necessity for any CEM. Such

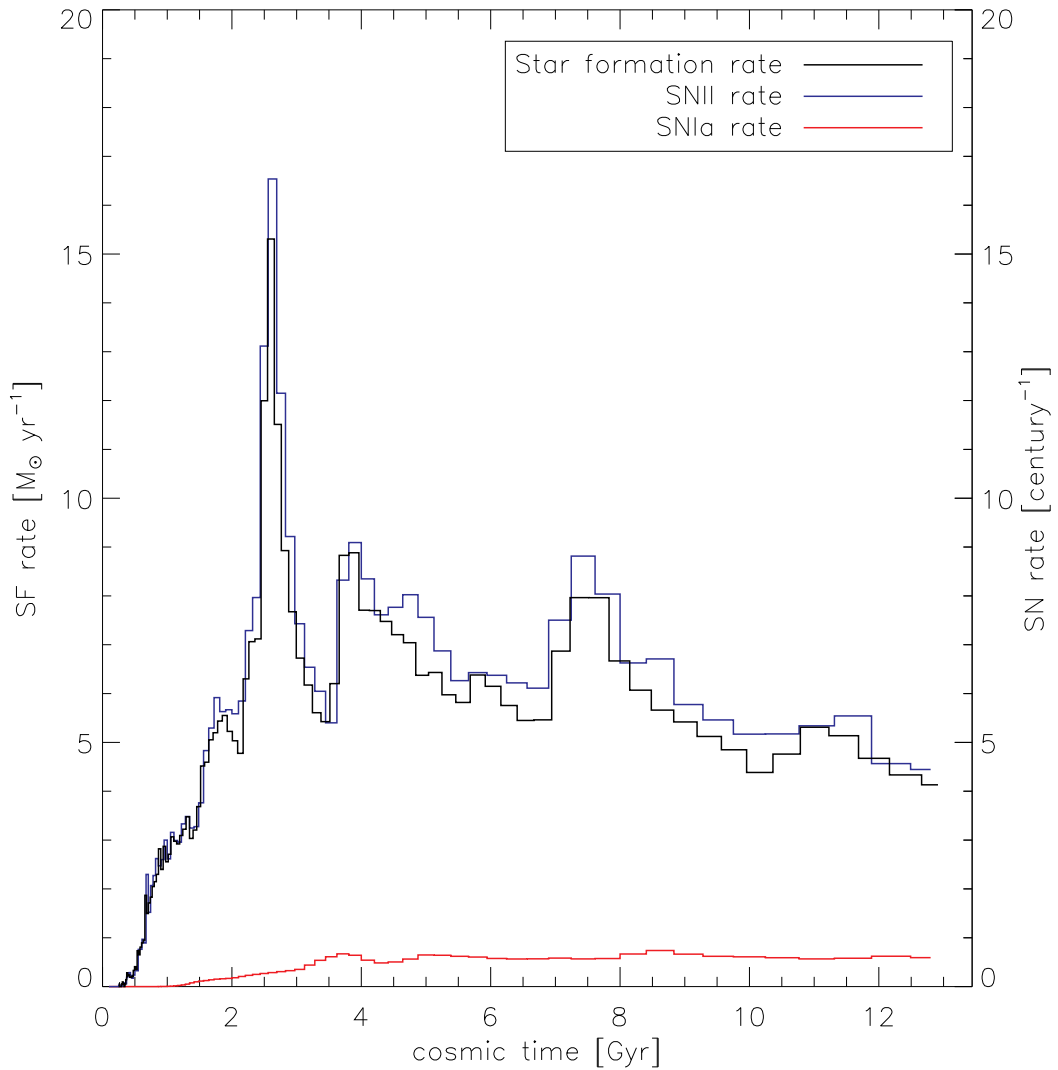


Figure 4.6: The star formation rate for 109-CH is shown in black (refer to the left axis) and the corresponding SNeII and SNeIa rates are shown (refer to the right axis) in blue and red, respectively. The SNeIa rate is scaled up by a factor of 5 for clarity. Note that the SNeII rate is not precisely proportional to the star formation rate as would be the case for data simulated using the ‘standard’ version of RAMSES. The SNeII rate at each time is now dependent on the star formation rate of past as well as present time-steps.

observations demonstrate a clear correlation between α -process element and iron abundances, in the sense of there being an α -enhanced plateau at lower metallicities (below $[\text{Fe}/\text{H}] \sim -0.7$) with a systematic decline to solar values, at higher metallicities (e.g. Edvardsson et al. 1993; Gratton et al. 2003; Reddy et al. 2003; Cayrel et al. 2004; Bensby et al. 2005; Reddy et al. 2006). This empirical behaviour in $[\alpha/\text{Fe}]$ - $[\text{Fe}/\text{H}]$ can be seen in Figure 4.7, where in this case, we are showing the observational trends for $[\text{O}/\text{Fe}]$ vs $[\text{Fe}/\text{H}]$. Also shown in Figure 4.7 is the same distribution of $[\text{O}/\text{Fe}]$ - $[\text{Fe}/\text{H}]$ for the star particles at redshift $z=0$ within an analogous ‘solar neighbourhood’ for the simulated disc 109-CH, an annulus of stars with galactocentric radius between 5 and 11 kpc with height above (or below) the disc plane of not more than 3 kpc. We emphasise that the solar normalisation of element abundances for both simulated and observed data is that of Anders & Grevesse (1989).

From the results of this initial test it is clear that the qualitative chemical properties are not inconsistent with observations of the local plateau and decline behaviour seen in the $[\alpha/\text{Fe}]$ - $[\text{Fe}/\text{H}]$ plane. Abundance ratios are recovered and the qualitative behaviour of the $[\text{Fe}/\text{H}] \sim -0.7$ knee is also seen in the simulated data. The knee-feature seen in Figure 4.7 at $[\text{O}/\text{Fe}] = 0.15$, $[\text{Fe}/\text{H}] = -0.2$ is attributed to the bursty star formation profile which naturally creates multiple knee features as the SNII:SN Ia rate fluctuates. The inset colour coding in Figure 4.7 denotes stellar age and reveals a rapid early enrichment in $[\text{Fe}/\text{H}]$ similar to the age-metallicity relations predicted by classical CEM. Specifically, it takes ~ 3 Gyr to reach a metallicity $[\text{Fe}/\text{H}] \approx -0.4$, driven by the initial phases of intense star formation, after which the age-metallicity relation flattens and the rate of growth of $[\text{Fe}/\text{H}]$ consequently slows (even while SNe Ia are becoming more important). This phase is characterised by the abundance ratio ‘strata’ seen in Figure 4.7, with discrete ‘arcs’ appearing at decreasing values of $[\text{O}/\text{Fe}]$ as time progresses. These abundance ‘strata’ are identified more clearly in Figure 4.8 where the strata corresponding to the four peaks of star

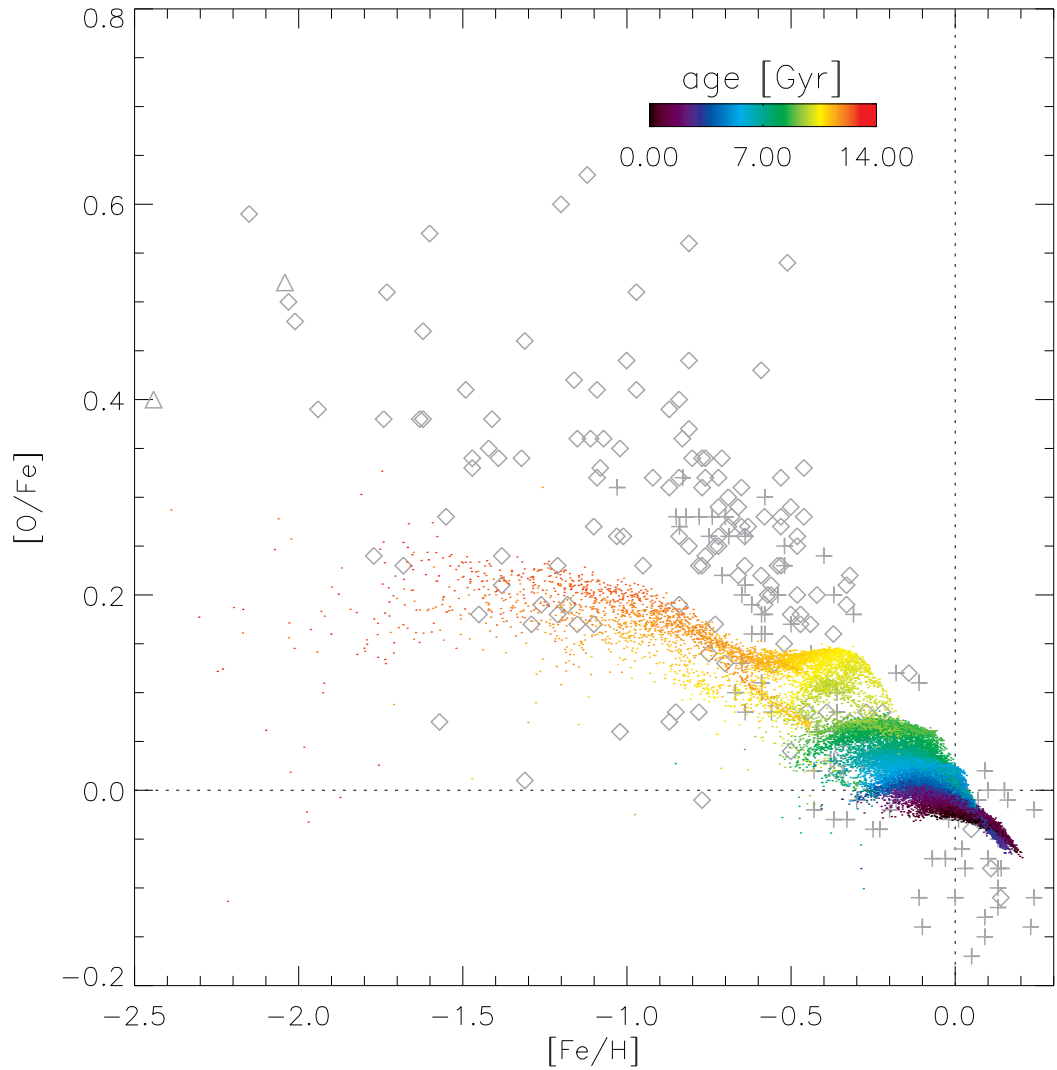


Figure 4.7: Abundance ratios of stars in a disc region of galactocentric radius between 5 and 11 kpc and within 3 kpc of the disc plane. Particles are coloured according to their age. Observational data is plotted in grey, triangles are very metal-poor stars from Cayrel et al. (2004), diamonds are thick disc and halo stars from Gratton et al. (2003), plusses are disc dwarf stars from Edvardsson et al. (1993). All data have been normalised to the solar abundance determination of Anders & Grevesse (1989).

formation seen in Figure 4.6 are identified with the letters a, b, c and d.

The influence of the cosmological environment of this simulation is apparent in the abundance patterns of the galaxy. The sub-sample displayed in Figure 4.7 exhibits the signature of merger events, e.g. the feature at $[\text{O}/\text{Fe}]=0.15$, $[\text{Fe}/\text{H}]=-0.2$. The full extent of this is only apparent when examining all stars in the galaxy where discrete ‘streams’ with chemical properties distinct from the rest of the galaxy are seen. These arise from accretion of satellites that have lower $[\text{Fe}/\text{H}]$ values and remain chemically distinct. Figure 4.8 shows one such abundance ‘stream’ at arrow ‘e’. This stream in fact corresponds to a distinct satellite orbiting at a distance of 70 kpc from the centre of the galaxy itself but it serves to illustrate the usefulness of these features. The satellite galaxy is easily seen in Figure 4.8 because of the colour used to plot its stars, but other streams are visible in the plot which are chemically distinct but without any obvious spatial displacement with respect to other stars. These stars likely correspond to objects that merged in the past to form the galaxy as seen today. In future work a full decomposition of abundance space will be conducted to demonstrate how stars may be associated with separate merged objects and hence deduce the time at which these merger occurred. The ‘strata’ discussed in the previous paragraph may be used to date star formation bursts and thus obtain a full understanding of galaxy assembly. Larger mergers may have a similar abundance to the primary galaxy but bring gas that can reignite a quiescent galaxy and accelerates the production of Fe in the short term.

4.5 Model Comparison

The galaxy is now resimulated with a number of CEMs with different IMFs, SNII upper mass limits and SNeIa delayed time distributions. The run parameters are detailed in Table 4.1. The simulations are performed with the same SN and star formation efficiencies and thresholds. The fiducial model described above is reshown

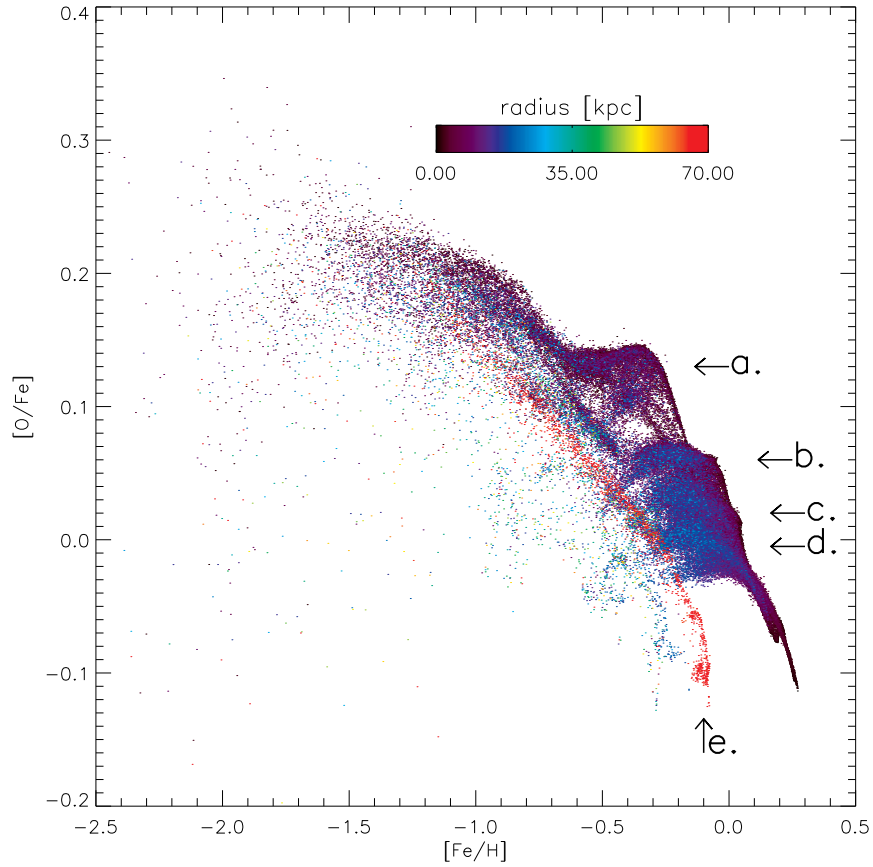


Figure 4.8: Abundance ratios for stars within a sphere of 70 kpc for the *K01-uM40-IaH* model. Stars are coloured according to their distance from the centre of the galaxy. Arrows are labelled to draw the readers attention to particular features. Arrow ‘a’ indicates stars associated with the strongest star formation episode at a time of 2.5 Gyr (see Figure 4.6), arrows ‘b’, ‘c’ and ‘d’ indicate the peaks in star formation at 4.0 Gyr, 7.5 Gyr and 11.0 Gyr respectively. The common age of stars belonging to each of these abundance ‘strata’ is clear from Figure 4.7. Chemically distinct streams are also visible, the clearest of these is indicated by arrow ‘e’ and consists of stars approximately 70 kpc from the galactic centre, these stars all belong to an orbiting satellite.

here for comparison and is labelled as *K01-uM40-IaH*. The cumulative SN rates for each model are shown in Figure 4.9 for a single SSP. The effective (instantaneous) SN rate for a single star particle in the standard implementation of RAMSES is shown for comparison.

Table 4.1: Properties of the chemical evolution models presented here, the precise form of the IMFs used is described in §4.2.1. SNIa DTD are taken from either Greggio & Renzini 1983 (GR1983), Kawata & Gibson 2003 (KG2003) or Mannucci et al. 2006 (M2006).

Model name	IMF	SNIi upper mass limit (M_{\odot})	SNIa DTD
S-uM40-IaH	Salpeter (1955)	40	KG2003
K93-uM40-IaH	Kroupa et al. (1993)	40	KG2003
K01-uM40-IaH	Kroupa (2001)	40	KG2003
K01-uM100-IaH	Kroupa (2001)	100	KG2003
K01-uM40-IaGR	Kroupa (2001)	40	GR1983
K01-uM40-IaM	Kroupa (2001)	40	M2006

4.5.1 Supernovae Rates

Supernovae rates are a key constraint on subgrid physics, imposing an upper limit on the magnitude of feedback allowed in models. The star formation histories for each realisation of 109-CH are plotted in Figure 4.10 with the supernovae rates as a function of cosmic time for the entire galaxy, a spatial cut is made only to exclude satellites. The first noteworthy feature of Figure 4.10 is that the star formation rate is not dramatically different for different models. One might expect that differing SN rates affect the star formation rate. The stellar mass of the realisation (at $z=0$) varies no more than 10% as a function of the CEM, the models with the least stellar

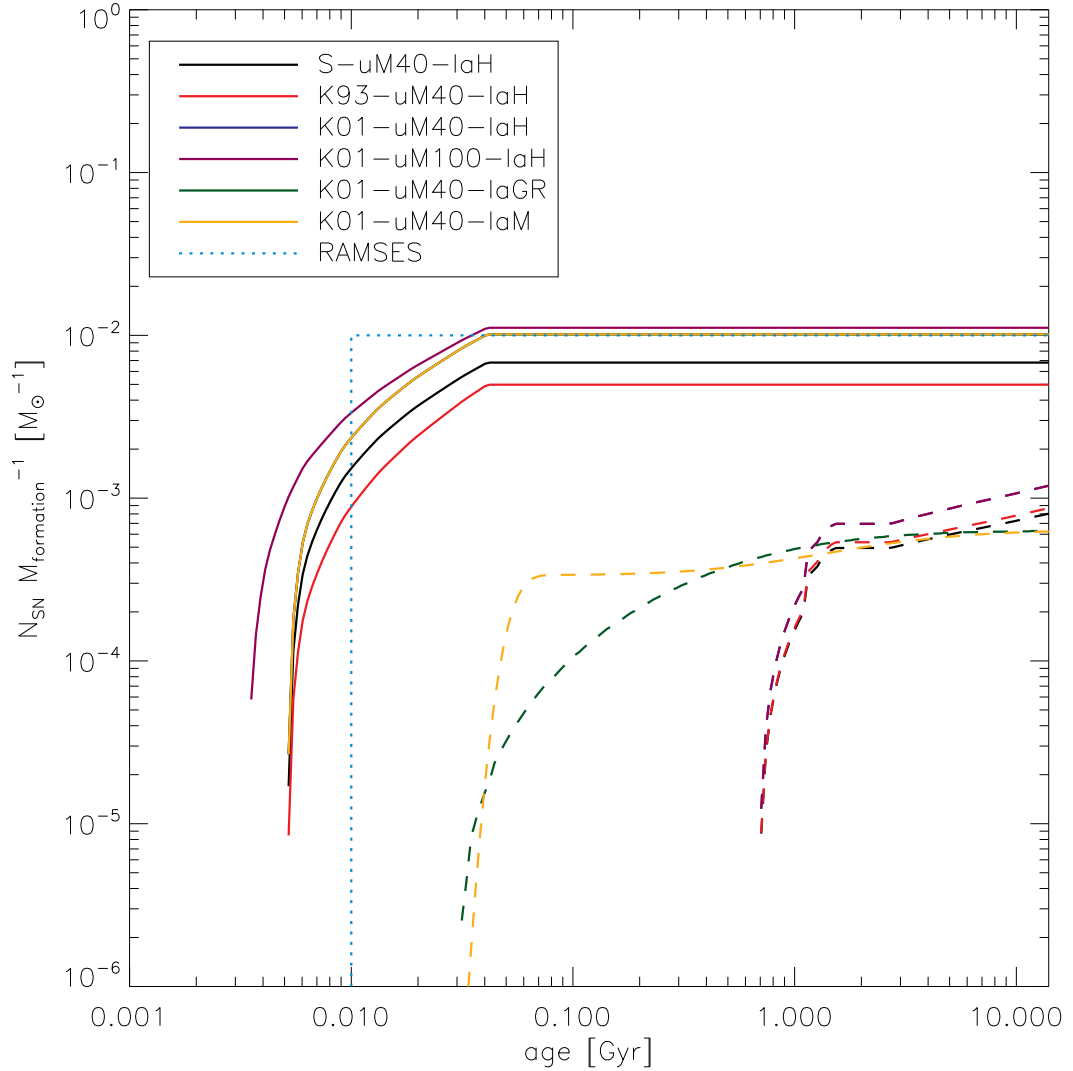


Figure 4.9: Cumulative SN rates for a $1 M_{\odot}$ stellar particle (with solar metallicity) for the models tested. Solid lines are the rates of SNII and dashed lines are SNIa, the light blue dotted line is the equivalent SN rate for a standard run with RAMSES. The SNII lines of models with the same mass limits and IMF overlay one another and are not visible, i.e. models with a name starting “*K01-uM40*” have the same SNII rates.

mass are the two with the highest SN rates, *K01-uM40-IaH* and *K01-uM100-IaH* at $4.75 \times 10^{10} M_{\odot}$ and $4.87 \times 10^{10} M_{\odot}$ respectively. The model with the overall lowest SN rate is *S-uM40-IaH* also has the greatest stellar mass at $5.29 \times 10^{10} M_{\odot}$. All the models have stellar-to-halo mass ratios that are excessive compared with the observed stellar-to-halo mass function (Leauthaud et al. 2012). In Leauthaud et al. (2012) and references therein, the stellar-to-halo mass ratio is typically found in the range 0.01–0.03 for galaxies with halo masses of $\sim 10^{11}$ – $10^{12} M_{\odot}$. The stellar-to-halo mass ratio of the 109-CH realisations are all in the range 0.07–0.08 with halo masses of $\sim 7 \times 10^{11} M_{\odot}$. While the simulated ratios are quite a bit higher than the majority of observational estimates there are a couple of published observational estimates that are higher than the others and should be considered. Springob et al. (2005) find some objects with a ratio of ~ 0.25 and Mandelbaum et al. (2006) find the highest ratio at ~ 0.16 ; please note that in both of these sources the values stated here are the *greatest* stellar fractions and other values within are consistent with the body of literature. The simulated model with the least discrepancy is *K01-uM40-IaH* ($M_{\text{stellar}}/M_{\text{total}} = 0.078$) and also has the best abundance ratios. The inability of the model with the highest SN feedback (*K01-uM100-IaH*) to sufficiently reduce the stellar fraction suggests that if varying the star formation efficiency does not provide a solution then the numerical resolution and/or implementation is lacking something important. An alternative explanation could be that additional feedback mechanisms should be considered, e.g. AGN or radiation from massive stars may be required. A parameter study is currently underway which should make it clear how we might minimise M_{stellar} .

The SNII rate closely follows the form of the star formation rate and should be examined relative to it, for instance the SNII rate of *K01-uM40-IaGR* is different to that of *K01-uM40-IaM* but this merely reflects slight differences in the star formation rate. The biggest difference is seen in the four models with different

IMFs, *S-uM40-IaH*, *K93-uM40-IaH*, *K01-uM40-IaH* and *K01-uM100-IaH* (the top four panels of Figure 4.10). The influence of the IMF on the global SNII rate is clearly apparent, the steepness of the IMF (at masses above $8 M_{\odot}$) corresponds to the global SNII rate. The steepest IMF tested here is the Kroupa et al. (1993) which results in the lowest SNII rates while the shallower IMFs, Salpeter (1955) and Kroupa (2001) give greater SNII rates. The Kroupa (2001) IMF is the one that is most skewed towards massive stars (top-heavy) in the literature.⁵ To further test the IMF we chose to extend the upper mass of the SNII progenitors from $40 M_{\odot}$ to $100 M_{\odot}$ in the *K01-uM100-IaH* model which leads to increased SNII activity of $\sim 10\%$ in comparison with the *K01-uM40-IaH* model. A similar effect may be achieved by varying the upper mass limit of SNeII progenitors for any IMF but note that the effect is much weaker than that of reasonable variations in the slope of the IMF.

Compared to SNeII, the differences in the SNIa rates are far more subtle but the influence they have upon the abundance ratios is significant and so they are discussed here. The models suffixed with *IaH* use the modified Kawata & Gibson (2003) SNIa progenitor model that uses a white dwarf as the primary, the number of white dwarfs is calculated by integration of the IMF over the range $3\text{--}8 M_{\odot}$ and therefore the high mass slope of the IMF influences the SNIa rates as it does the SNII rates. While the SNIa rate also depends upon the low mass end of the IMF, specifically from $0.9\text{--}2.6 M_{\odot}$, it is not until stars below $\sim 0.5 M_{\odot}$ are considered that the IMFs begin to diverge from one another. This means that the high mass end still has a strong influence on the SNIa rates. Comparing the *IaH* models again reveals that the steeper IMFs lead to reduced SN rates, with the low mass end of the IMF manifesting only in the slightly reduced rate of *S-uM40-IaH* compared with *K93-uM40-IaH*. Two models use a different formalism for the SNIa progenitors,

⁵the most top-heavy IMF is actually that of Chabrier (2003) but by a very small margin.

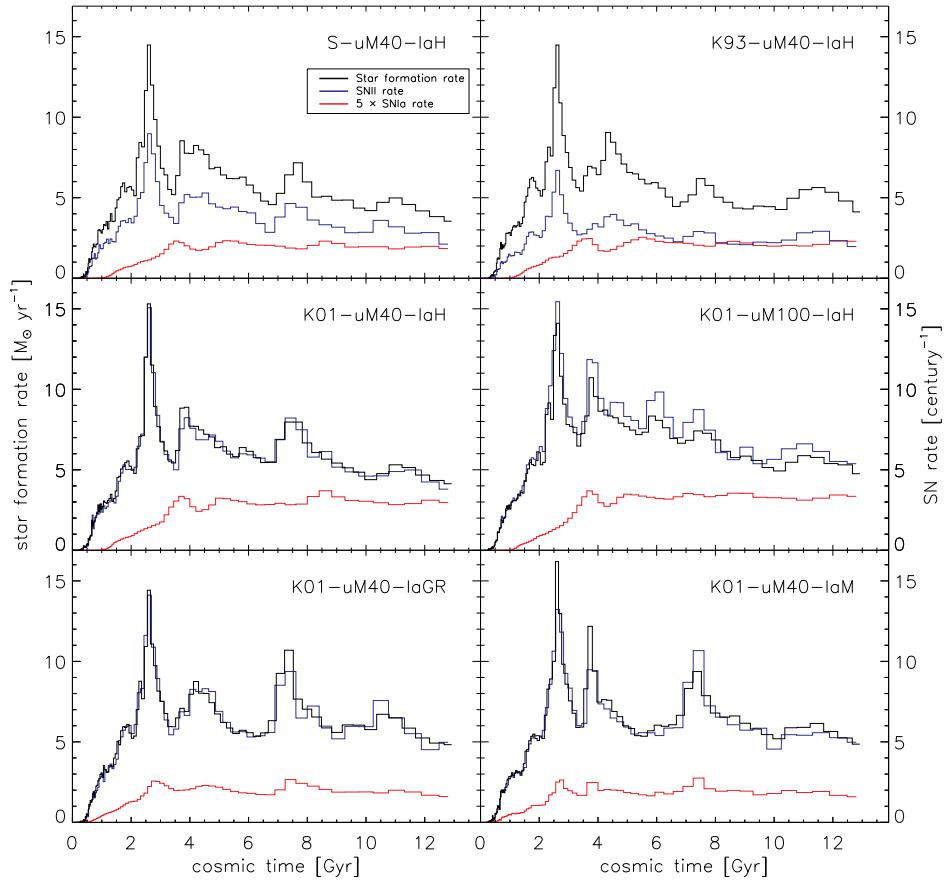


Figure 4.10: Star formation and supernovae rates of each CEM. The black line indicates the star formation rate with the scale given on the left axes. The SN rates are plotted in blue for SNIi and red for SNIa. The units are given on the right axes but note that for clarity the SNIa rates are scaled up by a factor of 5.

parametrising the SNIa rate of a SSP as a function, these are the *K01-uM40-IaGR* (using the Greggio & Renzini (1983) DTD) and *K01-uM40-IaM* (which uses the Mannucci et al. (2006) DTD). The overall rate of SNIa in these models is lower, the cause is easy to see from Figure 4.9 which clearly illustrates that these SNeIa DTDs produce less SNeIa progenitors than the *IaH* models do. The DTD however only defines how the SNeIa are distributed over the lifetime of the stellar population and

a scaling factor is what really defines the SNeIa numbers. The scaling factor used here was chosen to match the SNIa rate per unit stellar mass to the rate calculated with semi-numerical models (Portinari et al. 2004).⁶ This value is in some sense a free parameter and could be varied to easily recover the present day SNIa rate. It is however the DTD that makes these models poor at recovering observed abundance ratios. This is apparent when the onset of SNeIa is examined, the delayed onset of SNeIa in the *IaH* scheme can be seen at ~ 0.7 Gyr after star formation while the onset in the *K01-uM40-IaGR* and *K01-uM40-IaM* models takes only ~ 0.03 Gyr. The peaks of the SNIa rate are also very close in time to the peaks in the SNII rate for these ‘short-delay’ models, this is an obvious consequence of the previous point but will become important when the spread of $[\alpha/\text{Fe}]$ is considered.

Note also that the rotation curves (Figure 4.11) of the different realisations are not vastly different. There are small variations in the extent of the young stellar disc (solid red line) which roughly follows the strength of SN feedback in each model. The most extended disc belongs to the pair of *K01* models which have the highest SN rates while the shortest discs correspond to the models with the lowest SNIa rates (*K01-uM40-IaM* and *K01-uM40-IaGR*), these differences are however only of order 5%.

4.5.2 Abundance Ratios

The abundance ratios of stars present an interesting look at the effect of the initial mass function and SNeIa progenitors on galactic chemical evolution. The abundance ratios $[\text{O}/\text{Fe}]$ and $[\text{Fe}/\text{H}]$ are plotted in Figure 4.12 for the stars enclosed by an annulus of galactocentric radius between 5 and 11 kpc, with height above (or below) the disc plane of not more than 3 kpc. The initial impression of this comparison is that quite dramatic differences are seen between the models with variations of up

⁶Francesco Calura, private correspondence.

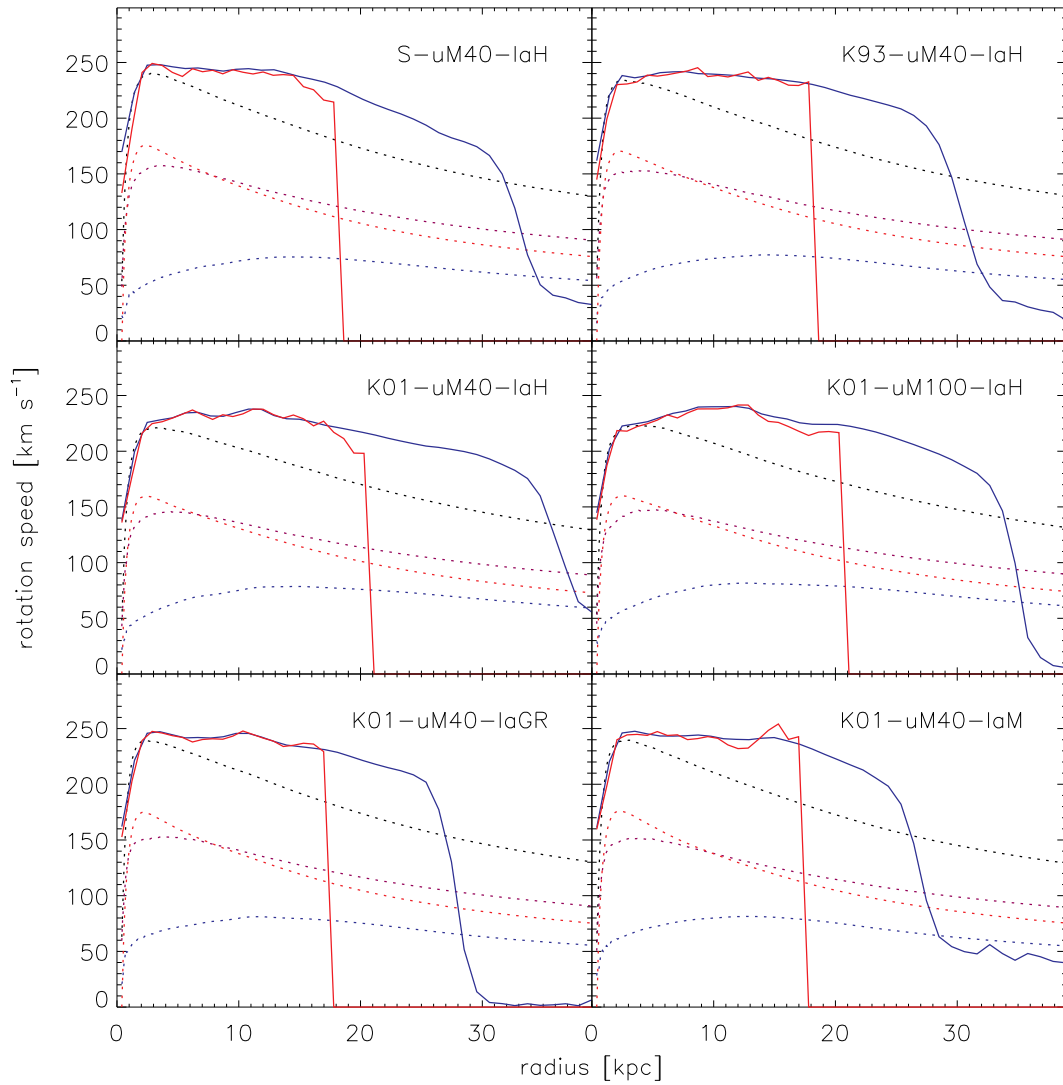


Figure 4.11: Rotation curves for the six realisations of 109-CH. Dotted lines are the circular velocity curve contributions from different phases of matter; dark matter (purple), stars (red), gas (blue) and the total (black). Rotation curves for gas (solid blue line) and young stars (<100 Myr, solid red line) are also shown.

to ~ 0.4 dex possible.

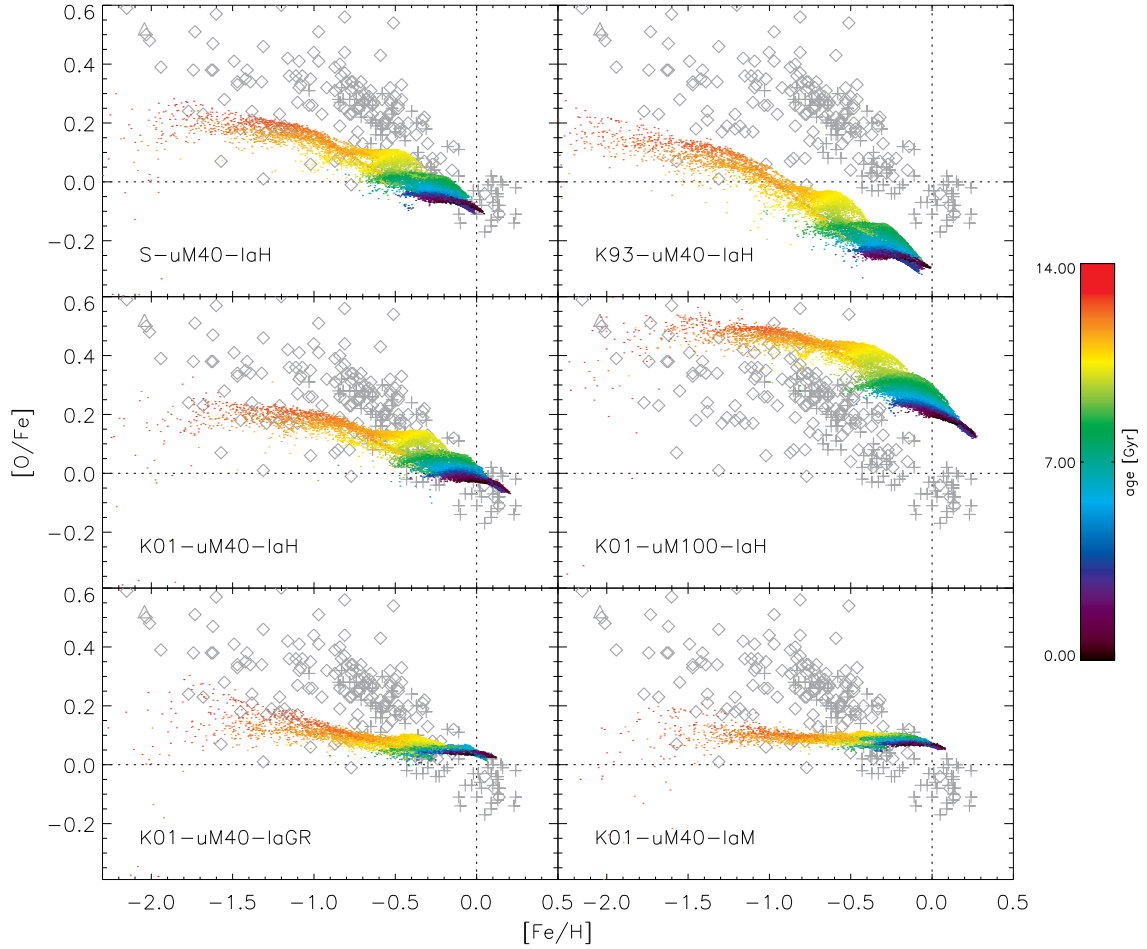


Figure 4.12: Abundance ratios for each CEM, $[O/Fe]$ versus $[Fe/H]$ for stars within an annulus of galactocentric radius 5–11 kpc and with height above (or below) the disc plane of no more than 3 kpc. The age of each stellar particle is indicated by its colour, refer to the colour bar for the scale. Dotted lines indicate solar abundances.

The IMF affects the $[Fe/H]$ growth but its most pronounced effect is upon the $[O/Fe]$ value, with clear links to the respective SN rates. In the same way as with the SN rates the steeper the IMF is at the high mass end the less efficient the production of oxygen becomes (the same may be said of other elements predominantly produced in SNI), therefore the steep IMF of *K93-uM40-IaH* creates an $[O/Fe]$ that is 0.2 dex

less than observations dictate. This is also true of the *S-uM40-IaH* where $[O/Fe]$ is approximately 0.1 dex too low at all values of $[Fe/H]$, note also that these low SN rate models also underproduce Fe. Figure 4.13 and Figure 4.14 show the abundance of oxygen and iron in stars as a function of age so as to allow the reader to see which element is affected the most by changes in the model. In these plots the colour coding of particles denotes the height from the disc plane with stars at greater heights overplotted on those lower down; in this way the stars with the greatest height at a given abundance and age are most visible. It can be seen that the youngest stars are those that are lowest in the disc and that they are also the most abundant in both oxygen and iron. Comparing the offset in oxygen and iron for the models *K93-uM40-IaH* and *S-uM40-IaH* in Figures 4.13 and 4.14 show that oxygen is affected far more than iron.

The *K01-uM40-IaH* model is compared with observations in Figure 4.7 where the $[O/Fe]$ matches well at $[Fe/H] > -0.5$ dex but fails at $[Fe/H] < -0.5$ dex; either because stars are not forming in oxygen rich environments in the galaxy or because there are no regions of gas with $[O/Fe]$ greater than 0.3 dex. Nevertheless this model provides the best fit to observed abundance ratios (in addition to the previously described successes). It seems important to note that increasing the upper mass limit of SNeII progenitors has a major effect on the $[O/Fe]$, this is seen in the $[O/Fe]$ values of the *K01-uM100-IaH* that increase by approximately 0.2 dex. If we consider Figures 4.13 and 4.14 we see that the $[Fe]$ is overabundant (comparing young stars with the zero-point of the solar abundance) and yet $[O]$ is even more so, pushing the $[O/Fe]$ value to the high values seen in Figure 4.7.

In contrast with the *K01-uM40-IaH* model, the *K01-uM100-IaH* model reproduces the $[O/Fe]$ of the low metallicity stars but not above $[Fe/H] = -0.5$ dex. The SNIa rate of this model fits reasonably well with observations so it is unlikely that

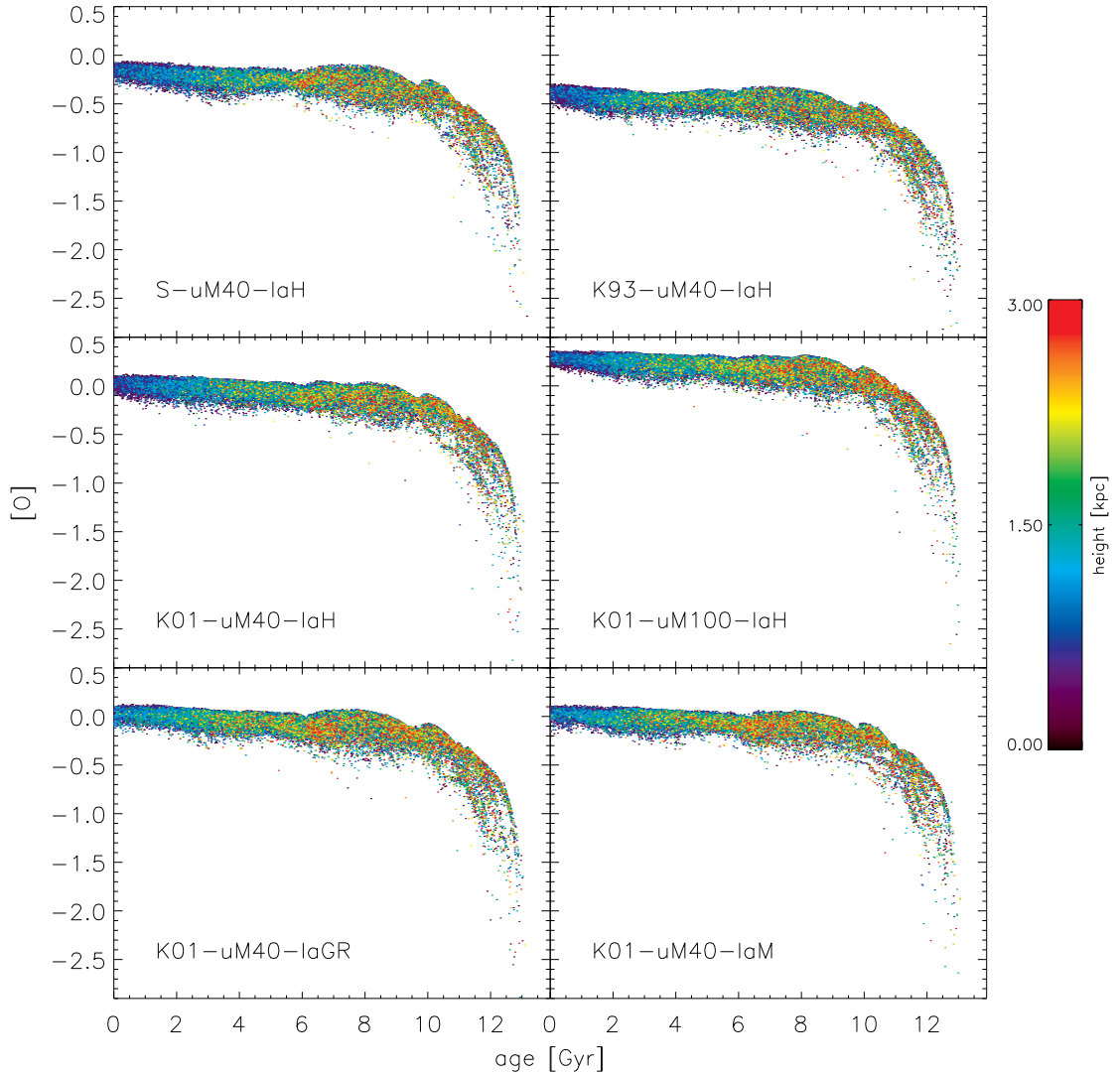


Figure 4.13: Stellar oxygen abundance (normalised to solar) versus stellar age. Stars are colour coded by the magnitude of their height from the disc plane. Stars with greater height are overplotted on this with lesser heights such that the stars that are furthest from the disc plane at a given abundance are the most visible.

the unreasonably high $[O/Fe]$ (of the high $[Fe/H]$ stars) could be tempered by increasing the SNIa rate making this model a poor fit to observations. Relaxation of the upper mass limit for SNeII however may provide a distinctly beneficial effect on the abundance ratios of the models with steeper IMFs while also providing a boost

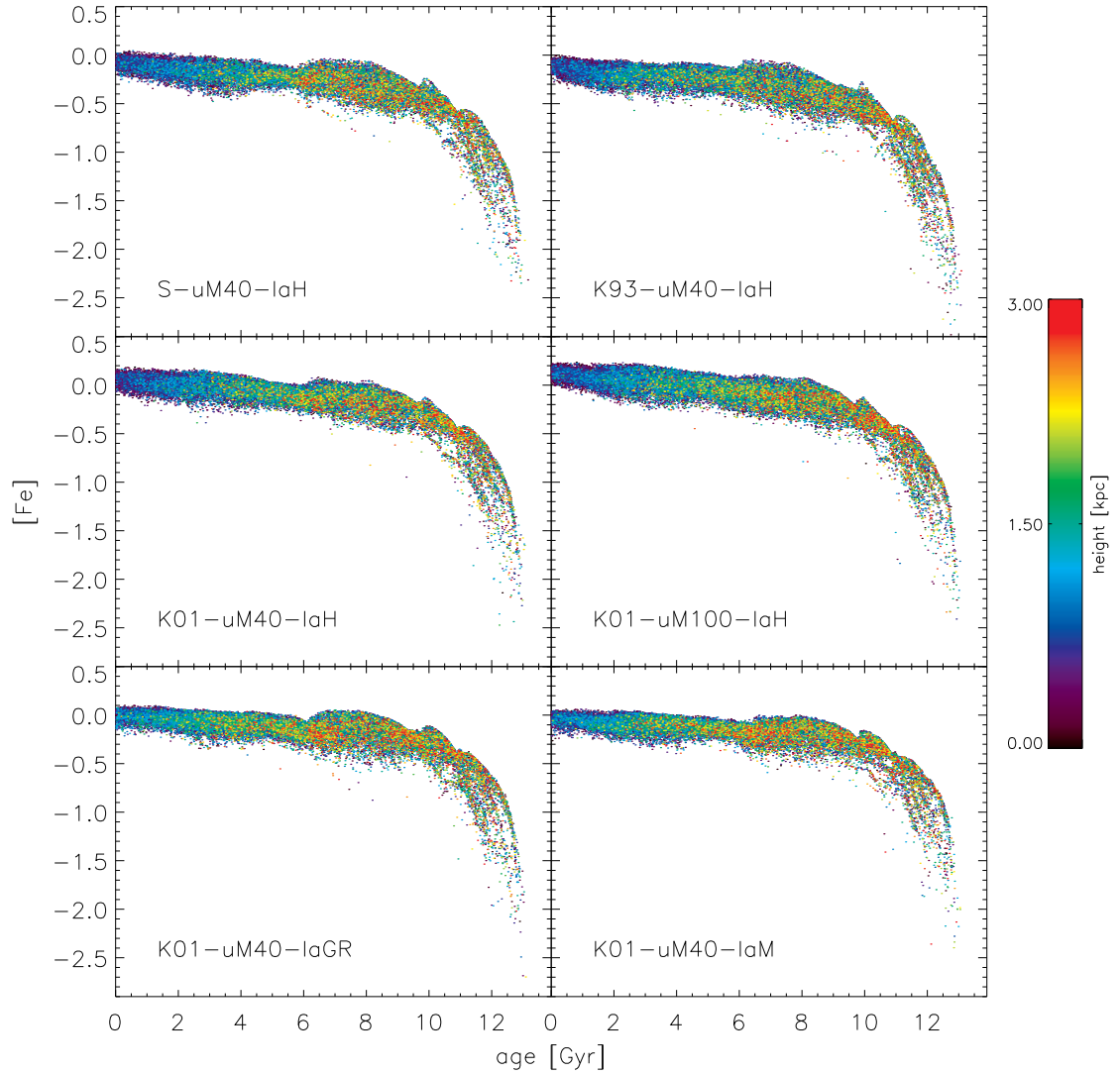


Figure 4.14: Stellar iron abundance (normalised to solar) versus stellar age. Colour coding and overplotting are as described in Figure 4.13.

to their slightly low $[\text{Fe}/\text{H}]$ values. This would also help to bring the SNII:SN Ia ratio up to a value closer to observed rates. This issue will be considered in future CEM comparisons but has not been included here due to time constraints; the models shown here nevertheless serve to demonstrate the extent of the influence the models have on chemical evolution.

In Figure 4.12, models *K01-uM40-IaGR* and *K01-uM40-IaM* appear very different to the models with *IaH*, the dispersion in $[O/Fe]$ is much smaller and the characteristic ‘knee’ feature of the observed abundance ratios is much weaker. As the SNeIa onset time is much earlier with these models, the high $[O/Fe]$ plateau never occurs due to the early production of Fe. SNeIa occur throughout the galaxy’s formation and peaks in the SNIa rate match those in the SNII rate, thus the dispersion in $[O/Fe]$ seen in the other models (arising from variations in the SNeII/SNeIa ratio) is diminished. The *K01-uM40-IaGR* SSPs have a lower SNIa rate at early times compared with those in the *K01-uM40-IaM* and a hint of this can be seen in the slightly higher $[O/Fe]$ at low metallicities.

4.6 Conclusions

We present a development to the N-body and hydrodynamical code RAMSES that adds two levels of sophistication to the feedback scheme. Supernovae feedback may now occur throughout a star particle’s history, allowing the energetic contribution of SNeIa to be accounted for and removing the need to parametrise the time at which feedback processes occur. Secondly, the time resolved feedback scheme presents the ability to include more sophisticated chemical feedback and to self-consistently determine the number of supernovae. This chemical feedback injects metals into the gas phase which is then traced hydrodynamically as individual elements. The new code is then applied to a test case using a particular CEM and then to six differing CEMs to test the response of a typical L_* disc galaxy to variations in the initial mass function and SNIa delayed time distribution. These initial tests are intended to demonstrate the validity of the approach and to understand how the features of the chemical evolution model manifest in the galaxy properties. For instance, to what extent do the stellar abundance ratios depend upon the IMF or SNIa progenitor model. Substructure in abundance space is presented and connections are made to

both star formation episodes and the merging of chemically distinct satellites.

The IMF steepness at the high mass end influences the SNII and SNIa rates, with steeper IMFs resulting in reduced SN rates. The stellar mass of the realisations is found to be too high relative to the halo mass in comparison with observations even for the models with the maximum possible SN rate per unit stellar mass. The model with the lowest stellar mass also has SN rates that are closest to the observed values in galaxies with a similar morphology to the simulated one. It is therefore clear that if the star formation efficiency of the entire galaxy is reduced then adjustments need to be made to the CEM, i.e. the IMF slope, upper mass and the SNIa DTD should be changed to increase the SN rate to meet the observational constraints. This is unfortunately independent of how the stellar mass fraction of these galaxies is reduced, it will be necessary to alter the underlying IMF. This is an informative revelation as it implies that the ‘best’ CEM found here is only ‘best’ at the current galactic star formation efficiency. This is a necessary word of warning for the study of these models but it does not mean that nothing may be learned from the study, indeed it acts as evidence against the steeper initial mass functions which are already deficient in the number of massive stars both in terms of energetic feedback and the production of α -process elements.

One reassuring feature is that the model producing the most agreeable SN rates and stellar mass (*K01-uM40-IaH*) also has abundance ratios that match fairly well with observations. This means that the nucleosynthetic yields are trustworthy (at least to first order), and that the abundance ratios of stars and gas in the simulated galaxies are discriminating of the IMF and SNIa progenitor model. A detailed examination of the elements should be conducted in future work to see if the characteristic behaviour of key elements such as nitrogen and carbon is reproduced. The abundance ratios of stars again reveal the steepness of the IMF via the SN rates. Models using a steeper IMF are under-abundant in iron and much more so in oxygen.

Taking the favoured model and extending the upper mass limit of SNeII progenitors has a small effect on the SN rates but a quite extreme effect on abundance ratios, increasing $[\text{O}/\text{Fe}]$ by around 0.2 dex. This suggests that were the upper mass limit to be increased for models where $[\text{O}/\text{Fe}]$ is too low, then agreeable results may be obtained. In a forthcoming paper the models chosen for comparison will be informed by the results found here: a SNeII upper mass limit will be chosen that is appropriate for the IMF in question. While the models are in some sense constrained in this way there is an unavoidable lack of uniqueness in the solutions provided by each of the CEMs. In future work these models will also be tested and other element abundance will be considered to see if there is any way of breaking the degeneracy between the upper mass limit of SNeII and the IMF slope.

The SNIa delayed time distributions are quite well constrained by this technique, while the 0.7 Gyr onset of SNeIa in the Kawata & Gibson (2003) model (*IaH*) does a good job in replicating the high $[\text{O}/\text{Fe}]$ plateau at low $[\text{Fe}/\text{H}]$ and the ‘knee’ feature at approximately $[\text{Fe}/\text{H}]=-1$. The two other SNIa rate models (*IaGR* and *IaM*) not only result in too much Fe at early times but also lead to a less variable SNeII/SNeIa ratio that means α -process elements and iron-peak elements are produced roughly in proportion to each other throughout the galaxy’s evolution. The abundance ratio plots exhibit a less obvious ‘knee’ and have an extremely small dispersion in $[\text{O}/\text{Fe}]$. This is particularly pronounced in the model testing the Mannucci et al. (2006) model (*IaM*) that has a greater fraction of its SNeIa at earlier times. The Greggio & Renzini (1983) model (*IaGR*) places more of its SNeIa slightly later and while the $[\text{O}/\text{Fe}]$ dispersion is still very low, there is at least a hint of a ‘knee’ separating the earlier SNeII dominated abundances from the later iron rich phase. In Hachisu et al. 1999 (from which the more successful SNIa progenitor model studied here originates) it is also suggested that SNIa progenitor systems should not exist at metallicities below $[\text{Fe}/\text{H}]=-1.1$ dex. This constraint was not included in the models here for the

sake of simplicity but one can easily imagine the effect it might have. Metallicity of $[\text{Fe}/\text{H}] = -1.1$ dex is reached approximately 1–2 Gyr into the galaxies evolution, this represents an almost insignificant reduction in the number of SNe at early times and may induce a slight delay to the down-turn of $[\text{O}/\text{Fe}]$. The effect of introducing this metallicity cut on the morphology of the galaxy perhaps warrants investigation. As has been shown in Chapter 3 the metallicity gradient of the forming galaxy is steeper at high redshift than at the present day. This means that as the metallicity of the galaxy grows, the galactocentric radius at which SNeIa are contributing energetic feedback grows as well. We speculate that this may influence disc formation. If a metallicity constraint exists the amount of SN energy that is output by stars at a given radius may be more concentrated than if SNIa are permitted at low metallicities. This is likely to influence only the evolution at high redshift.

The presentation of this code has been published as Few et al. (2012) where the code methodology is described. Further work in comparing the different chemical evolution models is to be presented in a forthcoming paper. It is also prudent to consider the abundance ratios of different elements to determine if it is possible to break the degeneracy of specific combinations of parameters. It remains a challenge for the future to fit the stellar mass of simulated galaxies to observations across the whole range of galaxy halo masses This method does however provide a means of studying chemical evolution with self-consistent dynamics in a cosmological context and with large surveys such as Gaia and its spectroscopic companion the Gaia chemodynamical survey producing vast catalogues of data for the study of abundances in tandem with galactic dynamics, now is an exciting time to consider chemical tagging and chemical evolution in the context of galaxy formation.

Chapter 5

CONCLUSIONS AND FUTURE WORK

Doubt is not a pleasant condition,
but certainty is absurd.

Voltaire

In this chapter we restate the conclusions of each component of my postgraduate work before discussing potential avenues for future work in this area.

5.1 The Milky Way Environment

Chapter 2 presents the RaDES suite of galaxies, 19 cosmologically simulated disc galaxies in either a loose group or field environment. The samples were created with the intention of comparing galaxies in the field (as are commonly simulated) with those in environments similar to the Local Group. While the environment of the two samples are distinct, other aspects of the galaxies are kept as similar as possible. The spin parameters of the haloes, the virial mass range and merger histories are matched as closely as possible. The two different environments are defined by the dark matter distribution such that loose groups roughly emulate the density of dark

haloes around the Local Group whilst the field environments have very sparse halo populations.

The disc stars of each galaxy are identified through kinematic decomposition and are used for comparing the properties of galaxies in the loose group and field samples. The morphology, metallicity gradients and stellar velocity dispersions of the simulated galaxies are compared, finding in general that there is no *obvious* difference between galaxies in the different environments. There does however appear to be a systematic increase in the prevalence of ‘steps’ in the age-velocity dispersion relation for loose group galaxies compared with those in the field. This suggests that impulsive heating is more significant in the denser environments of the loose group in spite of the two samples having similar major mergers rates (including mergers with mass ratios of 1:10). This appears to have a minimal impact on the metallicity distribution and morphology. The main findings of this work are now listed.

1. The morphology of the galaxies is measured by the ratio of the stellar spheroid mass to the stellar disc mass. The galaxies are mostly found to be disc dominated without the excessive spheroid fraction that is traditionally found in numerically simulated galaxies. This metric reveals a great deal about the environmental effect on morphology as *no apparent distinction exists between the two samples*.
2. The disc-to-spheroid ratio does reveal a dependence upon major merger activity with both loose group and field galaxies that have experienced recent mergers having larger spheroid fractions than those with more quiescent evolution. The most spheroid dominated galaxies in the two samples are those with the lowest mass; this may be because they are at an early stage in their evolution at $z=0$ or because their low mass makes them more susceptible to kinematic heating.
3. The simulated metallicity gradients are consistent with observations of local

disc galaxies (Zaritsky et al. 1994; Garnett et al. 1997; van Zee et al. 1998) when expressed in units of dex kpc^{-1} . The gradients are also considered relative to the disc scale length and in this case are found to be an order of magnitude flatter than observations suggest. These two findings imply that although the galaxies are disc dominated, the discs themselves are overly concentrated.

4. The metallicity gradients are found to have a dependence on the galaxy mass (total mass within the virial radius). More massive galaxies have flatter gradients, this is consistent with the predictions of semi-analytical models using scaling relations (Prantzos & Boissier 2000) but has been demonstrated here using dynamically simulated galaxies. The metallicity gradient does not share this trend when it is normalised by the disc scale length. The correlation of the scale length with the metallicity gradient suggests that there is some degree of co-evolution of the two and points to a common origin of these features which corroborates evidence in Garnett et al. (1997) and van Zee et al. (1998). In Chapter 3, the star formation rate is shown to connect the scale length and the metallicity gradient.
5. At a given total mass, the metallicity gradients of the loose group galaxies are similar to those of the field galaxies. The lack of any clear distinction and the fact that the gradients of both samples are consistent with the gradients measured in close interacting binaries by Kewley et al. (2010b) suggests that the environmental differences of the loose group compared with the field produces no appreciable change in the metallicity gradients for these simulated galaxies.
6. The present day velocity dispersion of stars is measured for different age bins in each galaxy. The simulated old stars have higher velocity dispersions than old Milky Way stars do while the younger stellar populations are only slightly too hot compared with observations (Soubiran & Girard 2005; Holmberg et al.

2007; Soubiran et al. 2008). A quantitative analysis of the gradient of the age-velocity dispersion relations reveals hints of a difference in the relations of the loose group and field samples. Discrete steps are found to be more prevalent in the loose group galaxies suggesting that mergers or harassment have a stronger effect on the disc stars. Either this is because these galaxies are more susceptible to disruption or merger events are not adequately detected via the dark matter merger histories used to ensure homogeneity between the two samples. We do note however that the number of galaxies used in this study is not high enough to rule out statistical noise affecting the interpretation. This interpretation is also contrary to what is understood based on the other measured properties of the galaxies and given the unreliability of the statistics involved this facet of the study warrants further testing with a larger sample size before it is believable.

There is an obvious dispersion in each of the measured quantities and together with the lack of clearly separate trends for the loose group and field samples we conclude that it is the formation history of the individual galaxies and not the environment that is the dominant driver in shaping most of the observable properties of galaxies. This comparison is made between the relatively similar field and loose group (where interaction between members is weak) environments and the interpretation is only applicable to environmental differences on this scale, i.e. we say nothing concerning the comparison of dense clusters and groups. We also do not probe the effect on closely interacting binary galaxies, indeed if such close interactions are to be referred to as ‘environment’ then close interactions should be a common occurrence for the galaxies in questions.

In contrast with the other results, the age-velocity dispersion relation presents a puzzling difference in the kinematic heating history between the two samples. This is similar to the conclusions of McGee et al. (2008) that cluster galaxies are shaped

by secular evolution and direct mergers rather than by indirect interactions with the large-scale environment. While the statistical validity might be questionable with galaxy samples this size the result is at least intriguing, suggesting that impulsive heating is stronger for the loose group galaxies. Alternatively it may be that the efforts to ensure homogeneity of merger histories between the two samples failed because the definition used is insufficient to connect mergers and the signature they leave upon galaxy properties. The mergers are defined using dark matter merger trees and a disparity exists between this definition and the ‘real’ merger, i.e. the merging of baryons and the interaction of dark matter with the galaxy disc itself. This work focusses on relatively similar environments (evidenced by the similar galaxy properties) and the number of galaxies studied may not be sufficient to detect subtle differences. Future studies of this topic should focus on simulations with only dark matter to quantify the satellite distribution and minor merger rates in more detail.

This work does however answer the question that originally inspired it, “Can simulated field galaxies be profitably compared with observations of Local Group galaxies?” It appears that as the individual merger properties, mass and secular evolution of the galaxies dominates over environmental effects (at resolutions of ~ 400 pc), the answer is that they can. The aforementioned dominating effects must however be considered carefully for comparisons to be relevant.

5.2 Inside-out Formation

Building on the suite of simulations presented in Chapter 2 we use the galaxies in a comparison with simulations from other codes, primarily GASOLINE but also GCD+ and GRAPE-SPH. The results obtained with semi-numerical methods are also compared.

Star formation rate profiles are calculated at different redshifts to demonstrate

how the formation of stars proceeds from initially concentrated star formation to an even distribution across the disc supporting the concept of ‘inside-out’ formation. Vertical metallicity gradients are measured for the galaxies and the evolution of radial metallicity gradients in the young stellar population is compared across all the models. We have demonstrated that inside-out formation is a natural phenomenon in Eulerian and Lagrangian hydrodynamical simulations. We examine how this formation mechanism creates evolving abundance gradients in the simulated galaxies and consider the role of radial migration in flattening the gradients of older stellar populations.

Vertical metallicity gradients are measured for the simulated galaxies and are comparable to the observed thick disc metallicity gradient of the Milky Way. It is important to bear in mind with this result that the resolution of the simulations is insufficient to differentiate between the thick and thin disc, thus comparison with thin disc gradients is inappropriate. In spite of the vertical resolution issue it is reassuring that a vertical gradient exists that fits the behaviour of the total stellar disc.

The fundamental result of this work is that with no initial conditions explicitly imposing inside-out formation in the simulated galaxies, such formation is seen in all the simulations. The concentration of the early star formation profile does depend on the specific star formation and feedback scheme employed by each simulation code, but the qualitative behaviour is ubiquitous. The semi-numerical models of Chiappini et al. (2001) and Mollá & Díaz (2005) are included as benchmarks and have inside-out formation ‘enforced’ by the radial infall rates as a function of time. Figure 3.5 clearly shows how the normalised star formation profile proceeds through time to increasing activity at greater radii. The evolving profile in the star formation rate directly affects the metallicity gradient of young stars. The signature of the star formation profile is not a long-lived feature and is quickly dissipated by radial

migration. This means that while the steep star formation profile at high redshift creates an initially steep metallicity gradient, these stars are observed at the present day (as ‘old’ stars) with flatter metallicity gradients than the younger populations.

The star formation profile is strongly influenced by the details of the sub-grid physics in each code. It is difficult to make direct connections between the star formation density threshold or the star formation and supernovae efficiencies and the specific star formation profile that is found for each galaxy without making an unbiased study using a single code in a parameter study. What is clear is that simulated galaxies with more centrally-concentrated star formation have initially steeper abundance gradients. The initial steepness of the metallicity gradient is consistent with the limited observations that exist of high redshift grand design spiral galaxies (Yuan et al. 2011). Despite the wide variation in metallicity gradients at high redshift, the majority of the simulated gradients are similar at $z=0$ and are consistent with observed local spiral galaxies, see Figure 3.9. In almost all cases the young stellar metallicity gradient flattens as a function of time. The single exception is the Chiappini et al. (2001) semi-numerical model that starts with an initially positive metallicity gradient and proceeds to invert into a negative gradient with a similar steepness to the other models at $z=0$.

An unexpected (and novel) result is the diversity of metallicity gradients that can arise at high redshift in different codes, the galaxies simulated with GASOLINE show a much greater spread in gradients and a volatile temporal evolution compared with the RAMSES galaxies which start much flatter as a consequence of the less concentrated star formation. These results indicate that the formation processes that shape disc galaxies may be probed through observations of metallicity gradients at high redshift ($z>1$). This will also provide constraints on sub-grid physics in simulations where it appears that high redshift metallicity gradients are sensitive to the model parameters.

Future work to understand these results further should concentrate on studying the effect of different parameters with a single code on numerous realisations of a single galaxy to avoid biases from the hydrodynamical schemes and formation histories. The study would be profitably continued using either GASOLINE or RAMSES although we remind the reader here that the new and more sophisticated feedback mechanism employed in RAMSES-CH make it an attractive option for this kind of study. This will ensure that the diversity in the metallicity gradients is indeed a function of differing subgrid physics, independent of the quirks of each hydrodynamical scheme. The volatility of the gradients in the GASOLINE galaxies suggests that a finer temporal cadence is required to allow the effect of merger events to be traced accurately, both in terms of tracing the magnitude of the effect and the time taken to regrow a measurable gradient after the merger has disrupted the disc. Now that it is known that high redshift gradients and star formation profiles are sensitive discriminators of the formation mechanism, it would again be interesting to repeat the experiment with RAMSES-CH.

5.3 A New Chemical Evolution Code

In Chapter 4 we describe the main features of CEMs and present a new code, RAMSES-CH published in Few et al. (2012). This new code builds upon the N-body, hydrodynamical method used for the simulation work in chapters 2 and 3 to include a time-resolved treatment of feedback, naturally allowing the inclusion of SNeIa and sophisticated chemical feedback. Multiple elements are traced by the hydrodynamical scheme to follow their flow in the galaxy and imprint their abundance on newly formed stars. By combining an initial mass function, a SNIa progenitor model and nucleosynthetic yields, the energetic and elemental feedback is self-consistent and significantly, the SN rates are motivated by stellar physics via the IMF. Stellar yields are dependent on the mass and metallicity of the stars and

account for the elements ejected by SNeII, SNeIa and AGB stars. The validity of the approach is first demonstrated for a particular chemical evolution model followed by a study of various combinations of different IMFs and SNIa models while keeping the nucleosynthetic yields of stars unchanged. The CEMs are applied to the simulation of a typical L_* disc galaxy to test the SN rates and abundance ratios that are created.

All cases produce a disc galaxy with a reasonable star formation history and rotation curve. In each case the global supernovae rates are calculated in addition to the abundance ratios which are examined to determine the influence of the chemical evolution model on the galaxy properties. The steepness of the high mass end of the IMF is extremely important as it defines the number of SNe per star particle. The steeper IMFs of Salpeter (1955) and Kroupa et al. (1993) lead to SNII rates that are slightly less than observations of disc galaxies would suggest, while the IMF suggested by Kroupa (2001) gives reasonably good agreement with observation. Each of these models are tested assuming an upper mass limit of $40 M_\odot$ for SNeII, but for the IMF resulting in the highest SNII rate we have also tested a model with an upper mass limit of $100 M_\odot$ which increases the SNII rate. The higher SNII rate of this model leads to an increase of 0.2 dex in the [O/Fe] which reproduces the low metallicity plateau but overestimates the oxygen abundance at high metallicities. Conversely, by limiting the SNII to below $40 M_\odot$ the high metallicity oxygen abundance is recovered but the low metallicity stars are oxygen deficient. The degeneracy between the high mass slope of the IMF and the upper mass limit presents the awkward possibility that a unique solution does not exist based upon [O/Fe] or supernovae rates alone, i.e. a Salpeter (1955) IMF with a mass limit at $100 M_\odot$ may be very similar to Kroupa (2001) with a lower mass limit. Examination of elements produced predominantly by low mass stars such as nitrogen or carbon may provide a means of breaking this degeneracy.

For each model we plot [O/Fe] versus [Fe/H] (Figure 4.12) where the IMF slope

is again apparent, $[\text{O}/\text{Fe}]$ is particularly sensitive to variations in the slope. The steeper IMF models tend to underproduce oxygen relative to iron while the steepest IMF tested, Kroupa (2001), produces stars with $[\text{O}/\text{Fe}]$ values consistent with observations of the solar neighbourhood, however even this model has relatively low $[\text{O}/\text{Fe}]$ for metal poor stars with the spread in $[\text{O}/\text{Fe}]$ being too small. The steeper IMF models also exhibit a slight deficit in $[\text{Fe}/\text{H}]$ that also stems from the reduced SNII rate. Reassuringly, the model that best reproduces observed oxygen and iron abundances is the same model that best reproduces the respective supernovae rates, that is a Kroupa (2001) IMF, a SNIa progenitor model that delays the SNeIa onset until around 1 Gyr after star formation with SNeII limited to less than $40 M_{\odot}$. Again it is found that extending the upper mass limit for SNeII progenitors creates an upward shift in $[\text{O}/\text{Fe}]$ by 0.2 dex, an increase of which order would be almost enough to counteract the low $[\text{O}/\text{Fe}]$ of the steeper IMF models.

Three SNIa progenitor models from literature are tested, DTDs from Greggio & Renzini (1983) and Mannucci et al. (2006) which start to produce SNeIa at ~ 0.03 Gyr, and a two phase model after Hachisu et al. (1999); Kawata & Gibson (2003) with an onset time of ~ 0.7 Gyr. The short onset time of the Greggio & Renzini (1983) and Mannucci et al. (2006) models mean that the SNIa rate of the galaxy co-evolves with the SNII rate such that the $[\text{O}/\text{Fe}]$ maintains a relatively constant (and low) value. The Hachisu et al. (1999) style SNIa model, with its longer onset time allows a high $[\text{O}/\text{Fe}]$ plateau to form at low metallicities with a down-turn at $[\text{Fe}/\text{H}] \approx -1$ and a larger dispersion in the $[\text{O}/\text{Fe}]$. It is hard to imagine how the two DTD approaches with short onset times could match this observation, particularly in the case of the Greggio & Renzini (1983) model. There is perhaps hope that the Mannucci et al. (2006) model might be able to reproduce the ‘knee’ with the right choice of IMF but the $[\text{O}/\text{Fe}]$ dispersion will still be too small.

The final point we wish to make with regard to this work concerns the implications of the stellar mass fraction of the galaxies being too great. Commonly simulations will employ the maximum possible efficiency to couple the SNe to the ISM in hope of reducing star formation. Of the IMFs examined in this work, the Kroupa (2001) is the most top-heavy and produces the greatest number of SNe per unit stellar mass, however even in this case the stellar fraction is too great, $M_{\star}/M_{\text{total}} = 0.08$ (within the virial radius) compared with the observed maximum value of approximately 0.03 (Springob et al. 2005; Mandelbaum et al. 2006; Leauthaud et al. 2012). This model (in the case of the upper SNeII mass limit being $40 M_{\odot}$) does however reproduce the global SN rate of the galaxy, presenting an interesting dichotomy. If the simulation correctly matched the stellar mass fraction by reducing the stellar mass by a factor of 2 (regardless of the means by which this is achieved) then the SN rates will be deficient by a factor of 2. Therefore we should not rule out models that overestimate the SN rates and bias our belief away from models that underestimate it for as long as we still form too many stars. Perhaps the obvious consequence of this, in light of the results presented in this thesis, is that the upper mass limit of SNeII should always be higher than $40 M_{\odot}$ because even the model with the highest SN rates overproduces stars. In this case however the predicted [O/Fe] is extremely high, so in tandem with such measures, some means of increasing the SNIa rate should be contrived, possibly through the relatively free parameters used to emulate the binary fraction.

5.4 Future Work

The RaDES project compares the properties of galaxies in subtly different environments and finds that loose groups galaxies have metallicity gradients and spheroid-to-disc ratios that are indistinguishable from those of the field galaxies. The effect of unique events in the galaxies history, like a merger occurring early or late with any

of a variety of trajectories and gas contents, utterly dominates over the effect of the local environment. The velocity dispersion however seems to exhibit characteristic steps more commonly when they inhabit a loose group environment than they would in the field. With the unanswered question of why this is the case hanging over the results it would be interesting to continue this experiment with a larger sample of galaxies to confirm the result and aid in interpreting it. A possible explanation is that these environments carry an inherently increased merger severity which is perhaps due to the ambient potential or from smaller mergers. It is also true that the method by which mergers are detected in this work may be unable to identify merger events with enough precision to examine this aspect and thus two approaches are suggested. Either dark matter only simulations should be conducted in greater numbers and with greater resolution to look for evidence of increased minor merger rates in these environment or even better the mergers could be redefined in terms of real interaction with the baryonic disc itself.

While not a specific concept for future work, we would like to note here that there is an ‘ugly duckling problem’ with simulations of single galaxies: the individuality of galaxies in similar environments poses the question, is this a duck or a swan? While an educated guess can be made about the properties that a given simulated galaxy should fit when ‘optimal’ parameters are used, it is quite impossible to be certain about which observational counterpart is most appropriate for comparison. Put another way, how do we guarantee that the simulated merger/accretion history is the same as the galaxy we are trying to fit? The only acceptable recourse is to abandon the attempt to replicate individual galaxy properties at all and instead widen the search to explore the parameter space in terms of scaling relations of galaxy populations. Fitting the behaviour of simulated galaxy populations to observed ones, particularly in terms of the dispersion in properties such as metallicity

gradients, brightness, colour and dynamics, will be far more instructive in the nature and influence of cosmological formation than will studying individual galaxies in detail. Of course recovering all properties of galaxy populations is the holy grail of theoretical studies of galaxy formation and is by no means easy, but we are now approaching a time when computational resources and techniques will make such undertakings, while still daunting, at least feasible.

The work in Chapter 3 on changing abundance gradients as the galaxy evolves provides some insight into inside-out formation and the connection between the star formation profile and the metallicity gradient. For the large sample size of the RaDES galaxies the evolution of the young stellar gradient through time is demonstrated to be quite subtle with minimal perturbations. In contrast, the several MUGS galaxies have extremely volatile gradients with jumps of $0.05\text{--}0.1$ dex kpc^{-1} between adjacent snapshots. It is clear from Figure 3.9 that the number of snapshots is not adequate to resolve this temporal evolution of the metallicity gradient. It would be extremely interesting to examine these large fluctuations in the gradient and connect them to the merger history and star formation profile.

The significant differences in the high redshift metallicity gradients of the galaxies from different simulations and models is also intriguing. It is at least partly due to differences in the particular implementations used. There are limited observational constraints on metallicity gradients at high redshift with only Yuan et al. (2011) and Cresci et al. (2010) providing observations and then with widely differing results. Yuan et al. (2011) finds a negative gradient that is much steeper than those in the local Universe and Cresci et al. (2010) finds positive gradients. It is clear that the astrophysics community will learn a great deal from continued observational efforts in this field. From the theoretical side we would suggest an examination of high redshift metallicity gradients in cosmological simulations; varying simulation

parameters for a single numerical simulation code to find if the star formation efficiency and threshold or the feedback treatment have a strong effect. This kind of theoretical study is perhaps not entirely enlightening at the present time, but as more high redshift galaxies become resolvable this may be a useful constraint if the large variations found here are caused either by parametrised sub-grid physics or a resolved phenomenon.

With the work in Chapter 4 being the creation of a new code there are many options for applying the code to a wide variety of situations. The most obvious is extending the experimentation of the feedback table to explore different (more contemporary) nucleosynthesis models as those used for the simulations presented here are becoming a little dated. One example is the Karakas (2010) model for AGB stars that predicts less carbon than does the van den Hoek & Groenewegen (1997) model. A particularly intriguing avenue of investigation is the possibility of a metallicity variant IMF. The notion of a variable IMF is discussed in §4.2.1 and the feedback table used by RAMSES-CH provides the perfect method for exploring this possibility. The SNe/AGB feedback rates are already a function of progenitor metallicity (albeit very weakly) via the metallicity dependence of the stellar lifetimes. By altering the IMF so that it is more top-heavy in low metallicity star particles the SN rate will increase at early times, perhaps having the desirable effect of reducing the bulge fraction of the simulated galaxy. Investigation of whether this effect is helpful in recovering galaxy properties would be extremely interesting given the uncertainty in measurements of the IMF in different environments.

Perhaps the most important lesson learned from this work is that there may not be a single chemical evolution model that is capable of uniquely reproducing galactic SN rates or elemental abundances (at least when considering only oxygen and iron abundances). Future work on this topic will choose the chemical evolution model carefully, adjusting the binary fraction (to adjust SNIa rates) and the upper

mass limit on SNeII to mediate the effect of the particular IMF chosen. In these cases the models may be differentiated through the abundance of silicon or iron relative to oxygen. This is made possible by the reduced abundance of these iron-peak elements in SNII above $30 M_{\odot}$ relative to lower mass SNII progenitors in the Woosley & Weaver (1995) nucleosynthesis models.

The added sophistication to the subgrid physics model in these simulations has illuminated an inherent problem in trying to constrain the IMF using the SN rate of the galaxy. To simulate a galaxy that has properties close to those observed we require that the SN rate be constrained, but once we realise that SN rate per unit mass is in fact too low due to the excessive stellar mass in galaxy simulations do we opt for an IMF that overestimates the galactic SN rate? The ideal solution is of course to conceive of a way of fitting the stellar mass fraction first. This is a long standing issue in galaxy simulations, although tantalising results are being obtained, for instance in Brook et al. (2012) where, in addition to SN feedback (motivated by a Chabrier (2003) IMF, similar to the Kroupa (2001) IMF of the fiducial model in Chapter 4), some additional energy is injected to account for radiation energy from massive stars. The amount of energy contributed by massive stars in the model is greater than that by SNeII at $2 \times 10^{49} \text{ erg } M_{\odot}^{-1}$ in the first 4.5 Myr. This figure gives one an idea of how much more energy is required for simulations to meet scaling relations. We offer no details here about how this may be achieved but simply warn that beyond making an (extremely) informed guess about absolute SN rates (the ratio of SNeII to SNeIa is still useful) it will be necessary to reproduce the stellar-to-halo mass fraction to constrain the IMF using this method.

It is fortunate that the benefits the new code offers are not entirely diminished by the issue we have just described. The great novelty of this approach is that it is the first cosmological AMR code to include chemistry in this way, and as such includes turbulent effects and metal mixing in the gas quite naturally. As long as the

production rate of the elements is correct, i.e. while the global SN rates match observed values, then gas abundances, metallicity gradients and intergalactic medium enrichment may be studied. Chemical tagging also becomes a viable topic of study using RAMSES-CH, the ability to trace stars to their birth location making it possible to decompose a galaxy into accreted and in-situ forming stars and to consider the effect of migration on broadening the metallicity distribution of stars. All these topics are of interest in light of the truly vast quantities of spectroscopic and phase space data that will come from LAMOST, Gaia and the GREAT Chemodynamical Survey.

Bibliography

- Abadi, M. G., Navarro, J. F., Steinmetz, M., & Eke, V. R. 2003, *Astrophys. J.*, 597, 21
- Abel, T., Bryan, G. L., & Norman, M. L. 2000, *Astrophys. J.*, 540, 39
- Afflerbach, A., Churchwell, E., & Werner, M. W. 1997, *Astrophys. J.*, 478, 190
- Agertz, O., Moore, B., Stadel, J., et al. 2007, *Mon. Not. Roy. Astron. Soc.*, 380, 963
- Anders, E. & Grevesse, N. 1989, *Geochimica et Cosmochimica Acta*, 53, 197
- Andrievsky, S. M., Kovtyukh, V. V., Luck, R. E., et al. 2002, *Astron. Astrophys.*, 381, 32
- Andrievsky, S. M., Luck, R. E., Martin, P., & Lépine, J. R. D. 2004, *Astron. Astrophys.*, 413, 159
- Arnett, W. D. 1978, *Astrophys. J.*, 219, 1008
- Asplund, M., Grevesse, N., Sauval, A. J., & Scott, P. 2009, *Ann. Rev. Astron. Astrophys.*, 47, 481
- Asplund, M., Nordlund, Å., Trampedach, R., Allende Prieto, C., & Stein, R. F. 2000, *Astron. Astrophys.*, 359, 729
- Aubert, D., Pichon, C., & Colombi, S. 2004, *Mon. Not. Roy. Astron. Soc.*, 352, 376

- Baade, W. 1944, *Astrophys. J.*, 100, 137
- Bailin, J. & Harris, W. E. 2008, *Astrophys. J.*, 681, 225
- Bailin, J., Kawata, D., Gibson, B. K., et al. 2005, *Astrophys. J. Letters*, 627, L17
- Baldry, I. K., Glazebrook, K., & Driver, S. P. 2008, *Mon. Not. Roy. Astron. Soc.*, 388, 945
- Balogh, M., Eke, V., Miller, C., et al. 2004a, *Mon. Not. Roy. Astron. Soc.*, 348, 1355
- Balogh, M. L., Baldry, I. K., Nichol, R., et al. 2004b, *Astrophys. J. Letters*, 615, L101
- Bamford, S. P., Nichol, R. C., Baldry, I. K., et al. 2009, *Mon. Not. Roy. Astron. Soc.*, 393, 1324
- Barnes, J. E. 2002, *Mon. Not. Roy. Astron. Soc.*, 333, 481
- Barnes, J. E. & Hernquist, L. 1996, *Astrophys. J.*, 471, 115
- Bartašiūtė, S., Aslan, Z., Boyle, R. P., et al. 2003, *Baltic Astronomy*, 12, 539
- Barton, E. J., Geller, M. J., & Kenyon, S. J. 2000, *Astrophys. J.*, 530, 660
- Bate, M. R. 2009, *Mon. Not. Roy. Astron. Soc.*, 397, 232
- Bazan, G. & Mathews, G. J. 1990, *Astrophys. J.*, 354, 644
- Bekki, K. & Couch, W. J. 2011, *Mon. Not. Roy. Astron. Soc.*, 415, 1783
- Bensby, T., Feltzing, S., Lundström, I., & Ilyin, I. 2005, *Astron. Astrophys.*, 433, 185
- Berger, M. J. & Collela, P. 1989, *Journal of Computational Physics*, 82, 64

- Berger, M. J. & Olinger, J. 1984, *Journal of Computational Physics*, 53, 484
- Bertschinger, E. 1998, *Ann. Rev. Astron, Astrophys.*, 36, 599
- Biemont, E., Baudoux, M., Kurucz, R. L., Ansbacher, W., & Pinnington, E. H. 1991, *Astron. Astrophys.*, 249, 539
- Bigiel, F., Leroy, A., Walter, F., et al. 2008, *Astron. J.*, 136, 2846
- Blumenthal, G. R., Faber, S. M., Primack, J. R., & Rees, M. J. 1984, *Nature*, 311, 517
- Bournaud, F., Jog, C. J., & Combes, F. 2005, *Astron. Astrophys.*, 437, 69
- Bovy, J., Rix, H.-W., & Hogg, D. W. 2012, *Astrophys. J.*, 751, 131
- Brook, C. B., Kawata, D., Gibson, B. K., & Flynn, C. 2004, *Mon. Not. Roy. Astron. Soc.*, 349, 52
- Brook, C. B., Stinson, G., Gibson, B. K., Wadsley, J., & Quinn, T. 2012, *Mon. Not. Roy. Astron. Soc.*, 3222
- Brooks, A. M., Solomon, A. R., Governato, F., et al. 2011, *Astrophys. J.*, 728, 51
- Bryan, G. L. & Norman, M. L. 1997, ArXiv Astrophysics e-prints
- Carbon, D. F., Barbuy, B., Kraft, R. P., Friel, E. D., & Suntzeff, N. B. 1987, *Pub. Astron. Soc. Pac.*, 99, 335
- Carigi, L. 1994, *Astrophys. J.*, 424, 181
- Carrera, R., Gallart, C., Aparicio, A., et al. 2008, *Astron. J.*, 136, 1039
- Castellani, V., Degl'Innocenti, S., & Prada Moroni, P. G. 2001, *Mon. Not. Roy. Astron. Soc.*, 320, 66

- Cayrel, R., Depagne, E., Spite, M., et al. 2004, *Astron. Astrophys.*, 416, 1117
- Cen, R. & Ostriker, J. P. 1992, *Astrophys. J. Letters*, 399, L113
- Chabrier, G. 2003, *Astrophys. J. Letters*, 586, L133
- Chen, L., Hou, J. L., & Wang, J. J. 2003, *Astron. J.*, 125, 1397
- Chiappini, C., Matteucci, F., & Gratton, R. 1997, *Astrophys. J.*, 477, 765
- Chiappini, C., Matteucci, F., & Romano, D. 2001, *Astrophys. J.*, 554, 1044
- Chieffi, A. & Limongi, M. 2004, *Astrophys. J.*, 608, 405
- Chiosi, C. & Caimmi, R. 1979, *Astron. Astrophys.*, 80, 234
- Clowe, D., Gonzalez, A., & Markevitch, M. 2004, *Astrophys. J.*, 604, 596
- Cole, S. 1991, *Astrophys. J.*, 367, 45
- Collela, P. 1990, *Journal of Computational Physics*, 87, 171
- Cooper, M. C., Tremonti, C. A., Newman, J. A., & Zabludoff, A. I. 2008, *Mon. Not. Roy. Astron. Soc.*, 390, 245
- Couchman, H. M. P., Thomas, P. A., & Pearce, F. R. 1995, *Astrophys. J.*, 452, 797
- Cox, T. J., Dutta, S. N., Di Matteo, T., et al. 2006, *Astrophys. J.*, 650, 791
- Cresci, G., Mannucci, F., Maiolino, R., et al. 2010, *Nature*, 467, 811
- Dalcanton, J. J. & Bernstein, R. A. 2002, *Astron. J.*, 124, 1328
- David, L. P., Jones, C., & Forman, W. 1996, *Astrophys. J.*, 473, 692
- de Blok, W. J. G. 2010, *Advances in Astronomy*, 2010

- Deharveng, L., Peña, M., Caplan, J., & Costero, R. 2000, *Mon. Not. Roy. Astron. Soc.*, 311, 329
- Dehnen, W. & Read, J. I. 2011, *European Physical Journal Plus*, 126, 55
- Delahaye, F. & Pinsonneault, M. H. 2006, *Astrophys. J.*, 649, 529
- Delahaye, F., Pinsonneault, M. H., Pinsonneault, L., & Zeippen, C. J. Zeippen, C. J. 2010, ArXiv e-prints
- Devriendt, J. E. G. & Guiderdoni, B. 2000, *Astron. Astrophys.*, 363, 851
- Di Matteo, P., Lehnert, M. D., Qu, Y., & van Driel, W. 2011, *Astron. Astrophys.*, 525, L3
- Doherty, C. L., Siess, L., Lattanzio, J. C., & Gil-Pons, P. 2010, *Mon. Not. Roy. Astron. Soc.*, 401, 1453
- Donzelli, C. J. & Pastoriza, M. G. 2000, *Astron. J.*, 120, 189
- Dors, Jr., O. L. & Copetti, M. V. F. 2005, *Astron. Astrophys.*, 437, 837
- Dressler, A. 1980, *Astrophys. J.*, 236, 351
- Dressler, A., Oemler, Jr., A., Couch, W. J., et al. 1997, *Astrophys. J.*, 490, 577
- Dubois, Y. & Teyssier, R. 2008, *Astron. Astrophys.*, 477, 79
- Dutil, Y. & Roy, J.-R. 1999, *Astrophys. J.*, 516, 62
- Edvardsson, B., Andersen, J., Gustafsson, B., et al. 1993, *Astron. Astrophys.*, 275, 101
- Eggen, O. J., Lynden-Bell, D., & Sandage, A. R. 1962, *Astrophys. J.*, 136, 748
- Ellison, S. L., Patton, D. R., Simard, L., & McConnachie, A. W. 2008, *Astron. J.*, 135, 1877

- Ellison, S. L., Simard, L., Cowan, N. B., et al. 2009, *Mon. Not. Roy. Astron. Soc.*, 396, 1257
- Esteban, C., García-Rojas, J., Peimbert, M., et al. 2005, *Astrophys. J. Letters*, 618, L95
- Fabbiano, G., Baldi, A., King, A. R., et al. 2004, *Astrophys. J. Letters*, 605, L21
- Fall, S. M. & Efstathiou, G. 1980, *Mon. Not. Roy. Astron. Soc.*, 193, 189
- Feltzing, S., Gilmore, G., & Wyse, R. F. G. 1999, *Astrophys. J. Letters*, 516, L17
- Ferland, G. J., Korista, K. T., Verner, D. A., et al. 1998, *Pub. Astron. Soc. Pac.*, 110, 761
- Few, C. G., Courty, S., Gibson, B. K., et al. 2012, *Mon. Not. Roy. Astron. Soc.*, L463
- Flores, R. A. & Primack, J. R. 1994, *Astrophys. J. Letters*, 427, L1
- François, P., Matteucci, F., Cayrel, R., et al. 2004, *Astron. Astrophys.*, 421, 613
- Franx, M. & Illingworth, G. 1990, *Astrophys. J. Letters*, 359, L41
- Fryxell, B., Olson, K., Ricker, P., et al. 2000, *Astrophys. J. Supple.*, 131, 273
- Fu, J., Hou, J. L., Yin, J., & Chang, R. X. 2009, *Astrophys. J.*, 696, 668
- Galarza, V. C., Waltherbos, R. A. M., & Braun, R. 1999, *Astron. J.*, 118, 2775
- Garnett, D. R., Shields, G. A., Skillman, E. D., Sagan, S. P., & Dufour, R. J. 1997, *Astrophys. J.*, 489, 63
- Gibson, B. K. 1997, *Mon. Not. Roy. Astron. Soc.*, 290, 471
- Gilmore, G. & Reid, N. 1983, *Mon. Not. Roy. Astron. Soc.*, 202, 1025

- Gilmore, G., Wyse, R. F. G., & Kuijken, K. 1989, *Ann. Rev. Astron. Astrophys.*, 27, 555
- Gingold, R. A. & Monaghan, J. J. 1977, *Mon. Not. Roy. Astron. Soc.*, 181, 375
- Giovagnoli, A. & Tosi, M. 1995, *Mon. Not. Roy. Astron. Soc.*, 273, 499
- Giuricin, G., Limboz Tektunali, F., Monaco, P., Mardirossian, F., & Mezzetti, M. 1995, *Astrophys. J.*, 450, 41
- Gnedin, N. Y. 1995, *Astrophys. J. Supple.*, 97, 231
- Gnedin, N. Y. & Bertschinger, E. 1996, *Astrophys. J.*, 470, 115
- Gómez, P. L., Nichol, R. C., Miller, C. J., et al. 2003, *Astrophys. J.*, 584, 210
- Goodwin, S. P. & Kouwenhoven, M. B. N. 2009, *Mon. Not. Roy. Astron. Soc.*, 397, L36
- Gottlöber, S., Klypin, A., & Kravtsov, A. V. 2001, *Astrophys. J.*, 546, 223
- Gottlöber, S., Hoffman, Y., & Yepes, G. 2010, ArXiv e-prints
- Governato, F., Mayer, L., Wadsley, J., et al. 2004, *Astrophys. J.*, 607, 688
- Governato, F., Willman, B., Mayer, L., et al. 2007, *Mon. Not. Roy. Astron. Soc.*, 374, 1479
- Gratton, R. G., Carretta, E., Claudi, R., Lucatello, S., & Barbieri, M. 2003, *Astron. Astrophys.*, 404, 187
- Greggio, L. & Renzini, A. 1983, *Astron. Astrophys.*, 118, 217
- Grevesse, N. & Sauval, A. J. 1998, *Space Sci. Rev.*, 85, 161
- Guedes, J., Callegari, S., Madau, P., & Mayer, L. 2011, *Astrophys. J.*, 742, 76

- Guo, Q., White, S., Li, C., & Boylan-Kolchin, M. 2010, *Mon. Not. Roy. Astron. Soc.*, 404, 1111
- Guzik, J. A., Watson, L. S., & Cox, A. N. 2005, *Astrophys. J.*, 627, 1049
- Haardt, F. & Madau, P. 1996, *Astrophys. J.*, 461, 20
- Hachisu, I., Kato, M., & Nomoto, K. 1999, *Astrophys. J.*, 522, 487
- Hartwick, F. D. A. 1976, *Astrophys. J.*, 209, 418
- Hatton, S., Devriendt, J. E. G., Ninin, S., et al. 2003, *Mon. Not. Roy. Astron. Soc.*, 343, 75
- Hernquist, L. & Katz, N. 1989, *Astrophys. J. Supple.*, 70, 419
- Hockney, R. W. & Eastwood, J. W. 1981, *Computer Simulation Using Particles*
- Holmberg, J., Nordström, B., & Andersen, J. 2007, *Astron. Astrophys.*, 475, 519
- Holweger, H., Bard, A., Kock, M., & Kock, A. 1991, *Astron. Astrophys.*, 249, 545
- Hopkins, P. F., Somerville, R. S., Cox, T. J., et al. 2009, *Mon. Not. Roy. Astron. Soc.*, 397, 802
- House, E. L., Brook, C. B., Gibson, B. K., et al. 2011, *Mon. Not. Roy. Astron. Soc.*, 415, 2652
- Hoversten, E. A. & Glazebrook, K. 2008, *Astrophys. J.*, 675, 163
- Huchra, J. & Brodie, J. 1987, *Astron. J.*, 93, 779
- Ibata, R. A., Richer, H. B., Gilliland, R. L., & Scott, D. 1999, *Astrophys. J. Letters*, 524, L95
- Iben, Jr., I. & Truran, J. W. 1978, *Astrophys. J.*, 220, 980

- Iben, Jr., I. & Tutukov, A. V. 1984, *Astrophys. J. Supple.*, 54, 335
- Iwamoto, K., Brachwitz, F., Nomoto, K., et al. 1999, *Astrophys. J. Supple.*, 125, 439
- Izzard, R. G., Tout, C. A., Karakas, A. I., & Pols, O. R. 2004, *Mon. Not. Roy. Astron. Soc.*, 350, 407
- Jeans, J. H. 1902, Royal Society of London Philosophical Transactions Series A, 199, 1
- Jeffries, R. D., Naylor, T., Devey, C. R., & Totten, E. J. 2004, *Mon. Not. Roy. Astron. Soc.*, 351, 1401
- Jessop, C., Duncan, M., & Chau, W. Y. 1994, *Journal of Computational Physics*, 115, 339
- Jones, T., Ellis, R., Jullo, E., & Richard, J. 2010, *Astrophys. J. Letters*, 725, L176
- Jones, T., Ellis, R. S., Richard, J., & Jullo, E. 2012, ArXiv e-prints
- Jonsson, P. 2006, *Mon. Not. Roy. Astron. Soc.*, 372, 2
- Karakas, A. & Lattanzio, J. C. 2007, *Pub. Astron. Soc. Australia*, 24, 103
- Karakas, A. I. 2010, *Mon. Not. Roy. Astron. Soc.*, 403, 1413
- Katz, N. 1992, *Astrophys. J.*, 391, 502
- Katz, N., Weinberg, D. H., & Hernquist, L. 1996, *Astrophys. J. Supple.*, 105, 19
- Kaufer, A., Szeifert, T., Krenzlin, R., Baschek, B., & Wolf, B. 1994, *Astron. Astrophys.*, 289, 740
- Kawata, D. 2001, *Astrophys. J.*, 558, 598

- Kawata, D. & Gibson, B. K. 2003, *Mon. Not. Roy. Astron. Soc.*, 340, 908
- Kawata, D., Gibson, B. K., & Windhorst, R. A. 2004, *Mon. Not. Roy. Astron. Soc.*, 354, 387
- Kay, S. T., Pearce, F. R., Frenk, C. S., & Jenkins, A. 2002, *Mon. Not. Roy. Astron. Soc.*, 330, 113
- Kay, S. T., Pearce, F. R., Jenkins, A., et al. 2000, *Mon. Not. Roy. Astron. Soc.*, 316, 374
- Kazantzidis, S., Bullock, J. S., Zentner, A. R., Kravtsov, A. V., & Moustakas, L. A. 2008, *Astrophys. J.*, 688, 254
- Kennicutt, Jr., R. C. 1998, *Astrophys. J.*, 498, 541
- Kewley, L. J., Geller, M. J., & Barton, E. J. 2006a, *Astron. J.*, 131, 2004
- Kewley, L. J., Geller, M. J., & Barton, E. J. 2006b, *Astron. J.*, 131, 2004
- Kewley, L. J., Rupke, D., Jabran Zahid, H., Geller, M. J., & Barton, E. J. 2010a, *Astrophys. J. Letters*, 721, L48
- Kewley, L. J., Rupke, D., Zahid, H. J., Geller, M. J., & Barton, E. J. 2010b, *Astrophys. J. Letters*, 721, L48
- Khokhlov, A. 1998, *Journal of Computational Physics*, 143, 519
- Klypin, A., Kravtsov, A. V., Bullock, J. S., & Primack, J. R. 2001, *Astrophys. J.*, 554, 903
- Klypin, A., Kravtsov, A. V., Valenzuela, O., & Prada, F. 1999, *Astrophys. J.*, 522, 82
- Kobayashi, C. 2004, *Mon. Not. Roy. Astron. Soc.*, 347, 740

- Kobayashi, C. & Nakasato, N. 2011, *Astrophys. J.*, 729, 16
- Kobayashi, C., Tsujimoto, T., & Nomoto, K. 2000, *Astrophys. J.*, 539, 26
- Kobayashi, C., Umeda, H., Nomoto, K., Tominaga, N., & Ohkubo, T. 2006, *Astrophys. J.*, 653, 1145
- Kodama, T. 1997, PhD thesis, Institute of Astronomy, Univ. Tokyo, (1997)
- Kodama, T. & Arimoto, N. 1997, *Astron. Astrophys.*, 320, 41
- Kormendy, J. & Djorgovski, S. 1989, *Ann. Rev. Astron. Astrophys.*, 27, 235
- Kravtsov, A. V. & Klypin, A. A. 1999, *Astrophys. J.*, 520, 437
- Kravtsov, A. V., Klypin, A. A., & Khokhlov, A. M. 1997, *Astrophys. J. Supple.*, 111, 73
- Kroupa, P. 2001, *Mon. Not. Roy. Astron. Soc.*, 322, 231
- Kroupa, P., Tout, C. A., & Gilmore, G. 1993, *Mon. Not. Roy. Astron. Soc.*, 262, 545
- Lacey, C. & Silk, J. 1991, *Astrophys. J.*, 381, 14
- Lambas, D. G., Tissera, P. B., Alonso, M. S., & Coldwell, G. 2003, *Mon. Not. Roy. Astron. Soc.*, 346, 1189
- Larson, D., Dunkley, J., Hinshaw, G., et al. 2011, *Astrophys. J. Supple.*, 192, 16
- Larson, R. B. 1972, *Nature*, 236, 21
- Larson, R. B. 1998, *Mon. Not. Roy. Astron. Soc.*, 301, 569
- Leauthaud, A., Tinker, J., Bundy, K., et al. 2012, *Astrophys. J.*, 744, 159

- Leitherer, C., Schaerer, D., Goldader, J. D., et al. 1999, *Astrophys. J. Supple.*, 123, 3
- Lemasle, B., François, P., Bono, G., et al. 2007, *Astron. Astrophys.*, 467, 283
- Lewis, I., Balogh, M., De Propriis, R., et al. 2002, *Mon. Not. Roy. Astron. Soc.*, 334, 673
- Lia, C., Portinari, L., & Carraro, G. 2002, *Mon. Not. Roy. Astron. Soc.*, 330, 821
- Libeskind, N. I., Knebe, A., Hoffman, Y., et al. 2011, *Mon. Not. Roy. Astron. Soc.*, 411, 1525
- Lilly, S. J., Le Fevre, O., Hammer, F., & Crampton, D. 1996, *Astrophys. J. Letters*, 460, L1
- Limongi, M. & Chieffi, A. 2003, *Astrophys. J.*, 592, 404
- Loewenstein, M. 2006, *Astrophys. J.*, 648, 230
- Lotz, J. M., Jonsson, P., Cox, T. J., & Primack, J. R. 2010, *Mon. Not. Roy. Astron. Soc.*, 404, 590
- Lucy, L. B. 1977, *Astron. J.*, 82, 1013
- Macciò, A. V., Paduroiu, S., Anderhalden, D., Schneider, A., & Moore, B. 2012, *Mon. Not. Roy. Astron. Soc.*, 3204
- Maciel, W. J., Costa, R. D. D., & Uchida, M. M. M. 2003, *Astron. Astrophys.*, 397, 667
- Maeder, A. 1992, *Astron. Astrophys.*, 264, 105
- Maeder, A. & Meynet, G. 1989, *Astron. Astrophys.*, 210, 155

- Magrini, L., Vílchez, J. M., Mampaso, A., Corradi, R. L. M., & Leisy, P. 2007, *Astron. Astrophys.*, 470, 865
- Mandelbaum, R., Seljak, U., Kauffmann, G., Hirata, C. M., & Brinkmann, J. 2006, *Mon. Not. Roy. Astron. Soc.*, 368, 715
- Mannucci, F., Della Valle, M., & Panagia, N. 2006, *Mon. Not. Roy. Astron. Soc.*, 370, 773
- Mannucci, F., Maoz, D., Sharon, K., et al. 2008, *Mon. Not. Roy. Astron. Soc.*, 383, 1121
- Marigo, P. 2001, *Astron. Astrophys.*, 370, 194
- Marigo, P., Girardi, L., Bressan, A., et al. 2008, *Astron. Astrophys.*, 482, 883
- Márquez, I., Masegosa, J., Moles, M., et al. 2002, *Astron. Astrophys.*, 393, 389
- Marsakov, V. A. & Borkova, T. V. 2005, *Astronomy Letters*, 31, 515
- Marsakov, V. A. & Borkova, T. V. 2006, *Astronomy Letters*, 32, 376
- Martig, M. & Bournaud, F. 2008, *Mon. Not. Roy. Astron. Soc.*, 385, L38
- Martinelli, A. & Matteucci, F. 2000, *Astron. Astrophys.*, 353, 269
- Martínez, H. J., Coenda, V., & Muriel, H. 2008, *Mon. Not. Roy. Astron. Soc.*, 391, 585
- Martínez-Serrano, F. J., Domínguez-Tenreiro, R., & Mollá, M. 2008a, in IAU Symposium, Vol. 245, IAU Symposium, ed. M. Bureau, E. Athanassoula, & B. Barbuy, 35–36
- Martínez-Serrano, F. J., Serna, A., Domínguez-Tenreiro, R., & Mollá, M. 2008b, *Mon. Not. Roy. Astron. Soc.*, 388, 39

- Martinez-Vaquero, L. A., Yepes, G., Hoffman, Y., Gottlöber, S., & Sivan, M. 2009, *Mon. Not. Roy. Astron. Soc.*, 397, 2070
- Mathews, W. G. 1978, *Astrophys. J.*, 219, 413
- Matteucci, F. & Francois, P. 1989, *Mon. Not. Roy. Astron. Soc.*, 239, 885
- McGee, S. L., Balogh, M. L., Henderson, R. D. E., et al. 2008, *Mon. Not. Roy. Astron. Soc.*, 387, 1605
- Méndez, R. A. & Minniti, D. 2000, *Astrophys. J.*, 529, 911
- Metzler, C. A. & Evrard, A. E. 1994, *Astrophys. J.*, 437, 564
- Meusinger, H., Stecklum, B., & Reimann, H. 1991, *Astron. Astrophys.*, 245, 57
- Michel-Dansac, L., Lambas, D. G., Alonso, M. S., & Tissera, P. 2008, *Mon. Not. Roy. Astron. Soc.*, 386, L82
- Mollá, M. & Díaz, A. I. 2005, *Mon. Not. Roy. Astron. Soc.*, 358, 521
- Mollá, M., Ferrini, F., & Diaz, A. I. 1997, *Astrophys. J.*, 475, 519
- Mollá, M., Hardy, E., & Beauchamp, D. 1999, *Astrophys. J.*, 513, 695
- Monaghan, J. J. 1992, *Ann. Rev. Astron, Astrophys.*, 30, 543
- Montuori, M., Di Matteo, P., Lehnert, M. D., Combes, F., & Semelin, B. 2010, *Astron. Astrophys.*, 518, A56+
- Moore, B., Ghigna, S., Governato, F., et al. 1999, *Astrophys. J. Letters*, 524, L19
- Moore, B., Katz, N., Lake, G., Dressler, A., & Oemler, A. 1996, *Nature*, 379, 613
- Moster, B. P., Somerville, R. S., Maulbetsch, C., et al. 2010, *Astrophys. J.*, 710, 903

- Myers, A. T., Krumholz, M. R., Klein, R. I., & McKee, C. F. 2011, *Astrophys. J.*, 735, 49
- Nagamine, K. 2002, *Astrophys. J.*, 564, 73
- Nagashima, M., Lacey, C. G., Okamoto, T., et al. 2005, *Mon. Not. Roy. Astron. Soc.*, 363, L31
- Navarro, J. F., Abadi, M. G., Venn, K. A., Freeman, K. C., & Anguiano, B. 2011, *Mon. Not. Roy. Astron. Soc.*, 89
- Navarro, J. F. & Benz, W. 1991, *Astrophys. J.*, 380, 320
- Navarro, J. F., Frenk, C. S., & White, S. D. M. 1995, *Mon. Not. Roy. Astron. Soc.*, 275, 56
- Navarro, J. F. & Steinmetz, M. 1997, *Astrophys. J.*, 478, 13
- Nikolic, B., Cullen, H., & Alexander, P. 2004, *Mon. Not. Roy. Astron. Soc.*, 355, 874
- Nomoto, K., Iwamoto, K., Nakasato, N., et al. 1997, *Nuclear Physics A*, 621, 467
- Nomoto, K., Thielemann, F.-K., & Wheeler, J. C. 1984, *Astrophys. J. Letters*, 279, L23
- Nordström, B., Mayor, M., Andersen, J., et al. 2004, *Astron. Astrophys.*, 418, 989
- Okamoto, T., Nemmen, R. S., & Bower, R. G. 2008, *Mon. Not. Roy. Astron. Soc.*, 385, 161
- Oppenheimer, B. D. & Davé, R. 2008, *Mon. Not. Roy. Astron. Soc.*, 387, 577
- O'Shea, B. W., Nagamine, K., Springel, V., Hernquist, L., & Norman, M. L. 2005, *Astrophys. J. Supple.*, 160, 1

- Ostriker, J. P. & Peebles, P. J. E. 1973, *Astrophys. J.*, 186, 467
- Padoan, P., Nordlund, A., & Jones, B. J. T. 1997, *Mon. Not. Roy. Astron. Soc.*, 288, 145
- Padovani, P. & Matteucci, F. 1993, *Astrophys. J.*, 416, 26
- Pagel, B. E. J. 1997, *Nucleosynthesis and Chemical Evolution of Galaxies* (Cambridge University Press)
- Pagel, B. E. J. & Patchett, B. E. 1975, *Mon. Not. Roy. Astron. Soc.*, 172, 13
- Peebles, P. J. E. 1969, *Astrophys. J.*, 155, 393
- Peebles, P. J. E. 1980, *The large-scale structure of the universe*
- Peirani, S. 2010, *Mon. Not. Roy. Astron. Soc.*, 407, 1487
- Peirani, S., Jung, I., Silk, J., & Pichon, C. 2012, ArXiv e-prints
- Peletier, R. F., Davies, R. L., Illingworth, G. D., Davis, L. E., & Cawson, M. 1990, *Astron. J.*, 100, 1091
- Pen, U.-L. 1995, *Astrophys. J. Supple.*, 100, 269
- Perez, J., Michel-Dansac, L., & Tissera, P. B. 2011, *Mon. Not. Roy. Astron. Soc.*, 1286
- Persic, M., Salucci, P., & Stel, F. 1996, *Mon. Not. Roy. Astron. Soc.*, 281, 27
- Pflamm-Altenburg, J. & Kroupa, P. 2008, *Nature*, 455, 641
- Pilkington, K., Few, C. G., Gibson, B. K., et al. 2012a, *Astron. Astrophys.*, 540, A56

- Pilkington, K. & Gibson, B. K. 2012, in Galactic Archaeology: Near Field Cosmology and the Formation of the Milky Way, ed. W. Aoki, Astronomical Society of the Pacific Conference Series, in press
- Pilkington, K., Gibson, B. K., Brook, C. B., et al. 2012b, ArXiv e-prints
- Pinsonneault, M. H. & Delahaye, F. 2009, *Astrophys. J.*, 704, 1174
- Pipino, A., Devriendt, J. E. G., Thomas, D., Silk, J., & Kaviraj, S. 2009, *Astron. Astrophys.*, 505, 1075
- Pontzen, A. & Governato, F. 2012, *Mon. Not. Roy. Astron. Soc.*, 421, 3464
- Portinari, L., Chiosi, C., & Bressan, A. 1998, *Astron. Astrophys.*, 334, 505
- Portinari, L., Sommer-Larsen, J., & Tantaló, R. 2004, *Mon. Not. Roy. Astron. Soc.*, 347, 691
- Prantzos, N. & Aubert, O. 1995, *Astron. Astrophys.*, 302, 69
- Prantzos, N. & Boissier, S. 2000, *Mon. Not. Roy. Astron. Soc.*, 313, 338
- Price, D. J. 2012, *Mon. Not. Roy. Astron. Soc.*, 420, L33
- Queyrel, J., Contini, T., Kissler-Patig, M., et al. 2012, *Astron. Astrophys.*, 539, A93
- Quilis, V. 2004, *Mon. Not. Roy. Astron. Soc.*, 352, 1426
- Quinn, P. J., Hernquist, L., & Fullagar, D. P. 1993, *Astrophys. J.*, 403, 74
- Rahimi, A., Kawata, D., Allende Prieto, C., et al. 2011, *Mon. Not. Roy. Astron. Soc.*, 725
- Rahimi, A., Kawata, D., Brook, C. B., & Gibson, B. K. 2010, *Mon. Not. Roy. Astron. Soc.*, 401, 1826

- Raiteri, C. M., Villata, M., & Navarro, J. F. 1996, *Astron. Astrophys.*, 315, 105
- Ramírez, I., Allende Prieto, C., & Lambert, D. L. 2007, *Astron. Astrophys.*, 465, 271
- Rasera, Y. & Teyssier, R. 2006, *Astron. Astrophys.*, 445, 1
- Reddy, B. E., Lambert, D. L., & Allende Prieto, C. 2006, *Mon. Not. Roy. Astron. Soc.*, 367, 1329
- Reddy, B. E., Tomkin, J., Lambert, D. L., & Allende Prieto, C. 2003, *Mon. Not. Roy. Astron. Soc.*, 340, 304
- Rieke, G. H., Lebofsky, M. J., Thompson, R. I., Low, F. J., & Tokunaga, A. T. 1980, *Astrophys. J.*, 238, 24
- Robertson, B., Bullock, J. S., Cox, T. J., et al. 2006, *Astrophys. J.*, 645, 986
- Robertson, B., Yoshida, N., Springel, V., & Hernquist, L. 2004, *Astrophys. J.*, 606, 32
- Rocha-Pinto, H. J. & Maciel, W. J. 1996, *Mon. Not. Roy. Astron. Soc.*, 279, 447
- Romano, D., Chiappini, C., Matteucci, F., & Tosi, M. 2005, *Astron. Astrophys.*, 430, 491
- Romano, D., Karakas, A. I., Tosi, M., & Matteucci, F. 2010, *Astron. Astrophys.*, 522, A32
- Romeo, A. D., Portinari, L., & Sommer-Larsen, J. 2005, *Mon. Not. Roy. Astron. Soc.*, 361, 983
- Rosen, A. & Bregman, J. N. 1995, *Astrophys. J.*, 440, 634
- Rubin, V. C. & Ford, Jr., W. K. 1970, *Astrophys. J.*, 159, 379

- Rudolph, A. L., Fich, M., Bell, G. R., et al. 2006, *Astrophys. J. Supple.*, 162, 346
- Rupke, D. S. N., Kewley, L. J., & Barnes, J. E. 2010a, *Astrophys. J. Letters*, 710, L156
- Rupke, D. S. N., Kewley, L. J., & Chien, L. 2010b, *Astrophys. J.*, 723, 1255
- Rupke, D. S. N., Veilleux, S., & Baker, A. J. 2008, *Astrophys. J.*, 674, 172
- Ryu, D., Ostriker, J. P., Kang, H., & Cen, R. 1993, *Astrophys. J.*, 414, 1
- Salpeter, E. E. 1955, *Astrophys. J.*, 121, 161
- Saltzman, J. 1994, *Journal of Computational Physics*, 115, 153
- Sánchez-Blázquez, P., Courty, S., Gibson, B. K., & Brook, C. B. 2009, *Mon. Not. Roy. Astron. Soc.*, 398, 591
- Sánchez-Blázquez, P., Ocvirk, P., Gibson, B. K., Pérez, I., & Peletier, R. F. 2011, *Mon. Not. Roy. Astron. Soc.*, 415, 709
- Sawala, T., Guo, Q., Scannapieco, C., Jenkins, A., & White, S. 2011, *Mon. Not. Roy. Astron. Soc.*, 413, 659
- Scalo, J. 1998, in *Astronomical Society of the Pacific Conference Series*, Vol. 142, *The Stellar Initial Mass Function (38th Herstmonceux Conference)*, ed. G. Gilmore & D. Howell, 201
- Scalo, J. M. 1986, *Fundamentals of Cosmic Physic*, 11, 1
- Scannapieco, C., Tissera, P. B., White, S. D. M., & Springel, V. 2005, *Mon. Not. Roy. Astron. Soc.*, 364, 552
- Scannapieco, C., Tissera, P. B., White, S. D. M., & Springel, V. 2008, *Mon. Not. Roy. Astron. Soc.*, 389, 1137

- Scannapieco, C., Wadepuhl, M., Parry, O. H., et al. 2012, *Mon. Not. Roy. Astron. Soc.*, 2970
- Scannapieco, C., White, S. D. M., Springel, V., & Tissera, P. B. 2009, *Mon. Not. Roy. Astron. Soc.*, 396, 696
- Schmidt, M. 1959, *Astrophys. J.*, 129, 243
- Schmidt, M. 1963, *Astrophys. J.*, 137, 758
- Searle, L. & Zinn, R. 1978, *Astrophys. J.*, 225, 357
- Sedov, L. I. 1993, *Similarity and Dimensional Methods in Mechanics*
- Shaver, P. A., McGee, R. X., Newton, L. M., Danks, A. C., & Pottasch, S. R. 1983, *Mon. Not. Roy. Astron. Soc.*, 204, 53
- Shen, S., Wadsley, J., & Stinson, G. 2010, *Mon. Not. Roy. Astron. Soc.*, 407, 1581
- Simon, J. D. & Geha, M. 2007, *Astrophys. J.*, 670, 313
- Simpson, J. P., Colgan, S. W. J., Rubin, R. H., Erickson, E. F., & Haas, M. R. 1995, *Astrophys. J.*, 444, 721
- Snaith, O. N., Gibson, B. K., Brook, C. B., et al. 2011, *Mon. Not. Roy. Astron. Soc.*, 415, 2798
- Sol Alonso, M., Michel-Dansac, L., & Lambas, D. G. 2010, *Astron. Astrophys.*, 514, A57
- Soubiran, C., Bienaymé, O., Mishenina, T. V., & Kovtyukh, V. V. 2008, *Astron. Astrophys.*, 480, 91
- Soubiran, C. & Girard, P. 2005, *Astron. Astrophys.*, 438, 139
- Springel, V. 2005, *Mon. Not. Roy. Astron. Soc.*, 364, 1105

- Springel, V. 2010a, *Mon. Not. Roy. Astron. Soc.*, 401, 791
- Springel, V. 2010b, *Ann. Rev. Astron, Astrophys.*, 48, 391
- Springel, V., White, S. D. M., Jenkins, A., et al. 2005, *Nature*, 435, 629
- Springel, V., Yoshida, N., & White, S. D. M. 2001, *New Astron.*, 6, 79
- Springob, C. M., Haynes, M. P., Giovanelli, R., & Kent, B. R. 2005, *Astrophys. J. Supple.*, 160, 149
- Stinson, G., Seth, A., Katz, N., et al. 2006, *Mon. Not. Roy. Astron. Soc.*, 373, 1074
- Stinson, G. S., Bailin, J., Couchman, H., et al. 2010, *Mon. Not. Roy. Astron. Soc.*, 408, 812
- Sutherland, R. S. & Dopita, M. A. 1993, *Astrophys. J. Supple.*, 88, 253
- Talbot, Jr., R. J. & Arnett, W. D. 1971, *Astrophys. J.*, 170, 409
- Tasker, E. J., Brunino, R., Mitchell, N. L., et al. 2008, *Mon. Not. Roy. Astron. Soc.*, 390, 1267
- Tegmark, M. 1996, *Astrophys. J. Letters*, 464, L35
- Tegmark, M. & Zaldarriaga, M. 2002, *Phys. Rev. D*, 66, 103508
- Teyssier, R. 2002, *Astron. Astrophys.*, 385, 337
- Teyssier, R., Moore, B., Martizzi, D., Dubois, Y., & Mayer, L. 2011, *Mon. Not. Roy. Astron. Soc.*, 414, 195
- Timmes, F. X., Woosley, S. E., & Weaver, T. A. 1995, *Astrophys. J. Supple.*, 98, 617
- Tinsley, B. M. 1980, *Fundamentals of Cosmic Physic*, 5, 287

- Tomkin, J., Lambert, D. L., & Balachandran, S. 1985, *Astrophys. J.*, 290, 289
- Tornatore, L., Borgani, S., Matteucci, F., Recchi, S., & Tozzi, P. 2004, *Mon. Not. Roy. Astron. Soc.*, 349, L19
- Toro, E. F. 1997, *Riemann Solvers And Numerical Methods for Fluid Dynamics: A Practical Introduction*
- Tosi, M. 1982, *Astrophys. J.*, 254, 699
- Tosi, M. 1996, in *Astronomical Society of the Pacific Conference Series*, Vol. 98, *From Stars to Galaxies: the Impact of Stellar Physics on Galaxy Evolution*, ed. C. Leitherer, U. Fritze-von-Alvensleben, & J. Huchra, 299–+
- Truelove, J. K., Klein, R. I., McKee, C. F., et al. 1997, *Astrophys. J. Letters*, 489, L179
- Trundle, C., Dufton, P. L., Lennon, D. J., Smartt, S. J., & Urbaneja, M. A. 2002, *Astron. Astrophys.*, 395, 519
- Tsujimoto, T. & Bekki, K. 2011, *Astron. Astrophys.*, 530, A78
- Tully, R. B. & Fisher, J. R. 1977, *Astron. Astrophys.*, 54, 661
- Twarog, B. A. 1980, *Astrophys. J.*, 242, 242
- Tweed, D., Devriendt, J., Blaizot, J., Colombi, S., & Slyz, A. 2009, *Astron. Astrophys.*, 506, 647
- Tyson, J. A., Wenk, R. A., & Valdes, F. 1990, *Astrophys. J. Letters*, 349, L1
- Valdarnini, R. 2003, *Mon. Not. Roy. Astron. Soc.*, 339, 1117
- van den Bergh, S. 1962, *Astron. J.*, 67, 486

- van den Hoek, L. B. & Groenewegen, M. A. T. 1997, *Astron. Astrophys. Suppl.*, 123, 305
- van Dokkum, P. G. 2008, *Astrophys. J.*, 674, 29
- van Zee, L., Salzer, J. J., Haynes, M. P., O'Donoghue, A. A., & Balonek, T. J. 1998, *Astron. J.*, 116, 2805
- Villalobos, Á. & Helmi, A. 2008, *Mon. Not. Roy. Astron. Soc.*, 391, 1806
- Wadsley, J. W., Stadel, J., & Quinn, T. 2004, *Nature*, 9, 137
- Wadsley, J. W., Veeravalli, G., & Couchman, H. M. P. 2008, *Mon. Not. Roy. Astron. Soc.*, 387, 427
- Webbink, R. F. 1984, *Astrophys. J.*, 277, 355
- Weinmann, S. M., van den Bosch, F. C., Yang, X., & Mo, H. J. 2006, *Mon. Not. Roy. Astron. Soc.*, 366, 2
- Whelan, J. & Iben, Jr., I. 1973, *Astrophys. J.*, 186, 1007
- White, S. D. M. & Rees, M. J. 1978, *Mon. Not. Roy. Astron. Soc.*, 183, 341
- Wiersma, R. P. C., Schaye, J., & Theuns, T. 2011, *Mon. Not. Roy. Astron. Soc.*, 732
- Wiersma, R. P. C., Schaye, J., Theuns, T., Dalla Vecchia, C., & Tornatore, L. 2009, *Mon. Not. Roy. Astron. Soc.*, 399, 574
- Woosley, S. E. & Weaver, T. A. 1995, *Astrophys. J. Supple.*, 101, 181
- Wyse, R. F. G. & Gilmore, G. 1992, *Astron. J.*, 104, 144
- Wyse, R. F. G. & Gilmore, G. 1995, *Astron. J.*, 110, 2771

- Yahagi, H. & Yoshii, Y. 2001, *Astrophys. J.*, 558, 463
- Yong, D., Carney, B. W., Teixeira de Almeida, M. L., & Pohl, B. L. 2006, *Astron. J.*, 131, 2256
- Yuan, T.-T., Kewley, L. J., Swinbank, A. M., Richard, J., & Livermore, R. C. 2011, *Astrophys. J. Letters*, 732, L14+
- Zaritsky, D., Kennicutt, Jr., R. C., & Huchra, J. P. 1994, *Astrophys. J.*, 420, 87
- Zolotov, A., Willman, B., Brooks, A. M., et al. 2010, *Astrophys. J.*, 721, 738